

Université du Québec  
Institut national de la recherche scientifique  
Centre Énergie Matériaux Télécommunications

**Probing and controlling few-femtosecond dynamics with ultrashort laser pulses:  
from gases to solids**

By  
Vincent Wanie

Thesis presented for the degree of  
*Philosophiae Doctor*, Ph.D.  
in Energy and Material Sciences

**Evaluation committee**

External examiner	Prof. Réal Vallée Université Laval
External examiner	Prof. Anne L'Huillier Lund University
Internal examiner	Prof. Tsuneyuki Ozaki INRS-ÉMT
Research supervisor	Prof. François Légaré INRS-ÉMT



# Remerciements

D’abord je tiens à remercier les Professeur(e)s Anne L’Huillier, Réal Vallée et Tsuneyuki Ozaki d’avoir accepté de faire partie du comité d’évaluation de ma thèse, ainsi que pour l’intérêt qu’ils ont porté à mes travaux à travers leurs commentaires et les échanges intéressants lors de la soutenance.

François, je suis plus qu’heureux d’avoir fait ta rencontre il y a déjà plusieurs années. Merci pour ta confiance ainsi que pour l’appui inconditionnel et la liberté que tu m’as offert tout au long de la thèse. Une grande partie du leadership que j’ai acquis est sans aucun doute inspirée du tien. Ce fût (et sera toujours) un plaisir de travailler avec toi.

À Francesca, merci de m’avoir si bien accueilli à Milan ainsi que pour ton support qui m’a permis de m’intégrer rapidement (jusqu’à en apprendre à parler italien!). Nous avons depuis vécu plusieurs moments, incluant un changement de pays (et de culture) qui aura mené à une multitude de projets intéressants. Je vous remercie également toi et Maureen pour le support considérable concernant la (trop) grande quantité de procédures administratives nécessaires pour un couple non européen, ça en aura néanmoins valu la peine.

Merci à tous les gens avec qui j’ai eu la chance de travailler dans les divers laboratoires de Varennes, Milan et Hambourg: Nico, Sam, Bruno, Vincent, Guilmot et Heide pour ces premières années qui m’ont fait découvrir ce milieu. Erik, j’ai la chance de travailler avec toi depuis mon arrivée à Milan, puis maintenant à Hambourg, et c’est quelque chose que j’apprécie énormément. Merci pour les nombreuses heures à discuter science (même lors de nos voyages de ski, les remontepentes deviennent beaucoup moins longs), j’ai énormément appris grâce à toi. Heide et Andrea T. pour votre collaboration et vos conseils, particulièrement pour la rédaction d’un bon nombre de documents. Philippe, ce fût un plaisir de me faire initier à l’ablation et de réaliser ces nombreux ‘beamtimes’ à ALLS avec toi, j’espère qu’on aura la chance de retravailler ensemble. À Nico, je me souviendrai des conférences ‘divertissantes’ passées à tes côtés ainsi que de nos sorties ‘après beamtime’ avec Sam sur le Plateau, ce fût agréable de travailler avec toi. Merci à Lorenzo, Sergey, Krishna, Mara, Andrea C., Gaia et Laura pour les bons moments passés au labo (et en dehors) à Hambourg, à Davide, Mario, Matteo et Mauro pour les nombreux lunches à Milan passés à discuter de sujets parfois sérieux, parfois très comiques. Enfin, merci à Antoine Laramée, Carol Morissette, Mauro Scarparo, Antonio Di Natale, Carlos Brambilla, Giuseppe Romano et Klas Pikull pour le support technique indispensable qui a contribué au succès de plusieurs projets.

Un merci particulier à deux amis (et un peu collègues), Sam et Comby. Antoine, nos parcours se sont croisés à plusieurs reprises, à Varennes, Bordeaux et Milan. Je te remercie spécialement pour le temps qu’on a passé ensemble à mon arrivée en Italie, cela a certainement facilité l’intégration. C’est toujours un plaisir de te côtoyer, que ce soit pour un ‘roadtrip’ haut en couleur en Croatie ou pour surfer sur les vagues d’Hossegor, que cela continue. Sam, on part de très loin: des 5 @ 8 de l’Université de Sherbrooke jusqu’à un mariage à Skopje, je te dois aussi ma première rencontre

avec François. C'est un plaisir de te fréquenter un peu partout dans le monde, j'ai hâte de voir ce qui suivra.

J'aimerais également remercier les gens de Bordeaux: Yann, depuis mon premier stage de maîtrise avec toi, merci pour ton hospitalité et tes conseils (ainsi que pour nourrir ma passion pour les kebabs), tu es quelqu'un que je respecte énormément. Merci également à Valérie, Baptiste, Etienne, Dominique et Bernard avec qui j'ai eu la chance de travailler à quelques reprises, vous êtes une équipe très motivante.

Tout ce travail aurait été beaucoup plus difficile sans le support de ma famille et d'amis: Je remercie mon coloc (et oncle) Pierre pour son hospitalité lors de mes multiples périodes passées à Varennes, et me souviendrai des moments à discuter de nos sujets de thèse complètement différents, cela a été une expérience intéressante. Merci à plusieurs ami(e)s, Martine, Alec, JP<sup>2</sup>, Pat, Fred, François, Charles, Iza, Juan, Alicia et Chris qui sont toujours présents et prêts à me voir (lorsque je suis au bon endroit). Un remerciement plus qu'important à mes parents et à ma soeur, car ce sont souvent les personnes les plus proches qui reçoivent le moins d'éloges. Vous avez toujours su me supporter malgré la distance: d'un premier départ vers Drummondville jusqu'à l'Europe. Merci pour l'attention que vous me portez depuis toujours, vous êtes une famille extraordinaire et ce que j'ai achevé jusqu'à maintenant est en grande partie grâce à vous. Merci milles fois pour tout.

Enfin, merci à toi Magda. Derrière cette thèse nous avons surmonté plusieurs défis qui n'ont fait que démontré ta générosité, ta patience et ta persévérance. Merci pour tous ces moments que nous vivons ensemble, je suis plus qu'heureux de débiter ce qui nous attend avec toi.

---

# Abstract

This thesis document treats the utilization of femtosecond and attosecond light pulses to study dynamical properties of molecules and solids with high temporal resolution. The first part describes the development of new light sources – based on high harmonic generation – opening new perspectives in attosecond science and strong-field physics. Experiments are presented subsequently.

A tabletop soft x-ray source was developed, covering the water window between 284 and 543 eV where carbon- and nitrogen-based molecules absorb light more efficiently than water. Providing site-specificity for experiments in the gas phase, this coveted spectral range is also highly relevant to study bio-relevant and organic molecules in aqueous environment. To improve the performances of the soft x-ray source, the development of few-cycle, high intensity 1.8  $\mu\text{m}$  pulses via hollow-core fiber post-compression is also presented.

A novel beamline combining attosecond XUV pulses, few-femtosecond UV and NIR pulses with an attosecond delay stability was built. Offering an unprecedented temporal resolution for experiments involving photoexcitation/ionization by UV radiation, this light source will be used to study UV-induced electron dynamics in the neutral states of bio-relevant molecules.

We used the sub-cycle resolution of two-color laser fields (1800 & 900 nm) to control the electron localization in molecular hydrogen. Reproduced by theoretical calculations, the results highlight the interplay between nuclear and electronic degrees of freedoms providing an enhanced level of control for this benchmark reaction. The same two-color technique was transposed to solid samples to study the strong-field ionization of lithium niobate. Borrowing concepts from molecular science, we demonstrate the control of the ionization rate in the material using laser-ablation measurements. The results highlight the role of the permanent polarization of materials in strong-field ionization, bridging a gap between the gas phase and the solid state.

An attosecond experiment is presented where isolated attosecond XUV pulses were employed to ionize inner-valence orbitals of adenine, one of the DNA building blocks. With the help of state-of-the-art calculations, a shake-up dynamics was identified for the first time in a polyatomic molecule with a characteristic time of 2.3 fs. It is further demonstrated that acting with a properly delayed NIR pulse allows stabilizing the molecule before non-adiabatic effects take place, preventing fragmentation.

Finally, we demonstrate the capabilities of our new beamline by investigating the UV-induced chiral dynamics of methyl-lactate through photoelectron circular dichroism measurements. The high sensitivity of the method reveals an inversion of the chiral response of the molecule after 20 fs, possibly originating from the competition between the temporal evolution of electronic wavepackets.

**Keywords:** photoionization, pump-probe, high-harmonic generation, attosecond beamline, ultrashort UV pulses, electron correlations, non-adiabatic dynamics, laser ablation, LiNbO<sub>3</sub>, chirality



# Résumé

Ce travail de thèse traite de l'utilisation d'impulsions lumineuses femtosecondes et attosecondes pour étudier les propriétés dynamiques de molécules et de solides avec une résolution temporelle élevée. La première partie décrit le développement de nouvelles sources de lumière - basées sur la génération d'harmoniques d'ordres élevés - ouvrant de nouvelles perspectives en science attoseconde et en physique des champs forts. Les expériences sont par la suite présentées.

Une source de rayons X mous de table a été développée, couvrant la fenêtre de l'eau entre 284 et 543 eV, où les molécules à base d'atomes de carbone et d'azote absorbent la lumière plus efficacement que l'eau. Fournissant une spécificité de site pour des expériences en phase gazeuse, cette gamme spectrale convoitée est également très pertinente pour l'étude de molécules organiques et d'intérêt biologique en milieu aqueux. Afin d'améliorer la source de rayons X mous, le développement d'impulsions à 1.8  $\mu\text{m}$  de quelques cycles optiques et de haute intensité obtenues par post-compression dans une fibre creuse est également présenté.

Une nouvelle ligne de lumière combinant des impulsions attosecondes XUV, ainsi que des impulsions UV et NIR de quelques femtosecondes avec une stabilité de délai attoseconde a été construite. Offrant une résolution temporelle sans précédent pour réaliser des expériences impliquant une photoexcitation/ionisation par du rayonnement UV, cette source de lumière sera utilisée pour étudier la dynamique des électrons induite par des impulsions UV dans les états neutres de molécules d'intérêt biologique.

Nous avons utilisé la résolution sous-cycle de champs lasers à deux couleurs (1800 & 900 nm) pour contrôler la localisation de densité électronique dans l'hydrogène moléculaire. Reproduits par des calculs théoriques, les résultats mettent en évidence l'interaction entre les degrés de liberté nucléaires et électroniques qui permet une amélioration du niveau de contrôle pour cette réaction prototype. La même technique à deux couleurs a été transposée à des échantillons solides pour étudier l'ionisation en champ fort du niobate de lithium. En empruntant des concepts de science moléculaire, nous démontrons le contrôle du taux d'ionisation dans le matériau en utilisant l'ablation laser comme observable. Les résultats mettent en évidence le rôle de la polarisation permanente des matériaux dans l'ionisation en champ intense, faisant le pont entre la phase gazeuse et l'état solide.

Une expérience attoseconde est présentée, où des impulsions attoseconde isolées XUV ont été utilisées pour ioniser l'adénine, l'une des bases nucléiques de l'ADN. À l'aide de calculs de pointe, une dynamique électronique de type 'shake-up' a été identifiée pour la première fois dans une molécule polyatomique, se produisant en un temps caractéristique de 2.3 fs. Nous démontrons également qu'en utilisant une impulsion NIR correctement synchronisée, il est possible de stabiliser la molécule avant que des effets non-adiabatiques ne se produisent, prévenant de cette manière une fragmentation.

Enfin, nous démontrons les capacités de notre nouvelle ligne de lumière en étudiant la dynamique chirale du lactate de méthyle induite par des impulsions UV ultrabrèves, ceci grâce à des mesures de dichroïsme circulaire de photoélectrons. La grande sensibilité de la méthode révèle une inversion de la réponse chirale de la molécule après 20 fs, provenant possiblement de la compétition entre l'évolution temporelle de paquets d'ondes électroniques.

**Mots-clés:** photoionisation, pompe-sonde, génération d'harmoniques d'ordres élevés, ligne de lumière attoseconde, impulsions UV ultrabrèves, corrélations électroniques, dynamiques non-adiabatiques, ablation laser,  $\text{LiNbO}_3$ , chiralité

## List of publications

The articles with an asterisk (\*) are presented in this thesis.

- **\*Wanie, V.**, Galli, M.; Månsson, E. P.; Trabattoni, A.; Frassetto, F.; Colaizzi, L.; Cartella, A.; Saraswathula, K.; Lopes, D. P.; Vázquez, R. M.; Osellame, R.; Poletto, L.; Légaré, F.; Nisoli, M.; Calegari, F. *A flexible beamline combining XUV attosecond pulses with few-femtosecond UV and near-infrared pulses for time-resolved experiments*. Review of Scientific Instruments (under review).
- **\*Månsson, E.P.**, Latini, S.; Covito, F.; **Wanie, V.**; Galli, M.; Perfetto, E.; Stefanucci, G.; Hübener, H.; De Giovannini, U.; Castrovilli, M. C.; Trabattoni, A.; Frassetto, F.; Poletto, L.; Greenwood, J. B.; Légaré, F.; Nisoli, M.; Rubio, A.; Calegari, F. *Laser-assisted stabilisation of ionised adenine: preventing molecular dissociation by acting at extreme time scales*. Nature Physics (under review).
- Endo, T.; Neville, S. P.; **Wanie, V.**; Beaulieu, S.; Qu, C.; Deschamps, J.; Lassonde, P.; Schmidt, B. E.; Fujise, H.; Fushitani, M.; Hishikawa, A.; Houston, P. L.; Bowman J. M.; Schuurman, M. S.; Légaré, F.; Ibrahim, H. *Capturing roaming molecular fragments in real-time*. Science (Accepted).
- **\*Wanie, V.**; Shao, T. J.; Lassonde, P.; Calegari, F.; Vidal, F.; Ibrahim, H.; Bian, X. B.; Légaré, F. *Laser polarization dependence of strong-field ionization in lithium niobate*. Physical Review B 2020, 101, 214311.
- Trabattoni, A.; Colaizzi, L.; Ban, L.; **Wanie, V.**; Saraswathula, K.; Månsson, E. P.; Rupp, P.; Liu, Q.; Seiffert, L.; Herzig, E. A.; Cartella, A.; Yoder, B. Y.; Légaré, F.; Kling, M. F.; Fennel, T.; Signorell, R.; Calegari, F. *Photoelectron spectroscopy of large water clusters ionized by an XUV comb*. Journal of Photonics 2020, 2, 035007.
- **\*Wanie, V.**; Shao, T. J.; Lassonde, P.; Ibrahim, H.; Deschamps, J.; Liu, J. Q.; Vargas, F. A.; Vidal, F.; Ruediger, A.; Calegari, F.; Bian, X. B.; Légaré, F. *Control of strong-field ionization in ferroelectric lithium niobate: Role of the spontaneous polarization*. Physical Review B 2020, 101, 184103.
- **\*Galli, M.**; **Wanie, V.**; Lopes, D. P.; Månsson, E. P.; Trabattoni, A.; Colaizzi, L.; Saraswathula, K.; Cartella, A.; Frassetto, F.; Poletto, L.; Légaré, F.; Stagira, S.; Nisoli, M.; Vázquez, R. M.; Osellame, R.; Calegari, F. *Generation of deep ultraviolet sub-2-fs pulses*. Optics Letters 2019, 44, 1308-1311.
- Cardin, V.; Schmidt, B. E.; Thiré, N.; Beaulieu, S.; **Wanie, V.**; Negro, M.; Voizzi, C.; Tosa, V.; Légaré, F. *Self-channelled high harmonic generation of water window soft x-rays*. Journal of Physics B: Atomic, Molecular and Optical Physics 2018, 17, 174004.
- Bionta, M. R.; **Wanie, V.**; Gruson, V.; Chaillou, J.; Émond, N.; Lepage, D.; Lassonde, P.; Chaker, M.; Légaré, F. *Probing the phase transition in VO<sub>2</sub> using few-cycle 1.8 μm pulses*. Physical Review B 2018, 97, 125126.
- Beaulieu, S.; Camp, S.; Descamps, D.; Comby, A.; **Wanie, V.**; Petit, S.; Légaré, F.; Schafer, K. J.; Gaarde, M. B.; Catoire, F.; Mairesse, Y. *Role of Excited States In High-order Harmonic Generation*. Physical Review Letters 2016, 117, 203001.

- Nahon, L.; Nag, L.; Garcia, G. A.; Myrgorodska, I.; Meierhenrich, U.; Beaulieu, S.; **Wanie, V.**; Blanchet, V.; Génaux, R.; Powis, I. *Determination of accurate electron chiral asymmetries in fenchone and camphor in the VUV range: sensitivity to isomerism and enantiomeric purity.* Physical Chemistry Chemical Physics 2016, 18, 12696-12706.
- \***Wanie, V.**; Ibrahim, H.; Beaulieu, S.; Thiré, N.; Schmidt, B. E.; Deng, Y.; Alnaser, A. S.; Litvinyuk, I.; Tong, X. M.; Légaré, F. *Coherent control of D<sub>2</sub>/H<sub>2</sub> dissociative ionization by a mid-infrared two-color laser field.* Journal of Physics B: Atomic, Molecular and Optical Physics 2016, 49, 025601.
- \*Cardin, V.; Thiré, N.; Beaulieu, S.; **Wanie, V.**; Légaré, F.; Schmidt, B. E. *0.42 TW 2-cycle pulses at 1.8 μm via hollow-core fiber compression.* Applied Physics Letters 2015, 107, 181101.
- Thiré, N.; Beaulieu, S.; Cardin, V.; Laramée, A.; **Wanie, V.**; Schmidt, B. E.; Légaré, F. *10 mJ 5-cycle pulses at 1.8 μm through optical parametric amplification.* Applied Physics Letters 2015, 106, 091110.
- Ibrahim, H.; Wales, B.; Beaulieu, S.; Schmidt, B. E.; Thiré, N.; Fowe, E. P.; Bisson, É.; Hebeisen C. T.; **Wanie, V.**; Giguère, M.; Kieffer, J. C.; Spanner, M.; Bandrauk A. D.; Sanderson, J.; Schuurman, M. S.; Légaré, F. *Tabletop imaging of structural evolutions in chemical reactions demonstrated for the acetylene cation.* Nature Communications 2014, 5, 4422.
- Guilbault, A. A.; Basdevant, B.; **Wanie, V.**; Legault, C. Y. *Catalytic Enantioselective α-Tosyloxylation of Ketones Using Iodoaryloxazoline Catalysts: Insights on the Stereoinduction Process.* The Journal of Organic Chemistry 2012, 77, 24, 11283–112958.

# Table of Contents

Acknowledgements/Remerciements	iii
Abstract	v
Résumé	vii
Table of Contents	xi
List of acronyms	xv
<b>I Main Text</b>	<b>1</b>
<b>1 Introduction, thesis plan and objectives</b>	<b>3</b>
1.1 Introduction . . . . .	3
1.2 Thesis plan and objectives . . . . .	5
1.3 Introduction . . . . .	9
1.4 Plan de thèse et objectifs . . . . .	11
<b>2 High energy, few-cycle 1.8 <math>\mu\text{m}</math> pulses for strong-field interactions</b>	<b>15</b>
2.1 Femtosecond lasers . . . . .	15
2.2 Optical parametric amplifiers . . . . .	16
2.3 Spectral broadening and post-compression . . . . .	18
2.4 Hollow-core fiber post-compression . . . . .	20
2.5 Article I – Summary . . . . .	21
2.6 Article I – 0.42 TW 2-cycle pulses at 1.8 $\mu\text{m}$ via hollow-core fiber compression . . . . .	22
2.7 High-harmonic generation . . . . .	29
2.7.1 Three-step model . . . . .	29
2.7.2 Quantum aspect of HHG . . . . .	31
2.7.3 Phase matching . . . . .	33
2.8 Water window . . . . .	34
2.9 Soft x-ray generation at the Advanced Laser Light Source . . . . .	35
2.10 Supplementary article – Self-channelled high harmonic generation of water window soft x-ray . . . . .	38
<b>3 An attosecond beamline for pump-probe experiments using few-femtosecond UV pulses</b>	<b>39</b>
3.1 Third-harmonic generation in gases . . . . .	40
3.2 Generation of isolated attosecond pulses . . . . .	42

3.3	Article II – Summary . . . . .	43
3.4	Article III – Summary . . . . .	44
3.5	Article II – Generation of deep ultraviolet sub-2-fs pulses . . . . .	48
3.6	Article III – A flexible beamline combining XUV attosecond pulses with few-femtosecond UV and near-infrared pulses for time-resolved experiments . . . . .	56
<b>4</b>	<b>Coherent control in the dissociative ionization of molecular hydrogen</b>	<b>75</b>
4.1	Coherent control for a two-level system . . . . .	76
4.2	Article IV – Summary . . . . .	78
4.3	Article IV – Coherent control of D <sub>2</sub> /H <sub>2</sub> dissociative ionization by a mid-infrared two-color laser field . . . . .	80
<b>5</b>	<b>Strong-field ionization of lithium niobate</b>	<b>95</b>
5.1	Strong-field ionization in non-centrosymmetric systems . . . . .	96
5.2	LiNbO <sub>3</sub> and its spontaneous polarization . . . . .	98
5.3	Laser-induced ablation . . . . .	98
5.4	Density functional theory . . . . .	99
5.5	Summaries for articles V and VI . . . . .	100
5.6	Article V – Laser polarization dependence of strong-field ionization in lithium niobate	103
5.7	Article VI – Control of strong-field ionization in ferroelectric lithium niobate: role of the spontaneous polarization . . . . .	115
<b>6</b>	<b>Probing electron dynamics in bio-relevant molecules</b>	<b>125</b>
6.1	Few-femtosecond dynamics following photoionization of bio-relevant molecules . . . . .	125
6.2	Article VII - Summary . . . . .	127
6.2.1	Fitting of the fragmentation dynamics . . . . .	129
6.3	Laser-assisted stabilisation of ionised adenine: preventing molecular dissociation by acting at extreme time scales . . . . .	131
<b>7</b>	<b>Femtosecond-resolved Rydberg states dynamics in chiral molecules</b>	<b>141</b>
7.1	Introduction . . . . .	141
7.2	Context of the work . . . . .	144
7.3	Experiment . . . . .	145
7.4	Results . . . . .	146
7.5	Interpretation . . . . .	149
7.6	Conclusion . . . . .	153
<b>8</b>	<b>General conclusions and perspectives</b>	<b>155</b>
<b>II</b>	<b>Résumé de la thèse en français</b>	<b>159</b>
9.1	Article I - Impulsions de 0.42 TW et 2 cycles optiques à 1.8 $\mu\text{m}$ par compression dans une fibre creuse . . . . .	161
9.2	Article supplémentaire - Auto-guidage de la génération d'harmonique dans la fenêtre de l'eau . . . . .	162
9.3	Article II - Génération d'impulsions ultraviolettes sub-2-fs . . . . .	163
9.4	Article III – Ligne de lumière versatile combinant des impulsions attosecondes XUV avec des impulsions UV et infrarouges proches de quelques femtosecondes pour expériences résolues en temps . . . . .	164

9.5	Article IV – Contrôle cohérent de l’ionisation dissociative dans $D_2/H_2$ à l’aide d’un champ laser à deux couleurs dans l’infrarouge moyen . . . . .	165
9.6	Article V – Dépendance en polarisation laser de l’ionisation en champ fort du niobate de lithium & Article VI – Contrôle de l’ionisation en champ fort dans le niobate de lithium : rôle de la polarisation spontanée . . . . .	166
9.7	Article VI – Stabilisation assistée par laser de l’adénine ionisée: prévenir la dissociation moléculaire en agissant à des échelles temporelles extrêmes . . . . .	168
9.8	Dynamiques moléculaires induites par excitation UV ultrabrève et sondée par dichroïsme circulaire de photoélectrons . . . . .	170

**III Appendices and References 173**

<b>Appendix A: Supplemental Material for article V – Laser polarization dependence of strong-field ionization in lithium niobate</b>	<b>177</b>
--------------------------------------------------------------------------------------------------------------------------------------	------------

<b>Appendix B: Supplementary Material for article VI: Control of strong-field ionization in ferroelectric lithium niobate: Role of the spontaneous polarization</b>	<b>183</b>
---------------------------------------------------------------------------------------------------------------------------------------------------------------------	------------

<b>Appendix C: Supplementary Information for article VII – Laser-assisted stabilisation of ionised adenine: preventing molecular dissociation by acting at extreme time scales</b>	<b>195</b>
------------------------------------------------------------------------------------------------------------------------------------------------------------------------------------	------------

<b>References</b>	<b>209</b>
-------------------	------------



# List of acronyms

<b>XUV</b>	extreme ultraviolet	<b>GDD</b>	group delay dispersion
<b>UV</b>	ultraviolet	<b><math>I_p</math></b>	ionization potential
<b>IR</b>	infrared	<b>SFA</b>	strong-field approximation
<b>DNA</b>	deoxyribonucleic acid	<b>FT</b>	Fourier transform
<b>RABBIT</b>	Reconstruction of Attosecond Beating By Interference of Two-photon transitions	<b>XAS</b>	X-ray absorption spectroscopy
<b>HHG</b>	high harmonic generation	<b>CCD</b>	charge-coupled device
<b>OPA</b>	optical parametric amplification	<b>THG</b>	third-harmonic generation
<b>NIR</b>	near-infrared	<b>SVEA</b>	slowly varying envelope approximation
<b>TDSE</b>	time-dependent Schrödinger equation	<b>GVD</b>	group velocity dispersion
<b>CPA</b>	chirped pulse amplification	<b>IAP</b>	isolated attosecond pulse
<b>Ti:Sapphire</b>	titanium sapphire	<b>PG</b>	polarization gating
<b>TL</b>	transform limit	<b>CEP</b>	carrier-envelope phase
<b>HCF</b>	hollow-core fiber	<b>PCF</b>	photonic crystal fiber
<b>MIR</b>	mid-infrared	<b>TG-FROG</b>	transient-grating frequency-resolved optical gating
<b>LIED</b>	laser-induced electron diffraction	<b>NMR</b>	nuclear magnetic resonance
<b>DFG</b>	difference frequency generation	<b>REMPI</b>	resonance-enhanced multiphoton ionization
<b>OPCPA</b>	optical parametric chirped pulse amplification	<b>SH</b>	second harmonic
<b>FOPA</b>	frequency domain optical parametric amplification	<b>FC</b>	Franck-Condon
<b>SPM</b>	self-phase modulation	<b>NWP</b>	nuclear wavepacket
<b>BBO</b>	beta barium borate	<b>LIA</b>	laser-induced ablation
		<b>SBEs</b>	semiconductor Bloch equations
		<b>ATI</b>	above-threshold ionization

<b>ADK</b>	Ammosov-Delone-Krenov	<b>FWHM</b>	full width at half maximum
<b>SAW</b>	surface acoustic wave	<b>VIS</b>	visible
<b>PPLN</b>	periodically poled lithium niobate	<b>SHG</b>	second harmonic generation
<b><math>P_s</math></b>	spontaneous polarization	<b>FLICE</b>	femtosecond laser irradiation followed by chemical etching
<b>SFI</b>	strong-field ionization	<b>RGA</b>	residual gas analyzer
<b>DFT</b>	density functional theory	<b>SVLS</b>	spherical varied-line-space
<b>CT</b>	charge transfer	<b>CW</b>	continuous wave
<b>VMI</b>	velocity map imaging	<b>KE</b>	kinetic energy
<b>TD-DFT</b>	time-dependent density functional theory	<b>RCE</b>	recollision excitation
<b>LUMO</b>	lowest unoccupied molecular orbital	<b>BS</b>	bond softening
<b>HOMO</b>	highest occupied molecular orbital	<b>ATD</b>	above-threshold dissociation
<b>CPL</b>	circularly polarized light	<b>CEI</b>	Coulomb explosion imaging
<b>CD</b>	circular dichroism	<b>DOS</b>	density of states
<b>PECD</b>	photoelectron circular dichroism	<b>VASP</b>	Vienna Ab initio Simulation Package
<b>PAD</b>	photoelectron angular distribution	<b>MF-PADs</b>	molecular frame photoelectron angular distributions
<b>PES</b>	photoelectron spectrum	<b>AC</b>	alternating current
<b>MCP</b>	microchannel plate	<b>ICD</b>	interatomic Coulomb decay
<b>VUV</b>	vacuum ultraviolet	<b>KS</b>	Kohn-Sham
<b>TR-PECD</b>	time-resolved photoelectron circular dichroism	<b>BZ</b>	Brillouin zone
<b>IRF</b>	instrument response function	<b>GAA</b>	generalized gradient approximation
<b>VTZ</b>	valence triple zeta	<b>LDA</b>	local density approximation
<b>VDZ</b>	valence double zeta	<b>PAW</b>	projector augmented wave
<b>CREI</b>	charge-resonance-enhanced ionization	<b>AFM</b>	atomic force microscopy
<b>FS</b>	fused silica		

**Part I**

**Main Text**



# Chapter 1

## Introduction, thesis plan and objectives

### 1.1 Introduction

Light waves that interact with atoms, molecules and solids constitute a powerful tool to investigate the static and dynamical properties of matter. In X-ray science for instance, diffraction techniques have enabled the elucidation of structures including crystalline materials, proteins and DNA. For these static measurements, the requirement to record an image with a proper resolution is that the diffraction limit of the wavelength must be smaller than the interatomic distances constituting the sample structure, typically of a few Ångström. In analogy, the resolution requirement to track dynamical events with a camera is that the exposure time – the amount of time for which the device collects light – must be shorter than the event itself. In this way, a succession of snapshots (images) acquired during the motion of an object constitutes a well-resolved movie. However, if the event to be captured is faster than the exposure time, the images appear blurred since they do not show the object at a fixed position in space but an average of this object over several positions. Thus the movie cannot be resolved.

Several fundamental properties of matter affecting our daily lives involve dynamics that occur at ultrafast timescales. For instance, the processes of vision, UV-induced damage of DNA and photosynthesis are triggered by molecular photoexcitation. In molecules, rotational and vibrational dynamics that are responsible for chemical reactions take place on the picosecond ( $1 \text{ ps} = 10^{-12} \text{ s}$ ) to femtosecond timescales ( $1 \text{ fs} = 10^{-15} \text{ s}$ ). Intrinsically fast, the study of such dynamics required major technological advances to provide an ultrafast camera capable of providing sufficient temporal resolution. In 1960, Maiman introduced the laser technology [1] for which the development expanded extremely rapidly, allowing for the creation of shorter and shorter coherent light pulses. Using

laser pulses with femtosecond duration, a common approach to follow the temporal evolution of nuclear motion in molecules utilizes the pump–probe scheme: A first pump pulse creates a coherent superposition of states that triggers molecular motion. Snapshots of the molecular dynamics are then captured by a delayed probe pulse. Through the femtosecond laser technology, the field of femtochemistry has revolutionized our understanding of molecular processes and led to the Nobel Prize in chemistry in 1999, awarded to Zewail for his research on transition states in photochemical reactions [2].

Another important timescale in molecular dynamics is within the attosecond domain (1 as =  $10^{-18}$  s) where electronic motion occurs. The discovery of high harmonic generation in the late 80's [3, 4] together with the semi-classical description of the process a few years afterwards [5, 6] provided the groundwork to produce XUV attosecond pulses. The first demonstrations of attosecond pulses in 2001 [7, 8] and the development of methods to characterize the temporal properties of the XUV radiation, such as RABBIT [7, 9] and the attosecond streak camera [10], provided the tools to perform attosecond pump-probe experiments for tracking electron dynamics in atoms, molecules and solids. Seminal works include the measurement of photoionization delays in atomic gases [11, 12], molecules [13] and solids [14]. Another important exploitation of attosecond pulses to study and control molecular systems was performed by Sansone *et al.* [15]. In this latter case, the electron localization in hydrogen served as an observable to track the molecular dynamics. An impressive experiment also demonstrated the real-time tracking of the charge migration process in a biomolecule [16].

Of particular interest in molecules is the large mass difference between nuclei and electrons, resulting in their motions often occurring on distinct timescales. For a number of cases, after molecular photoionization, the variation of the electronic density on the attosecond timescale can be considered to instantaneously adapt to variation of the nuclear coordinates on the femtosecond timescale. Electrons and nuclei are treated separately. In larger molecules however, this (adiabatic) Born-Oppenheimer approximation is often not valid as the energy difference between electronic states narrows down and couplings between nuclear and electronic degrees of freedoms become more frequent. In this case, attosecond experiments can address the role of the early electron dynamics upon photoionization on the subsequent molecular relaxation and determine if they can ultimately be exploited to control the outcome of photochemical reactions [17].

In this context, the work presented in this thesis was realized with the general objective to resolve ultrafast dynamics in molecules, potentially involving couplings between nuclear and electronic degrees of freedom at the femtosecond and attosecond timescales. As the tools to perform the experiments were not always available, a significant amount of time of the Ph.D. has also been spent to develop new light sources for applications in strong-field physics and attosecond science. Most of the experiments rely on pump-probe schemes involving photoionization and detection of charged particles (electrons and ions) using different types of spectrometers. Photoionization playing a key role in molecular science, understanding its analog in materials – the photoelectric effect – is

key for several technological applications. Therefore, part of the Ph.D. work has also been devoted to transpose concepts from molecules to solids by studying the strong-field ionization response of materials. The results obtained in this thesis finally show that understanding the processes underlying ultrafast dynamics often offers a mean to control the properties of matter.

## 1.2 Thesis plan and objectives

The thesis consists of eight chapters and follows the format of a thesis by articles. Subsequent to this introduction, chapters 2 and 3 describe cutting edge laser sources that were developed during the Ph.D., opening new perspectives in strong-field physics and attosecond science. Chapters 4-7 present experiments that disclose inner workings of ultrafast processes relevant in physics, chemistry and materials science. Chapter 8 contains a general conclusion and a personal point of view regarding future research activities.

### Chapter 2: High energy, few-cycle 1.8 $\mu\text{m}$ pulses for strong-field interactions

The development of ultrashort and high energy infrared pulses is mandatory to approach several challenges in ultrafast science:

- (i) High harmonic generation (HHG) in gases is the groundwork of attosecond science and extending the harmonic spectra towards higher photon energies is a route to several breakthroughs in spectroscopy. Achieving this crucial task, however, requires increasing the driving field wavelength towards the infrared and reaching higher peak intensities by reducing the pulse duration.
- (ii) To study the transient properties of solids in the strong-field regime, infrared pulses with wavelengths carrying photon energies below the bandgap energy of materials must be employed with sufficient intensity.
- (iii) Longer optical periods in the infrared (6 fs at 1800 nm) compared to the near-infrared (2.7 fs at 800 nm) approach the vibrational periods in molecules and may significantly affect the outcome of subcycle interactions during photochemical processes.

To address these challenges, a first objective for the Ph.D. concerned the *development of few-cycle, high-energy laser pulses in the infrared spectral range*. We first worked on the generation and characterization of 10 mJ pulses centered at 1800 nm obtained through a high energy optical parametric amplifier (OPA) at 100 Hz repetition rate, as described in Thiré *et al.* 2015 [18]. In

article I, we compressed the high energy infrared pulses down to two optical cycles (12 fs, 5 mJ) via spectral broadening in a stretched hollow-core fiber. Additionally, we used the high energy OPA for the generation of soft x-ray and generated spectra covering the entire water window (from 284 to 543 eV) with sufficient photon flux for single shot measurements at the carbon *K*-edge.

### **Chapter 3: An attosecond beamline for pump-probe experiments using few-femtosecond UV pulses**

The major part of the Ph.D. was spent on *the construction of an attosecond beamline combining XUV and ultraviolet (UV) pulses with an unprecedented temporal resolution*. Several key processes in bio-relevant systems are initiated by molecular excitation in the neutral states. However, these dynamics are not accessible with XUV-pump pulses as the photon energies inevitably ionize the target and therefore restrict time-resolved studies to ionic states. To investigate the role of electron dynamics in the neutral states of bio-relevant molecules, the use of ultrashort UV pulses is of strong interest. In this perspective, we have developed a laser source exploiting nonlinear third-harmonic generation in argon gas, delivering one of the shortest available UV pulses (article II). We integrated this unique setup to an all-vacuum beamline providing also near-infrared (NIR) pulses and isolated attosecond XUV pulses (article III). While typical attosecond XUV-pump NIR-probe experiments can still be realized, the performances of the beamline allow to design pump-probe experiments for tracking UV-induced electron dynamics in the neutral states of bio-relevant molecules, paving the way for attosecond ultraviolet spectroscopy.

### **Chapter 4: Coherent control in the dissociative ionization of molecular hydrogen**

This chapter describes the utilization of 1800 nm pulses to control photo-induced molecular dynamics. In article IV, we combined a 1800 nm field to its second harmonic to demonstrate an enhanced level of control when steering the electron density during the dissociative ionization of the hydrogen molecule ( $H_2$ ). We identified four distinct fragmentation channels for this benchmark reaction and compared the experimental data with time-dependent Schrödinger equation (TDSE) calculations for the molecular ion. From this work, the objective of *reaching a better understanding towards the control of photochemical reactions* was achieved.

### **Chapter 5: Strong-field ionization in lithium niobate**

In this chapter, we extend to solid systems the control of ultrafast dynamics with 1800 nm fields. In article V, we first characterized the strong-field ionization response of lithium niobate ( $LiNbO_3$ ) crystals when varying the orientation of the incident polarization in laser-induced ablation of the material. By studying different crystal cuts, we demonstrate the possibility to identify the presence

or absence of mirror symmetries which are characteristic of the crystal structure. We also identified the main chemical bonds that contribute to the ionization of the material. In article VI, we studied the role of a fundamental property of ferroelectric materials, the spontaneous polarization, in strong-field ionization of  $\text{LiNbO}_3$ . Through two-color laser-induced ablation measurements, we demonstrated how the spontaneous polarization can be exploited for the control of the ionization rate in non-centrosymmetric crystals, *bridging a gap between the gas phase and the solid state*.

## Chapter 6: Probing electron dynamics in bio-relevant molecules

One important challenge in attosecond science is to *understand the primary electron dynamics occurring in molecules forming our own biological system*. Notably, ionizing radiation can cause irreparable damage to DNA and its subunits, yet it is unclear what is the role of electrons in the very first instants following ionization. In article VII, we tracked the early molecular response that develops in adenine, a nucleobase of DNA, upon ionization by an isolated attosecond XUV pulse in the 17-35 eV energy range. With the help of theoretical calculations, we characterized for the first time a shake-up dynamics in a polyatomic molecule, taking place in a characteristic time of 2.3 fs. We further identified a laser-assisted stabilization mechanism to control the fragmentation of the molecule following XUV ionization. This work provides a clear example of control scheme that takes place before the occurrence of non-adiabatic effects.

## Chapter 7: Time-resolved UV-induced molecular dynamics probed by photoelectron circular dichroism

This chapter presents the first experiment that was realized using the UV pulses and the beamline described in Chapter 3. Via time-resolved photoelectron circular dichroism measurements, we studied the chiral dynamics of methyl-lactate, a derivative of lactic acid, following excitation by a few-femtosecond UV pulse. Since the theoretical model for this experiment is being developed during the writing of this thesis, we present the experimental results and possible interpretations. Due to the unique characteristics of the beamline developed during the Ph.D., this work reveals a dynamical inversion of the photoelectron forward/backward asymmetry in a chiral molecule occurring within few femtoseconds.

## Context of the thesis

Most of the Ph.D. was part of an international collaboration between the research teams of Prof. François Légaré and Prof. Francesca Calegari. For this reason, the results presented in the thesis document were obtained in three different laboratories with an amount of working time equally distributed. The development of ultrashort 1800 nm pulses at high energy, the generation of soft

x-ray and the redaction of the manuscript treating on molecular hydrogen were realized at the beginning of the Ph.D. at the Advanced Laser Light Source (ALLS, Canada). Afterwards, the development of ultrashort UV pulses and the construction of the XUV-UV attosecond beamline was initiated at the Politecnico di Milano (Italy), former institution of Prof. Calegari. During this period, the measurements in the adenine molecule were also performed. At that time, the group with whom I worked constituted of one Ph.D. student (Mara Galli) and one postdoctoral fellow (Erik P. Månsson). Finally, the entire beamline was moved to the Deutsches Elektronen-Synchrotron (DESY, Germany), current institution of Prof. Calegari. It was reconstructed with the help of a larger group (two additional Ph.D. students, one additional postdoctoral fellow and a team leader). Then, the time-resolved experiments on chiral molecules were completed in close collaboration with the Harmonics and Applications group of the CELIA laboratory (France), more precisely Etienne Bloch (Ph.D. student), Valérie Blanchet, Yann Mairesse and Bernard Pons. Finally, the work on  $\text{LiNbO}_3$  consisted of four experimental campaigns at ALLS that were distributed over the entire Ph.D.

### 1.3 Introduction

Les ondes lumineuses qui interagissent avec les atomes, les molécules et les solides constituent un outil puissant pour étudier les propriétés statiques et dynamiques de la matière. En science des rayons X par exemple, les techniques de diffraction ont permis d'élucider plusieurs structures incluant des matériaux cristallins, des protéines et l'ADN. Pour ces mesures statiques, le prérequis pour enregistrer une image avec une résolution appropriée est que la limite de diffraction de la longueur d'onde doit être plus petite que les distances interatomiques constituant la structure de l'échantillon, généralement de quelques Ångström. Par analogie, le prérequis en terme de résolution pour suivre des événements dynamiques avec une caméra est que le temps d'exposition - la durée pendant laquelle l'appareil collecte la lumière - doit être plus court que l'événement lui-même. De cette façon, une succession d'instantanés (images) acquis pendant le mouvement d'un objet constitue un film bien résolu. Cependant, si l'événement à capturer est plus rapide que le temps d'exposition, les images apparaissent floues car elles ne montrent pas l'objet à une position fixe dans l'espace mais une moyenne de cet objet sur plusieurs positions. Le film ne peut donc pas être résolu.

Plusieurs propriétés fondamentales de la matière affectant notre vie quotidienne impliquent des dynamiques qui se produisent à des échelles de temps ultrarapides. Par exemple, les processus de la vision, de la dégradation de l'ADN induite par les UV et de la photosynthèse sont déclenchés par la photoexcitation moléculaire. Dans les molécules, les dynamiques rotationnelles et vibrationnelles qui sont responsables des réactions chimiques se produisent à des échelles de temps allant de la picoseconde ( $1 \text{ ps} = 10^{-12} \text{ s}$ ) à la femtoseconde ( $1 \text{ fs} = 10^{-15} \text{ s}$ ). Intrinsèquement rapide, l'étude de ces dynamiques a nécessité des avancées technologiques majeures pour fournir une caméra ultrarapide capable d'offrir une résolution temporelle suffisante. En 1960, Maiman a introduit la technologie laser [1] dont le développement s'est développé extrêmement rapidement, permettant la création d'impulsions de lumière cohérente de plus en plus courtes. En utilisant des impulsions laser de durée femtoseconde, une approche commune pour suivre l'évolution temporelle du mouvement nucléaire dans les molécules utilise la technique pompe-sonde : Une première impulsion pompe crée une superposition cohérente d'états qui déclenche le mouvement moléculaire. Des instantanés de la dynamique moléculaire sont ensuite captés par une impulsion sonde retardée. Grâce à la technologie laser femtoseconde, le domaine de la femtochimie a révolutionné notre compréhension des processus moléculaires et a conduit au prix Nobel de chimie en 1999, décerné à Zewail pour ses recherches sur les états de transition lors de réactions photochimiques [2].

Une autre échelle de temps importante en dynamique moléculaire se situe dans le domaine de l'attoseconde ( $1 \text{ as} = 10^{-18} \text{ s}$ ) où le mouvement électronique se produit. La découverte du processus de génération d'harmoniques d'ordres élevées à la fin des années 80 [3, 4] ainsi que sa description semi-classique quelques années plus tard [5, 6] ont fourni les bases pour produire des impulsions attosecondes XUV. Les premières démonstrations d'impulsions attosecondes en 2001 [7, 8] et le développement de méthodes pour caractériser les propriétés temporelles du rayonnement

XUV, telles que RABBIT [9, 7] et la caméra à balayage attoseconde [10], ont fourni les outils pour réaliser des expériences pompe-sonde attosecondes pour suivre les dynamiques électroniques dans les atomes, les molécules et les solides.

D'importants travaux incluent des mesures de délai de photoionisation dans les gaz atomiques [11, 12], les molécules [13] et les matériaux solides [14]. Une autre exploitation importante d'impulsions attosecondes pour l'étude et le contrôle de systèmes moléculaires a été réalisée par Sansone *et al.* [15]. Dans ce dernier cas, la localisation de l'électron dans le cation de l'hydrogène a servi d'observable pour suivre la dynamique moléculaire. Une expérience impressionnante a également démontré le suivi en temps réel du processus de migration de charges dans une biomolécule [16].

Dans les molécules, la grande différence de masse entre les noyaux et les électrons est particulièrement intéressante, faisant en sorte que leurs mouvements se produisent souvent sur des échelles de temps distinctes. Dans un certain nombre de cas suivant la photoionisation d'une molécule, on peut assumer que la variation de la densité électronique sur l'échelle de temps attoseconde s'adapte instantanément à la variation des coordonnées nucléaires sur l'échelle de temps femtoseconde. Les électrons et les noyaux sont traités séparément. Cependant, dans les molécules plus complexes, cette approximation de Born-Oppenheimer (adiabatique) n'est souvent pas valide car la différence d'énergie entre les états électroniques devient de plus en plus petites, favorisant les couplages entre les degrés de liberté nucléaires et électroniques. Dans ce cas, les expériences attosecondes peuvent aborder le rôle de la dynamique des électrons, suivant la photoionisation, sur la relaxation moléculaire ultérieure et déterminer si elles peuvent finalement être exploitées pour contrôler le résultat de processus photochimiques [17].

Dans ce contexte, les travaux présentés dans cette thèse ont été réalisés avec l'objectif général de résoudre des dynamiques ultrarapides dans les molécules, impliquant potentiellement des couplages entre les degrés de liberté nucléaires et électroniques à l'échelle de la femtoseconde et de l'attoseconde. Comme les outils nécessaires à la réalisation des expériences n'étaient pas toujours disponibles, une période importante du doctorat a également été consacrée au développement de nouvelles sources de lumière pour des applications en physique des champs forts et en science attoseconde. La plupart des expériences s'appuient sur des schémas pompe-sonde impliquant la photoionisation et la détection de particules chargées (électrons et ions) à l'aide de différents types de spectromètres. La photoionisation jouant un rôle clé en science moléculaire, la compréhension de son analogue dans les matériaux – l'effet photoélectrique – est essentielle pour plusieurs applications technologiques. Une partie des travaux de doctorat a donc également été consacrée à la transposition de concepts bien établis en spectroscopie moléculaire vers la matière condensée en étudiant la réponse de matériaux lors de l'ionisation en champ intense. Les résultats obtenus dans le cadre de cette thèse montrent enfin que la compréhension des mécanismes sous-jacents de dynamiques ultrarapides offre souvent un moyen de contrôler les propriétés de la matière.

## 1.4 Plan de thèse et objectifs

Le document de thèse est divisé en huit chapitres et suit le format d'une thèse par articles. Suite à cette introduction, les chapitres 2 et 3 décrivent les sources lasers de pointe qui ont été développées pendant la thèse, ouvrant de nouvelles perspectives en physique des champs forts et en science attoseconde. Les chapitres 4 à 7 présentent des expériences qui révèlent les mécanismes sous-jacents de processus ultrarapides pertinents en physique, chimie et en science des matériaux. Le chapitre 8 contient une conclusion générale et un point de vue personnel concernant de futures activités de recherche.

### Chapter 2: Développement d'impulsions de quelques cycles optiques centrées à $1.8 \mu\text{m}$ et de haute énergie pour interactions en champ fort

Le développement d'impulsions infrarouges ultracourtes et de haute énergie est indispensable pour aborder plusieurs défis en science ultrarapide :

- (i) La génération d'harmoniques d'ordres élevés (HHG) dans les gaz est le fondement de la science attoseconde et l'extension du spectre harmonique vers des énergies de photon plus élevées est une voie vers plusieurs percées en spectroscopie. Cependant, pour réaliser cette tâche cruciale, il faut augmenter la longueur d'onde du champ générateur vers l'infrarouge et atteindre des intensités crêtes plus élevées en réduisant la durée des impulsions.
- (ii) Pour étudier les propriétés transitoires des solides dans le régime de champ fort, des impulsions infrarouges avec des longueurs d'onde transportant des énergies de photon inférieures à l'énergie de bande interdite des matériaux doivent être employées avec une intensité suffisante.
- (iii) Les périodes optiques étant plus longues dans l'infrarouge (6 fs à 1800 nm) par rapport à l'infrarouge proche (2,7 fs à 800 nm), elles approchent les périodes de vibration dans les molécules et peuvent affecter de manière significative le résultat des interactions se produisant à l'intérieur du cycle optique au cours des processus photochimiques.

Pour relever ces défis, un premier objectif du Ph.D. traite du *développement d'impulsions laser à haute énergie et de quelques cycles optiques dans le domaine spectral infrarouge*. Nous avons d'abord travaillé sur la génération et la caractérisation d'impulsions de 10 mJ centrées à 1800 nm obtenues par un amplificateur paramétrique optique (OPA) de haute énergie à une fréquence de

répétition de 100 Hz, tel que décrit dans Thiré *et al.* 2015 [18]. Dans l'article I, nous avons comprimé les impulsions infrarouges de haute énergie à deux cycles optiques (12 fs, 5 mJ) par élargissement spectral dans une fibre creuse flexible. Également, nous avons utilisé l'OPA à haute énergie pour la génération de rayons X mous et généré des spectres couvrant la fenêtre d'eau (de 284 à 543 eV) avec un flux de photons suffisant pour des mesures monocoups au seuil  $K$  du carbone.

### **Chapter 3: Une ligne de lumière attoseconde pour des expériences de type pompe-sonde utilisant des impulsions UV de quelques femtosecondes**

La majeure partie du Ph.D. a été consacrée à *la construction d'une ligne de lumière attoseconde combinant des impulsions XUV et ultraviolettes (UV) avec une résolution temporelle sans précédent.* Plusieurs processus clés se produisant dans les systèmes biologiques sont initiés par une excitation moléculaire dans les états neutres. Cependant, ces dynamiques ne sont pas accessibles avec des impulsions pompes XUV car les énergies des photons ionisent inévitablement la cible, ce qui limite les études résolues en temps aux états ioniques uniquement. Pour étudier le rôle de la dynamique des électrons dans les états neutres de molécules d'intérêt biologique, l'utilisation d'impulsions UV ultracourtes est donc d'un grand intérêt. Dans cette perspective, nous avons développé une source laser exploitant le processus non-linéaire de génération de troisième harmonique dans un gaz d'argon, délivrant l'une des impulsions UV les plus courtes disponibles (article II). Nous avons intégré cette source laser à une ligne de lumière entièrement sous ultra-haut vide fournissant également des impulsions dans l'infrarouge proche (NIR) et des impulsions XUV attosecondes isolées (article III). Alors que des expériences attosecondes peuvent être réalisées employant le schéma pompe-sonde typique, soit XUV-pompe/NIR-sonde, les performances uniques de cette nouvelle ligne de lumière permettent également d'effectuer des expériences résolues en temps pour suivre la dynamique des électrons induite par le rayonnement UV dans les états neutres de biomolécules, ouvrant la voie à la spectroscopie ultraviolette attoseconde.

### **Chapter 4: Contrôle cohérent lors de l'ionisation dissociative de l'hydrogène moléculaire**

Ce chapitre traite de l'utilisation d'impulsions infrarouges à 1800 nm pour contrôler des dynamiques moléculaires photo-induites. Dans l'article IV, nous avons utilisé un champ laser bicolore (1800 & 900 nm) pour démontrer un niveau de contrôle amélioré de la localisation de la densité électronique pendant l'ionisation dissociative de l'hydrogène moléculaire ( $H_2$ ). Nous avons identifié quatre canaux de fragmentation distincts pour cette réaction prototype et comparé les données expérimentales avec des calculs solvant l'équation de Schrödinger dépendante du temps (TDSE) pour l'ion moléculaire. Ces travaux ont permis d'atteindre l'objectif consistant à *mieux comprendre le contrôle de réactions photochimiques.*

## Chapter 5: Ionisation en champ fort du niobate de lithium

Dans ce chapitre, nous étendons aux systèmes solides le contrôle de dynamiques ultrarapides avec des champs infrarouges à 1800 nm. Dans l'article V, nous avons d'abord caractérisé la réponse d'ionisation en champ fort de cristaux de niobate de lithium ( $\text{LiNbO}_3$ ) en faisant varier l'orientation de la polarisation incidente lors de l'ablation du matériau induite par laser. En étudiant différentes coupes de cristaux, nous démontrons la possibilité d'identifier la présence ou l'absence de symétries miroirs caractéristiques de la structure cristalline. Nous avons également identifié les principales liaisons chimiques qui contribuent à l'ionisation du matériau. Dans l'article VI, nous avons étudié le rôle d'une propriété fondamentale des matériaux ferroélectriques, la polarisation spontanée, dans l'ionisation en champ fort du  $\text{LiNbO}_3$ . Par des mesures d'ablation induite par des champs lasers bicolores, nous avons démontré comment la polarisation spontanée peut être exploitée pour le contrôle du taux d'ionisation dans les cristaux non-centrosymétriques, *faisant le pont entre la phase gazeuse et l'état solide*.

## Chapter 6: Études de dynamiques électroniques dans des molécules d'intérêt biologique

Un défi important en science attoseconde est de *comprendre la dynamique primaire des électrons qui se produit dans les molécules formant notre propre système biologique*. Notamment, les rayonnements ionisants peuvent causer des dommages irréparables à l'ADN et à ses sous-unités, mais le rôle des électrons lors des tout premiers instants qui suivent l'ionisation reste à être clarifié. Dans l'article VII, nous avons suivi la réponse moléculaire primaire qui se développe dans l'adénine, une base nucléique de l'ADN, lors de son ionisation par une impulsion attoseconde XUV isolée dans la gamme d'énergie 17-35 eV. À l'aide de calculs théoriques de pointe, nous avons caractérisé pour la première fois une dynamique de type 'shake-up' dans une molécule polyatomique, celle-ci se produisant en un temps caractéristique de 2,3 fs. Nous avons également identifié un mécanisme de stabilisation assisté par laser pour contrôler la fragmentation de la molécule après l'ionisation XUV. Ce travail fournit un exemple clair de schéma de contrôle ayant lieu avant l'apparition d'effets non-adiabatiques.

## Chapter 7: Dynamiques moléculaires induites par excitation UV ultrabrève et sondée par dichroïsme circulaire de photoélectrons

Ce chapitre présente la première expérience ayant été réalisée en utilisant la ligne de lumière et les impulsions UV ultracourtes décrites au chapitre 3. Par l'entremise de mesures de dichroïsme circulaire de photoélectrons, nous avons étudié la dynamique chirale du lactate de méthyle, un dérivé de l'acide lactique, après excitation par une impulsion UV de quelques femtosecondes. Puisque le

support théorique pour cette expérience est en cours d'élaboration pendant la rédaction de cette thèse, nous présentons les résultats expérimentaux et les interprétations possibles. Grâce aux caractéristiques uniques de la ligne de lumière développée pendant le doctorat, ce travail révèle une inversion dynamique de l'asymétrie avant/arrière des photoélectrons provenant d'une molécule chirale se produisant en quelques femtosecondes.

## Contexte de la thèse

La majeure partie du doctorat s'inscrit dans le cadre d'une collaboration internationale entre les équipes de recherche des Professeurs François Légaré et Francesca Calegari. Pour cette raison, les résultats présentés dans le document de thèse ont été obtenus dans trois laboratoires différents avec un temps de travail également réparti. Le développement d'impulsions ultracourtes à haute énergie centrées à 1800 nm, la génération de rayons X mous et la rédaction du manuscrit traitant de l'hydrogène moléculaire ont été réalisés au début du doctorat à l'Advanced Laser Light Source (ALLS, Canada). Par la suite, le développement d'impulsions UV ultracourtes et la construction de la ligne de lumière XUV-UV attoseconde ont été initiés au Politecnico di Milano (Italie), ancienne institution de la Professeure Calegari. Pendant cette période, les mesures dans la molécule d'adénine ont également été effectuées et le groupe avec lequel je travaillais était constitué d'une doctorante (Mara Galli) et d'un post-doctorant (Erik P. Månsson). Finalement, l'ensemble de la ligne de lumière a été déplacé vers le Deutsches Elektronen-Synchrotron (DESY, Allemagne), l'institution actuelle de la Professeure Calegari. J'ai reconstruit la ligne de lumière avec l'aide d'un groupe plus important (deux doctorants supplémentaires, un post-doctorant supplémentaire et un assistant de recherche). Ensuite, les expériences résolues en temps dans les molécules chirales ont été réalisées en étroite collaboration avec le groupe Harmoniques et Applications du laboratoire CELIA (France), plus précisément Etienne Bloch (doctorant), Valérie Blanchet, Yann Mairesse et Bernard Pons. Enfin, le travail sur  $\text{LiNbO}_3$  a fait l'objet de quatre campagnes expérimentales à ALLS qui ont été réparties sur l'ensemble du doctorat.

## Chapter 2

# High energy, few-cycle 1.8 $\mu\text{m}$ pulses for strong-field interactions

### 2.1 Femtosecond lasers

The laser source development presented in Chapter 2 and 3 is based on the use of femtosecond lasers, which are essential for the generation of ultrashort and intense laser pulses, independently on the desired spectral range. Substantial efforts have been devoted to scale up the pulse energy through amplification techniques, and to shorten the pulse duration. The most common method for energy scaling is the *chirped pulse amplification* (CPA, for which was awarded the 2018 Nobel Prize in physics) [19]. Fig. 2.1 shows the working principle of a typical femtosecond laser system based on CPA. An oscillator delivers a few hundred milliwatt pulse train at a repetition rate of 80-100 MHz, defined by the cavity length. A pulse picker composed of a Pockels cell and a set of polarizers selects a number of seeding pulses for amplification. Decreasing the repetition rate minimizes the undesired heat load on the crystal in the next amplification step. CPA is achieved by first stretching temporally the frequency components of the laser pulses to reduce the peak intensity. Stretching is typically achieved by using grating pairs or a number of dispersion prisms. A multi-Watt pump laser is then used to amplify the seeding pulses at intensities below damage threshold for the optical components of the laser system. Titanium sapphire (Ti:Sapphire) crystals emitting at about 800 nm are generally employed as gain medium because of their relatively large gain bandwidth and heat capacity that minimize thermal effects. Ytterbium-doped crystals are also employed in high average power systems for which the development is nowadays rapidly growing. After amplification, the pulses can be recompressed to their Fourier transform limit (TL) with a pair of gratings.

At kHz repetition rate, CPA led to multi-mJ Ti:Sapphire lasers with pulse duration down to about 25 fs [20]. However, this duration is limited by a reduction of the spectral content – *gain*

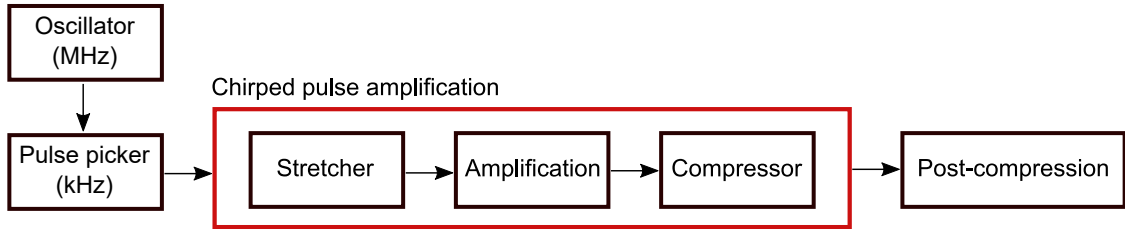


**Figure 2.1 – Sketch of the chirped pulse amplification technique followed by post-compression**

*narrowing* – during amplification in the Ti:Sapphire crystal. This is despite the use of spectral reshaping units (such as a Dazzler) prior to amplification that are employed to minimize this effect and to correct high-order chromatic dispersion terms [21]. To further reduce the pulse duration, post-compression techniques involving spectral broadening followed by pulse compression have been developed. Filamentation and hollow-core fiber (HCF) post-compression are the most widespread techniques and made it possible to reach the few-cycle regime [22, 23], and few-fs pulses in the near-infrared (800 nm) have been employed for a wide range of application in time-resolved spectroscopy.

Following such developments, there has been an interest for extending laser systems to the mid-infrared (MIR) spectral range. In high-harmonic generation (HHG) for instance, the cutoff energy scales with the intensity and wavelength ( $E_{cutoff} \propto I\lambda^2$ ) and thus few-cycle pulses at longer wavelength than 800 nm provide a mean to reach high photon energies in the soft x-ray [24, 25]. Section 2.9 describes our approach for the generation of soft x-ray with 1800 nm pulses. In condensed matter, intense MIR pulses offer the possibility to study photoionization of semiconductors and dielectrics in the tunneling regime where photon energies are off resonance and well below the bandgap energy of materials [26]. Articles V and VI will treat on this topic. Intense IR pulses can also be used to investigate ultrafast molecular dynamics in the gas phase through techniques such as laser-induced electron diffraction (LIED) [27, 28], or for the control of photochemical processes, as presented in article IV.

## 2.2 Optical parametric amplifiers

For the generation of intense IR pulses, amplification through nonlinear parametric processes can be employed. Fig. 2.2 shows an example of *optical parametric amplification* (OPA, for an extensive review see [29]). When seeding a second-order nonlinear crystal with a weak 1440 nm pulse, a pump pulse at 800 nm is converted into an amplified Signal (1440 nm) and an Idler (1800 nm) pulse, given proper phase-matching conditions ( $\Delta\vec{k} = 0$ ). The seed pulse can be generated for instance through supercontinuum generation in a glass plate or from intrapulse DFG (difference frequency generation) of spectrally broadened pulses in a gas-filled HCF [30, 31]. After a first amplification, either the Signal or the Idler can be further amplified through additional OPA stages. Because

parametric processes only rely on virtual states (no net absorption) in the nonlinear crystal, energy is conserved to generate the Signal and Idler beams. For this reason the heat load in the crystal is reduced compared to other amplification techniques.

One approach to obtain multi-mJ level IR pulses is the application of the CPA technique to OPA systems (OPCPA) [32]. Another method implies optical parametric amplification in the Fourier plane (FOPA), providing optimized phase matching over a broad spectral range and minimal gain narrowing [33]. However, these amplification systems are relatively complex to develop and standard multi-stage OPA is often sufficient to reach the desired pulse energy. In all cases however, parametric sources must be combined to a post-compression stage when few-cycle pulses are desired.

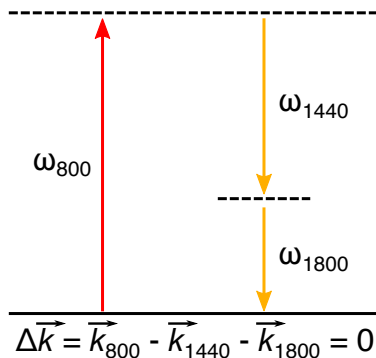


**Figure 2.2 – Principle of optical parametric amplification with energy and momentum conservation. Dashed lines correspond to virtual states.**

This chapter describes applications of the high energy OPA that was developed at the Advanced Laser Light Source (ALLS). A sketch of the setup is shown in Fig. 2.3. A 100 Hz, Ti:Sapphire laser exploiting the CPA technique is split to be sent to two distinct grating compressors. A low energy compressor delivers 5 mJ pulses (40 fs) that serve as a pump for a commercial three-stage OPA (HE-TOPAS from Light Conversion). The seed of this OPA is obtained from a white-light continuum generated by SPM in a sapphire plate [30]. After three subsequent amplification stages and spectral filtering, the OPA delivers IR pulses (900  $\mu\text{J}$ ) centered at about 1800 nm. The output beam is spatially filtered by focusing it in vacuum through a small diameter pinhole. The filtered beam (750  $\mu\text{J}$ ) is collimated to about 20 mm and serves to seed a custom amplification stage in a large aperture type II BBO crystal ( $\theta = 30^\circ$ ). This last OPA stage is pumped by a high energy compressor delivering up to 45 mJ. The low and high energy compressors are decoupled to permit control over the pump energy for this last amplification stage. The characteristics of the high energy pulses are summarized in Fig. 2.4. In (a), the spectrum after amplification (black line) supports a 28 fs TL and was characterized in (b) by a second-harmonic autocorrelator to be 30 fs (black line).

The work presented in this chapter was realized in the beginning of the Ph.D. In section 2.6, we present a post-compression setup for high energy 1800 nm pulses. Pulse compression down to 12 fs (5 mJ) via spectral broadening in a flexible HCF was achieved, setting a new record for the

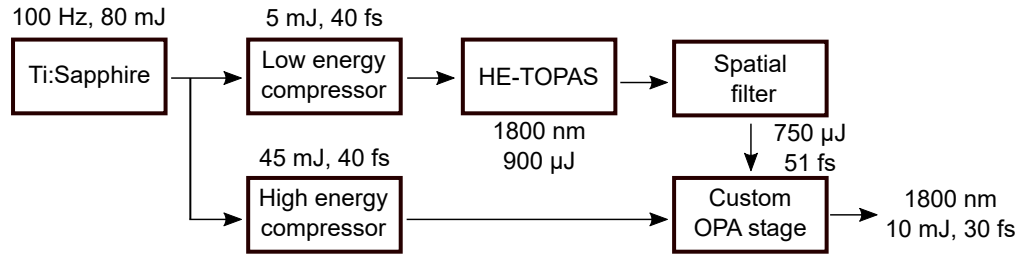


**Figure 2.3 – High energy OPA system developed at the ALLS**

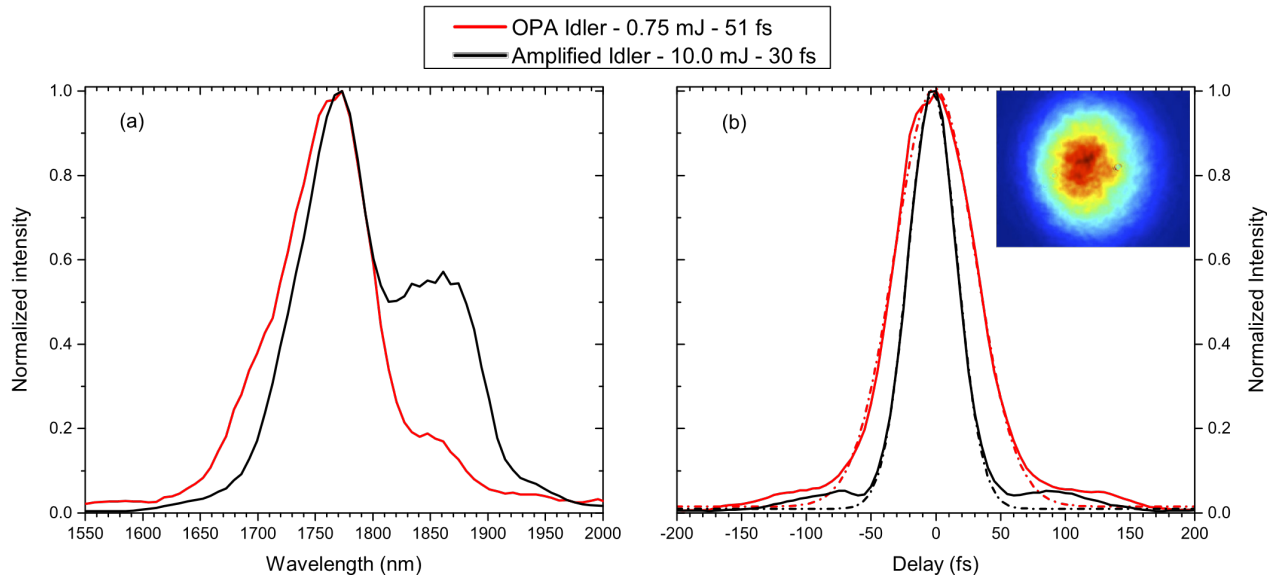


**Figure 2.4 – Spectral (a) and temporal (b) properties of the high energy pulses. The amplified Idler (black) is compared to the seed only (red). Figure adapted from Thiré *et al.* 2015 [18].**

highest peak intensity in the IR<sup>1</sup>. In section 2.10 we used the high energy OPA described above to develop a high flux soft x-ray source reaching energies up to the oxygen *K*-edge (543 eV). Prior to each section, the concepts of HHG and HCF post-compression are detailed as these important techniques are also employed in article III where the realization of an UV-XUV attosecond beamline is presented.

## 2.3 Spectral broadening and post-compression

As discussed in Sec. 2.1, the pulse duration from multi-mJ Ti:Sapphire lasers is typically limited to about 25 fs. To further reduce this duration, additional spectral broadening of the pulses is necessary and is typically achieved through self-phase modulation in a waveguide.

<sup>1</sup>Further development of the FOPA technique led to higher peak intensities a couple of years later [34].

The spectral broadening induced by the propagation of an intense laser pulse in a waveguide originates from the third-order Kerr effect. The nonlinear refractive index of the medium  $n_2$  changes as a function of the intensity  $I(t)$  of the laser pulse. During the propagation, a nonlinear phase  $\phi_{NL}$  is accumulated:

$$\phi_{NL} = \frac{k_0 n_2}{A} I(t) L = \gamma I(t) L \quad (2.1)$$

where  $k_0 = 2\pi/\lambda$  is the wave vector,  $A$  the spatial mode area and  $L$  corresponds to the distance the laser pulse has propagated in the medium. The variation of the phase in time gives rise to an instantaneous frequency:

$$\omega_i = \omega_0 - \frac{\partial \phi_{NL}}{\partial t} = \gamma \frac{\partial I}{\partial t} L \quad (2.2)$$

Fig. 2.5 displays the typical behavior of this *self-phase modulation* (SPM) effect for a 200 fs pulse ( $1/e^2$ ) with arbitrary values  $\omega_0, \gamma$  and  $L$ . Depending on the slope of the intensity profile, frequency below and above the central frequency  $\omega_0$  are generated, leading to spectral broadening over the entire propagation distance. The rising edge of the pulse creates redshifted frequencies while the trailing edge results in blueshifted components.

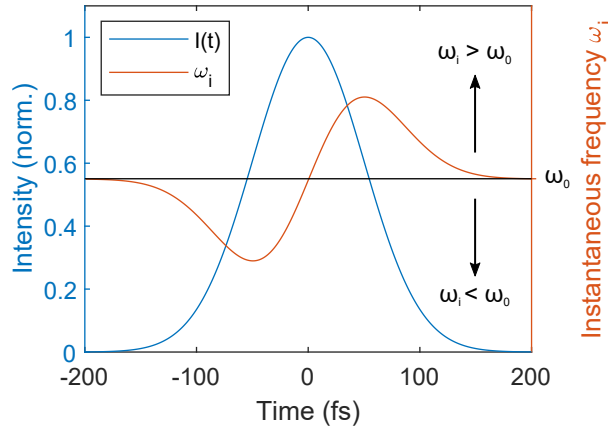


**Figure 2.5 – Self-phase modulation profile for a 200 fs gaussian pulse ( $1/e^2$ ).**

Because each frequency components develops at a unique time, the resulting spectral content of the pulse at the exit of the waveguide exhibit a chirp that is characterized by the linear slope in the center of the SPM profile. To compensate this positive group delay dispersion (GDD) induced during the nonlinear propagation, multi-layer mirrors with negative GDD are typically employed [35]. As will be shown in article I however, when SPM is applied to a 1.8  $\mu\text{m}$  central wavelength, the spectral content of the pulse finds itself in the anomalous dispersion regime of a few materials such as fused silica. In this case, because the refractive index increases with the wavelength ( $\partial n/\partial \lambda$ ) the laser beam can simply be propagated through bulk in order to achieve near TL compression.

## 2.4 Hollow-core fiber post-compression

Spectral broadening in HCF post-compression schemes is achieved by propagating laser pulses in a glass capillary (fiber) filled with a noble gas. At the entrance of the capillary, the beam is focused to obtain a Gaussian profile with a diameter ( $1/e^2$  of intensity) of about 64% the size of the hollow-core. This theoretical value was found to maximize the energy contained in the fundamental mode that is coupled into the fiber [36]. Because of the reduced nonlinear refractive index ( $n_2$ ) of the gas medium compared to bulk materials, the fiber must be several centimeters long to acquire sufficient nonlinear phase during SPM.

First demonstrations of the hollow-core fiber capabilities for the generation of ultrabroadband few-cycle pulses were reported in the late 90's by Nisoli *et al.* Not only the technique demonstrated impressive compression factors (from 140 fs to 10 fs in [22]), it offered a route for the spectral broadening of high energy pulses [35]. Indeed, compared to small aperture single-mode fibers for which the damage threshold of the material is limiting the input energy (nanojoule level), multi-mJ pulses can be coupled into HCF's with hollow-core diameters of hundreds of microns. In this case, the damage of the material is limited to the low intensity wings of the gaussian beam profile at the focus. SPM in rigid HCF of about 1 m length permits nowadays to generate few-cycle NIR pulses at the mJ level [37].

As described in the previous section, spectral broadening is achieved through the third-order Kerr effect and due to the high intensity involved, other nonlinear processes must be considered when designing an HCF setup. In the temporal domain, the Kerr effect manifests itself through self-steepening. The increase of refractive index with intensity leads to a reduction of the group velocity at the peak of the pulse envelope, leading to a slow rise for the leading edge of the pulse and a sharp decrease on the trailing edge. This temporal reshaping of the pulse envelope affects the SPM. By considering Eq. 2.2, this leads to an enhanced spectral broadening on the blue side of the spectrum as the slope of the trailing edge becomes more important. While this behavior is not detrimental for the generation of few-cycle pulses, self-steepening can also induce third-order dispersion which can be difficult to compensate in the subsequent compression stage.

In the spatial domain, the Kerr effect induces self-focusing, potentially leading to filamentation of the gas medium. This effect must be avoided to preserve the guiding properties of the HCF. Self-focusing can be particularly important at the input of the fiber where the laser is focused and intensity is highest, leading to a mismatch of the predefined beam size to be coupled into the HCF for optimal transmission. To prevent self-focusing, HCF setups can be employed with a pressure gradient by injecting the gas at the exit side of the fiber and pumping at the entrance side. In this way, diffusion through the capillary leads to a reduced gas density at the input, minimizing undesired ionization and self-focusing effects in the gas medium. The disadvantage is that a longer propagation length is required to acquire sufficient nonlinear phase during SPM

and that the processing of straight rigid HCF's with large core is technically difficult to achieve. Straightness is particularly important because unlike typical optical fibers where light is transmitted by total internal reflection ( $n_{core} > n_{ext}$ ), the propagation in a HCF depends on grazing incidence reflections ( $n_{gas} < n_{glass}$ ) that are strongly dependent on the fiber bending [38, 39]. The fiber quality hence strongly affects the overall transmission of the setup.

## 2.5 Article I – Summary

As an alternative to rigid HCF's, it is possible to employ several meter long flexible HCF's with large core, easier to manufacture. Nagy *et al.* have demonstrated a scheme where such a flexible fiber can be mechanically straightened, ensuring a good transmission and showing promising results in the NIR [38, 40]. In article I, we demonstrate the capabilities of the flexible HCF technology for the generation of few-cycle 1800 nm pulses, with the aim of increasing the available peak power in this spectral range. In this context are discussed the wavelength dependence of the relevant parameters in HCF post-compression such as the nonlinear refractive index  $n_2$ , the plasma contribution to the refractive index, the waveguide attenuation and the critical power for self-focusing. Notably,  $n_2$  at 1800 nm is only 60% the value at 800 nm (Table 2.1). An increase of either the laser intensity or the gas density could compensate for this effect, but would at the same time increase losses due to an increase of the plasma refractive index, which is more important at longer wavelengths. For this reason, extending the propagation length for SPM is preferable. Experimentally, the OPA system described in Sec. 2.2 was thus coupled to a 3-m long hollow-core fiber of 1 mm diameter and filled with argon gas (Fig. 2.6). A gas gradient along the fiber was employed, with a decreasing gas density towards the entrance in order to minimize ionization. By evaluating the output energy with increasing input energy (Fig. 2.7), 5 mJ pulses were obtained for the maximal available input energy of 11 mJ at the entrance of the HCF setup, corresponding to a 45% efficiency. Fig. 2.8 shows the resulting spectral broadening and the temporal characterization of the pulses. Compression with fused silica plates in the anomalous dispersion regime allowed to reach 12 fs pulses (two optical cycles).

## 2.6 Article I – 0.42 TW 2-cycle pulses at 1.8 $\mu\text{m}$ via hollow-core fiber compression

Vincent Cardin<sup>1</sup>, Nicolas Thiré<sup>1</sup>, Samuel Beaulieu<sup>1</sup> Vincent Wanie<sup>1</sup>, François Légaré<sup>1</sup> and Bruno E. Schmidt<sup>1,2</sup>

<sup>1</sup>Institut National de la Recherche Scientifique, Centre Énergie Matériaux et Télécommunications, 1650 Boulevard Lionel-Boulet, Varennes, Quebec J3X 1S2, Canada

<sup>2</sup>Few-Cycle, Inc., 2890 Rue de Beaurivage, Montreal, Quebec H1L 5W5, Canada

Applied Physics Letters **106**, 091110 (2015)

Received 14 January 2015

Published online 6 March 2015

doi: <http://dx.doi.org/10.1063/1.4914344>

With the support of the ALLS technical team, Dr Bruno Schmidt developed the stretched hollow-core fiber system and was the main investigator with Vincent Cardin. My personal contribution has been to assist in the installation/modification of the experimental setup and for the optimization of the performances, together with Dr Nicolas Thiré and Samuel Beaulieu. I also participated to the revision of the manuscript, which was written by Vincent Cardin. François Légaré supervised the project.

## Abstract

By employing pulse compression with a stretched hollow-core fiber, we generated 2-cycle pulses at 1.8  $\mu\text{m}$  (12 fs) carrying 5 mJ of pulse energy at 100 Hz repetition rate. This energy scaling in the mid-infrared spectral range was achieved by lowering the intensity in a loose focusing condition, thus suppressing the ionization induced losses. The correspondingly large focus was coupled into a hollow-core fiber of 1 mm inner diameter, operated with a pressure gradient to further reduce detrimental nonlinear effects. The required amount of self-phase modulation for spectral broadening was obtained over 3 m of propagation distance.

## Main text

Gain narrowing in chirped pulse amplification (CPA) [19] sets limits for the achievable bandwidth of high power ultrafast laser systems operating in the multi-millijoule (mJ) regime. Although this limitation may be overcome with ultra-broadband optical parametric amplifiers (OPAs) [41, 42, 43, 44, 45, 33], such lasers are not yet readily available commercially. Therefore, post-compression subsequent to multi-cycle laser systems remains the most proven way to generate high energy few-cycle pulses. At the mJ level of pulse energy, filamentation [46, 47, 48, 49] and hollow-core fiber (HCF) [22] based propagation schemes still remain the most popular ones. Self-guided filamentation offers the advantages of wide spectral broadening and ease of operation. Although harder to implement, guided-mode propagation in a HCF is a much more universal method that produces spatially homogenous beams of high quality. With a proper waveguide, HCF propagation can be realized from the XUV [50] to the THz spectral range [51] and at very different energy levels (1 nJ – 10 mJ), respectively [52, 53]. The concept is even applicable at average input power levels reaching 150 W [54].

In this paper, the challenges of few-cycle HCF compression in the mid-infrared range are discussed in the context of upscaling the peak power towards the TW regime. An experimental route to circumvent these challenges is presented where pulses at 1.8  $\mu\text{m}$  wavelength containing up to 11 mJ (100 Hz repetition rate) were coupled into a HCF without damaging the fiber. The maximum output energy after recompression to 2 cycles (12 fs) was 5 mJ.

The principal challenge of nonlinear pulse compression with HCFs is to provide sufficient nonlinearity for maximum self-phase modulation (SPM) while avoiding harmful nonlinear effects like self-focusing, ionization, or nonlinear mode coupling [55]. In this manner, a unique measurement of 5 fs, 5 mJ pulses at 800 nm wavelength has been reported [56]. When transferring this experiment to longer wavelengths, several quantities need to be reconsidered: the third order nonlinearity ( $n_2$ ), the free electron contribution to the refractive index ( $n_e$ ), the critical power for self-focusing ( $P_{cr}$ ), and the waveguide attenuation ( $\alpha$ ). Table 2.1 summarizes their respective wavelength dependence.

$n_2$	$n_e$	$P_{cr}$	$\alpha$
$\frac{n_2(\lambda_1)}{n_2(\lambda_2)} = \left[ \frac{n_0^2(\lambda_1)-1}{n_0^2(\lambda_2)-1} \right]^4$	$n_e \propto \sqrt{1 - \frac{\rho_e e^2}{\varepsilon_0 m_e} \left( \frac{\lambda}{2\pi c} \right)^2}$	$\propto \frac{\lambda^2}{n_2}$	$\propto \frac{\lambda^2}{A^3}$

**Table 2.1 – Wavelength dependencies of critical parameters for the energy scaling of HCF post-compression systems. From left to right: nonlinear refractive index, free electron refractive index, critical power for self-focusing, and waveguide attenuation. The equation for the nonlinear index is part of the generalized Miller formulae as obtained in Ref. [57] and shows a monotonic decrease of  $n_2$  with wavelength.**

The nonlinear refractive index of noble gases decreases with wavelength [57] (in argon,  $n_2(1800 \text{ nm})/n_2(800 \text{ nm}) = 0.59$  [58]). At first sight, a reduced  $n_2$  holds promise to enable higher propagation intensities to reach the same nonlinear phase shift via SPM. Compensating the lower  $n_2$  by increasing the intensity, however, causes an increased ionization rate. The ionization rate remains roughly constant as a function of wavelength in the tunneling regime, which is the case for peak intensities in excess of  $10^{14} \text{ W/cm}^2$ . Yet, the contribution of free electrons to the refractive index,  $n_e$ , increases with laser frequency  $\omega$  ( $n_e^2 \propto \rho_e/\omega^2$ ), where  $\rho_e$  is the free electron density. Similarly, increasing  $n_2$  by increasing the gas pressure equally leads to an increased free electron density. This means that gas pressure must be kept low, even though the higher critical power for self-focusing in the mid-infrared could support a much higher pressure before undesirable effects like nonlinear mode coupling come into play [59, 60].

On the other hand, lowering the intensity by using a large fiber aperture  $A$  (see Table 2.1) reduces the ionization rate in the nonlinear medium as well as the attenuation of the fundamental mode, which scales as  $\lambda^2/A^3$ . The lower intensity needs to be compensated by using a longer propagation length to yield the same spectral broadening without affecting the other parameters. This, however, requires perfectly straight waveguides, since the mode spacing becomes smaller for larger mode sizes, which increases the probability of linear mode coupling.

Conventional setups using capillary channels enclosed in stiff glass rods mounted on v-shaped grooves [22, 61, 35, 62, 30] are typically limited in length due to the fabrication processes and handling. Nagy et al. [38, 40] demonstrated the use of a flexible HCF, mechanically stretched, and thus, enabling good straightness even at 3 m length. The stretched fiber was enclosed in a rigid metal tube with the fiber ends fixed permanently. In this letter, we report on an improved design which allows one to freely change the fiber length or diameter depending on the given experimental conditions. Furthermore, we demonstrate good mode guiding for waveguides of 1 mm inner diameter which is more than 500 times the wavelength ( $1.8 \mu\text{m}$ ).

Figure 2.6 illustrates the HCF setup (shaded gray area) together with the high energy optical parametric amplifier (HE-OPA) line at the Advanced Laser Light Source (ALLS, Varennes, Canada).

This OPA line is pumped by an 800 nm Ti:Sa laser at 100 Hz repetition rate. Its output is divided into 2 parts; 7 mJ are sent to a low-energy compressor (LEC) to pump a TOPAS (Light Conversion) which delivers up to 750  $\mu\text{J}$ , 50 fs pulses at 1.8  $\mu\text{m}$  wavelength. The TOPAS output is spatially filtered (SF1) to ensure a clean and defined mode which is preserved in the subsequent amplification process. A clean spatial mode is a necessary requirement for optimum HCF performance. The larger energy fraction of 70 mJ is compressed in a high-energy compressor (HEC) delivering up to 50 mJ to the large aperture BBO crystal (type II,  $22 \times 22 \times 2$  mm). This high energy OPA stage delivers up to 11 mJ pulses with 35 fs duration and is described in more detail in Ref. [18].

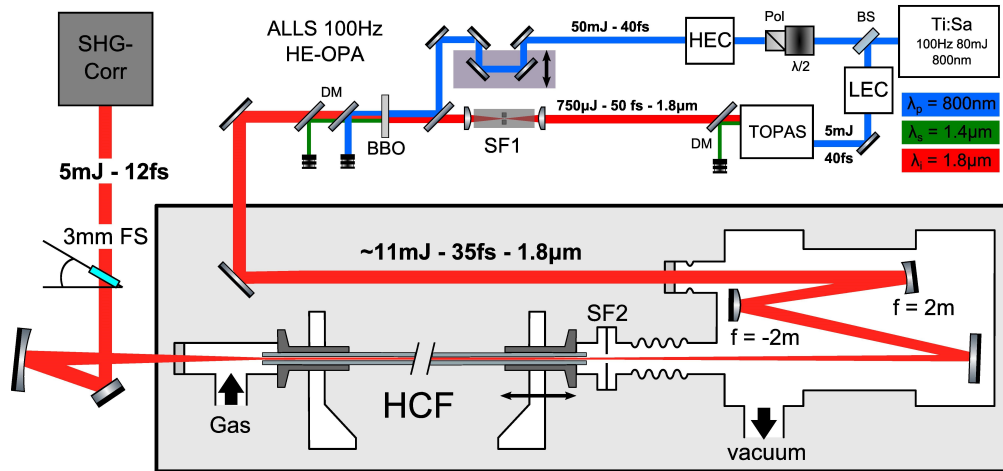


**Figure 2.6** – Illustration of the experimental setup for the generation of high intensity few-cycle mid-infrared pulses. The top area depicts the HE-OPA of the Advanced Laser Light Source [18]. The stretched hollow-core fiber length is 3 m with 1 mm inner diameter. Depicted telescope effective focal length is 3.8 m with an  $1/e^2$  beam waist of 750  $\mu\text{m}$  diameter. Front vacuum chamber and exit gas inlet chamber are enclosed by 2 mm  $\text{CaF}_2$  windows. (DM: various dichroic mirrors (as shown); Pol: Polarizer; BS: Beam splitter; LEC/HEC: Low/High Energy grating compressors; TOPAS: commercial OPA; SF: Spatial filter pinhole; SHG-Corr: all-reflective second harmonic auto-correlator.)

The HCF setup consists of three elements: a folded beam coupling telescope, the fiber, and the compression stage. Beam coupling is carried out with a reflective telescope. A  $f = 2\text{m}$  concave mirror placed 105 cm before a  $f = -2\text{m}$  convex mirror gives an effective focal length of 3.8 m with an  $1/e^2$  focal size close to 750  $\mu\text{m}$ . The focal spot, imaged with a Flea2 CCD (PointGrey) to characterize the spatial mode, is shown in the inset of Figure 2.8(a). A spatial filtering pinhole (SF2) with the same diameter as the fiber is installed directly in front of the fiber tip to prevent the fiber damage in case of beam drifts.

The fiber itself is a 3 m long, 1 mm inner diameter flexible HCF with a 300  $\mu\text{m}$  thick fused silica (FS) cladding surrounded by a polymer layer. The fiber ends are permanently glued into small metal sleeves. These sleeves are clamped to holders (dark gray pieces in Figure 2.6) with

three screws. This fast clamping solution allows one to change the propagation condition by using different fiber lengths or diameters, respectively. To straighten the fiber, tension is applied by translating one holder along the optical axis, as indicated by the arrow in Figure 2.6. On both sides, a two axis tilt mechanism ensures the correct alignment of the fiber tip with respect to the optical axis and allows to optimize the mode quality and transmission. The two fiber holders are connected to a KF vacuum tube through which the beam propagates under controlled pressurized conditions. High energy operation is usually achieved by applying pressure on the exit side while pumping continuously at the input. This pressure gradient provides the lowest amount of gas at entrance where the beam is the most intense, thus reducing ionization and self-focusing [63]. Indeed, ionization would hamper the waveguide qualities of the HCF, thus reducing transmission and stability. At maximum input energy of 11 mJ and 2-cycle operation, the argon pressure on the beam-input side was 300 mTorr. This value was adjusted to optimize the compression, and it is pointed out that further energy scaling seems feasible by using either Ne or He, but Ar was preferred due to its higher nonlinear index and lower cost.

Furthermore, we adjusted the ratio of focal beam waist ( $1/e^2$  of intensity) over the fiber aperture to 0.75 instead of the theoretically required value of 0.64 for optimum mode coupling to the fundamental EH11 mode [39, 36, 64]. We empirically found that this slightly increased focal spot size leads to the best transmission at lower input energies around 1 mJ. The linear coupling losses were verified experimentally by inserting low energy pulses of 100  $\mu\text{J}$  in a 5 cm short HCF where propagation losses are negligible. The high transmission of 97% in this case confirmed the good beam quality achieved with the spatial filter SF1 prior to the last amplification stage and the mode matched coupling of the setup. For the 3 m long fiber, the highest transmission measured was 80% at an input energy of 750  $\mu\text{J}$  (without amplification in the last stage), which underlines the excellent guiding properties of the 3 m long HCF. The obtained output energy as a function of input energy is shown in Figure 2.7, with the highest output energy of 5 mJ for an input of 11 mJ. This corresponds to 45% total transmission including vacuum windows, vacuum optics, and the spatial filter SF2 in front of the fiber. The spatial beam profile subsequent to the HCF is seen in the second inset of Figure 2.8(a). Its  $1/e^2$  diameter, after collimation at 2 m distance from the fiber output, is 7.5 mm.

Finally, 2-cycle pulse compression at 1.8  $\mu\text{m}$  wavelength subsequent to the HCF was achieved by the bulk compression technique which relies on the interplay of nonlinear propagation in the fiber and linear propagation through FS subsequently [62, 30, 65]. By placing FS windows of correct thickness (between 2 and 4 mm), one can compress pulses close to their corresponding transform limit. The temporal characterization was performed with a second harmonic autocorrelator.

Figure 2.8 shows the spectral (Figure 2.8(a)) and temporal (Figure 2.8(b)) characterization of the few-cycle pulse. We achieved a spectral width spanning from 1200 nm to 2200 nm associated with a transform limited duration of 11.3 fs. The broadened spectrum in Fig. 2.8(a) shows the typical shape of a SPM broadened pulse with the noticeable asymmetric shape associated with self-steepening during nonlinear fiber propagation [40, 66, 67].<sup>29,36,37</sup> The temporal shape exhibits

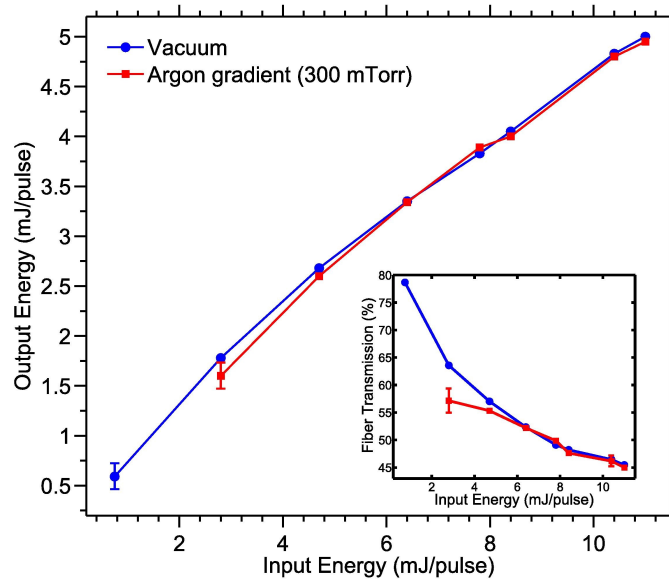


**Figure 2.7** – Compressed output energy as a function of the fiber input energy for an evacuated (blue circles) and argon-filled (red squares) hollow-core fiber. A pressure gradient with 300 mTorr at entrance side and 520 Torr at the exit side, respectively, was applied. Inset: Corresponding transmission curve (including all vacuum windows and coupling optics) for the same data points.

a Gaussian profile with a FWHM of  $(12.3 \pm 0.4)$  fs corresponding to 2 cycles at 1.8  $\mu\text{m}$  wavelength. A Gaussian fit is presented for comparison by the dashed lines.

To address the question about the origin for the transmission loss, we compared the throughput of an Ar filled with an evacuated fiber (40 mTorr residual pressure measured at the entrance side). Virtually no difference is observed by comparing the blue (evacuated) and red (Ar filled) curves of Figure 2.7 at high energy. The fact that the gas filling shows no effect on the transmission suggests an origin upstream of the fiber. Possible candidates are (i) SPM in the last BBO crystal, (ii) nonlinear effects in the vacuum window, (iii) nonlinear absorption in the dielectric mirror coatings, or (iv) beam degradation when propagating the high power midinfrared through ambient air. Regarding the latter, we noticed a  $\sim 10\%$  energy loss for propagation over 6–7 m of distance without any sign of self-focusing. We did, however, not observe a degradation of the focus quality at the fiber entrance at maximum energy, indicating negligible effects on the wave front upon propagation in ambient air.

Concerning (i), the nonlinearities in the BBO amplification crystal, we point out that the energy adjustment of the final OPA stage output was carried out by varying the pump pulse energy of the Ti:Sa by rotating its polarization with a half wave plate in combination with a polarizer, as shown in Fig. 2.6. Since this is done before the compressor, there is no influence on other pump pulse properties by this method. On the other hand, the amplification conditions might change as a

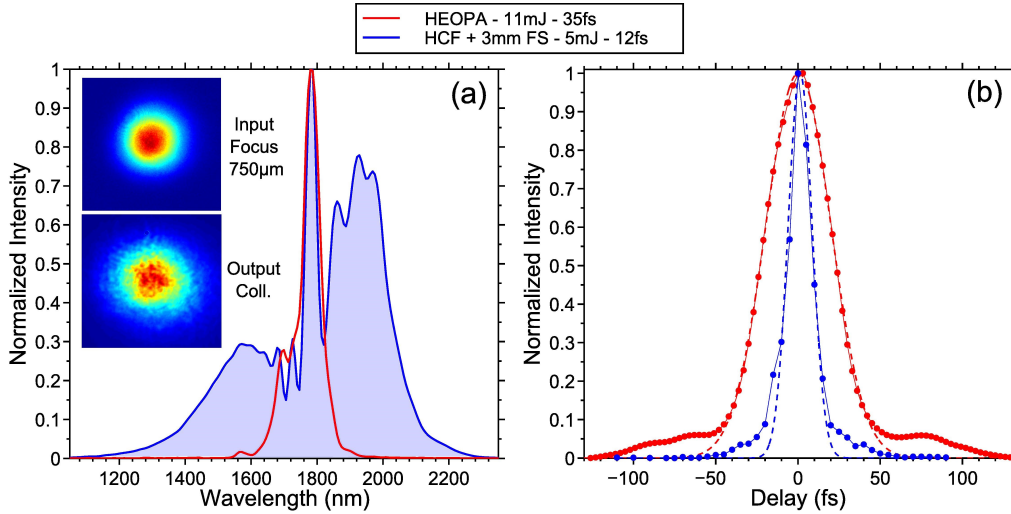


**Figure 2.8 – Characterization of the fiber input and output pulses.** (a) Spectrum of the multi-cycle input pulse in red compared with the broad spectrum at a pressure 300 mTorr at the exit side in shaded blue. Inset: CCD images of the input pulse focal spot (up) and of the output pulse collimated at 2 m after the fiber. (b) Autocorrelation trace of the multi-cycle input pulse in red and of the compressed 2-cycle pulse. Dotted lines denote a Gaussian fit.

function of pump intensity. Therefore, we monitored the pulse duration as a function of pump energy and observed a pulse shortening towards higher energies from 50 fs in the unpumped case down to 40 fs at maximum intensity [18]. The on-axis B-integral of the 800 nm pump beam in the 2 mm thick BBO (extraordinary axis) is calculated to be 0.5 rad. As mentioned previously, the focal spot quality did not change and the 20% change in pulse duration would not explain a significant drop of fiber transmission. The next possibility (ii), nonlinearities in the vacuum window or beam splitters, seems less likely since the total on axis B-integral is estimated to be less than about 1 rad. The low average power of only 1 W is not expected to cause any thermal effect. Compared with this, the most strained optic is the last folding mirror of the input telescope, as shown in Figure 2.6. We estimated the on axis peak intensity to go beyond  $10 \text{ TW}/\text{cm}^2$ . This high intensity is caused by the fact that we had to build a compact telescope due to space restrictions. A very recent publication reports reversible, nonlinear absorption effects in dielectric mirrors already at much lower intensities for fs pulses, see cf. Fig. 2 in Ref. [68] 38. In their study, they report on a dramatic reflectivity drop from 100% down to 20% at elevated intensities. Since we observed a similar reversible effect, this nonlinear absorption is currently our prime suspect to explain our observation.

In conclusion, improving upon the design of the stretched flexible hollow-core fiber scheme, we demonstrated pulse compression to 2-cycles (12 fs) at  $1.8 \mu\text{m}$  wavelength with an energy of 5 mJ at 100 Hz repetition rate. The clean spatial profile together with a to date unmatched pulse power of  $0.42 \text{ TW}$  make it a very promising source for a large variety of strong field driven experiments like generation of high harmonics and high-field THz pulses. Further energy scaling seems feasible

when using He or Ne as the nonlinear medium instead of Ar, or by employing circularly polarized pulses [69].

## Acknowledgements

The authors wish to acknowledge research funding from NSERC (Natural Sciences and Engineering Research Council of Canada), FRQNT (Fonds de recherche du Québec–Nature et technologies), Canada Foundation for Innovation–Major Science Initiatives, NanoQuébec, Ministère du développement économique, de l’Innovation et de l’exportation (MDEIE) du Québec, and DARPA PULSE Program through a Grant from AMRDEC. V.C., S.B., and V.W. express their gratitude for the scholarships awarded by NSERC. All authors are grateful for the efficient and dedicated work done by Antoine Laramée and Philippe Lassonde in ALLS.

## 2.7 High-harmonic generation

### 2.7.1 Three-step model

High-order harmonics produced from the interaction between a dense atomic medium and intense laser pulses were discovered in the late 80’s [3, 4]. In 1993, a semi-classical model was proposed to elucidate the underlying mechanism of HHG [6, 70], and the interpretation laid the foundation for the development of ultrashort laser pulses with attosecond duration [7, 8]. This semi-classical model, known as the *three-step model*, is described in Fig. 2.9. In (a), the Coulomb potential of an atom under the effect of a linearly polarized strong-laser field is sufficiently lowered to enable an electron to undergo tunnel ionization [71]. The ionized electron propagates in a direction parallel to the laser polarization until the polarity of the field is reversed. From this instant, shown in (b), the electron decelerates, then returns towards its original position as it is accelerated by the laser field. In (d), a recombination with the parent ion takes place and energy is released in the form of a single attosecond pulse with continuous spectrum. When HHG is driven by a multi-cycle laser pulse, the successive half-cycles of the electric field that are sufficiently intense to ionize an electron create a train of attosecond pulses, leading to a comb of odd-order harmonics in the spectral domain that are separated by twice the energy of the fundamental frequency. A typical HHG spectrum is produced in the extreme ultraviolet (XUV) or soft x-ray spectral range and exhibits a rapid intensity decrease for the lowest harmonic orders followed by a plateau that sharply ends in a high-energy cutoff region.

The equation of motion in the *three-step model* is the Newton law  $F(t) = m_e a(t)$  for an electron with mass  $m_e$  and charge  $q$  under a Lorentz force  $F(t) = qE_0 \cos(\omega_0 t)$ . This force is applied by a

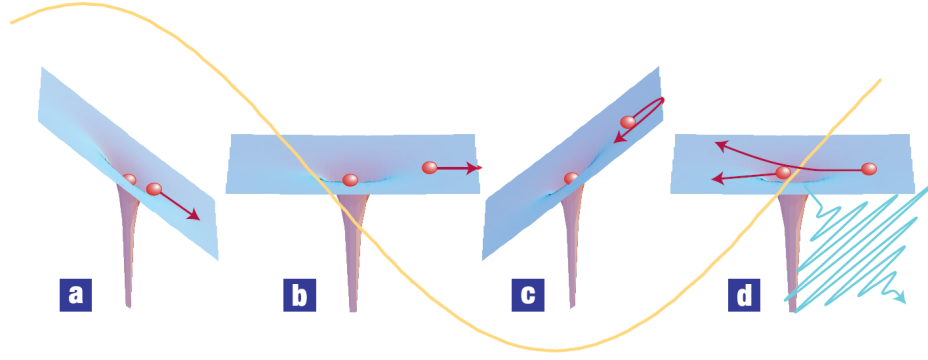


**Figure 2.9 – Three-step model of HHG, adapted figure from Corkum and Krauz 2007 [72].**

strong oscillating laser field of amplitude  $E_0$  with frequency  $\omega_0$ . The mean kinetic energy of the electron in the oscillating field is:

$$U_p = \frac{(eE_0)^2}{4m_e\omega_0^2} \propto I\lambda^2 \quad (2.3)$$

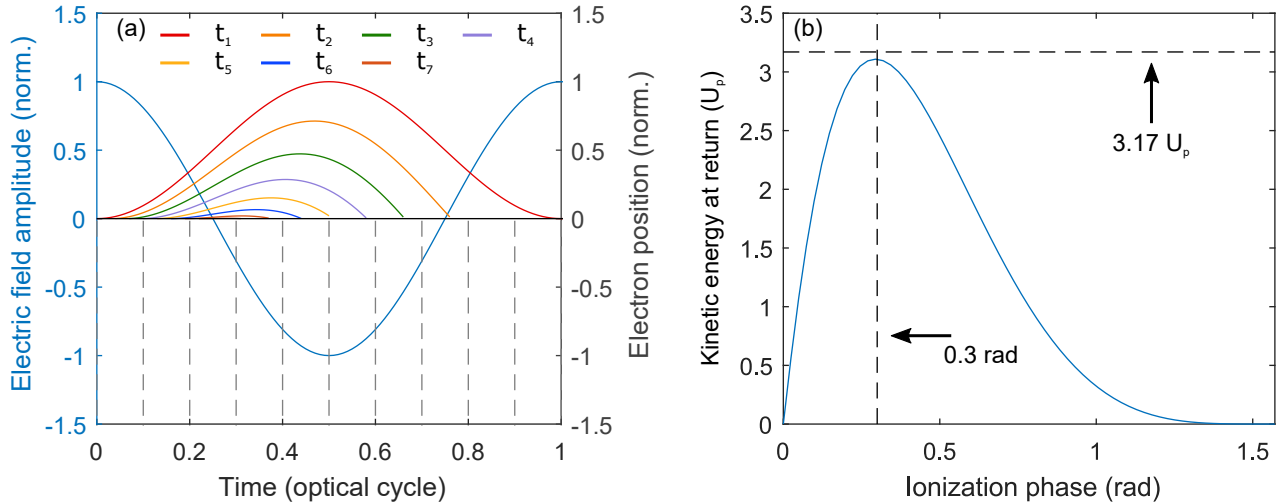
scaling with the intensity  $I$  and the square of the wavelength  $\lambda$ . By solving the equation of motion for this single atom response, one can observe several features underlying the HHG process, as presented in Fig. 2.10. In (a), the electron trajectory under the effect of the laser electric field  $E$  (blue line) is displayed for different ionization times  $t_i$  within the first quarter-cycle of  $E$ . After leaving the atom at  $t_i$ , recombination takes place when the electron position returns to zero. The round-trip duration is largest when the electron is ionized at the peak of the electric field. Ionization at later times results in shorter round-trips. An electron that is ionized within the second quarter-cycle of  $E$  drifts away from the ionic core and never returns. During the second half-cycle of the electric field, the ionized electron is emitted in the opposite direction but the trajectory behavior is identical to the first-half cycle. Note that due to the exponential dependence of tunnel ionization on the electric field [71], ionization is in fact confined to the regions where the field amplitude is maximal.

Fig. 2.10b displays the kinetic energy acquired by an electron at the moment of recombination with its parent ion for different ionization phases, corresponding to the phase of the electric field  $E$  at the instant of ionization. The maximal kinetic energy at an ionization phase of 0.3 rad ( $17^\circ$ ) corresponds to  $\sim 3.17 U_p$ . Therefore, the highest photon energy that can be obtained by HHG, the *cutoff energy*, is:

$$E_{cutoff} \approx I_p + 3.17 U_p \quad (2.4)$$

where  $I_p$  is the ionization potential energy of the atom that is also recovered during recombination. The curve also illustrates that two different ionization phases can lead to the same kinetic energy. Interpreting these results with the help of Fig. 2.10a, an early ionization time  $t_i$  leads to a long

trajectory while a late ionization time results in a short trajectory, hence the name *long* and *short trajectories* that are given to electrons emitted below and above an ionization phase of 0.3 rad, respectively. It is important to note that as  $U_p \propto I\lambda^2$ , increasing the wavelength of the driving field allows to extend the cutoff energy of HHG. We will also take advantage of this relationship in Sec. 2.9 to extend  $E_{cutoff}$  to the soft x-ray.



**Figure 2.10** – (a) Electron trajectory for different ionization times  $t_i$  within the electric field  $E$  (blue curve). (b) Kinetic energy of the electron returning to the ionic core with respect to the phase of  $E$  at ionization. The highest kinetic energy of  $\sim 3.17 U_p$  is acquired at 0.3 rad ( $17^\circ$ ). These two values are identified by dashed lines.

### 2.7.2 Quantum aspect of HHG

To describe the quantum nature of HHG, Lewenstein *et al.* proposed to solve the TDSE within a physical framework known as the *strong-field approximation* (SFA) [73]. In this framework, it is assumed that only the electronic ground state is ionized by the laser field. The ionization conditions must also ensure that depletion of this state is negligible and that a very limited population of the ground state wavefunction leaves the parent ion to propagate into the continuum. During this propagation, the Coulomb interaction between the parent ion and the electron is considered to be negligible.

To solve the TDSE, the saddle point method is employed and the resulting time-dependent dipole moment contains the amplitude and phase information of the HHG spectrum, extracted by Fourier transform (FT). The phase of the frequency components in such spectrum is directly linked to the accumulated phase acquired by the electron during propagation in the continuum, i.e. the atomic

dipole phase. As shown in Fig. 2.10a, each trajectory has unique ionization and recombination times, leading to a unique phase. This dipole phase for each harmonic order  $q$  corresponds to:

$$\Phi(r, t) \approx -\alpha_q^j I(r, t) \quad (2.5)$$

where  $\alpha_q^j$  is a phase coefficient describing the slope of the phase variation for different intensities of the laser field (see Fig. 2.11a). It depends on the harmonic order  $q$  and on the trajectory type  $j$  of the electron.  $I(r, t)$  is the spatio-temporal intensity profile of the laser pulse. The above phase dependence on intensity contains the information to describe the spectral and spatial properties of a HHG spectrum.

Fig. 2.11a adapted from [74] illustrates the typical phase dependence on intensity for short (solid line) and long (dashed line) trajectories, calculated within the SFA for the 19th harmonic of argon. The slope for long trajectories is much more pronounced than for the short ones, resulting in very different phase coefficients  $\alpha_q^j$ .

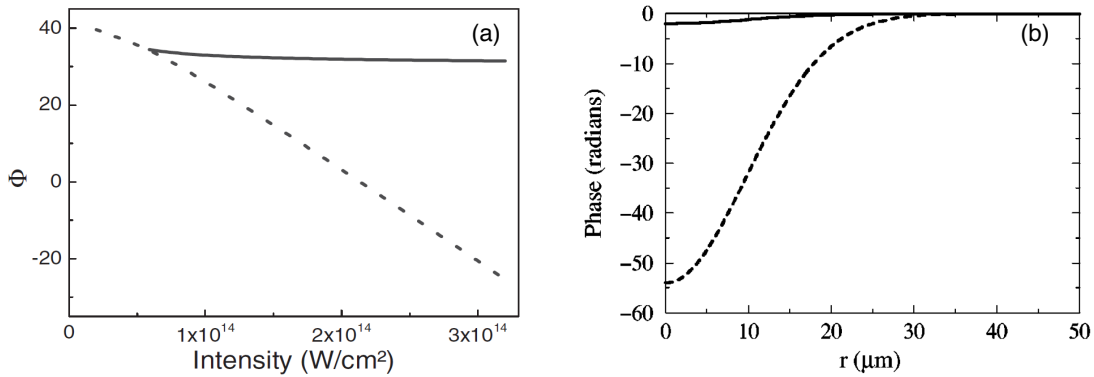


**Figure 2.11 – Phase properties in HHG for short (solid lines) and long (dashed lines) trajectories. (a) Example for the intensity dependence of the phase for the 19th harmonic of argon calculated by Varju *et al.* 2005 [74]. (b) Effect of the phase coefficient on the radial phase profile for the 15th harmonic of argon calculated from Gaarde *et al.* 1999 [75].**

An example of the impact of  $\alpha_q^j$  on the HHG spatial property is presented in Figure 2.11b adapted from [75]. Shown is the result of Eq. 2.5 at the geometrical focus of a 810 nm (100 fs) Gaussian pulse (Rayleigh length = 1.5 mm) with an intensity ( $I_0$ ) of  $2 \times 10^{14}$  W/cm<sup>2</sup>. The wavefront curvature created at the focus by this effect for harmonics issued from long trajectories (large  $\alpha_q^j$ ) leads to a strong divergence of the beam and is experimentally observed in the far-field as a larger illuminated area on a detector compared to short trajectory harmonics.

In a similar manner as for the radial phase profile, the temporal profile of the dipole phase affects the spectral properties of the harmonics. In Section 2.3, the spectral broadening issued from self-phase modulation (SPM) in a waveguide is described by Eq. 2.2. The equation shows

that a variation of phase in time leads to an instantaneous frequency  $\omega_i$  that depends on  $\partial\Phi/\partial t$ , characterized by the temporal intensity profile of the laser pulse. In HHG, the typically large phase coefficient for long trajectory harmonics leads to a sharp temporal profile of the phase that is less pronounced for short trajectories (Eq. 2.5). In the same way as described for SPM, this leads to a spectral broadening that is more important for harmonics issued from long trajectories.

Finally, as described in the following section, because of the very different phase properties between long and short trajectories, only a selected type can be optimized through phase matching when considering HHG from a large number of atoms.

### 2.7.3 Phase matching

The semi-classical model as well as the quantum mechanical description presented above allow to describe the spectral, temporal and spatial properties of a HHG spectrum. In practice, one must however consider the coherent nature of the harmonics emitted by a macroscopic ensemble of atoms. In this case, phase matching conditions must be met in order to obtain a constructive signal and a sufficient photon flux for performing experiments.

The HHG signal is optimized when the wave vector mismatch between the harmonic order  $q$  ( $\vec{k}_{\omega q}$ ) and the driving field ( $\vec{k}_{\omega_0}$ ) is minimized according to [76, 77, 78]:

$$\Delta k = q\vec{k}_{\omega_0} - \vec{k}_{\omega q} = \Delta\vec{k}_{gas} + \Delta\vec{k}_{plasma} + \Delta\vec{k}_{Gouy} + \Delta\vec{k}_{dipole} = 0 \quad (2.6)$$

with the relation  $k(\omega) = \frac{\omega}{c}n(\omega)$  where  $n(\omega)$  is the refractive index. Here,  $\Delta\vec{k}_{gas}$  corresponds to the dispersion induced by the neutral atoms. This contribution scales linearly with the gas pressure and is always positive because the refractive index of the fundamental frequency is always larger than for its high order harmonics.

$\Delta\vec{k}_{plasma}$  is the dispersion induced by the free electrons of the plasma with frequency  $\omega_p$  that is generated by the ionizing laser pulse. When  $\omega \gg \omega_p$ , the refractive index of the plasma  $n(\omega)_{plasma}$  is a real value and absorption from the plasma is limited (see Eq. 2.7). Since in typical HHG setup this criterion is always met for both the driving field and the high-order harmonics,  $\Delta\vec{k}_{plasma}$  is always negative. This term also scales linearly with the gas pressure.

$$k_{plasma}(\omega) = \frac{\omega}{c}n(\omega)_{plasma} = \frac{\omega}{c}\sqrt{1 - \left(\frac{\omega_p}{\omega}\right)^2} \quad (2.7)$$

$\Delta\vec{k}_{Gouy} = q\partial\phi_{Gouy}/\partial z$  refers to the phase variation that occurs along the laser focus (here along  $z$ ). Fig. 2.12 displays the Gouy phase for a 1800 nm field that is focused to a 50  $\mu\text{m}$  radius

( $1/e^2$  of intensity). It can be observed that the derivative of the phase with respect to the position along the geometrical focus is always negative, hence  $\Delta\vec{k}_{Gouy}$  is always negative. Additionally, since the divergence of high order harmonics is significantly lower than for the fundamental field, the contribution of the Gouy phase for the harmonics  $q$  can be neglected when  $\Delta\vec{k}_{Gouy}$  is evaluated.

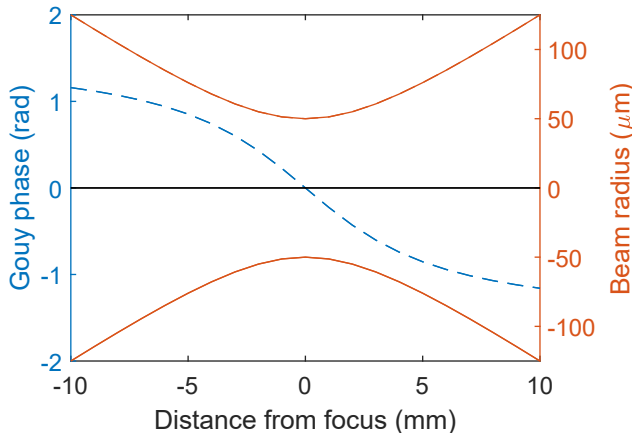


**Figure 2.12 – Gouy phase for a 1800 nm laser field focused to a 100  $\mu\text{m}$  diameter focal size ( $1/e^2$  of intensity).**

Finally  $\Delta\vec{k}_{dipole} = -\alpha_q \partial I / \partial z$  refers to the dipole phase discussed in the previous section. Since it depends on the intensity profile along the geometrical focus, this term is negative when the beam is converging ( $z < 0$ , positive slope) and positive when the beam is diverging ( $z > 0$ , negative slope). Because of this term, phase matching conditions are generally optimized for a selected type of trajectories by moving the interaction medium along the geometrical focus. For short trajectories this term is however often negligible.

Experimentally, minimization of the wave vector mismatch can be achieved by controlling parameters such as the focusing geometry, the gas pressure in the focal volume as well as the pulse intensity and duration of the driving field. In Sec. 2.9, we optimized these parameters in order to achieve a high photon flux in the water window spectral region.

## 2.8 Water window

Each chemical element has a specific electronic configuration that typically leads to energetically distinct electronic transitions upon excitation. This ‘atomic fingerprint’ led to the development of analytical techniques in chemistry such as atomic emission spectroscopy, where the emitted spectrum from the relaxation of an excited gaseous sample describes the composition and concentration of each atomic species. Alternatively, the absorption spectrum of an irradiated sample provides similar information. This approach is at the basis of X-ray absorption spectroscopy (XAS). In this case,

core electrons can absorb X-ray radiation and the near edge spectrum for a specific atom is sensitive to its chemical environment.

In time-resolved spectroscopy, this concept offers the possibility to probe in a site-specific way the nuclear and electronic dynamics of a system. Of particular interest is the soft x-ray region that is delimited by the carbon and oxygen  $K$ -edges, respectively at about 284 eV and 543 eV. These absorption edges define a spectral region where the transmission of water is increased and thus offers better contrast for measurements, known as the *water window*. This opens new perspectives to study biological systems in their aqueous environment, but also to study relevant organic molecules (mostly composed of carbon and nitrogen atoms) in the gas phase. The water window also contains edges of transition metals of interest to study ultrafast demagnetization in condensed matter.

## 2.9 Soft x-ray generation at the Advanced Laser Light Source

Eqs. 2.3-2.4 describing the single atom response of HHG show that the generation of soft x-ray pulses in the water window can be achieved either by increasing the laser pulse intensity or the wavelength of the driving field as  $E_{cutoff} \propto I\lambda^2$ .

While increasing the intensity can extend linearly the cutoff energy, it also leads to higher ionization rates and creates additional free electrons in the generating medium. Above a critical electron density, the dispersion induced by the plasma cannot be compensated to meet the phase matching condition and is detrimental for the conversion efficiency. For this reason, an ionization fraction below 5% is typically considered [78, 79, 80]. The ionization fraction defines a saturation intensity that depends both on the ionization potential of the atomic medium and the pulse duration. A shorter pulse duration or/and larger ionization potential allows to reach higher saturation intensities and hence a higher cutoff photon energy that can be phase matched.

In addition to the saturation intensity, the common approach to extend the cutoff energy is to scale the driving wavelength towards the mid-infrared. However, in the single-atom response, the conversion efficiency of HHG also decreases  $\propto \lambda^{-6}$  [81] and this effect must inevitably be compensated by increasing the gas density. Fig. 2.13 shows how the gas pressure to phase match the cutoff energy in different gases varies in a quadratic way with the wavelength.

In this context, we developed at ALLS a high flux soft x-ray source driven at 1.8  $\mu\text{m}^2$ . To provide a high density medium, a 8-mm gas cell was interfaced to a pulsed Parker valve operating at 100 Hz and for which the opening time was optimized. Helium with a backing pressure of 45 bar was employed. The valve was synchronized with the OPA system that was presented in section 2.2, delivering 8 mJ pulses with a duration of 30 fs. A loose focusing geometry was employed with a 60 cm lens. Fig. 2.14 shows the harmonic spectra that were obtained, spanning from 100 to about

---

<sup>2</sup>While the full paper [82] will not be presented in this thesis, the main results are shown here.

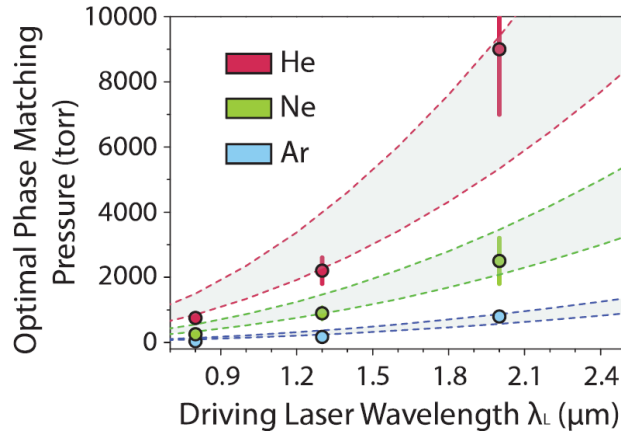


**Figure 2.13** – Example of calculated (dashed lines) vs experimental (circles) phase matching pressure for the cutoff photon energy as a function of wavelength. The calculations show the results at 96% and 98% of the ionization fractions defined in Chen *et al.* 2010, from which the figure is adapted [79].

550 eV and hence covering the entire water window. The obtained cutoff energy is in agreement with theoretical predictions considering our pulse duration and driving wavelength [78, 79]. To calibrate the spectra, a few filters were used: a 200-nm thick Mylar (polyethylene terephthalate) foil to identify the carbon *K*-edge at 284 eV and a 200-nm thick titanium (Ti) foil to identify the Ti *L*<sub>2</sub>-edge at 460 eV. The inset shows the region of the oxygen *K*-edge at 543 eV when employing an aluminum foil. To demonstrate the capabilities of the source for time-resolved measurements in the water window, Fig. 2.15 also shows single-shot measurements acquired with the Mylar filter. A clear cut at the carbon *K*-edge is visible in the spectra. By using an XUV CCD (PI-MTE, Princeton Instruments), a photon flux of  $8 \times 10^4$  photon/shot was measured for the water window region.

A number of tabletop sources delivering photons in the water window, including ours, have been reported in the last decade (for example see Refs. [79, 25, 83, 82]), but their applications in spectroscopy are relatively recent. A seminal experiment exploiting the water window for time-resolved measurements was realized by Pertot *et al.* [84]. The same group also used soft x-ray photons to study molecular dynamics in liquid jets [85]. As for the high flux source developed at ALLS, it is currently being used by the group of Prof. Légaré for X-ray magnetic scattering experiments [86]. Operating at 100 Hz, this source is particularly suitable for such experiments where the solid samples are sensitive to heat and require to minimize the average power.

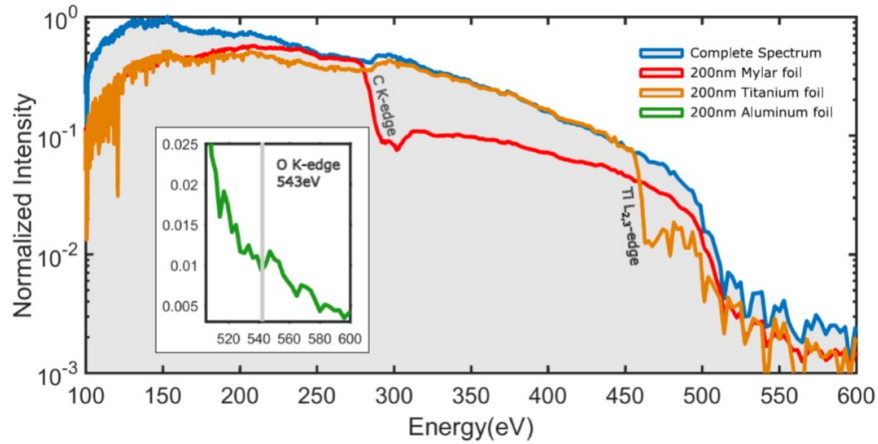


Figure 2.14 – High harmonic spectra from helium gas obtained by focusing 8-mJ, 30 fs pulses at 1800 nm in a 8-mm gas cell at a backing pressure of 45 bar. The unfiltered spectrum (blue curve) was acquired over 2000 laser shots. Spectra were also acquired with a Mylar filter (red curve) to identify the carbon  $K$ -edge (284 eV) and a titanium filter to identify the Ti  $L_{2,3}$ -edge (460 eV) Inset: Spectral region around the oxygen  $K$ -edge (543 eV) when using an aluminum filter.

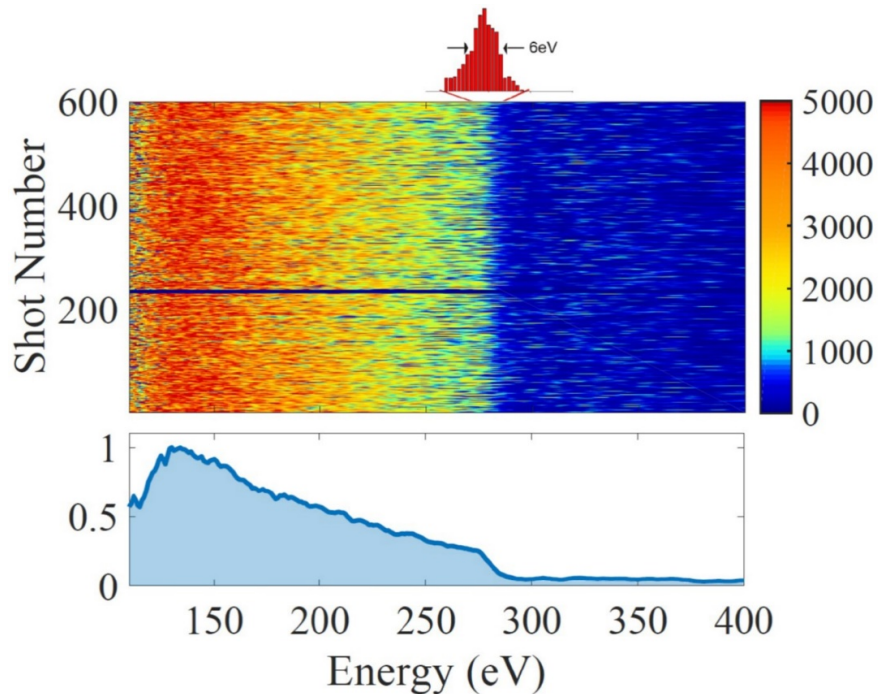


Figure 2.15 – Top: Single-shot spectra acquired with a Mylar filter. The histogram identifies the carbon  $K$ -edge using an edge-detection algorithm. The laser beam was blocked for laser shots 220-225 to acquire the background signal. Bottom: Integrated signal over 600 shots on a linear scale.

## 2.10 Supplementary article – Self-channelled high harmonic generation of water window soft x-ray

Vincent Cardin<sup>1</sup>, Bruno E. Schmidt<sup>1,2</sup>, Nicolas Thiré<sup>1</sup>, Samuel Beaulieu<sup>1,3</sup>, Vincent Wanie<sup>1,4</sup>, Matteo Negro<sup>4</sup>, Caterina Vozzi<sup>4</sup>, Valer Tosa<sup>5</sup> and François Légaré<sup>1</sup>

<sup>1</sup>Institut national de la Recherche Scientifique – Énergie, Matériaux, Télécommunications, Varennes, Qc. J3X1P7, Canada

<sup>2</sup>Few-cycle Inc., Montreal, Qc. H1L5W5, Canada

<sup>3</sup>Université de Bordeaux – CNRS – CEA, CELIA, UMR5107, F-33405 Talence, France

<sup>4</sup>Institute for Photonics and Nanotechnologies CNR-IFN, I-20133 Milano, Italy

<sup>5</sup>National Institute for R&D Isotopic and Molecular Technologies, 400293 Cluj-Napoca, Romania

Journal of Physics B: Atomic, Molecular and Optical Physics **51**, 174004 (2018)

Received 12 March 2018

Published 3 August 2018

doi: 10.1088/1361-6455/aad49c

B.E.S., N.T., S.B. and V.W. performed the experiments. M.N. and C.V. were guest scientists and participated to the experiments. V.C. took additional measurements and wrote the manuscript with the help of all co-authors. V.T. provided the numerical simulations. C.V. and F.L. supervised the collaboration.

## Chapter 3

# An attosecond beamline for pump-probe experiments using few-femtosecond UV pulses

The understanding of the high harmonic generation process described in the previous chapter provided a mean to obtain laser pulses with attosecond duration ( $1 \text{ as} = 1 \times 10^{-18} \text{ s}$ ). As described in the main introduction, first identifications of attosecond pulses were realized in 2001 by Paul *et al.* and by Hentschel *et al.* [7, 8], providing the necessary tools to perform XUV-pump NIR-probe experiments to study electron dynamics. Since then, several attosecond experiments have been carried out and have allowed, for instance, to characterize charge migration processes in molecules [16] and photoemission delays in solids [87].

In the following chapters (articles IV and VII), we demonstrate how one can manipulate the few-fs electron dynamics in molecules to predict the outcome of photochemical processes. In both cases, we study the dynamics of the molecule after a first ionization, i.e. in the cationic state. Particularly in the case of attosecond XUV-pump NIR-probe experiments, the photon energy of the XUV pulse is above the ionization potential of the molecule and inevitably leads to ionization. While a large class of interesting cation dynamics in molecules can be studied with such approach, several molecular processes of biological relevance occur in the neutral states following photoexcitation. In nucleobases for instance a number of relaxation processes through nonadiabatic couplings are triggered upon UV absorption [88, 89, 90]. For this reason, an interesting pump-probe scheme would consist in employing an ultrashort UV-pump pulse to initiate molecular processes in neutral states, followed by ionization by an XUV attosecond pulse to probe the dynamics. In order to preserve the high temporal resolution of the conventional XUV-pump NIR-probe configuration, the development of techniques to generate few-femtosecond UV pulses is mandatory. Furthermore, not only ultrashort UV pulses must be generated but they must also be integrated in a pump-probe

configuration to be used in combination with attosecond pulses. In this chapter, we present our approach for the construction of an attosecond beamline combining few-femtosecond UV pulses with isolated attosecond XUV pulses. Article II discusses the generation of few-femtosecond UV pulses via third harmonic generation in gases. The characteristics and performances of an attosecond beamline combining UV, NIR and attosecond XUV pulses is then discussed in article III.

### 3.1 Third-harmonic generation in gases

In centrosymmetric media, one of the first accessible nonlinear processes is third-harmonic generation, depicted in Fig. 3.1. Three photons with the same frequency ( $\omega_1 = \omega_2 = \omega_3 = \omega$ ) can induce a third-order polarization  $P^{(3)}$  of the medium, producing radiation at a tripled frequency  $\omega_4 = 3\omega$ . The specific case for THG in gas with negligible dispersion effects is detailed here. This process can be described by the wave equation for an isotropic nonlinear medium derived from Maxwell's equations [91]:

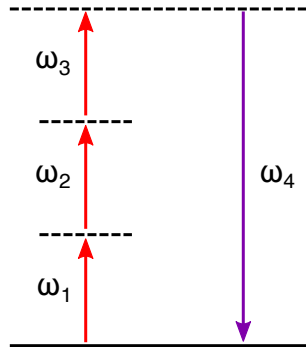


**Figure 3.1 – Principle of parametric third-harmonic generation. Three waves with the same frequency ( $\omega_1 = \omega_2 = \omega_3 = \omega$ ) are converted into a frequency tripled wave  $\omega_4 = 3\omega$ .**

$$\frac{\partial^2 E}{\partial z^2} + \frac{\epsilon_r}{c^2} \frac{\partial^2 E}{\partial t^2} = \frac{1}{\epsilon_0 c^2} \frac{\partial^2 P^{(3)}}{\partial t^2} \quad (3.1)$$

where the wave propagation is considered to be along the  $z$  direction,  $\epsilon_r$  and  $\epsilon_0$  are respectively the medium's relative permittivity and vacuum permittivity, and the third-harmonic field  $E$  is described as a plane wave:

$$E(z, t) = A_4(z) e^{i(k_4 z - \omega_4 t)} + c.c. \quad (3.2)$$

with wave vector  $k_4$  and field amplitude  $A_4(z)$ . The incoming pump waves are described by :

$$E^{\omega_i}(z, t) = E^{\omega_i} e^{-\omega_i t} + c.c. \quad (3.3)$$

with  $E^{\omega_i} = A_i e^{k_i z}$  and where the amplitude coefficients  $A_i$  are constant under the undepleted pump approximation, that is when the conversion of the fundamental field is negligible. For a linearly polarized driving field along the  $x$  direction, the third-order nonlinear polarization  $P_x^{(3)}$  that describes THG is:

$$P_x^{(3)} = \epsilon_0 \frac{1}{4} \chi_{xxxx}^{(3)} E_x^{\omega_1} E_x^{\omega_2} E_x^{\omega_3} \times e^{-i\omega_4 t} + c.c. \quad (3.4)$$

where all the frequency components ( $E_x^{\omega_i}$ , with  $i=1,2,3$ ) including the generated third-harmonic find their polarization along  $x$  and  $\chi_{xxxx}^{(3)} = \chi^{(3)}$  is a constant that depends on the isotropic gas medium (see table 3.1). Inserting equations 3.3 and 3.4 into the wave equation 3.1 results in:

$$\begin{aligned} & \left[ \frac{d^2 A_4(z)}{dz^2} + 2ik_4 \frac{dA_4(z)}{dz} - k_4^2 A_4(z) + \frac{\epsilon_r \omega_4^2 A_4(z)}{c^2} \right] e^{i(k_4 z - \omega_4 t)} + c.c. \\ & = \frac{-\chi^{(3)} \omega_4^2}{4c^2} A_1 A_2 A_3 e^{i[(k_1 + k_2 + k_3)z - \omega_4 t]} + c.c. \end{aligned} \quad (3.5)$$

which can be rewritten:

$$\frac{d^2 A_4}{dz^2} + 2ik_4 \frac{dA_4}{dz} = \frac{-\chi^{(3)} \omega_4^2}{c^2} A_1 A_2 A_3 e^{i(k_1 + k_2 + k_3 - k_4)z} \quad (3.6)$$

Within the slowly varying envelope approximation (SVEA) where the intensity envelope of the laser pulse varies significantly slower than the electric field underneath, the first term of the equation can be neglected, hence:

$$\frac{dA_4}{dz} = \frac{i\chi^{(3)} \omega_4^2}{2k_4 c^2} A_1 A_2 A_3 e^{i\Delta k z} \quad (3.7)$$

with  $A_1 = A_2 = A_3 = A_\omega$  and  $k_1 = k_2 = k_3$ . Equation 3.7 describes the evolution of the third-harmonic field amplitude along propagation in the nonlinear medium. It is observed that the main parameters that affects THG are the pump amplitude  $A_\omega^3$ , the third-order susceptibility  $\chi^{(3)}$  and the term  $\Delta k = 3k_1 - k_4$  which introduce the phase matching conditions.

Unlike for crystals, THG in gas cannot benefit from optimization of birefringent phase matching, which inevitably leads to a lower conversion efficiency. In this case, the phase matching parameters are similar to what has been described for the case of HHG in Chapter 2. Contributions from the focusing geometry (Gouy phase), the dispersion induced by the gas medium and the generated plasma can in principle be exploited. For example, the conversion efficiency can be enhanced by employing a mixture of xenon and rubidium vapor to balance the refractive indexes for the fundamental and frequency tripled fields [92, 93]. However such approach is rather difficult to implement, especially in the context of building a beamline. An alternative is to generate the third-harmonic in a high density medium to increases the number of emitters during THG.

In the work presented in this chapter, we employed a glass cell in which a high gas pressure was injected in order to produce few-femtosecond UV pulses through THG of 800 nm pulses. Table 3.1 reports the properties of the media that were considered for such approach. The third and fourth columns compare the group velocity dispersion (GVD) at 266 nm and the third-order susceptibility at  $1.06 \mu\text{m}^1$  for different rare gases. For comparison, the values for fused silica have also been added. First, it can be observed that the GVD in gases is negligible compared to glasses in which THG can also be produced. For instance, a 3-fs transform limited pulse passing through  $200 \mu\text{m}$  of fused silica would stretch above 30 fs, while in argon the dispersion effect is negligible. This example justifies the use of THG in gases when one prioritizes the shortest possible pulse duration. The first column of table 3.1 also provides the ionization potential for each gases, also affecting THG through ionization and plasma effects that can become detrimental to the process.

**Table 3.1 – Rare gas properties for the generation of few-femtosecond UV pulses**

Nonlinear medium	Ionization potential (eV)	GVD at 266 nm ( $\text{fs}^2/\text{mm}$ )	$\chi^{(3)}$ at $1.055 \mu\text{m}$ – Ref. [95] ( $\text{m}^2/\text{V}^2$ )
He	24.59	0.0036607	$3.43 \times 10^{-28}$
Ne	21.56	0.0091518	$6.17 \times 10^{-28}$
Ar	15.76	0.082890	$8.06 \times 10^{-27}$
Kr	14.00	0.19219	$2.20 \times 10^{-26}$
Xe	12.13	0.59199	$6.46 \times 10^{-26}$
Fused silica	–	197.53	$2.0 \times 10^{-22}$ ( $1.064 \mu\text{m}$ – Ref. [96])

## 3.2 Generation of isolated attosecond pulses

To obtain isolated attosecond XUV pulses (IAPs), we employ a polarization gating (PG) technique [97], exploiting the dependence of HHG on the ellipticity of the driving field [98]. An increase of ellipticity deviates the trajectory of the ionized electron such that the recombination probability is reduced, limiting the HHG yield. By reshaping the polarization of the laser pulse to obtain a linear field only for a narrow temporal window (gate) containing less than an optical cycle, it is possible to generate an IAP. This is achieved by using two birefringent plates as schematized in Fig. 3.2. A multi-order waveplate is placed with the optical axis at  $45^\circ$  relative to the linear polarization of the laser to create two distinct pulses orthogonal to each other. Then, a zero-order quarter waveplate (typically at  $0^\circ$ ) induces a circular polarization to the pulses, each rotating in opposite directions. After propagating through the quarter waveplate, the temporal gate where the

<sup>1</sup>The values at  $1.06 \mu\text{m}$  are often used as references when working with a 800 nm field, for examples see [22, 94].

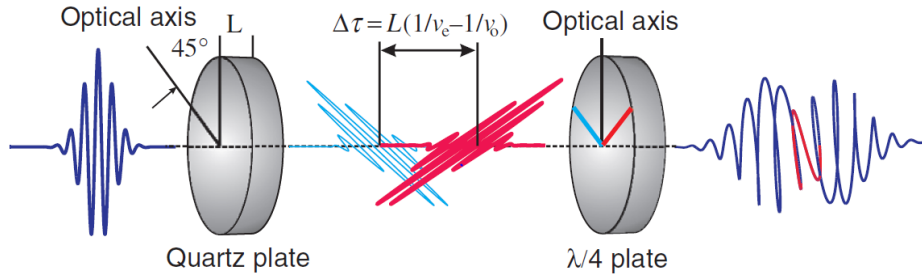


**Figure 3.2** – Principle of the polarization gating technique employing waveplates. The figure is adapted from Rykovanov *et al.* 2008 [100].

pulses overlap creates a linearly polarized field that can produce an IAP. The width of the gate for a Gaussian pulse is defined by:

$$\tau_g = \frac{\xi_{th}^q \tau_p^2}{\ln 2 \Delta_t |\cos(2\theta_{\lambda/4})|} \quad (3.8)$$

where  $\tau_p$  is the duration of the compressed pulse driving HHG,  $\Delta_t$  the delay between the two orthogonal pulses after the first waveplate and  $\theta_{\lambda/4}$  is the angle of the quarter waveplate relative to the initial laser polarization. An ellipticity threshold  $\xi_{th}^q$  is defined as the required ellipticity to reduce the signal of an harmonic order  $q$  by half [99]. The gate width is controlled by adjusting  $\theta_{\lambda/4}$  and  $\Delta_t$ , the latter depending on the thickness and refractive indexes of the axes of the first plate.

The PG method requires few-cycle pulses with a fixed carrier-envelope phase  $\phi_{CEP}$ , corresponding to the phase offset between the peak of the pulse intensity envelope and the peak electric field underneath. This is because within a polarization gate containing a single cycle, a CEP shift from  $\phi_{CEP} = \pi/2$  to  $\phi_{CEP} = \pi$  can produce two attosecond pulses rather than one, which can be detrimental for an attosecond experiment. In article III, the CEP stabilization is achieved within the laser system in a similar method as in [20]. Delivering 12-mJ pulses at a 1 kHz repetition rate, about 5 mJ are used to obtain 5-fs pulses via hollow-core fiber post-compression (described in section 2.4). The HCF setup consists of a 1-m long rigid HCF filled with helium and is operated with a pressure gradient.

### 3.3 Article II – Summary

In article II, we describe our approach for the generation of few-femtosecond UV pulses through THG of 5-fs (770 nm) pulses obtained by hollow-core fiber post-compression. Taking into account the restrictions described in section 3.1 to limit dispersion, we discuss the utilization of a glass cell that can support a large gas load in order to enhance the conversion efficiency of THG (Figure 3.5b,c). We investigated the scaling of the UV pulse energy and bandwidth (Figure 3.6) with the argon gas

pressure. For an absolute pressure above 1.1 bar, we find a saturation of the pulse energy when ionization and plasma effects become dominant. With 1.1 bar of argon, a pulse energy of 150 nJ is obtained with a conversion efficiency of  $10^{-4}$ . At this pressure, a large spectral broadening is obtained with a TL duration of 1.45 fs. Because of the large bandwidth obtained, the temporal characterization of the UV pulses cannot be easily performed with all optical techniques in which the transmissive medium would introduce significant dispersion. For this reason, we present a temporal characterization of the pulse duration using a cross-correlation method in xenon gas. By measuring the signal of photoionized atoms as a function of the UV-pump NIR-probe delay with a time-of-flight mass spectrometer, a pulse duration of 1.9 fs is retrieved.

To put our results in perspective, a comparison with the recent literature is presented in Table 3.2. Each technique that is reported is exploiting a gas medium for the generation of UV pulses. Together with the dispersion-wave emission technique in photonic crystal fibers (PCF), THG in gas can provide sub-3-fs pulses with nJ of energy. Another interesting technique to obtain short pulses was reported by Reislöhner *et al.* 2019 [101], but the pulse energy on the pJ level is not sufficient for our applications. Compared to the aforementioned works, the particularity of our setup is that care was also taken to integrate it within our attosecond beamline for time-resolved experiments, as described in article III.

**Table 3.2 – List of recent publications reporting few-femtosecond UV pulses**

Publication	Technique	Pulse energy	Pulse duration
Reislöhner <i>et al.</i> 2019 [101]	sequential THG + self-diffraction	pJ	1.5 fs
Galli <i>et al.</i> 2019 [102]	THG in gas	nJ	1.9 fs
Reiter <i>et al.</i> 2010 [103]	THG in gas	nJ	2.8 fs
Brahms <i>et al.</i> 2019 [104]	dispersive-wave emission in PCF	nJ	3 fs
Fuji <i>et al.</i> 2007 [105]	four-wave mixing in gas filament	$\mu$ J	12 fs
Belli <i>et al.</i> 2019 [106]	four-wave mixing in PCF	nJ	sub-15 fs

### 3.4 Article III – Summary

In article III, we provide a detailed description of the attosecond beamline that was constructed during the major part of the thesis. The novelty of the beamline resides in the combination of the few-fs UV pulses described in article II together with isolated attosecond XUV pulses and few-cycle NIR pulses. We present the technical aspects for the operation of the beamline together with the performances of each components.

One of the main challenges consisted in working in a high vacuum environment over six different chambers (Fig. 3.8), first to avoid dispersion of the UV pulses but also to prevent absorption of the XUV radiation. To preserve a good vacuum level despite the heavy gas load required for THG, the

highly pressurized gas cell (Fig. 3.9) is placed in a three-stage differential pumping system (Fig. 3.10). This configuration allows us to reach  $10^{-3}$  mbar in the vacuum chamber where THG occurs while having at the same time several bar at the input of the gas cell. In this way, a final pressure of  $10^{-7}$  mbar is obtained in the beamline exit chamber that is interfaced with the experimental apparatus for the detection of charged particles, where such a vacuum level is required to perform experiments.

Another difficulty that was encountered during the development of the beamline is the very large gas consumption during THG. In order to prevent costly operations, we developed a gas recycling system to collect and recompress the residual THG gas. We present the performances of the setup with an efficiency of 96% (Fig. 3.11), that is likely to be useful for other applications requiring heavy gas loads such as the generation of attosecond soft x-ray pulses [25, 83].

Then we describe the generation of XUV pulses via HHG and the optical setup to isolate attosecond pulses, employing the polarization gating technique described in section 3.2. The dependence of the XUV spectra on the CEP of the driving 800-nm pulse is demonstrated to identify the isolated attosecond pulses (Fig. 3.15).

We also present the XUV spectrometer of the beamline that was designed in collaboration with Luca Poletto and Fabio Frassetto from CNR-IFN (Fig. 3.14). By combining a conventional grating with a divergent cylindrical mirror, we show that it is possible to obtain a very compact spectrometer (80 cm) while keeping a long entrance arm that is necessary for inserting experimental apparatus with a large footprint.

Finally, we describe our approach to obtain an attosecond pump-probe delay stability over the 5.75-m long interferometric setup. By compensating for thermal drifts and mechanical instabilities that can affect the beamline, we obtain an in-loop stability below 20 attoseconds over several hours of acquisition (Fig. 3.16).

## Future work on UV generation

While the generation of few-femtosecond UV pulses has been demonstrated, there are a number of elements that must be further investigated.

As illustrated in Fig. 3.6a, the broadest UV spectra has a shorter TL than what can be expected from pure THG of 5-fs NIR pulses ( $5/\sqrt{3} \approx 3$  fs), indicating that other important nonlinear processes contribute to the spectral broadening. For a first interpretation, we compared our results with the work from Reiter *et al.* 2010 employing similar generation conditions in neon gas to identify a temporal gating effect [107]. Their calculations of the THG process is shown in Fig. 3.3. Notably, the first row shows the spatio-temporal profile of the UV pulse with (b) and without (f) including ionization effects during propagation. In the first case, ionization induced self-defocusing of the

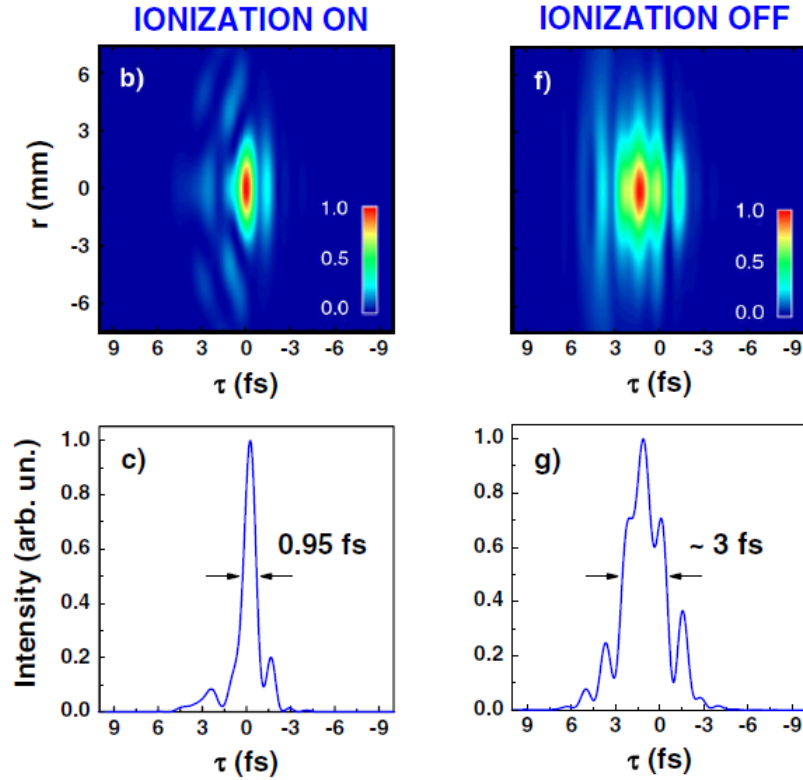


**Figure 3.3** – Effect of the ionization induced self-defocusing of the driving field during THG in neon gas. Left column: UV profile with ionization on. Right column: UV profile with ionization off. Figure adapted from Reiter et al. (2010) [107].

driving near-infrared field restricts the UV generation solely to the rising edge of the pulse, resulting in a UV duration as short as 1 fs (c), compatible with our observations. Without this contribution, the entire envelope of the driving field contributes to THG and a longer UV pulse is obtained (g).

While this effect supports our experimental results, to further optimize our UV generation, propagation simulations will be required. These will have to take into account our experimental conditions such as the focusing geometry employed, the NIR pulse duration and its intensity. For example, nonlinear contributions from self-phase modulation, self-defocusing and four-wave-mixing should be evaluated during the propagation of both the NIR and the generated UV pulses. An estimation of the gas density within the generation cell would also be necessary. Recently, Comby *et al.* 2018 have proposed a scheme to evaluate the density profile of gas jets during high-order harmonic generation [108]. The method relies on the characterization of the fluorescence emitted by the generated plasma and could possibly be implemented within our UV generation setup to evaluate the argon density during THG.

Also, a complete temporal characterization of the UV pulses will require to determine the amplitude and phase for each of their frequency components, which cannot be obtained with the cross-correlation approach presented in article II. The construction of an optical setup for transient-grating

frequency-resolved optical gating (TG-FROG, [109]) measurements would allow to obtain the spectral phase of our UV pulses. This however poses two technical challenges. First the optical setup must be built in a vacuum chamber with limited available space. Second the nonlinear medium must be dispersion free. To overcome this latter point, a variation of the TG-FROG technique employing a gas target as nonlinear medium has recently been reported [110]. Since the method should be applicable to UV pulses with energies on the nanojoule level, it would be interesting to further investigate in this direction.

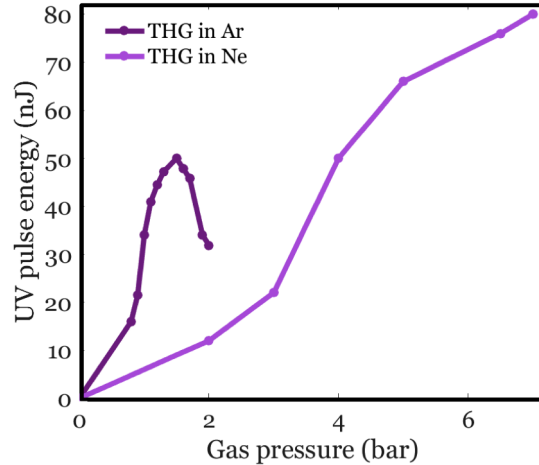


**Figure 3.4 – Comparison of the energy scaling between argon and neon. A 5-mm long gas cell and a 50 cm focusing mirror is employed.**

Finally, Fig. 3.4 compares the scaling of the UV pulse energy between THG in argon and THG in neon. Here, a 5-mm long cell and a 50 cm focusing mirror were employed and the tests were not performed in a high vacuum environment. While a saturation of the pulse energy is observed in argon, it is not the case in neon. However, the high pressure required for neon is not compatible with our current vacuum system. By improving the pumping scheme of the recirculation system described in article III, it should be possible to further investigate the UV generation in neon, which would be relevant for experiments requiring higher UV intensities.

### 3.5 Article II – Generation of deep ultraviolet sub-2-fs pulses

Mara Galli<sup>1,2,3</sup>, Vincent Wanie<sup>1,4</sup>, Diogo Pereira Lopes<sup>2</sup>, Erik P. Månsson<sup>1</sup>, Andrea Trabattoni<sup>1</sup>, Lorenzo Colaizzi<sup>1</sup>, Krishna Saraswathula<sup>1</sup>, Andrea Cartella<sup>5</sup>, Fabio Frassetto<sup>6</sup>, Luca Poletto<sup>6</sup>, François Légaré<sup>1</sup>, Salvatore Stagira<sup>2,3</sup>, Mauro Nisoli<sup>2,3</sup>, Rebeca Martinez Vazquez<sup>3</sup>, Roberto Osellame<sup>3</sup> and Francesca Calegari<sup>1,3,5,7</sup>

<sup>1</sup>Center for Free-Electron Laser Science (CFEL), DESY, 85 Notkestraße, Hamburg, 22607, Germany

<sup>2</sup>Physics Department, Politecnico di Milano, 32 Piazza Leonardo da Vinci, Milano 20133, Italy

<sup>3</sup>Institute for Photonics and Nanotechnologies, IFN-CNR, 32 Piazza Leonardo da Vinci, Milano 20133, Italy

<sup>4</sup>Institut National de la Recherche Scientifique, Centre Énergie Matériaux et Télécommunications, 1650 Blvd. Lionel-Boulet, Varennes, Québec J3X1S2, Canada

<sup>5</sup>The Hamburg Centre for Ultrafast Imaging, Universität Hamburg, 149 Luruper Chaussee, Hamburg 22761, Germany

<sup>6</sup>Institute for Photonics and Nanotechnologies, IFN-CNR, 7 Via Trasea, Padova 35131, Italy

<sup>7</sup>Department of Physics, Hamburg Universität, 9-11 Jungiusstraße, Hamburg 20355, Germany

Optics Letters **44**, 6 (2019)

Received 7 January 2019

Published 6 March 2019

doi: 10.1364/OL.44.001308

M.G., V.W. and E.P.M. built the experimental setup. M.G. and V.W. tested the UV generation and performed the measurements with the help of E.P.M., A.T., L.C., K.S. and A.C.. F.F., L.P. and F.C. designed the vacuum system. D.P.L., S.S., R.M.V., and R.O. developed the laser microfabricated gas cell. F.L., M.N., and F.C. supervised the project.

## Abstract

We demonstrate the generation of few-cycle deep ultraviolet pulses via frequency upconversion of 5-fs near-infrared pulses in argon using a laser-fabricated gas cell. The measured spectrum extends from 210 to 340 nm, corresponding to a transform-limited pulse duration of 1.45 fs. We extract from a dispersion-free second-order cross-correlation measurement a pulse duration of 1.9 fs, defining a new record in the deep ultraviolet spectral range.

## Main text

Absorption of ultraviolet (UV) radiation is associated with electronic excitation. In most of the molecules, this excess of energy is often dissipated via nonradiative decay. Upon UV excitation, ultrafast conversion of electronic energy into vibrational modes has been demonstrated to be at the core of fundamental processes such as DNA damage and photoprotection [111, 112]. Owing to the natural temporal scale of electron motion, getting access to these ultrafast mechanisms requires extremely short laser pulses, such as the ones provided by femtosecond or even attosecond laser sources. Nowadays, attosecond science is able to provide subfemtosecond laser pulses with a tunable spectrum over an extremely broad range, from the vacuum UV (VUV) [113] or extreme UV (XUV) [114, 115, 116] to the soft x rays [117]. Recently, even subfemtosecond visible (VIS) pulses have been generated [118]. At the same time, few-fs pulses in the visible or nearinfrared (NIR) spectral range can be routinely generated via hollow-core fiber compression [22] and filamentation [23]. Nevertheless, the generation of few-fs deep UV (200 to 300 nm) pulses is still extremely challenging. The hurdle arises from the need to optimize a nonlinear optical process over a broad spectral range where compression and phase control are currently not available. In the last two decades, many different techniques have been tested to generate ultrashort UV pulses, such as frequency upconversion [119], optical parametric amplification [120], four-wave mixing [121], or self-phase modulation in hollow-core [122] and photonic crystal fibers [123, 104]. Starting from NIR pulses, third harmonic generation (THG) is the most suitable process to be exploited for UV generation. Despite the high conversion efficiency nonlinear crystals can provide, they strongly limit the lowest duration of the upconverted pulses because of intrinsic dispersion and phase matching constraints [124]. A valid alternative is to use a noble gas as a nonlinear medium for THG [103, 125]. This method allows a broad spectral bandwidth to be upconverted without inducing significant dispersion to the generated UV pulses, at the expenses of a lower conversion efficiency. Using this technique, the generation of sub-3-fs pulses has been achieved [103].

In this Letter, we report the generation of 1.9-fs UV pulses centered at 260 nm using THG driven by few-fs NIR pulses in a high-pressure gas cell specifically designed to optimize the process. A pulse energy of 150 nJ was measured on target. To our knowledge, these are the shortest pulses

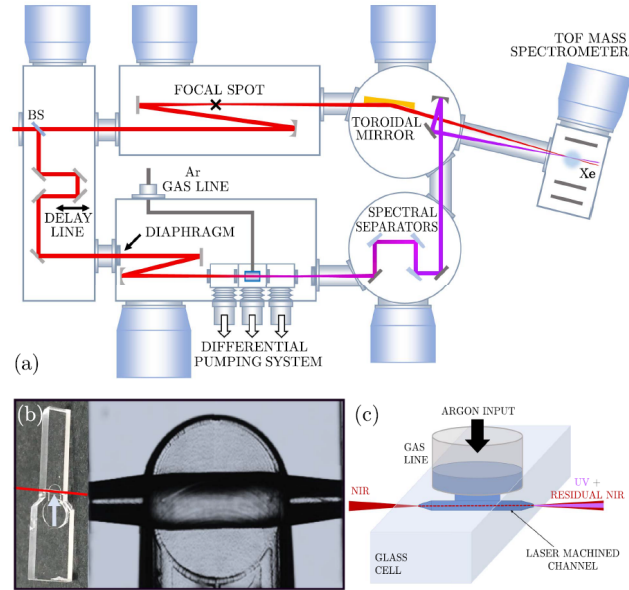


**Figure 3.5** – (a) Experimental setup used for generation and characterization of the sub-2-fs deep UV pulses. (b) Picture of the glass cell used to generate the UV pulses (the red line represents the laser propagation direction, while the light arrow represents the gas flow) and a magnified image of the channel acquired with a microscope. (c) Schematic representation of the gas cell showing the laser beam, the gas inlet, and the channel shape.

ever generated in the deep UV spectral range, opening up new perspectives for resolving the UV-photoactivated molecular processes at the time scale of electronic motion.

As schematically shown in Figure 3.5, 5-fs waveform-controlled NIR pulses (carrier wavelength of 770 nm) are used to seed an interferometric setup: a portion of the NIR beam (250  $\mu\text{J}$ ) is driving the UV generation process, while the remaining part of the NIR beam is either used to temporally characterize the UV radiation via cross-correlation or to generate XUV attosecond pulses. The whole setup is kept under vacuum to avoid dispersion of the UV pulses.

The NIR beam used to generate the UV radiation is focused with an 800-mm focal-length silver mirror into a gas cell filled with argon where the THG process is induced. The beam waist of the NIR pulse in the interaction point is estimated to be  $50 \pm 5 \mu\text{m}$ , with a peak intensity in the range of  $1$  to  $5 \times 10^{14} \text{ W/cm}^2$ . The gas cell has been fabricated in a fused silica slab using femtosecond laser irradiation followed by chemical etching (FLICE) [126, 127], and it has been interfaced to a 3-mm metallic tube supplying the gas. The gas cell, shown in panels b and c of Figure 3.5, is designed to have a 1-mm-diameter channel in the central section, acting as a reservoir, which is then progressively reduced at the extremities down to 400  $\mu\text{m}$ . The size of the holes has been chosen to fit that of the laser beam and to minimize the outflowing gas. This approach allows the UV generation to be confined within a few millimeters and the phase matching to be optimized. Channel lengths ranging from 3 to 5 mm have been tested to maximize the UV generation. The

use of a laser-machined fused silica cell presents several advantages with respect to a conventional metallic one: (1) the channel length and the hole size can be arbitrarily set with extremely high precision (few  $\mu\text{m}$ ); (2) contrary to metals, glass offers a high transmittance for VIS–NIR radiation, preventing the cell to be damaged by the impinging laser beam (with peak intensities in the order of  $10^{14}$   $\text{W}/\text{cm}^2$ ); and (3) the reservoir can be realized with any arbitrary geometry including guiding channels to further optimize the generation process. This design allows for efficient pumping, which is further improved by inserting the gas cell in a small chamber composed by three differentially pumped sections. This system allows a residual gas pressure of  $10^{-3}$  mbar to be achieved in the main chamber even when operating the setup with several bars of gas in the generation cell. A gas recirculation system has also been implemented to compensate for the high argon consumption.

Two sealed pumps are used to pump, respectively, the main vacuum chamber and the three sections of the differential pumping system. In this way, the recirculation of almost the entire gas volume is ensured. The pump exhaust lines are connected to a diaphragm pump, which compresses the gas in a tank up to 7 bars. The gas is then sent back to the UV generation cell through a metallic gas line, where a valve allows for the fine tuning of the pressure at the generation point.

The suppression of the copropagating fundamental NIR component after the UV generation is performed by three dichroic wedged beam separators (LAYERTEC GmbH). They have been installed in the UV optical path in order to transmit most of the NIR spectrum and reflect wavelengths below 350 nm. Attenuation of the NIR pulse energy by 4 orders of magnitude (residual energy 28 nJ) is achieved while preserving more than 85% of the UV pulse energy. In contrast to silicon wafers at Brewster’s angle used in previous setups [103], the reflectivity of the separators in the deep UV spectral region is higher than 85% for both s-polarized and p-polarized laser beams, thus allowing for both linear and circular UV radiation to be reflected. In this specific case, the generated UV radiation was linearly polarized. The generated UV pulses can be extracted before reaching the experimental region through a 300- $\mu\text{m}$ -thick UV-grade antireflection coated fused-silica window to characterize both spectrum and energy in air. In Figure 3.6(a) we compare the UV spectra obtained for THG in 0.2 bar (yellow solid line) and 1.1 bar (red solid line) of argon gas, respectively. The Fourier transforms of the two spectra are reported in the inset of the figure as black dots. A Gaussian fitting function is used to calculate the transform limited (TL) pulse durations, represented in yellow and red, respectively. The narrowest spectrum corresponds to a TL duration of 3 fs (FWHM), as expected by considering a pure THG process driven by 5-fs NIR pulses, as measured in Ref. [103]. Increasing the gas pressure above 1 bar leads instead to a remarkable spectral broadening of the UV pulse, corresponding to a TL duration of 1.45 fs (FWHM) and indicating the presence of other nonlinear effects. This spectral broadening can only be explained if we take into account pulse reshaping due to nonlinear effects for both the NIR driving pulses and the UV pulses. In particular, Kerr-effect-induced self-phase modulation as well as plasma phase modulation are expected to be the dominant effects. Ionization-induced spectral reshaping in THG has been previously investigated in neon at high gas pressures ( $>7$  bar) [107]. Owing to the lower

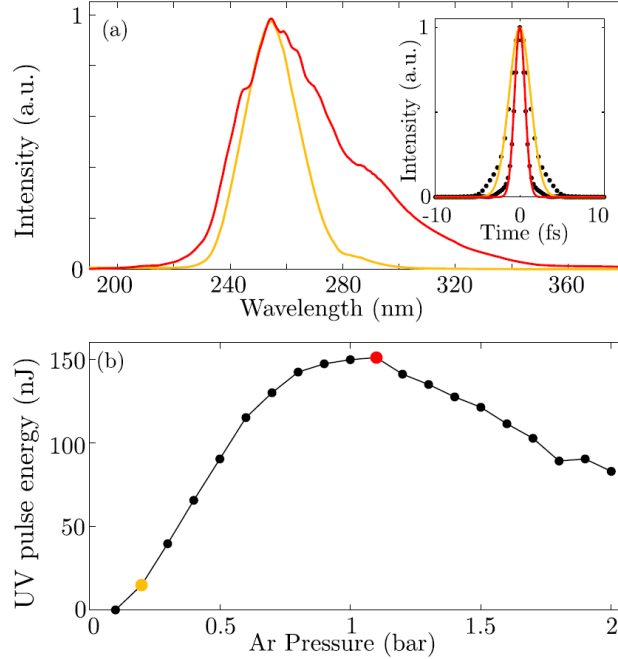


**Figure 3.6** – (a) Spectral intensity profile of the UV pulses acquired for 0.2 bar (yellow solid line) and 1.1 bar (red solid line) of argon. The inset shows the corresponding Fourier transforms (black dots) and the Gaussian fitting functions (solid lines, same color code as the main panel). (b) UV pulse energy measured as a function of the gas pressure. The red dot and the yellow dot correspond to the gas pressure values used for generating the red spectra and yellow spectra reported in (a), respectively.

ionization potential and the remarkably larger  $\chi^3$ , an even more pronounced effect is expected to occur in argon at much lower gas pressures. As demonstrated in Ref. [107], the ionization-induced self-defocusing occurring on the trailing edge of the driving pulse allows for a tight confinement of the nonlinear processes (including THG) to the leading edge of the pulse itself. This confinement can be interpreted as a gating effect on the THG process, thus resulting in the generation of a UV supercontinuum with a TL close to 1 fs. As shown in Ref. [107], the generated UV continuum is expected to experience a broadening on both sides of the spectrum while propagating in the gas target. It is worth noting that in our experimental conditions, the spectral broadening on the blue side, which also contains a strong contribution from fifth harmonic generation and a cascading of four-wave-mixing processes, cannot be detected due to the limited reflectivity of the optical setup in this spectral region.

Figure 3.6(b) shows the UV pulse energy as a function of the gas pressure at the generation cell. The maximum efficiency is achieved with 1.1 bar of argon. In this condition the pulse energy on target is around 150 nJ, which, considering the reflectivity of all the optics in the beam path, corresponds to more than 215 nJ at the source (pulse energy stability over several hours within 10%). Higher pressures lead to a reduction of the UV intensity due to strong ionization resulting from plasma-induced defocusing of the NIR beam accompanied by a deterioration of the spatial

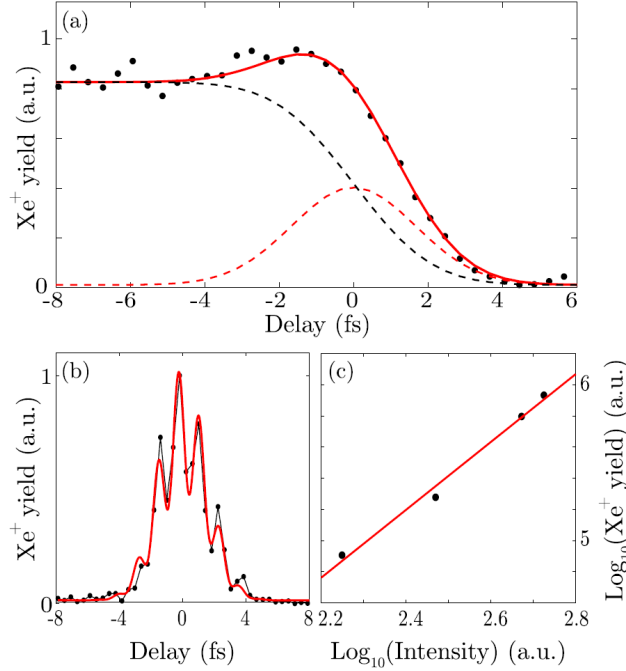


**Figure 3.7** – (a) UV-NIR cross-correlation signal acquired in xenon (black dots). The dashed lines represent the delay-dependent response of the two open ionization channels: (i) simultaneous absorption of 2 UV + 2 NIR photons (red dashed line) and (ii) resonance-enhanced transition (black dashed line). The red solid line corresponds to the sum of the two contributions. (b) Auto-correlation signal of the NIR pulses acquired in xenon (black line and dots) and auto-correlation fitting function (red solid line). (c) Scaling (black dots) of the peak cross-correlation signal as a function of the NIR intensity in bilogarithmic scale. The red solid line represents the linear function used to fit the data.

quality of the UV beam. In the interaction region, the UV pulses are noncollinearly recombined with XUV or NIR pulses. The estimated angle between the two beams is around 7 mrad. Given the photon energy and the spectral extension of our UV radiation, we could not rely on fully optical techniques to temporally characterize the pulses. For this reason, the temporal characterization of the UV pulses has been performed via UV-NIR cross-correlation in xenon [103, 128]. The generation yield of the cation  $\text{Xe}^+$  has been measured with a time-of-flight mass spectrometer as a function of the relative delay between the NIR and the UV pulses. The tight-angle noncollinear geometry has a small impact on the measured cross-correlation signal, i.e., the retrieved time duration of the UV pulses is 2% longer than for collinear geometry. Figure 3.7(a) shows the acquired cross-correlation signal: here, for negative delays the UV pulse precedes the NIR pulse. In our measurements, the relative delay was varied with 0.4-fs steps by a piezoelectric delay line.

While performing the cross-correlation measurement, the peak intensity of both the UV and the NIR pulses was checked to be low enough in order to prevent direct multiphoton ionization from each individual pulse. Therefore, ionization of xenon ( $I_p = 12.13$  eV) could result only from

the combination of the two pulses. This constraint, together with the absorption cross-sections of xenon [129, 130], allowed us to narrow down the set of possible nonlinear processes leading to ionization, i.e. either 1 or 2 UV photons combined with 5 or 2 NIR photons, respectively. The cross-correlation signal has been measured for different NIR intensities to disclose the number of NIR photons involved in the ionization process. The resulting intensity scaling is shown in Figure 3.7(c) in bilogarithmic scale. The linear fitting function  $y = mx + q$  used to fit the data has a slope coefficient  $m = 2.176 \pm 0.354$ . This result is thus indicating a second-order nonlinear process, demonstrating that the proposed cross-correlation scheme is involving 2 UV and 2 NIR photons. The experimental cross-correlation signal [black dots in Figure 3.7(a)] exhibits an overall steplike dynamics that has to be analyzed taking into account the electron energy structure of xenon. In fact, the acquired dynamics can be attributed to a sum of two different ionization channels. A simultaneous transition is occurring when the two pulses are temporally overlapped and 2 UV + 2 NIR photons are absorbed at the same time, leading to direct xenon ionization and thus giving rise to a Gaussian contribution in the dynamics [red dashed line in Figure 3.7(a)]. A resonance-enhanced sequential transition inducing xenon ionization is also occurring, and it involves a xenon long-lived electronically excited state accessible only after the absorption of 2 UV photons. Considering the UV second-order contribution and the dipole selection rules for the optical transition, the only possible metastable state responsible for the sequential ionization transition is the  $5p^5 6p$  state. The energy of this state (fine structure between 9.5 and 10 eV) is indeed compatible with the absorption of 2 UV photons, which can lead to ionization when followed by absorption of 2 NIR photons [131]. The sequential resonance-enhanced transition is described by an error function contribution to the overall dynamics, which is represented by the black dashed line in Figure 3.7(a). For this reason, the cross-correlation dynamics has been fitted with the function  $f(t)$  defined as a sum of a Gaussian function and an error function taking into account the direct and the sequential ionization transitions, respectively:

$$f(t) = A_1 \exp\left(- (t - t_0)^2 / 2\sigma^2\right) + A_2 \operatorname{erf}\left((t - t_0) / \sqrt{2}\sigma\right) \quad (3.9)$$

The time offset  $t_0$  and the width  $\sigma$  have been kept the same for the two contributions, while the relative amplitudes  $A_1$  and  $A_2$  have been left as free parameters. The time offset corresponds to the temporal overlap between the UV and NIR pulses, while the parameter  $\sigma$  has been used to retrieve the UV pulse duration as shown in Eq. (2) ( $\text{FWHM}_{UV} = 2.355\sigma_{UV}$ ):

$$\sigma = \sqrt{\sigma_{UV}^2/n_{UV} + \sigma_{NIR}^2/n_{NIR}} \quad (3.10)$$

Here  $n_{UV}$  and  $n_{NIR}$  represent the number of UV and NIR photons involved in the cross-correlation process, respectively. The cross-correlation fitting function [ $f(t)$  in Eq. 3.9] is represented by the red solid line in Figure 3.7(a). Furthermore, oscillations at twice the frequency of

the laser fundamental are visible on top of the cross-correlation dynamics, mainly for negative time delays. These can be attributed to interference between the residual NIR photons reflected by the separators in the UV arm and the NIR beam. To extract the time duration of the UV pulses from the cross-correlation measurement, an independent temporal characterization of the NIR pulse duration is required. This was done by means of an autocorrelation measurement in xenon, performed by replacing the spectral separators with silver mirrors and removing the gas from the UV generation cell. This allowed the combining of two replicas of the NIR pulses in the interaction region, each contributing to xenon ionization with 4 photons. Figure 3.7(b) reports both the experimental data (black line and dots) and the fitting function (red line). From the fit we retrieved a NIR pulse duration of  $5.2 \pm 0.2$  fs (FWHM).

By inserting the retrieved NIR pulse duration in Eq. 3.10, we extracted a UV pulse duration of  $1.9 \pm 0.4$  fs (FWHM). The measured UV pulse duration is very close to the transform limit, thus indicating that our generation scheme is almost dispersion free.

In conclusion, we have demonstrated the generation of sub- 2-fs deep UV pulses with a 150 nJ energy per pulse. A key aspect of our scheme is the use of a laser microfabricated gas cell allowing for the optimization of gas pressure and generation geometry. Further optimization of the UV generation process could be achieved by replacing the reservoir geometry with an integrated guiding channel [132]. These ultrashort UV pulses can be combined with few-fs NIR pulses or XUV attosecond pulses for time-resolved experiments. Our scheme opens new and important perspectives for investigating ultrafast processes at the electron time scale in UV-excited biochemically relevant molecules.

## Funding

H2020 European Research Council (ERC) (637756); Fonds de recherche du Québec–Nature et technologies (FRQNT); National Science and Engineering Research Council (SERC); Vanier Canada Graduate Scholarship (Vanier CGS); Deutsche Forschungsgemeinschaft (DFG) (390715994).

### 3.6 Article III – A flexible beamline combining XUV attosecond pulses with few-femtosecond UV and near-infrared pulses for time-resolved experiments

Vincent Wanie,<sup>1,2,3</sup> Mara Galli,<sup>1,3,4</sup> Erik P. Månsson,<sup>1</sup> Andrea Trabattoni,<sup>1</sup> Fabio Frassetto,<sup>5</sup> Lorenzo Colaizzi,<sup>1,6</sup> Andrea Cartella,<sup>1,7</sup> Krishna Saraswathula,<sup>1,6</sup> Diogo Pereira Lopes,<sup>4</sup> Rebeca Martinez Vazquez,<sup>3</sup> Roberto Osellame,<sup>3</sup> Luca Poletto,<sup>5</sup> François Légaré,<sup>2</sup> Mauro Nisoli,<sup>3,4</sup> and Francesca Calegari<sup>1,3,6,7</sup>

<sup>1</sup>Center for Free-Electron Laser Science, DESY, 22607 Hamburg, Germany

<sup>2</sup>Centre Énergie Matériaux Télécommunications, Institut National de la Recherche Scientifique, J3X 1S2 Varennes, Canada

<sup>3</sup>Institute for Photonics and Nanotechnologies CNR-IFN, 20133 Milano, Italy

<sup>4</sup>Physics Department, Politecnico di Milano, 20133 Milano, Italy

<sup>5</sup>Institute for Photonics and Nanotechnologies CNR-IFN, 35131 Padova, Italy

<sup>6</sup>Physics Department, Universität Hamburg, 22761 Hamburg, Germany

<sup>7</sup>The Hamburg Centre for Ultrafast Imaging, Universität Hamburg, 22761 Hamburg, Germany

Submitted to Review of Scientific Instruments

Received 15 May 2020

V.W., M.G. and E.P.M, developed the beamline at the Politecnico di Milano (Italy). A.T., L.C., A.C., and K.S. contributed to the reconstruction of the beamline in Hamburg (Germany) and to the measurements. F.F. and L.P. designed the vacuum chambers and the XUV spectrometer. D.P.L., R.M.V., and R.O. built the glass cell for the UV generation. F.L., M.N. and F.C. supervised the project. V.W. wrote the manuscript with the help of all co-authors.

## Abstract

We describe a beamline where few-femtosecond ultraviolet (UV) pulses are generated and synchronized to few-cycle near-infrared (NIR) and extreme ultraviolet (XUV) attosecond pulses. The UV light is obtained via third-harmonic generation in argon gas when focusing a phase-stabilized NIR driving field inside a glass cell that was designed to support high pressures for optimal conversion efficiency. A recirculation system allows reducing the large gas consumption required for the non-linear process. Isolated attosecond pulses are generated using the polarization gating technique and the photon spectrometer employed to characterize the XUV radiation consists of a new design based on the combination of a spherical varied-line-space grating and a cylindrical mirror. This design allows for compactness while providing a long entrance arm for integrating different experimental chambers. The entire interferometer is built under vacuum to prevent both absorption of the XUV light and dispersion of the UV pulses and it is actively stabilized to ensure an attosecond delay stability during experiments. This table-top source has been realized with the goal of investigating UV-induced electron dynamics in neutral states of bio-relevant molecules, but it also offers the possibility to implement a manifold of novel time-resolved experiments based on photo-ionization/excitation of gaseous targets by ultraviolet radiation.

## Introduction

The advent of attosecond ( $1 \text{ as} = 10^{-18} \text{ s}$ ) light sources based on high-order harmonic generation (HHG)[6, 5, 73] represented a breakthrough for ultrafast laser spectroscopy. Indeed, it paved the way for the investigation of electron dynamics in matter [133, 116]. In HHG, focusing an intense femtosecond (fs) laser pulse onto a gas target enables an electron to escape the atomic potential, gain substantial ponderomotive energy and recombine with the parent ion within a single cycle of the driving electric field. The recombination produces an attosecond light pulse in the extreme ultraviolet (XUV) or soft x-rays spectral domains, offering the shortest probe to date. Typically, XUV attosecond pulses are combined with near-infrared (NIR) pulses in a pump-probe configuration for time-resolved measurements, and attosecond beamlines are specifically designed for experiments in the gas phase [134, 135, 80, 136, 137], or with a particular interest for the solid-state [138, 139, 140, 141, 142, 143, 144]. In fact, the realization of XUV-pump XUV-probe schemes [145], although allowing for the highest temporal resolution, still presents several technological challenges mostly due to the limited photon flux of the XUV light sources.

When HHG is driven by few-cycle 800 nm pulses, the available photon energies for an experiment usually span in the 15-50 eV range and can further be extended depending on the generation parameters. Because these photon energies are above the ionization potential of most molecules, the use of XUV attosecond pulses inevitably leads to the ionization of the system under study. However, many processes playing key roles in biology and chemistry are triggered by photoexcitation of neutral

molecules, especially in the ultraviolet (UV) spectral region between 190 and 350 nm. For instance, the absorption of UV photons in nucleic acid bases can initiate molecular dynamics occurring on a timescale from few-femtosecond to several nanoseconds [88, 89, 90]. Since the electron dynamics that evolve on a much faster timescale can play a major role in UV-induced photochemistry, a promising probing scheme would entail the combination of attosecond XUV and few-fs ultraviolet pulses. This pump-probe scheme has not been reported yet.

In this article, we present a beamline for **STeering Attosecond electRon dynamics in biomolecules with UV-XUV LIGHT pulses (STARLIGHT)**. It combines isolated attosecond pulses and the recently reported few-femtosecond UV pulses [102], aiming at time-resolved experiments based on the photoexcitation of molecular gases by ultraviolet radiation with an unprecedented temporal resolution. Alternatively, also few-optical-cycle NIR pulses can be combined with the attosecond XUV pulses or the few-fs UV pulses, allowing for a remarkable flexibility of possible pump-probe schemes. The beamline is intended to be used for studying UV-induced electron dynamics in neutral bio-relevant molecules probed by XUV ionization. These experiments will follow recent investigations of molecular dynamics in aminoacids and nucleobases that provided insight on the charge migration process and the ultrafast photo-fragmentation dynamics [16, 146, 147]. An overview of the beamline is presented in Section 3.6 followed by a description of the UV pulse generation setup in section 3.6. Section 3.6 describes the generation and characterization of the isolated attosecond pulses as well as a new design of a compact XUV photon spectrometer. Section 3.6 reports the passive and active stabilization of the beamline required to reach an attosecond delay stability.

## Beamline overview

The beamline is seeded with 1.25-mJ, 1-kHz, 5-fs NIR pulses, obtained by hollow-core-fiber compression [22] of a Titanium:Sapphire laser (Femtopower, SpectraPhysics). In addition, the carrier-envelope-phase (CEP) of the laser pulses is actively stabilized, as a main ingredient to generate isolated attosecond pulses, see section 3.6. Fig. 3.8 depicts the optical setup of the beamline. In chamber 1, the seeding pulses are split by a 1-mm thin beamsplitter to create the pump-probe arms. 70% of the incoming beam is reflected by the beamsplitter (path A) and used for HHG, see section 3.6. In this arm, isolated attosecond pulses are obtained by using the polarization gating (PG) technique [97], while the residual NIR light co-propagating with the attosecond pulses is filtered out using metallic filters. The light transmitted by the beamsplitter (30% of the seeding energy) is sent onto a flat metallic mirror (M in chamber 1) that is mounted on a closed-loop linear positioner (SmarAct). By translating M, two arms can be alternatively seeded, i.e. path B or path C. In path B, the few-cycle NIR pulses are recombined with the XUV pulses in chamber 3 through a 3.5-mm drilled mirror and focused into the interaction region by a  $150 \times 20 \times 15$  mm gold-coated toroidal mirror that is installed in chamber 4. This XUV-NIR scheme allows, for example, the attosecond pulses to be characterized by using the attosecond streak camera method [148, 149].

In path C, instead, the NIR pulses are exploited for the generation of few-cycle UV pulses, see section III. The broadband UV pulses are generated in gas via third-harmonic generation (THG, chamber 6) and separated from the residual NIR in chamber 5 using spectral separators. In this chamber, a mirror placed on a linear positioner can be used to extract the UV beam through a UV-grade fused silica window for spectral and power measurement using an Avantes (AvaSpec-ULS2048XL-USB2) spectrometer and Gigahertz Optik (head model ISD-5P SiUV) power meter respectively. The beam is recombined with the XUV line in chamber 4 by using a narrow-angle noncollinear geometry ( $< 1$  degree). A mirror mounted on a linear positioner before the exit of chamber 4 can be used to extract the beams. This allows the foci at the interaction region to be imaged and the beams to be spatially and temporally overlapped by using a CCD camera. Wedge pairs are installed in both paths B and C to control the dispersion and the carrier-envelope phase. Delay lines are also integrated to synchronize the pump-probe interferometer arms. The pump-probe delay is controlled with attosecond precision by using piezo-based linear positioners (PiezoSystem Jena model PX100SG-V with ENV300CLE controller). An XUV photon spectrometer is installed behind the interaction region to monitor the spectral properties of the XUV radiation while running experiments, see section 3.6.

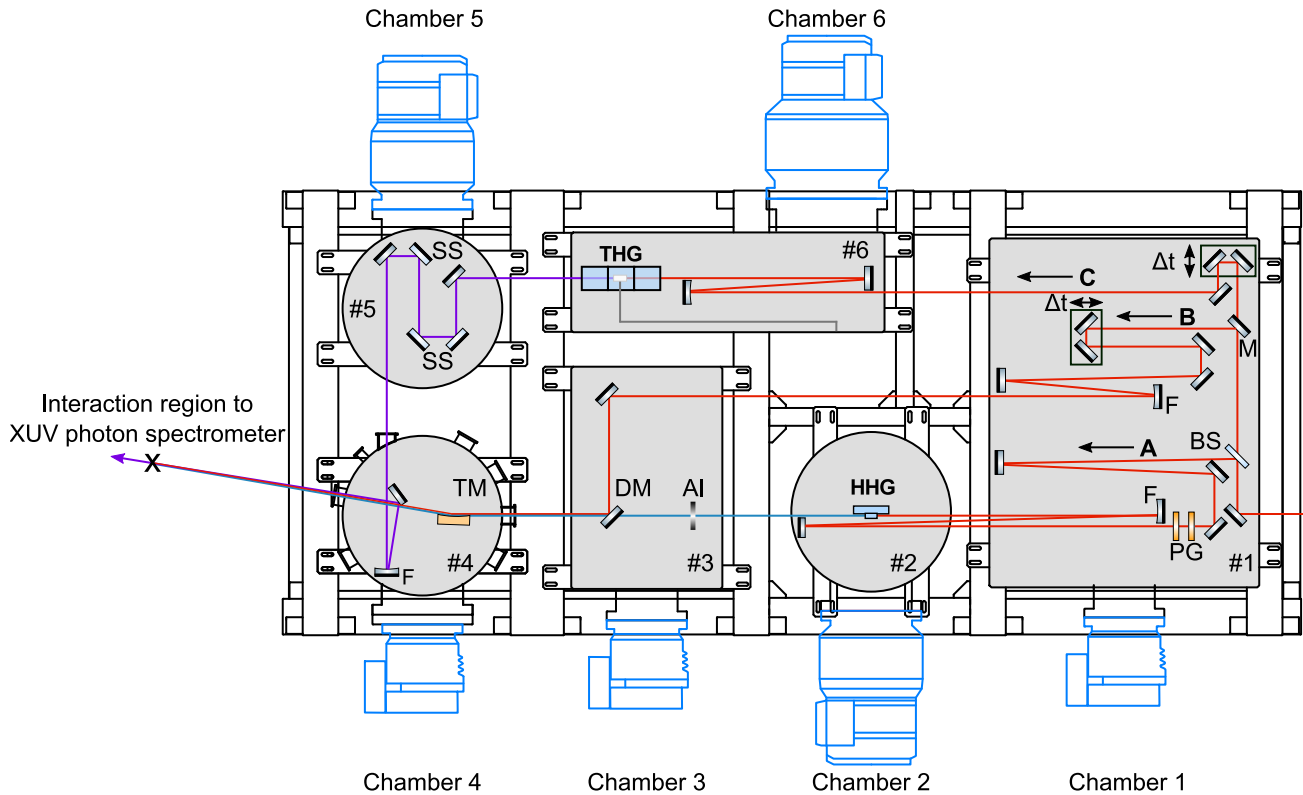


Figure 3.8 – Top view of the beamline. The NIR field is divided in chamber 1 using a beamsplitter (BS). The reflected beam in Path A undergoes a polarization gating (PG) for high-harmonic generation (HHG). The transmitted NIR can either be used as is via Path B or sent into Path C for third-harmonic generation (THG) by adding or removing a mirror placed on a motorized stage (M). A pulsed valved is used in chamber 2 where the NIR beam is focused for HHG. Chamber 3 is used to recombine Path A and B using a drilled mirror (DM). THG occurs in chamber 6 and the ultraviolet light is separated from the fundamental field in chamber 5 using spectral separators (SS). In this chamber the UV light can be extracted for characterization (energy and spectrum). All paths merge in chamber 4 where the XUV and NIR fields are focused into the interaction region by a toroidal mirror (TM). The UV field is focused using an aluminum mirror and sent into the interaction region in a noncollinear geometry. A mirror placed just before the output of the chamber can be translated to extract the beam for spatial imaging. The entire interferometer is actively stabilized for attosecond delay stability.

## Generation of few-femtosecond UV pulses

### Third-harmonic generation in gas

After the first demonstration of second harmonic generation (SHG) employing laser pulses [150], THG has been deeply investigated as a next step towards developing nonlinear optics. In crystals, multi-stage schemes starting with SHG followed by sum frequency generation are generally employed rather than direct THG due to the increased conversion efficiency provided by birefringent phase-matching [124]. Notably, it was demonstrated that for such a cascaded configuration, exploiting quasi-phase matching can lead to a high conversion efficiency [151]. In gases, other techniques such as spectral broadening or cross-phase modulation in hollow-core fibers followed by compression [152, 122], four-wave mixing through filamentation [105, 153] or direct frequency tripling [125, 154, 103, 102] have also been demonstrated. Recently, gas-filled hollow-core photonic crystal fibers (HC-PCF) have been used to generate broadband and tunable UV spectra either through dispersive-wave emission or four-wave mixing [155, 156, 104, 106]. The choice of the generating media depends on the desired pulse energy and bandwidth, defining the minimal pulse duration. In crystals, the dispersion induced during propagation intrinsically puts lower limits to the pulse duration. To achieve maximal temporal resolution, the quasi-dispersion-free properties of rare gases must be chosen, at the cost of lower conversion efficiency.

In this perspective, the latter approach has been selected. Fig. 3.9 shows a glass cell that has been designed to support high gas pressures. It allows to reach an increased density of emitters in order to compensate for the lower conversion efficiency of gases. Starting from a  $20 \times 5$  mm fused-silica slab, a portion is reduced to 3-mm width (top half in Fig. 3.9a). The reduced portion contains a 3-mm long channel for laser propagation, micro-machined using femtosecond laser irradiation followed by chemical etching FLICE [127]. On one of the large surface that is parallel to this channel, a hole is made to hold a 3-mm diameter metallic tube with Swagelok fittings used for injecting the gas. The middle of the cell consists of a large (non guiding) reservoir and the diameter of the channel is progressively decreased down to  $400 \mu\text{m}$  at the extremities to contain the gas in a restricted volume during THG and limit the outflow. The cell is integrated into a differential pumping system, see next section, making the THG setup compatible for a high-vacuum environment.

### Differential pumping and recirculation system

In order to ensure high vacuum in chamber 6, the glass cell is placed into a differential pumping system made of three sub-chambers, as shown in Fig. 3.10. The cell is installed in the central section and the gas for THG is evacuated towards the lateral sub-chambers through 0.8-mm diameter apertures. The apertures are realized on thin plates that can be easily mounted at the interface between the lateral sub-chambers and the central section. Similar plates are also mounted at the

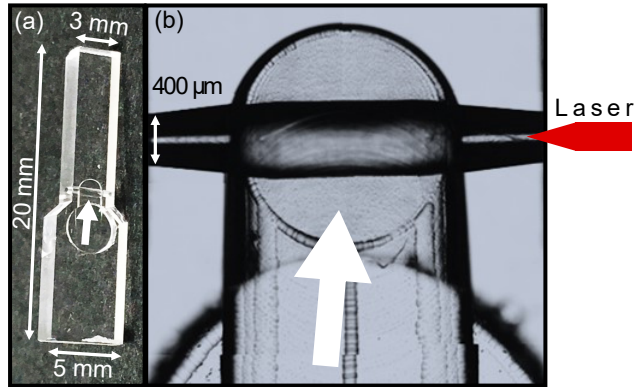


**Figure 3.9** – (a) Image of the  $20 \times 5$  mm fused silica cell used for THG. The arrow defines the gas flow direction. (b) Enlarged view of the in coupling region. The laser is focused into a  $400 \mu\text{m}$  aperture and propagates along a 3-mm gas-filled channel micro-machined using the FLICE technique.

interface between the lateral sub-chambers and the main vacuum chamber. Furthermore, the central section is connected to the wall of chamber 6 through a bellow and pumped by a roots pump ( $55 \text{ m}^3/\text{h}$ ) that collects most of the outflowing gas. In a similar manner, the lateral sub-chambers are evacuated by a second roots pump, that is also used as backing pump for the turbomolecular pump of chamber 6. To further improve the overall vacuum in the beamline, small-diameter apertures are also installed at the interface between chamber 6 and chamber 1 and between chamber 6 and chamber 5, as supplementary differential pumping elements. Although the gas load is spatially confined by the above-mentioned scheme, the local gas consumption is extremely high ( $2 \text{ bar L}/\text{min}$ ), making the entire setup hardly sustainable and potentially really expensive. To overcome this limitation, the THG setup has been equipped with a gas recirculation circuit, also shown in Fig. 3.10.

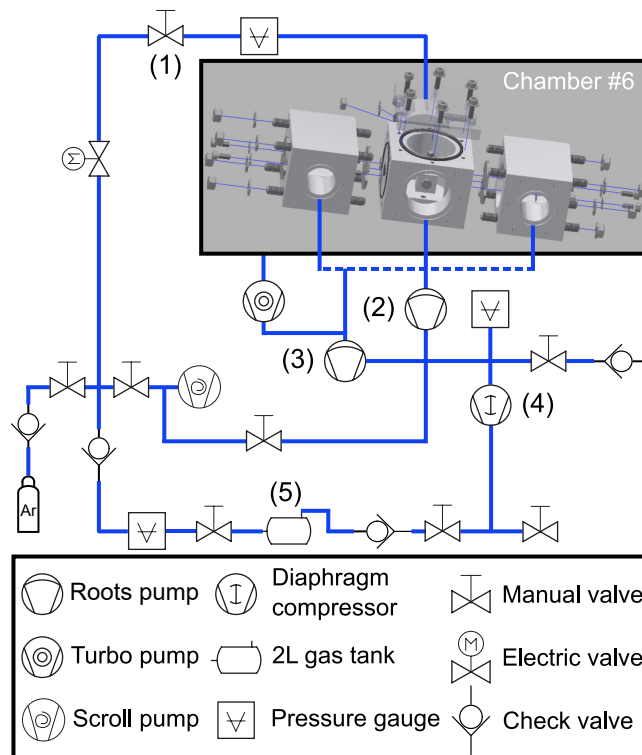


**Figure 3.10 – Differential pumping setup and gas recirculation system.** A manual valve (1) allows to control with precision the gas flow injected into the THG cell residing in the central part of a differential pumping arrangement made of three sub-chambers. A roots pump (2) collects the residual gas coming from the central subunit while a second one (3) collects the remaining gas flowing into the later sub-chambers. The latter pump is also used for backing the turbomolecular pump of the main chamber where a  $10^{-4}$  mbar vacuum level can be preserved when using argon. A diaphragm pump (4) is next used for compression and the gas is stocked into a 2L tank (5). The compressed gas from the tank can be sent back into the THG cell using the manual valve (1). A number of valves and pressure gauges are used to operate and monitor the system performances.

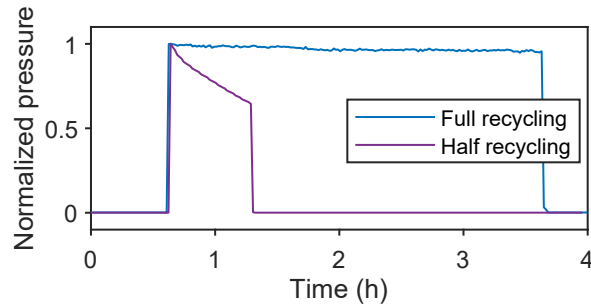


**Figure 3.11 – Argon recirculation performances.** After 3 hours (blue curve), 96% of the initial argon pressure is detected by a residual gas analyzer when the full recycling scheme is employed. When the gas collected from the turbomolecular pump of chamber 6 is not recycled (half recycling, purple curve), the efficiency goes down to 66% in 40 minutes.

The exhausts of the roots pumps are connected to a diaphragm pump via 6-mm Swagelok connections. The gas collected from the pumps exhausts is compressed into a 2-litre tank to a pressure up to 7 bar. Check valves are placed up- and downstream the tank to guarantee the right flow direction. The compressed gas is then sent back to the UV generation cell. In order to test the performances of the recirculation system, the argon pressure was measured with a residual gas analyzer (RGA) placed in chamber 5 and monitored as a function of time. The result is shown by the blue curve in Fig. 3.11.

Over 3-hour measurement, 96% of the initial gas pressure is preserved. The pressure measured at the tank (3 bar) and at the roots pump exhausts (0.52 bar) remained constant over the entire period. The excellent efficiency of the system would allow an operation over 37 hours with a consumption of only 1 litre of gas in the tank. Without recirculation, instead, the same gas consumption (1 litre) is reached after 1.5 min, with a consumption rate of 2 bar L/min. For comparison, a similar measurement was done by including in the recirculation system only the sub-chambers of the THG setup, i.e. excluding the residual gas pumped out by the turbomolecular pump of chamber 6. The result is reported in Fig.3.11, purple curve. This ‘half recycling’ scheme shows larger losses, with the initial argon pressure reduced to 66% after only 40 min. During this period of time, the tank pressure dropped from 3.1 to 1.5 bar and the exhaust pressure dropped from 0.52 to 0.34 bar. However, although requiring a continuous refill of the tank, the gas consumption in the ‘half recycling’ scheme is still significantly reduced compared to not using any recirculation system at all.

### Photoionization of Xe by few-fs UV pulses

The spectral and temporal properties of the UV pulses obtained from the setup described above have already been discussed in a previous publication [102]. Here, we briefly describe the capabilities of the beamline for time-resolved experiments implying UV photoionization and photoexcitation of gaseous targets. Figure 3.12a shows a typical UV spectrum, centered at 255 nm (4.86 eV). The intensity of the UV pulses is estimated to be  $1.1 \pm 0.4 \times 10^{12}$  W/cm<sup>2</sup>, which is expected to be sufficient to trigger nonlinear processes in atoms and molecules, and to perform UV-pump XUV-probes experiments [157]. To demonstrate this, the UV pulses were used to photoionize xenon (Xe). Considering the spectrum of (a) and the ionization potential ( $I_p$ ) energy of 12.13 eV for Xe, three UV photons are required to reach the ionization threshold. The experiment was performed in a velocity map imaging (VMI) spectrometer and the photoelectron angular distribution (PAD) from 30 000 laser shots (30 s) is shown in (b). The PAD presents a number of structures with photoelectron energies near 3 eV (dashed black circle), corresponding to the residual kinetic energy  $E_k$  from a 3-photon ionization ( $E_k = 3\hbar\omega - I_p$ ). The broadening of the features observed in the photoelectron spectrum is attributed to the large bandwidth of our UV pulses. Moreover, a fraction of the signal is attributed to a background originated by water ionization ( $I_p = 12.62$  eV), which has been confirmed by a simultaneous ion time-of-flight measurement. The PAD hence reveals that the UV photon flux will be sufficient to trigger 1- and 2-photon-induced dynamics in bio-chemically relevant molecules, that is the main aim of the beamline, see section 3.6.

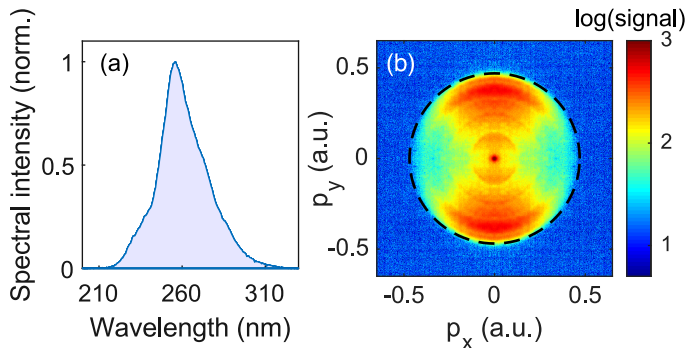


**Figure 3.12** – (a) Spectral content of the UV pulse and (b) corresponding photoelectron angular distributions of Xe from 3-photon ionization over 30 000 laser shots (logarithmic scale). The dashed black circle delimits a kinetic energy region below 3 eV.

## XUV generation and detection

The NIR laser pulses propagating along path A (see Fig. 3.8) are focused by a  $f = -700$  mm silver mirror into a 6-mm channel filled of gas for HHG. The gas target is delivered into the interaction by a water-cooled pulsed valve (Attotech, model GR020), that is triggered at 1 kHz repetition rate and synchronized with the laser. The opening time of the valve is typically adjusted from 120 to 150  $\mu\text{s}$  with a backing pressure between 1 and 2 bars. Argon, krypton and xenon are alternatively used for HHG, depending on the desired XUV spectral range. To optimize the alignment of the laser through the gas target, the valve is mounted on a structure with four motorized positioners, consisting of three translations and one rotation (Physik Instruments). Fig. 3.13 shows a typical XUV spectrum generated in krypton and measured with a customized photon spectrometer described in the following section.

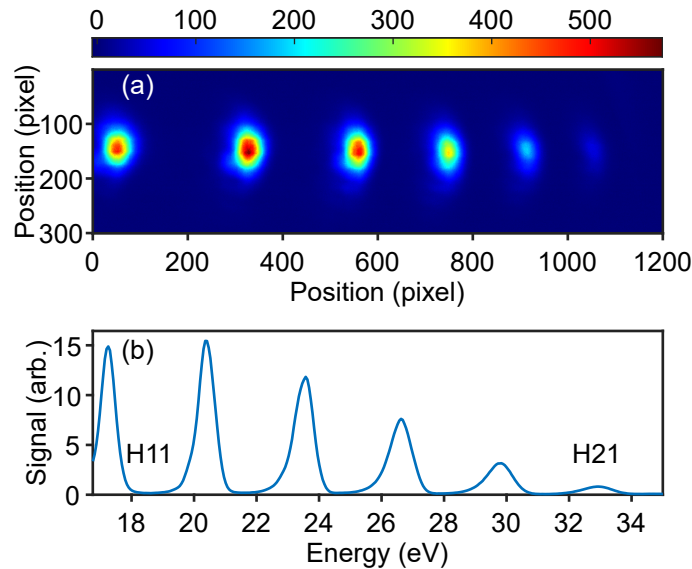


**Figure 3.13 – High-harmonic generation in krypton with 1-mJ, 5-fs pulses at 800 nm. (a) Raw image showing the spatial profile of the harmonics. (b) Corresponding spatially integrated signal with calibrated axis. Harmonics 11 to 21 are observed.**

## XUV photon spectrometer

We report here an innovative design of an XUV spectrometer for the spectral characterization of HHG pulses in the 15-50 eV range. In a prototypical spectrometer, the incoming light is spectrally dispersed by a grating and imaged in the Fourier space on a photodetector. Higher is the groove density of the grating, higher is the spectral resolution of the spectrometer. In order to further increase the spectral resolution of the instrument, an entrance slit is usually employed to spatially confine the light source to be imaged. Although narrow slit apertures allow for high spectral resolution, they also limit the amount of photons reaching the detector.

Common spectrometers for XUV light consist of a grazing-incidence mirror focusing the light source onto a slit placed at a fixed distance from a spherical varied-line-space (SVLS) grating. The SVLS provides the so-called ‘flat-field’ property, where all the spectral components are focused onto the same plane rather than on a cylindrical surface as for equal line-space gratings [158]. This allows the acquisition of XUV spectra using a two-dimensional detector.

Usually, the XUV light generated by HHG is refocused by a grazing-incidence toroidal mirror onto the target under study - i.e. into the interaction point where experiments occur. If the toroidal mirror works with a 1:1 refocusing magnification factor, the XUV focus at the interaction point presents minimal aberrations, allowing it to be directly used as source point for the spectrometer. This configuration shows several advantages. First, the XUV spectrometer can be installed directly behind the experimental chamber. Second, the small size and quality of the XUV focus makes the use of an entrance slit unnecessary, which maximizes the photon flux entering the spectrometer [159].

In our beamline, a 1-meter focal-length toroidal mirror is used to refocus the HHG light source into the interaction point for experiments. Such a long focusing arm is chosen to be compatible with large-footprint experimental setups. However, the entrance arm of the XUV spectrometer (specified by the grating) is much shorter, i.e., only 350 mm. As a common solution to overcome this limitation and realize a long entrance-arm spectrometer, a second toroidal mirror, that is a replica of the first one, can be installed behind the experimental chamber. It collects the XUV light from the interaction region and refocuses it, again with a 1:1 magnification factor, into the source point of the grating. This configuration usually requires that the second toroidal mirror and the grating are mounted in separate vacuum chambers, significantly increasing the overall footprint of the XUV spectrometer. As an alternative solution, a retractable spherical mirror can be placed before the first toroidal mirror, i.e. the one that focuses the XUV light into the experimental chamber. This spherical mirror can either be used to steer the beam towards an XUV spectrometer, or it can be retracted for the beam to reach the toroidal and the experimental interaction point [140]. The main disadvantage of this method is that the XUV spectrum cannot be monitored while running experiments.

In order to improve the compactness of our XUV spectrometer while keeping a long entrance arm, we combined a SVLS grating (Hitachi) with a convex (divergent) cylindrical mirror (Fig. 3.14). The gold-coated grating has a 5649 mm radius of curvature, a blaze angle of 3.7 deg. and a central groove density of 600 lines/mm. The gold-coated cylindrical mirror is used to create a virtual image of the XUV focus at the source point of the grating, while keeping a relatively long entrance arm of 750 mm. Then, the grating provides a flat spectral plane at a distance of 469 mm, where the detector is installed. The detector consists of a 40-mm-diameter microchannel plate (MCP) and a P43 phosphor screen (Photek) and it is placed on a translation stage to span the spectral plane. Typically, a translation of 10 mm is sufficient to acquire a spectrum spanning from 15 to 50 eV in two images. Since the cylindrical mirror does not focus along the sagittal (vertical) plane, the spatial profile of the harmonics can also be monitored along the vertical axis and used to measure the XUV divergence. The images produced by the phosphor screen are recorded by a CMOS camera (Hamamatsu C11440-36U). To further reduce the footprint of the instrument, a  $50 \times 50$  mm silver mirror is mounted at 45 deg., enabling the image to be recorded perpendicularly to the MCP detector, i.e. by mounting the CMOS camera vertically. The total length of the spectrometer is about 80 cm.

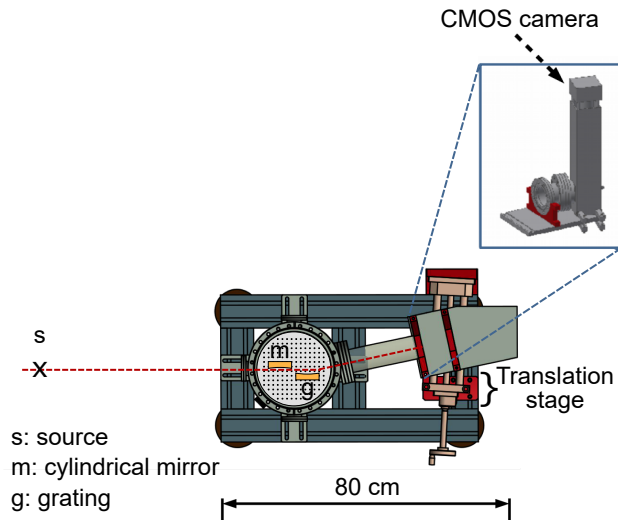


**Figure 3.14 – Scheme of the XUV photon spectrometer (top view).** 75 cm away from the source, a cylindrical mirror in combination with a spherical grating images the XUV radiation onto a microchannel plate (MCP) amplifier followed by a phosphor screen. The image is collected by a mirror placed at 45 degrees and sent to a CMOS camera. Due to the restricted area of the MCP, the detector is translated along the spectral axis to acquire the full spectrum. The physical length of the spectrometer is about 80 cm.

## Generation of isolated attosecond pulses

Isolated attosecond pulses (IAPs) are obtained using the polarization gating (PG) technique. In this method, a combination of two birefringent glass plates, i.e. a retarder plate and a  $\lambda/4$  plate, are used to reshape the polarization of the driving electric field [97]. The resulting pulses show a narrow gate of linear polarization across the envelope peak, while being circularly polarized on the rising and the trailing edges. Since HHG is efficient only for a linearly polarized driving field [98], attosecond pulses are generated only within the linear polarization gate. If the gate is narrower than a driving optical cycle and the CEP equal to  $k * \pi/2$  (with  $k = 1,3,5,\dots$ ), an IAP is produced through PG.

In the case of the 5-fs NIR pulses used to seed the beamline, the above-mentioned conditions are obtained by combining a 193  $\mu\text{m}$ -thick quartz retarder plate and an air-spaced, broadband  $\lambda/4$  waveplate (B-Halle). Fig. 3.15 shows the XUV spectra obtained by HHG in krypton as a function of the CEP of the driving pulse. The CEP was controlled by a motorized glass wedge translated in a direction perpendicular to the laser propagation axis. As can be observed in Fig. 3.15, for CEP values of  $\pi/2$  and  $3\pi/2$  continuous XUV spectra are generated (see 3.15b, blue curve), corresponding to IAPs. For CEP values of  $\pi$  and  $2\pi$ , instead, the condition of IAP is expected to be lost. Indeed, for these CEP values the XUV spectrum is strongly modulated (see 3.15b, orange curve), corresponding to a train composed of mainly two attosecond pulses. This configuration provides XUV isolated attosecond pulses with a duration of 300 attoseconds [16] and 100-pJ energy/pulse. The energy/pulse can reach the nanojoule range if the ionization gating approach is employed [160, 16] instead of the polarization gating. The intensity of the isolated attosecond pulses is estimated to be between  $10^8$  and  $10^9$   $\text{W}/\text{cm}^2$  depending on the gating method [97, 160].

The temporal resolution provided by the beamline for UV-pump XUV-probe experiments can be estimated by considering the full width at half maximum (FWHM) of an instrument response function (IRF), defined by the convolution of the Gaussian XUV and UV pulses. When the 300-as XUV pulse is combined with the 1.9-fs UV pulse[102] and both trigger 1-photon transitions, the temporal resolution can be well approximated to the duration of the UV pulse itself. In case of 2- or 3-photon transitions triggered by the UV pump, the temporal resolution of the experiment is even higher. The beamline here described hence offers the potential to disentangle UV-induced molecular dynamics with a sub-2-fs temporal resolution, corresponding to an important improvement in comparison to previously reported work[157].

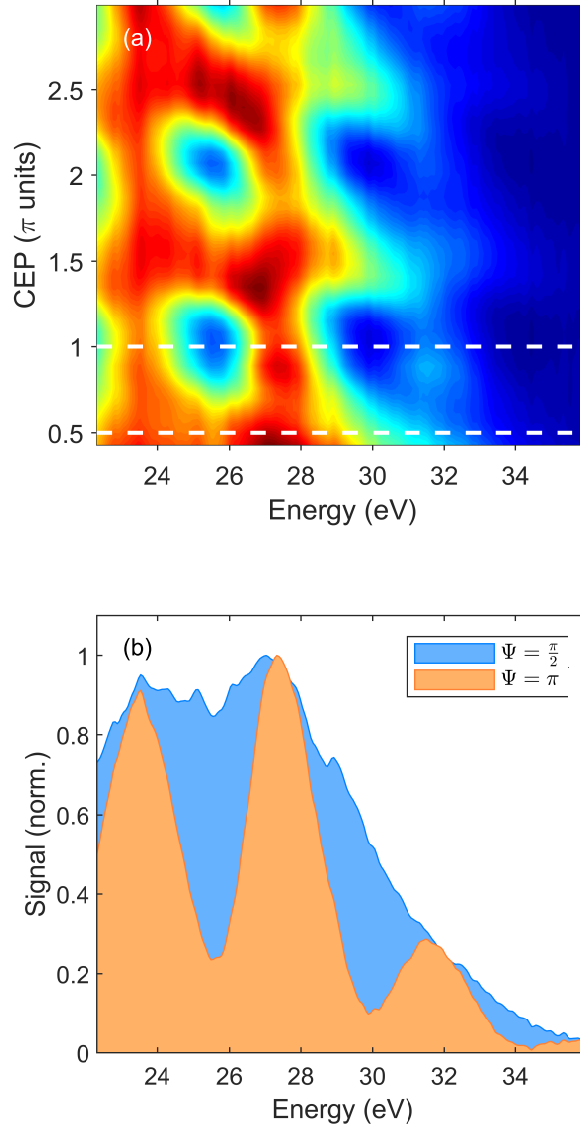


Figure 3.15 – (a) XUV spectrum of HHG in krypton as a function of the carrier-envelope phase of the NIR driving field when the polarization gating technique is applied. Each  $\pi/2$  dephasing of the CEP transforms the continuous spectrum characteristic of an isolated pulse into a harmonic comb and vice-versa. (b) Spectral cuts for CEP values  $\Psi = \frac{\pi}{2}$  and  $\pi$ , corresponding to the horizontal dashed lines displayed in (a)

## Pump-probe delay stabilization

To ensure an attosecond delay stability during experiments, the relative path between the pump and the probe arms must be kept constant within few nanometers. In this context, sources of high and low frequency noise such as vibrations from the vacuum pumps and temperature-driven effects must be identified, and the effect on the delay must be compensated by exploiting both passive and active stabilization schemes. In long (several meters) interferometers, the effect of such noise sources, especially low-frequency drifts, may be particularly harmful.

The interferometer arms of our beamline are about 5.75 m long. To passively stabilize the beamline, all vacuum chambers are mounted on an external frame made of aluminium profiles. The frame is decoupled from the optical table and carries vibrations from the turbomolecular pumps to the floor. The structure is also used to support gas panels, electronic control units and cables that are necessary to operate the beamline while being potential sources of noise. Inside the chambers, the breadboards on which the optical components stand are connected to a single optical table (TMC) using internal posts. Each post is vacuum-sealed by a surrounding CF40 bellow to damp any residual vibrations coming from the chambers. The flat surface at the bottom extremity of the bellow is welded to the post on the vacuum side while the air side is used for clamping on the optical table.

The active stabilization is obtained by using a continuous wave (CW) laser that co-propagates with the main laser along the pump-probe interferometer. Since the spectral separators installed in path C (see Section 3.6) are supposed to filter out any NIR spectral components, a standard 633 nm helium neon laser is not a suitable option to be used as CW stabilization laser. Therefore, a frequency-stabilized diode laser with a wavelength of 473 nm (Cobolt Blues 50) was employed. At the end of the interferometer the CW laser is extracted and the interference pattern produced by the two recombined paths is recorded on a CCD camera operating at 12.5 Hz. A narrow-bandpass interference filter centered at 470 nm (Thorlabs) is used to filter out the co-propagating NIR light. In order to set the active stabilization, the interference pattern is Fourier transformed and the main spatial frequency component is extracted together with the correspondent phase. Since any spatial jitter or drift in the pump-probe interferometer is directly imprinted in the value of the above-mentioned phase, the active stabilization aims to keep the phase constant with the lowest deviation. To do this, a proportional-integral (PI)-based feedback loop is used to act on a piezoelectric positioner, with the purpose of compensating for any phase variation [161]. We note that the same positioner is used to set the pump-probe delay during experiments.

Fig. 3.16 reports the stability of the beamline during 11 hours of active stabilization. Shown in (a) is the moving RMS of the phase error over the entire scan, employing a sliding window containing 1000 data points (1.4 minutes). For each translation of the window, the previous 500 points are conserved. An in-loop RMS of 51 mrad on the phase error is obtained over the full

measurement, corresponding to a 13 as delay stability. This value goes down to 7 for 20 min acquisitions. Moreover, we investigated the main sources of slow drifts in the interferometric delay. In this context, Fig. 3.16b shows a clear correlation between the room temperature (black curve) and the out-of-loop drift of the pump-probe delay over 11 hours. In particular, it is evident that already small temperature variations around  $0.6^{\circ}\text{C}$  reflect into delay drifts of several femtoseconds.

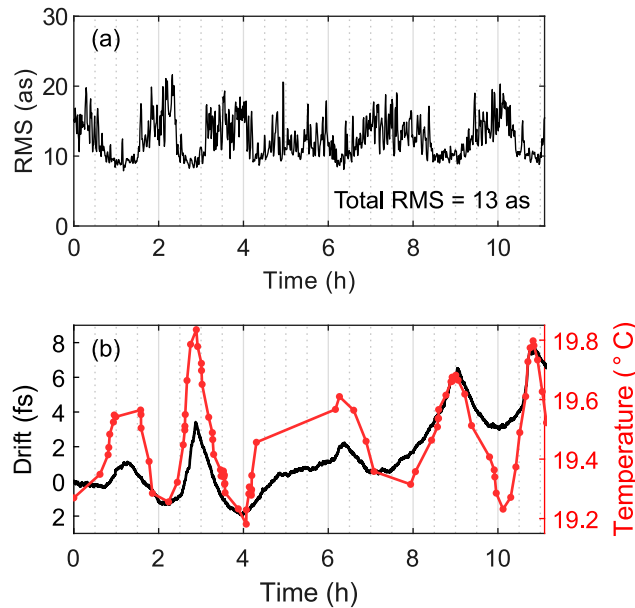


**Figure 3.16 – Beamline stability measurement over 11 hours. (a) Calculated in-loop RMS of the phase error using a moving window containing 1000 points (1.4 min). The RMS over the entire measurement is 51 mrad, corresponding to a delay stability of 13 as. (b) Comparison between the corrected drift (black curve) over the acquisition time and the room temperature variation (red curve).**

## Summary

We presented here a novel pump-probe beamline combining XUV isolated attosecond pulses, few-femtosecond UV pulses and few-cycle NIR pulses. We showed that the beamline is suitable for a new class of UV-based experiments. Furthermore, the innovative gas recirculation system that was developed allows for the realization of high-statistics, long-acquisition-time experiments, in which the gas consumption for the UV generation is minimized and kept sustainable. This method is likely to be extremely beneficial also for other purposes, such as the generation of soft x-rays through HHG, for which high gas pressures are required in-situ [25, 83]. A new design of a compact XUV spectrometer was also described, based on the combination of a SLVS grating and a cylindrical mirror. While keeping an extremely compact footprint, it provides a long entrance arm that is suitable

for the installation of large detection systems and sample sources such as two-sided spectrometers [162]. These will particularly benefit the investigation of large molecular systems, allowing for covariance measurements that can be used to access simultaneously nuclear and electronic degrees of freedom [163]. The STARLIGHT beamline provides a unique setup for the future investigation of UV-induced electron dynamics in biochemically-relevant molecules with temporal resolution from few femtoseconds down to a few hundreds of attoseconds.

## **Acknowledgments**

The authors are grateful to M. Scarparo, C. Brambilla, A. Di Natale, G. R. Romano and K. Pikull for the excellent technical support. We acknowledge the DESY machine vacuum systems (MVS) group for providing a residual gas analyzer. This project is supported by the ERC Starting Grant no. 637756 and by the Cluster of Excellence ‘CUI: Advanced Imaging of Matter’ of the Deutsche Forschungsgemeinschaft (DFG) - EXC 2056 – project ID 390715994. V.W. acknowledges support from the Vanier Canada Graduate Scholarship (Vanier CGS) program and the Fonds de recherche en Nature et technologies (FRQNT). L.C. acknowledges the DFG-Sonderforschungsbereich 925 ‘Light-induced dynamics and control of correlated quantum systems’ – project No. A7.



## Chapter 4

# Coherent control in the dissociative ionization of molecular hydrogen

Through nonlinear parametric processes such as optical parametric amplification, the access to longer wavelengths than the typical 800 nm from Titanium:Sapphire lasers offers new opportunities for control experiments that can be realized both in the gas phase and the solid state. The following two chapters describe such experiments where a 1.8  $\mu\text{m}$  laser field was employed, in a first time to control the photo-induced dissociation dynamics in molecular hydrogen. In chapter 5, we further extend our studies to lithium niobate, where we exploit the spontaneous polarization of the material to control its strong-field ionization.

One of the ultimate goals in photochemistry is to understand a molecular system well enough to succeed in controlling the outcome of its chemical reactions. As an example, theoretical calculations have demonstrated that steering few-fs electron dynamics following photoionization could prevent the dissociation of large organic molecules [164]. Such a control in biologically relevant molecules could have an important impact in biochemistry for instance. In the present chapter, we used 1.8  $\mu\text{m}$  femtosecond pulses to both ionize and steer electron dynamics during the dissociative ionization of hydrogen isotopes ( $\text{H}_2$  and  $\text{D}_2$ ). Being the simplest existing molecule,  $\text{H}_2$  has become over the last decades a benchmark in spectroscopy both for experiments and theory [165]. Indeed, for the molecular ion  $\text{H}_2^+$ , the time-dependent Schrödinger equation can be solved with high accuracy and hence allows for a direct comparison with experimental results. In the context of controlling molecular dynamics,  $\text{H}_2$  is also suitable because the two lowest electronic states of its molecular ion consist of a simple two-level quantum system for which the concept of coherent control, described in the following section, can be easily applied.

## 4.1 Coherent control for a two-level system

In spectroscopy, coherent control consists in exploiting the coherent properties of electromagnetic radiation to control the dynamics of a system. From a quantum mechanical point of view, controlling photochemical processes requires to be able to steer the electrons of the system, more specifically the electron density that governs the reactivity. To approach this challenge, it is useful to consider first a simple system composed of two quantum states  $\psi_1$  and  $\psi_2$  with their respective energy  $\epsilon_1$  and  $\epsilon_2$  and initial population  $c_1 = 1$  and  $c_2 = 0$ . After these two states have been coupled by a perturbative field such that, e.g.  $c_1 = c_2 = 1/\sqrt{2}$ , a wavepacket is created and evolves in time according to :

$$|\Psi_{tot}\rangle = \frac{1}{\sqrt{2}} |\psi_1\rangle + e^{-i\omega_{2,1}t} \frac{1}{\sqrt{2}} |\psi_2\rangle \quad (4.1)$$

where  $e^{-i\omega_{2,1}t}$  is the phase factor describing the temporal evolution of the coherent superposition with  $\omega_{2,1} = (\epsilon_2 - \epsilon_1)/\hbar$ . The corresponding probability density is:

$$|\Psi_{tot}|^2 = \frac{1}{2} |\psi_1|^2 + \frac{1}{2} |\psi_2|^2 + |\psi_1||\psi_2| \cos(\omega_{2,1}t) \quad (4.2)$$

where the last term in Eq. 4.2 is an interference term that depends on the energy difference between the two quantum states. This interference term is at the basis of coherent control and its effect is illustrated in Fig. 4.1 where Eq. 4.2 is evaluated for the first two eigenfunctions [Fig. 4.1(a)] of a particle in a box of length  $L$ . In this case, the probability density oscillates spatially from left to right. For such a localization to be achieved, the wavefunctions that interfere with each other must be of opposite parity.

The concept of coherent control is well known and routinely used, for example, in NMR spectroscopy for creating coherent superposition of nuclear spin states [166, 167]. Indeed, in NMR radio-frequencies carry sufficient energy for the transitions to occur. However, the possibility to couple electronic states in matter is relatively recent because of the large energy difference required for electronic transitions, typically on the order of the eV. This can now be achieved thanks to the energetic frequencies provided by lasers.

By including the selection rules of atomic and molecular systems to the concept of coherent control, Brumer and Shapiro proposed a simple method for the control of photo-induced processes using laser fields. They showed how the preparation of a system through linear combination of degenerated quantum states can alter the outcome of photochemical processes [168, 169]. An example is shown in Fig. 4.2. Considering two electronic states with different parity, here  $|e\rangle$  (even) and  $|o\rangle$  (odd), a transition is only allowed through the absorption of an odd number of photons.

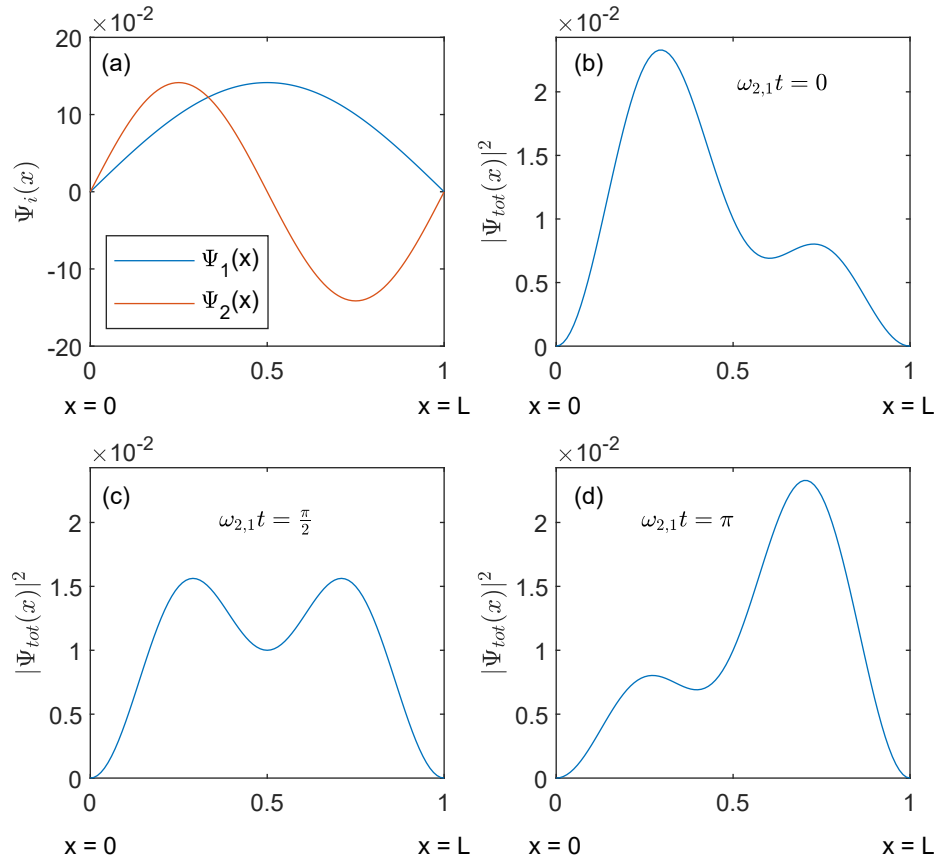


**Figure 4.1** – Temporal evolution of the density probability for the coherent superposition of the first two eigenfunctions of a particle in a box (Eq. 4.2).

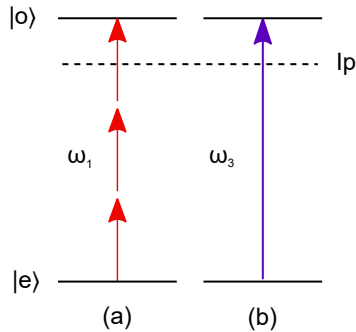


**Figure 4.2** – Coherent superposition of degenerated electronic states based on the method proposed by Brumer and Shapiro. Population of the  $|o\rangle$  (odd) state can occur via (a) a three-photon transition from the ground state  $|e\rangle$  (even) or (b) a single  $\omega_1$  photon resonant transition.

This selection rule must be respected in order to obtain a nonzero dipole matrix element between these two states. By employing a laser field composed of two distinct laser frequencies ( $\omega_1$  and  $\omega_3$ ),  $|o\rangle$  can be populated via two distinct pathways. Either by the absorption of three  $\omega_1$  photons or by absorption of a single  $\omega_3$  photon. In this way, the coherence property of the laser field can be exploited to control the interference between these quantum pathways. By varying the relative

phase between the  $\omega_1$  and  $\omega_3$  frequency components of the laser field, a destructive or constructive interference can be obtained, affecting the population of the  $|o\rangle$  state. Supposing that  $|o\rangle$  is a resonant state below the ionization potential, increasing its population (or transition probability) provides a mean to increase the resonance-enhanced multiphoton ionization (REMPI) yield, as it was first experimentally demonstrated in 1990 by Chen *et al.* [170]. As another example, if  $|o\rangle$  is a dissociative molecular state, control over the photodissociation of the molecule is also feasible [171].

## 4.2 Article IV – Summary

In article IV, we apply the concepts described in the above section to control the electron density during the dissociation of  $\text{H}_2^+$  and  $\text{D}_2^+$ . We combine a mid-infrared 1800 nm field and its second harmonic at 900 nm to couple the ion ground ( $1s \sigma_g$ ) and first excited ( $2p \sigma_u$ ) states (see article Fig. 4.3). During the dissociation, the single electron in the molecule can be selectively localized by the asymmetric two-color laser field<sup>1</sup> on one of the two hydrogen atoms with a given efficiency, in a similar manner as shown in Fig. 4.1. Two aspects motivated our interest to study this prototype reaction:

Ray *et al.* 2009 performed a similar two-color experiment employing laser pulses combining a 800 nm field and its SH at 400 nm [172]. A first objective was to verify the influence of using longer wavelengths to selectively localize the electron. Also, as an alternative to the use of two-color laser field to control the electron localization in the dissociative ionization of molecular hydrogen, several experiments employed CEP stabilized pulses. These experiments were carried out both at a 800 nm wavelength [173, 174, 175] and at 2.1  $\mu\text{m}$  [176]. Complementing the series of experiments previously mentioned allowed to draw further conclusions and understand better the benchmark reaction.

The results presented in article IV confirm that the use of two-color (1800 nm, 900 nm) laser fields rather than CEP stabilized pulses leads to an enhanced control over the electron localization in the molecule [177], supporting the observation made by Ray *et al.* 2009 [172]. Indeed, the above experiments employing CEP stable pulses all report a lower level of control. Furthermore, it was also observed that a two-color field at longer wavelengths than 800 nm allows to control an additional dissociation channel in the molecule.

Through a collaboration with Prof. Xiao-Min Tong from the University of Tsukuba, we also performed calculations solving the TDSE for the molecular ion, using the experimentally evaluated intensity of our laser pulses. While a qualitative agreement was obtained to reproduce the experimental results, the calculations demonstrate that the initial composition of the nuclear wavepacket (NWP) prepared on the  $\sigma_g$  state plays a crucial role in the electron localization during dissociation. The Franck-Condon (FC) principle is a concept that allows to describe the distribution of

---

<sup>1</sup>Illustrations of asymmetric waveforms of the electric field as a function of the relative two-color phase can be found in Fig. 5.12b

the populated vibrational wavefunctions following an electronic transition in a molecule. The distribution is obtained by assuming a vertical electronic transition that is instantaneous compared to vibrational motion and for which there is no energy exchange with the nuclei. The initial relative phase between each of the vibrational components is therefore zero. Our work suggests that the experimental conditions are not following the Franck-Condon principle, as the best agreement with the experimental results was not obtained with a FC distribution. Indeed, by using a pump-probe approach, it was demonstrated that the initial NWP on  $\text{H}_2^+$  can settle on a timescale of about 1 fs with vibrational components having different phases [178].

### 4.3 Article IV – Coherent control of $D_2/H_2$ dissociative ionization by a mid-infrared two-color laser field

Vincent Wanie<sup>1</sup>, Heide Ibrahim<sup>1</sup>, Samuel Beaulieu<sup>1</sup>, Nicolas Thiré<sup>1</sup>, Bruno E. Schmidt<sup>1,2</sup>, Yunpei Deng<sup>3</sup>, Ali S. Alnaser<sup>4</sup>, Igor V. Litvinyuk<sup>5</sup>, Xiao-Min Tong<sup>6,7</sup> and François Légaré<sup>1</sup>

<sup>1</sup>Institut national de la recherche scientifique, Centre Énergie Matériaux et Télécommunication, 1650 Blvd. Lionel-Boulet, Varennes, Qc, J3X 1S2, Canada

<sup>2</sup>fewcycle Inc., 2890 Rue de Beaurivage, Montreal, Qc, H1L 5W5, Canada

<sup>3</sup>Fritz-Haber-Institut der Max-Planck-Gesellschaft, Berlin D-14195, Germany

<sup>4</sup>Physics Department, American University of Sharjah, Sharjah, POB26666, UAE

<sup>5</sup>Centre for Quantum Dynamics, Griffith University, Nathan, Queensland 4111, Australia

<sup>6</sup>Center for Computational Sciences, University of Tsukuba, Ibaraki, 305-8577 Japan

<sup>7</sup>Faculty of Pure and Applied Sciences, University of Tsukuba, Ibaraki, 305-8577 Japan

Journal of Physics B : Atomic, Molecular and Optical Physics **49** (2015) 025601

Received 21 August 2015

Published 16 December 2015

doi:10.1088/0953-4075/49/2/025601

V.W., H.I. and S.B. performed the experiments. V.W. carried out the data analysis, wrote the manuscript with the help of H.I. and was in charge of the communication with the theory group. N.T. and B.E.S. provided the infrared laser source. Y.D., A.S.A. and I.V.L. were guest scientists and participated to the experiments. X.M.T. provided the theoretical support and F.L. supervised the project.

## Abstract

Steering the electrons during an ultrafast photo-induced process in a molecule influences the chemical behavior of the system, opening the door to the control of photochemical reactions and photobiological processes. Electrons can be efficiently localized using a strong laser field with a well-designed temporal shape of the electric component. Consequently, many experiments have been performed with laser sources in the near-infrared region (800 nm) in the interest of studying and enhancing the electron localization. However, due to its limited accessibility, the midinfrared (MIR) range has barely been investigated, although it allows to efficiently control small molecules and even more complex systems. To push further the manipulation of basic chemical mechanisms, we used a MIR two-color (1800 and 900 nm) laser field to ionize H<sub>2</sub> and D<sub>2</sub> molecules and to steer the remaining electron during the photo-induced dissociation. The study of this prototype reaction led to the simultaneous control of four fragmentation channels. The results are well reproduced by a theoretical model solving the time-dependent Schrödinger equation for the molecular ion, identifying the involved dissociation mechanisms. By varying the relative phase between the two colors, asymmetries (i.e., electron localization selectivity) of up to 65% were obtained, corresponding to enhanced or equivalent levels of control compared to previous experiments. Experimentally easier to implement, the use of a two-color laser field leads to a better electron localization than carrier-envelope phase stabilized pulses and applying the technique in the MIR range reveals more dissociation channels than at 800 nm.

## Introduction

Being the most fundamental units in chemistry, electrons ensure structural cohesion in matter and are responsible for a multitude of processes in a variety of systems including nano-chemical and biological ones. Therefore, steering their motion is an attractive goal since it opens the door to the control of photo-induced processes [179]. Recently, theoretical work has demonstrated the possibility to control charge migration in complex organic molecules by using ultrashort laser pulses [164]. Utility of such control has also been demonstrated experimentally in nano-systems where it was possible to uncover an electron acceleration mechanism in dielectric nanoparticles [180].

Localizing the electronic density in a particular system can be achieved with an intense laser pulse by controlling the temporal profile of its electric field such that an asymmetry between the up and down components is obtained. For electronic dynamics involving nuclear motion, this control requires a femtosecond (fs) resolution as chemical bonds in molecules break and form on this time scale. Offering such a resolution, the ability to lock the carrier-envelope phase (CEP) of few-cycle laser pulses has been exploited in order to control dissociations in diatomic molecules [173, 181, 174, 176, 175]. Control of these processes has also been demonstrated by tailoring the waveform of a laser pulse via the combination of a fundamental frequency with its second harmonic,

with fixed but variable relative phase [172], as well as via the use of attosecond pulses in the presence of a moderately intense near-infrared (NIR) fs field [15, 182, 183].

Molecular hydrogen  $\text{H}_2$  and its isotope  $\text{D}_2$  are well known molecules that have been studied for many years to develop molecular science, both theoretically and experimentally. Its photodissociation has become a prototype to understand and manipulate photochemical reactions via electron localization. Controlling the electronic density during a photo-induced molecular dissociation requires the coherent superposition of electronic states of opposite parity. From its electronic structure, the hydrogen molecule is thus a well suited system for coherent control as the electron localization during its dissociative ionization can be explained using the two lowest electronic states of its molecular ion. This two level quantum system consists of the ground gerade  $X^2\Sigma_g^+$  ( $1s \sigma_g$ ) and the first excited ungerade  $A^2\Sigma_u^+$  ( $2p \sigma_u$ ) states of  $\text{H}_2^+$ . Following radiative coupling of those two states, their coherent superposition can be generated, leading to the electron localization on either side of the molecule depending on the relative phase of the states. The level of control is defined by the phase relationship ( $\phi$ ) and the relative population ( $c_1$  versus  $c_2$ ) between both states according to the electronic wavefunction:

$$|\Psi_{tot}\rangle = c_1 |1s \sigma_g\rangle + e^{-i\phi} c_2 |2p \sigma_u\rangle \quad (4.3)$$

Indeed, to coherently control electron localization, two fundamental conditions have to be fulfilled. Firstly, the spatial overlap between both nuclear wavepackets (NWP) propagating along these two potential curves must be maintained. In the case of molecular hydrogen, this condition can be satisfied because the  $\sigma_g$  and  $\sigma_u$  states of the molecular ion are near degenerate at large internuclear distances where dissociation occurs. Secondly, temporal overlap is required because the instantaneous probability density at the internuclear distance where the interatomic potential cannot be overcome by the electron is defined by the interference of these wavepackets coming from electronic states with different parity. For such an interference to happen, the wavepackets must arrive at the same time in the dissociation region, which is likely to occur when their kinetic energy (KE) distribution is similar. Theoretical efforts have demonstrated that such a KE overlap—leading to coherent control—can be achieved from the interference between dissociation pathways, each populating electronic states of different parity via the concurrent net absorption of  $n$  and  $n+1$  photon(s) in the presence of a strong laser field [184].

Up to now, the potential of experimentally exploiting the mid-infrared (MIR) spectral range to control electron localization has barely been explored, except for [176] where CEP control of  $\text{D}_2^+$  dissociation was studied using 2100 nm pulses. However, because of its longer period of one optical cycle (6.0 fs at 1800 nm versus 2.7 fs at 800 nm), this spectral range enables a more efficient subcycle control of slower nuclear dynamics compared to 800 nm, which are the preponderant dynamics in more complex molecules. For the experiments reported here, relatively long (50 fs)

MIR twocolor (1800 and 900 nm) laser pulses were used to coherently control the dissociative ionization of  $\text{H}_2$  and  $\text{D}_2$  molecules. Compared to CEP stabilized pulses, the particularity of the two-color technique, which is experimentally significantly easier to achieve, is that it enables to tailor the electric field of a laser pulse on a much longer timescale. This is because in a long CEP stabilized pulse the difference between up and down components of the electric field vanishes, while it is imprinted on every single cycle of a two-color field. By applying this technique, simultaneous control of four fragmentation pathways was observed and identified to originate from recollision excitation (RCE) and MIR induced dissociation. We also discuss the effect of the initial vibrational distribution on the electron localization. The control mechanisms are interpreted and supported by our theoretical model based on the time-dependent Schrödinger equation (TDSE), which reproduces the experimental data with good agreement.

## Methods

Figure 4.3(a) illustrates the dynamics of interest in the frame of our experiment leading to the dissociation of  $\text{D}_2^+$  ( $\text{H}_2^+$ ): the two-color laser pulse first removes an electron from the ground  $\text{X}^1\Sigma_g^+$  state of the neutral molecule via tunnel ionization. A vibrational wavepacket is then launched on the ground electronic state  $\text{X}^2\Sigma_g^+$  ( $\sigma_g$ ) of the cation and starts to propagate. During this propagation, the following dissociation mechanisms involving different quantum pathways are likely to occur upon absorption of further photons:

- (i) Dissociation of the molecule can be induced by the MIR field. The molecule may dissociate in the bond softening (BS) region, where it has been demonstrated that bound vibrational levels become dissociative as the laser field opens up the gap at the avoided crossing in the one photon transition region [185]. At 1800 nm, this region is located at an internuclear distance of  $\sim 5.8$  a.u. where absorption of a single photon (G) results in dissociation via the  $\sigma_u$  cationic state (red region on the D+ KE axis in figure 4.3(a)). Furthermore, the second color (900 nm) of a two-color field can also lead to BS (E) and populate the  $\sigma_u$  state (blue region).
- (ii) Field induced dissociation can also occur via above-threshold dissociation (ATD), where the molecular ion absorbs additional photons on top of the energy required to dissociate [186]. For example, the absorption of three photons in a non-sequential way (C) followed by stimulated emission of one photon (F) may lead to the dissociation of the molecule via the  $\sigma_g$  cationic state (blue region in figure 4.3(a)).
- (iii) A wavepacket avoiding the previously mentioned processes may reach an internuclear distance where the ionization probability is significantly increased, leading to a second ionization of the molecule. This behavior is known as charge-resonance-enhanced ionization (CREI) [187, 188, 189]. Because the process is generating two ions ( $D^+ + D^+$ ), no localization of the electronic density can be observed. Nevertheless, these ions possess an intermediate KE as the dissociation occurs via a higher excited state (H) (orange region in figure 4.3(a)).
- (iv) Apart from radiative coupling with the laser field, recollision excitation (RCE) can lead to molecular dissociation. Under the influence of the laser field, the ionized electron may recollide with the molecular ion and cause an inelastic collision leading to an excitation of the molecule to the  $\sigma_u$  dissociative state (A). In analogy to the well known high harmonic generation process [6], many recollision orders can contribute to its population. Because the dissociative state is populated rather early, the generated ions possess a high KE (purple region in figure 4.3(a)).

In our experiments, control of molecular dissociation via the interference of dissociation pathways such as in (1) and (2) was observed in addition to the control of (4). As an example, because BS (pathway E) and ATD (pathways C + F) both lead to the same final KE but with wavepack-

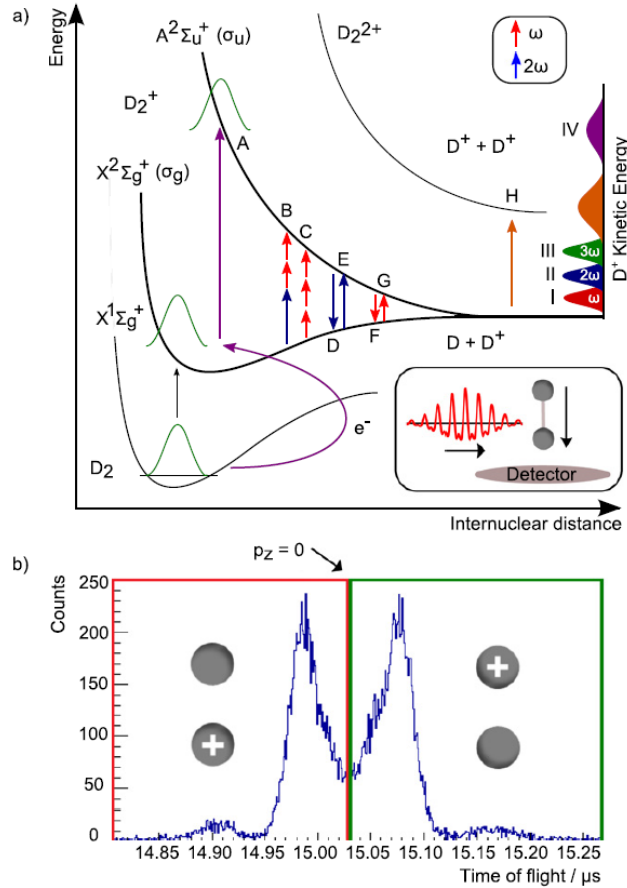


**Figure 4.3** – (a) Scheme of the reflection principle associated to the formation of  $D^+$  ions from bond softening (red KE region), above-threshold dissociation (blue KE region), three-photon dissociation (green KE region), charge-resonance-enhanced ionization (orange KE region) and recollision excitation (purple KE region). Capital letters correspond to different pathways and roman numerals indicate different control channels, as discussed in the text. The inset shows the geometry of the experimental setup, from the interaction of the molecule with the asymmetric two-color laser pulse in the focal volume, to the detection of the  $D^+$  fragments. (b)  $D^+$  time of flight spectrum for a specific relative phase  $\phi$ : calibration allows defining the time of arrival for fragments with a zero initial momentum  $p_z$  in the direction of the detector. Fragments that arrive before (red zone) and after (green zone) this time correspond to an electron localization (ion emission) of opposite direction.

ets propagating on different electronic states ( $\sigma_g$  and  $\sigma_u$ ), the resulting interference allows us to coherently control the dissociation channel II as will be presented in the discussion section.

We used the 2.5 kHz Titanium–Sapphire (800 nm) laser beam line of the advanced laser light source (ALLS) user facility in Varennes, Canada, to perform the experiments. From a 30 fs pulse, we generated the 1800 nm field through Idler amplification using a white light seeded optical parametric amplifier (OPA) [30]. A beta barium borate (BBO) crystal was used to generate the 900 nm second harmonic field at the output of the OPA. To compensate the group delay between the two pulses,

a second thick BBO crystal combined with a calcium fluoride window was used. Next, a zero-order half-waveplate was employed to rotate the 1800 nm polarization parallel to that of its second harmonic. The relative phase between the two colors was finally adjusted by rotating a 2 mm fused silica window around its vertical axis. The pulse duration of the 1800 nm field was evaluated to be 50 fs using second harmonic generation autocorrelation. The resulting two-color laser pulses were then focused into a Coulomb explosion imaging (CEI) apparatus by a spherical mirror of 100 mm effective focal length. The laser intensity at 1800 nm in the interaction region was determined from the distribution of the recoil momentum transferred to  $\text{H}_2^+$  and  $\text{D}_2^+$  ions when ionized by circularly polarized laser pulses [190].

## Results and Discussion

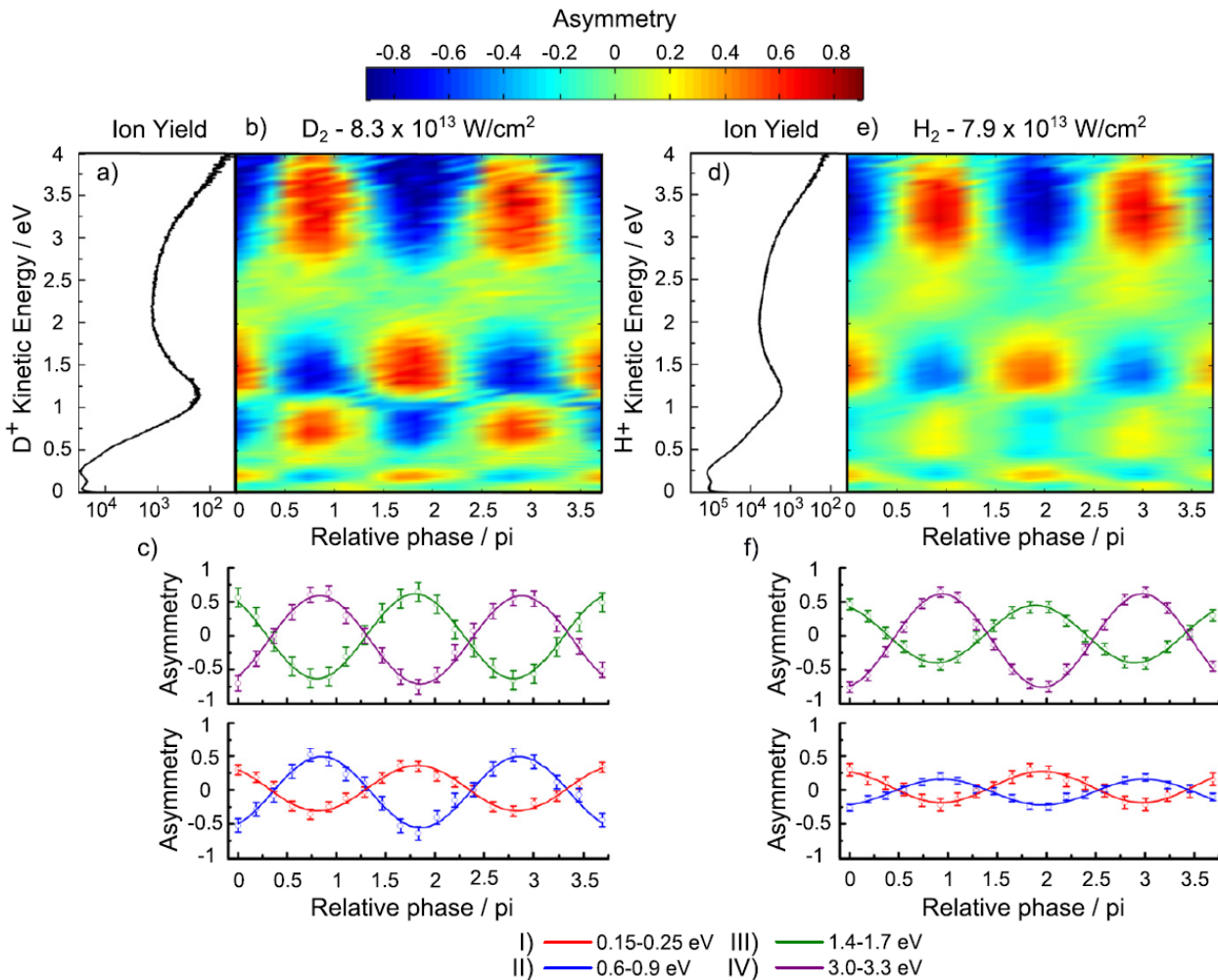


**Figure 4.4** – (a) Logarithmic energy distribution for the detected  $\text{D}^+$  fragments at an intensity of  $8.3 \times 10^{13} \text{ W cm}^{-2}$ ; (b) experimental calculated asymmetries; (c) averaged asymmetries for the specified KER cuts; (d)–(f) same for the isotope  $\text{H}^+$  at an intensity of  $7.9 \times 10^{13} \text{ W cm}^{-2}$ .

The time- and position-sensitive (RoentDek) detector of the CEI chamber allows us to reconstruct the full 3D momentum vector of the detected ions and to retrieve their KE. Following the reflection principle illustrated in figure 4.3(a), this energy is a signature of the dissociation pathways involved in the molecular dissociation. Because of the sigma symmetry of the molecular orbitals favoring radiative coupling with a laser field parallel to the molecular axis, by using a field linearly polarized along the time-of-flight axis, ions that are generated with an initial momentum towards (down) or away (up) from the detector can be distinguished by their flight time (figure 4.3(b)). For a fixed phase relationship between the two colors of the laser field, observing a preferential emission direction of the fragments is thus an indirect measure of the electron localization. To characterize this localization, we evaluate an asymmetry parameter, which is defined as:

$$A(\varphi, E) = \frac{N_{\text{up}}(\varphi, E) - N_{\text{down}}(\varphi, E)}{N_{\text{up}}(\varphi, E) + N_{\text{down}}(\varphi, E)} \quad (4.4)$$

where  $N_{\text{up}}$  and  $N_{\text{down}}$  correspond to the number of fragments emitted in the corresponding direction, in the laboratory frame, with a kinetic energy  $E$  and for a specific relative phase  $\varphi$  between  $\omega$  and  $2\omega$ . The experiments were performed for intensities ranging from  $5.5 \times 10^{13}$  to  $8.5 \times 10^{13}$  W cm<sup>-2</sup> for both D<sub>2</sub> and H<sub>2</sub> molecules. Whereas no significant control of electron localization could be observed for the lowest intensity, the main features are present for all the other ones. Figure 4.4 shows the results for intensities where the strongest asymmetries had been observed for each isotope. Figure 4.4(a) depicts the KE distribution of the detected D<sup>+</sup> fragments at an intensity of  $8.3 \times 10^{13}$  W cm<sup>-2</sup> and figure 4.4(b) contains the corresponding phase and energy resolved asymmetry parameter. Four channels in which efficient control has been achieved can be distinguished and the corresponding energy cuts are illustrated in figure 4.4(c): (I) from 0.15 to 0.25 eV with a maximal asymmetry of ~30%; (II) from 0.6 to 0.9 eV with maximal asymmetry of ~50%; (III) from 1.4 to 1.7 eV and (IV) from 3.0 to 3.3 eV, both with a maximal asymmetry of ~60%. We assign the contrast free region centered at 2.5 eV to CREI where the generation of two D<sup>+</sup> ions prevents any electron localization (orange region in figure 4.3(a)). Figures 4.4(d)–(f) show the corresponding results for H<sub>2</sub> where the same dissociation channels had been controlled. Smaller asymmetries are observed except for the highest energy region where the asymmetry reaches ~65%.

In order to identify each of the controlled dissociation mechanisms, we performed simulations for the two levels system of the molecular ion. As will be discussed below, our theoretical model confirms that the controlled dissociation channels originate from RCE and MIR induced dissociation, in accord with previous literature [173, 174, 176, 175, 172].

The time evolution of the NWP of D<sub>2</sub><sup>+</sup> (H<sub>2</sub><sup>+</sup>) is described by the TDSE as:

$$i \frac{\partial}{\partial t} \begin{pmatrix} \psi_{\text{g}}(R, t) \\ \psi_{\text{u}}(R, t) \end{pmatrix} = \begin{pmatrix} -\frac{1}{2\mu} \frac{d^2}{dR^2} + E_{\text{g}}(R) & -D(R)E(t) \\ -D(R)E(t) & -\frac{1}{2\mu} \frac{d^2}{dR^2} + E_{\text{u}}(R) \end{pmatrix} \begin{pmatrix} \psi_{\text{g}}(R, t) \\ \psi_{\text{u}}(R, t) \end{pmatrix} \quad (4.5)$$

with  $\mu$  being the reduced mass of  $D_2$  ( $H_2$ ),  $R$  the internuclear distance,  $D(R)$  the transition dipole between the  $\sigma_g$  and  $\sigma_u$  states as a function of  $R$ , and  $E(t)$  the time-dependent laser electric field.  $E_g(R)$  and  $E_u(R)$  correspond to the  $g$  and  $u$  potential curves of the molecular ion. We solve the above equation for the two-color MIR field induced dissociative ionization and RCE induced dissociation with different initial conditions.

For the MIR induced dissociative ionization, we first calculate the total ionization probability  $P_n(R)$  by the modified molecular tunneling ionization model for the  $n$ th peak of  $|E(t)|$  and assume the ionization happens at time  $t_n$  at which  $E(t)$  reaches a local maximum [191, 192]. Thus the initial condition for the NWP for  $D_2$  ionized at time  $t_n$  is written as:

$$\psi_g(R, t_n) = \sum_{v=0}^{n_v} \phi_v(R) \langle \phi_v(R) | \sqrt{P_n(R)} | \phi_g(R) \rangle \quad (4.6)$$

$$\psi_u(R, t_n) = 0 \quad (4.7)$$

with  $\phi_v(R)$  being the  $v$ th vibrational state of the ground state of  $D_2^+$ ,  $\phi_g(R)$  the ground vibrational state of  $D_2$  and  $n_v$  the highest vibrational state of  $D_2^+$  initially populated. By varying  $n_v$  we can study how the choice of initial vibrational states affects the final asymmetry parameter. When the laser pulse is over, we project the NWP [ $\psi_g(R, t = \infty)$ ,  $\psi_u(R, t = \infty)$ ] onto momentum space and further obtain the electron localization probability to the up (down) side. The total localization probability is obtained by summing over all the sub-peaks of  $|E(t)|$  over the pulse. For RCE induced dissociation, we trace the electron return time  $t_r$ , return energy  $E_r$  and rescattering probability  $P_{res}(t_r, t_i)$  for the electron ionized at time  $t_i$  using the semiclassical method from [193, 194]. With an empirical electron impact excitation probability  $P(E_r, R)$ , the initial conditions at the return time  $t_r$  can be expressed as:

$$\psi_g(R, t_r) = \sum_v \sqrt{1 - P_{res}(t_r, t_i) P(E_r, R)} \times e^{-i\epsilon_v(t_r - t_i)} \phi_v(R) \langle \phi_v(R) | \phi_g(R) \rangle \quad (4.8)$$

$$\psi_u(R, t_r) = \sum_v \sqrt{P_{res}(t_r, t_i) P(E_r, R)} \times e^{-i\epsilon_v(t_r - t_i)} \phi_v(R) \langle \phi_v(R) | \phi_g(R) \rangle \quad (4.9)$$

with  $\epsilon_v$  being the vibrational energy of  $\phi_v(R)$ . Physically, the above initial conditions represent a NWP which is suddenly created at time  $t_i$  (Franck-Condon (FC) approximation), then propagates freely in the ground state potential curve of  $D_2^+$  and finally is being excited to the  $\sigma_u$  state at time  $t_r$  by the rescattering electron impact excitation. Since the simulation is very time consuming, we only consider the ionization happening within a full cycle of the fundamental laser field and trace the later returns up to five returns. With the initial conditions, similar to the ones used for MIR

induced dissociative ionization, we obtain the electron localization probability to the up (down) side due to the RCE process.

Figure 4.5(a) illustrates the resulting simulation for the RCE process (control channel IV) in  $D_2$  for an intensity of  $8.3 \times 10^{13} \text{ W cm}^{-2}$  and a two-color ratio of 2% in terms of intensity. The control of electron localization is in good agreement with the experimental data (figure 4.5(b)) and is understood as follows: as the internuclear distance increases during the propagation on the  $\sigma_u$  state induced by RCE, the energy difference between the electronic states of the cation decreases and enables population transfers between the  $\sigma_u$  and the  $\sigma_g$  state via radiative coupling with the laser field. This leads to electron localization, as was described by Kling et al [173]. It is observed that in addition to a previous NIR two-color (800/400 nm) experiment where asymmetries of  $\sim 50\%$  were observed [172], the use of a 1800 nm field with its second harmonic (900 nm) leads to stronger asymmetries ( $\sim 60\%$  for  $D_2$  and  $\sim 65\%$  for  $H_2$ ) than previous CEP experiments (maximum of  $\sim 25\%$ ) [173, 176]. This shows that steering the relative phase of two-color pulses can control the electron localization more efficiently than steering the CEP of an ultrashort pulse.

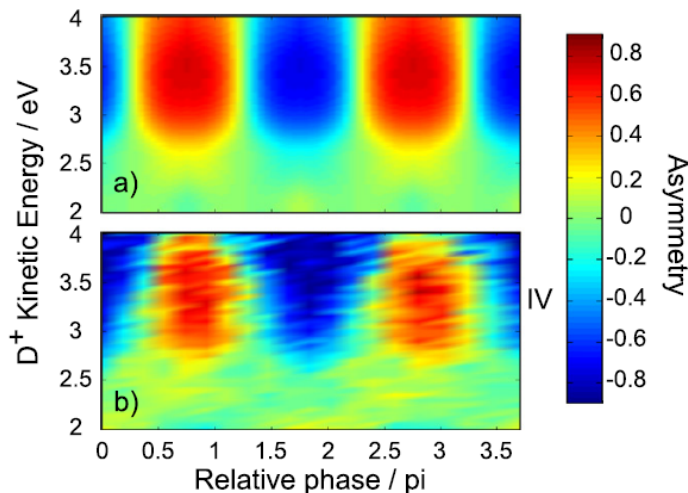


**Figure 4.5 – Control of the RCE induced dissociation: (a) simulation for an intensity of  $8.3 \times 10^{13} \text{ W cm}^{-2}$  and a two-color ratio of 2% in terms of intensity and (b)  $D_2$  experiment.**

Figure 4.6(a) illustrates the lower energy region (0–2 eV) from the experiment presented in figure 4.4(b). The corresponding simulations for MIR induced dissociation, all using an intensity of  $8.3 \times 10^{13} \text{ W cm}^{-2}$  and a two-color ratio of 2% in terms of intensity are presented in figures 4.6(b)–(d). In figure 4.6(b) we are assuming the initial vibrational states to be FC distributed, not considering the  $R$ -dependence of the tunneling ionization rate. In this case we observe a reasonable agreement for channel I appearing between 0 and 0.3 eV and channel II between 0.5 and 1 eV, but the phase relationship between channels II and III is significantly different from the experimental results in 4.6a. We therefore introduced the  $R$ -dependence on the tunneling ionization rate in 4.6c, keeping the FC type initial vibrational distribution. In this case, a  $\pi$  phase change from channel II (between

0.5 and 1.0 eV) to channel III (between 1.0 and 1.5 eV), which we also observe experimentally, is well reproduced. Channel III however, is compressed such that it already ends at 1.5 eV rather than at 2.0 eV as in the experiment shown in 4.6a. It is thus striking how strongly the initial vibrational distribution, influenced by the ionization step, affects the electron localization. The dependence on this parameter was therefore further investigated. Out of many simulations that have been carried out by varying initial vibrational distribution, figure 4.6(d) shows the results that match the experiment best, with an initial vibrational distribution from  $\nu = 0$  to 20 and an ionization rate independent of  $R$ . Modifying this distribution with the  $R$ -dependent ionization rate decreases the agreement with the experiment. In figure 4.6(d), all main features, including the phase relationship between the different energy regions, are well reproduced. Only channel II appears to be extended slightly towards higher energies, and thus the onset of channel III is shifted towards higher energies as well, in comparison with the experiment. This remaining discrepancy is therefore attributed to the chosen initial vibrational distribution. In addition, although the intensity and the ratio of the two colors were measured experimentally, the overlap of the focal spots of both colors might not have been perfect and the mentioned parameters also varied along the focal volume, which might also lead to minor discrepancies since they are not taken into account in the simulations. We therefore varied the intensity and two-color ratio in the simulations and figure 4.6(d) shows the best reproduction of the experimental results. Moreover, the phase integrated KE distributions from figures 4.6(a)–(d) are shown in figure 4.6(e). Although the experimental signal generated by CREI above 1 eV prevents any comparison with the simulations, the effect of the chosen vibrational distribution can be observed in the simulations where this process –CREI– is not taken into account. The combination of the simulations presented in figures 4.6(a)–(e) thus demonstrates that the initial vibrational distribution plays a very important role on electron localization and that the distribution in our experiment involves a narrower distribution than an FC one. A closer investigation into the role of the first step –the ionization process– which influences the initial vibrational distribution would help to fully elaborate the coherent control process. Finally, the experimental results for MIR induced dissociation were interpreted by carefully comparing them with the theoretical simulations.

For each energy region below 2 eV, the control of electron localization is attributed to interference effects between two dissociation pathways involving the net absorption of  $n$  and  $n+1$  photon(s) (see figure 4.3). Each pathway populates either the  $\sigma_g$  or  $\sigma_u$  state, resulting in NWP’s of same final KE, thus interfering and leading to the asymmetry. Due to the selection rules, only odd numbers of photons can be exchanged with the laser field. In a single color field, BS would lead only to the population of the  $\sigma_u$  state and no interference would be possible. However, in the presence of the two-color field, the  $\sigma_u$  state is populated by the absorption of one photon at energy  $\omega_{1800}$  (pathway G,  $n = 1$ ) while the  $\sigma_g$  state can be populated upon absorption of one  $\omega_{900}$  photon and stimulated emission of one  $\omega_{1800}$  photon (pathways E + F,  $n = 1 - 1 = 0$ ). Both pathways generate ions with energies below 0.3 eV, corresponding to channel I in figure 4.6. In the same manner, we assign the energy range from 0.5 to 1.0 eV (channel II) to the interference between pathways where the energy transferred to the molecule corresponds to the net absorption of two  $\omega_{1800}$  photons. The

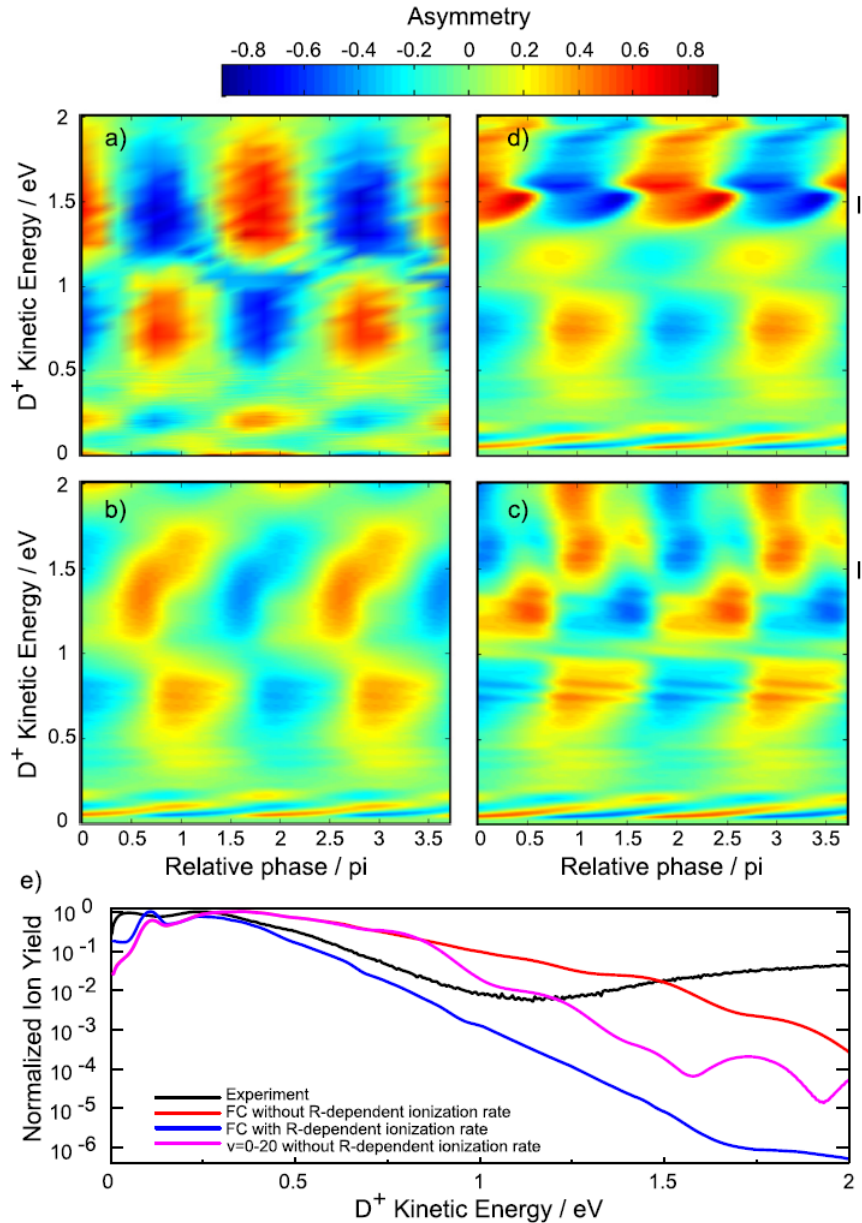


**Figure 4.6 – Control of MIR induced dissociation:** (a)  $D_2$  experiment; (b)–(c) simulations for an intensity of  $8.3 \times 10^{13} \text{ W cm}^{-2}$ , a two-color ratio of 2% in terms of intensity and assuming a Franck–Condon initial vibrational distribution without the  $R$ -dependent ionization rate (b) and with it (c). (d) Simulation with the same parameters as in (b) but assuming an initial vibrational distribution from  $\nu = 0$  to 20. (e) Phase integrated logarithmic energy distributions for a (black curve), b (red curve), c (blue curve) and d (magenta curve).

$\sigma_u$  state is populated by the absorption of one  $\omega_{900}$  photon (pathway E,  $n = 1$ ) via BS and the  $\sigma_g$  state is populated by the absorption of three  $\omega_{1800}$  photons and stimulated emission of one  $\omega_{1800}$  photon (pathways C + F,  $n = 3 - 1 = 2$ ) via ATD. The previous two controlled channels were also observed by Ray *et al.* in their NIR (800/400 nm) experiment [172]. However, in the MIR we

observe an additional channel (III) ranging from 1.1 to 2.0 eV which we assign to the net absorption of three  $\omega_{1800}$  photons as follows: population of the  $\sigma_u$  state occurs via the absorption of three  $\omega_{1800}$  photons (pathway C,  $n = 3$ ) while the  $\sigma_g$  state is populated by the absorption of one  $\omega_{900}$  and two  $\omega_{1800}$  photons followed by the stimulated emission of one  $\omega_{1800}$  photon (pathways B+ F,  $n = 1+2-1 = 2$ ). A similar channel involving three-photon dissociation [195] was observed by Xu *et al.* in their 800 nm CEP experiment [175], but was never reported for a two-color experiment. In all the suggested schemes, the relative phase between the two colors defines the phase relationship and the relative population between both wavepackets. The time-dependence of these two factors shows up in the phase relationship between the controlled dissociation channels. Indeed, the relative timing between the NWP propagation and the electric field evolution of the laser pulse defines the final electron localization as each radiative transition occurs at a different time. Therefore, depending on the dissociation pathways involved in each channel, different phase dependences are observed. Although our theoretical model allows to reproduce qualitatively the phase relationship between the control channels, it cannot quantitatively describe the exact contributions of each pathway to the NWP involved in the experiment. Efforts on elucidating the exact distribution (amplitude and initial phase of each vibrational state) of the initial wavepacket after ionization would allow to learn more about this aspect. Very recent advancements concerning this task has demonstrated that such a wavepacket in  $\text{H}_2^+$  prepared by an attosecond pulse train can take up to 1 fs to form with each vibrational wavefunction having a different initial phase [178]. Comparing our results to previous single pulse control experiments, we observe the following: in the first experimental demonstration of electron localization in  $\text{D}_2^+$  by Kling *et al.* [173], only the recollision channel could be controlled efficiently. This is because 5 fs, 800 nm CEP stabilized pulses at an intensity of  $1 \times 10^{14} \text{ W cm}^{-2}$  seem to be not capable to induce the required population transfers between the  $\sigma_g$  and  $\sigma_u$  states that lead to the control of NIR induced dissociation. The internuclear distances where these transfers occur are reached at times where the intensity of the pulse becomes too low (red and blue arrows in figure 4.3). To observe any asymmetry with 800 nm pulses, one needs to either increase their intensity at larger internuclear distances (longer time) and/or study a faster dynamic such as  $\text{H}_2^+$  dissociation in order to reach the coupling region more rapidly. These solutions were employed by Kremer *et al.* and Xu *et al.* [174, 175], who could observe, for example, asymmetries involving BS for  $\text{H}_2^+$  dissociations, both using 6 fs NIR pulse at respective intensities of  $4.4 \times 10^{14}$  and  $6 \times 10^{14} \text{ W cm}^{-2}$ . To control the slower  $\text{D}_2^+$  dissociation dynamics, the pulse duration can be increased to reach higher intensities at longer time. A first option is to use longer wavelengths, where longer CEP stabilized pulses are accessible. Znakovskaya *et al.* used MIR 2100 nm pulses to efficiently control dissociation involving BS in  $\text{D}_2^+$  [176]. However, in all the previously mentioned CEP experiments, the maximal achieved asymmetry was limited to 40% for NIR/MIR induced dissociation [175]. As an alternative to MIR CEP stable pulses, the pulse duration can also be extended by using a two-color laser field. Our results confirm that this experimentally convenient technique is capable to efficiently localize the electronic density in molecules, offering stronger asymmetries for most of the dissociation channels (up to 60% for MIR induced dissociation in  $\text{D}_2^+$  and 65% for RCE in  $\text{H}_2^+$

). Indeed, this increase of asymmetry using a two-color field in the NIR (800/400 nm) was also observed by Ray *et al.* [172], but applying the technique in the MIR opens up the control of an additional dissociation channel. While MIR CEP stable pulses do not provide  $2\omega$  photons to control this channel, NIR two-color pulses create ions with energies very close to the CREI region centered at 2.5 eV, which has a very high probability compared to three-photon absorption. The signal generated by this process –CREI– thus prevent the observation of any control in the ‘3-photons region’ when using a two-color 800/400 nm field.

## Conclusion

In conclusion, we used a MIR two-color (1800 and 900 nm) laser field to control the electron localization in D<sub>2</sub> and H<sub>2</sub> dissociative ionization, which led for the first time to the simultaneous control of four dissociation channels. Our theoretical model based on the TDSE reproduces the experiment with good agreement, giving insight into the RCE and MIR induced dissociation mechanisms involved. The control of electron localization for MIR induced dissociation was interpreted from interferences between processes involving the net absorption of  $n$  and  $n + 1$  photon(s), such as BS ( $n = 1$ ), ATD ( $n = 2$ ) and three-photon dissociation ( $n = 3$ ). The importance of the initial vibrational distribution on the electron localization has also been demonstrated, showing that for the presented experiment this distribution is different from a FC one and involves fewer vibrational states. Our experiment, in addition to a similar one performed in the NIR, confirms that the use of a two-color laser field is more efficient to localize the electronic density in molecules. From this technique, which is easier to implement experimentally, the level of control is stronger than what was obtained by using CEP stable pulses as a control tool. To the best of our knowledge, we measured the strongest asymmetry reported to date both for MIR (60%) and RCE (65%) induced dissociations. Finally, all the previously mentioned experiments (including ours) were limited to the manipulation of the initial NWP and relative population via radiative coupling between the two electronic states of different parity. Recently, theoretical efforts have demonstrated that the temporal overlap between these wavepackets can be strongly influenced by quasistatic fields as molecular potentials get Stark shifted [196] and the use of a terahertz field to enhance this temporal overlap was proposed [197]. It is thought that the addition of a terahertz field to previous control scheme would be of strong benefit to the control of electron localization in molecules.

## Acknowledgment

We thank Dr Catherine Lefebvre for constructive discussions and acknowledge research funding from NSERC (Natural Sciences and Engineering Research Council of Canada), FRQNT (Fonds de recherche du Québec—Nature et technologies), Canada Foundation for Innovation—Major Science Initiatives, NanoQuébec and Ministère du développement économique, de l’Innovation et de

l'exportation (MDEIE) du Québec. IVL was supported by Australian Research Council via Discovery Project DP11010101894. XMT was supported by Grant-in-Aid for Scientific Researches C24540421 from the Japanese Society for the Promotion of Science and HAPACS Project for advanced interdisciplinary computational sciences by exa-scale computing technology. ASA acknowledges support from the American University of Sharjah through FRG grant. VW and SB express their gratitude for financial support from NSERC and all authors are grateful for the efficient and dedicated work done by Antoine Laramée and Philippe Lassonde in ALLS.

## Chapter 5

# Strong-field ionization of lithium niobate

The work presented in the previous chapter provides an example for the application of intense 1800 nm laser pulses for the control of photo-induced molecular dynamics. We demonstrated the advantages of employing a 1800 nm laser field over a near-infrared one (800 nm) for controlling the dissociative ionization of molecular hydrogen.

With the continuous development of parametric sources [198], the availability of such intense pulses at wavelength above 800 nm also opens new perspectives for controlling dynamics in the solid state. With sufficient intensity, such pulses can photoionize semiconductor and dielectric materials with photon energies that are well below their bandgap energy, and the study of this particular type of light-matter interaction – strong-field ionization in solids – has gained a broad interest. Notably, the concept of HHG in atomic and molecular gases was extended to solids [199, 200], opening a research topic that is rapidly growing. Several laser micro-machining techniques, such as femtosecond laser-ablation, also rely on strong-field ionization of materials [201, 202]. However, this fundamental process – also the first step to HHG – is still not fully understood and its complexity arises as it depends not only on the laser pulse parameters but also strongly on a variety of materials properties.

In the next two articles, we studied the strong-field ionization of lithium niobate ( $\text{LiNbO}_3$ ), one of the most spread material in photonics due to its unique properties. In article V, we characterized the strong-field ionization response of  $\text{LiNbO}_3$  to the laser polarization orientation of 1800 nm pulses. The results presented in this article were obtained in preparation to our main experiment, presented in article VI. In the latter, we show how the spontaneous polarization of the ferroelectric material impacts on its ionization rate and exploit this property to control the generation of free carriers in the conduction band.

The necessary background for articles V and VI is discussed in sections 5.1-5.4. Strong-field ionization is described in 5.1. A brief summary on LiNbO<sub>3</sub> and its characteristic properties is presented in section 5.2. Since the experimental results were obtained through laser-induced ablation (LIA) measurements, details on this process are given in section 5.3. Finally, the interpretation of the results are supported by numerical simulation, combining first principles calculations and a two-band model for which the semiconductor Bloch equations (SBEs) are solved. While details on the SBEs can be found in the supplement material of article VI (see appendix III), a brief description of density functional theory is provided in section 5.4.

## 5.1 Strong-field ionization in non-centrosymmetric systems

With femtosecond laser pulses reaching intensities on the order of  $10^{13}$ - $10^{14}$  W/cm<sup>2</sup>, it is possible to ionize atoms, molecules and solids in the strong-field regime. To describe strong-field ionization, the Keldysh theory [71] is particularly useful to distinguish between two ionization regimes according to the Keldysh parameter  $\gamma$ ,

$$\gamma = \frac{\omega\sqrt{2mI_p}}{eE} = \sqrt{\frac{I_p}{2U_p}} \quad (5.1)$$

where  $\omega$ ,  $m$ ,  $I_p$ ,  $e$ ,  $E$  and  $U_p$  are the laser angular frequency, electron mass, ionization potential, elementary charge, field strength and ponderomotive energy<sup>1</sup>. For  $\gamma \gg 1$ , ionization is in the multiphoton regime. As shown on the left side of Fig. 5.1, several photons are required in order to reach the ionization potential. In this regime, above-threshold ionization (ATI) was observed for the first time in 1979 by Agostini *et al.* [203] that identified photoelectron spectra with more than one peak in the ionization of xenon atoms, and with an energy spacing corresponding to the photon energy.

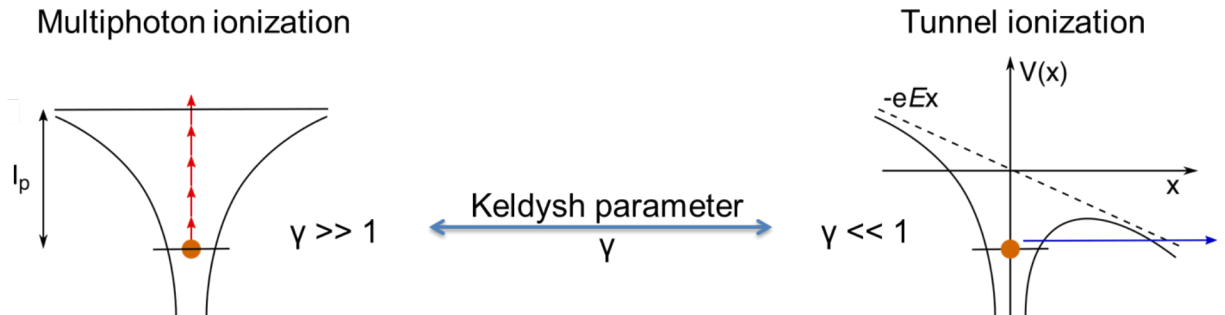


**Figure 5.1 – Strong-field ionization regimes according to the Keldysh parameter  $\gamma$**

<sup>1</sup>In solids,  $I_p$  and  $m$  are replaced by the bandgap energy  $E_g$  and an electron effective mass  $m^*$ . The Keldysh parameter also differs by a factor of  $1/\sqrt{2}$  ( $\gamma = \omega\sqrt{E_g m^*}/eE$ ).

When  $\gamma \ll 1$ , ionization is described by tunneling. In Fig. 5.1 (right), the atomic potential is sufficiently lowered by the electric field for tunneling to occur. In this limit, the ADK (Ammosov-Delone-Krenov) model is often used to describe the ionization rate  $w_{ADK}$ ,

$$w_{ADK}(E) = C_{n^*l^*}^2 G_{l,m} I_p \left( \frac{2(2I_p)^{\frac{3}{2}}}{E} \right)^{2n^* - |m| - 1} \times \exp \left( -\frac{2}{3} \frac{(2I_p)^{\frac{3}{2}}}{E} \right) \quad (5.2)$$

where  $C_{n^*l^*}$  and  $G_{l,m}$  are coefficients that depend on the quantum numbers  $n, l$  and  $m$ . The last term of Eq. 5.2 shows that the ionization rate has an exponential dependence on both the ionization potential ( $I_p$ ) and the electric field strength ( $E$ ), making tunneling a very sensitive probe to small variation of these parameters. In the context of non-centrosymmetric systems, the work presented in this chapter was motivated by previous studies of strong-field ionization in asymmetric molecules such as HCl by Akagi *et al.* (2009) [204] and OCS by Holmegaard *et al.* (2010) [205]. These molecules are characterized by a permanent polarization as shown for OCS in Fig. 5.2(a). In the aforementioned studies, photoelectron angular distributions were acquired in the molecular frame upon ionization. It was observed that the electron yield was enhanced when the laser electric field was pointing in the same direction as for the permanent dipole vector of the molecule. With the objective of bridging a gap between the gas phase and the solid state, we addressed the question whether it is possible to observe such a preferential ionization direction during the strong-field ionization of asymmetric materials. Lithium niobate was selected due to its large spontaneous polarization  $P_s$  along its  $c$  axis (Fig. 5.2b).

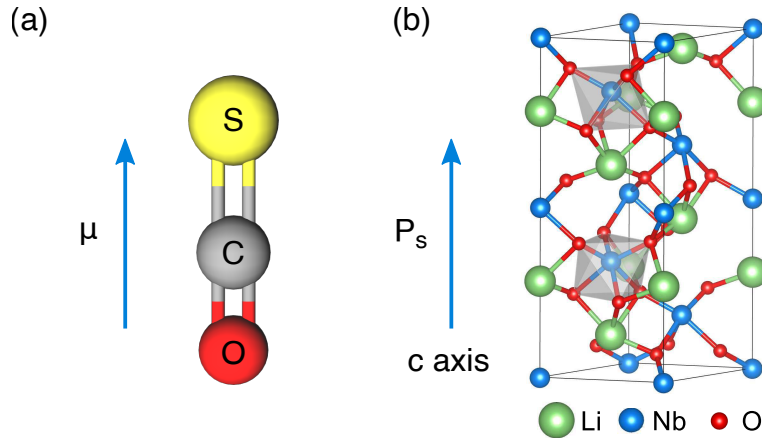


**Figure 5.2 – Non-centrosymmetric systems characterized by a permanent polarization. (a) Carbonyl sulfide. (b) Lithium niobate.**

## 5.2 LiNbO<sub>3</sub> and its spontaneous polarization

Lithium niobate (previously known as lithium colombite – LiCbO<sub>3</sub>) is a purely synthetic material and cannot be found in nature. Developed at Bell Laboratories, it was discovered to be ferroelectric in 1949 [206]. After several years to develop a method to obtain large single crystals, the properties of the material have been extensively studied. In 1964, a first characterization showed that LiNbO<sub>3</sub> exhibits a large birefringence [207]. Further investigations demonstrated that the material possess strong electro-optic, piezoelectric and photoelastic properties (for a review see [208]).

The numerous properties of lithium niobate justify why it is so widely employed, particularly in optical systems since the material is typically transparent between 370 and 5000 nm. It is a common component in surface acoustic wave (SAW) devices for instance. LiNbO<sub>3</sub> is also used for nonlinear applications such as Pockels cells in laser systems or for high efficiency parametric processes through periodically poled lithium niobate (PPLN) crystals. In high power laser technologies, doped LiNbO<sub>3</sub> is also convenient as the presence of dopants increases the damage threshold of the material.

Figure 5.3 illustrates a simplification of a centrosymmetric (a) and a non-centrosymmetric (b) crystal structure<sup>2</sup>. In non-centrosymmetric materials such as LiNbO<sub>3</sub>, the spatial distribution of the ions within the crystal structure is the origin of an intrinsic spontaneous polarization ( $P_s$ ), i.e. a nonzero dipole moment per unit of volume ( $C^*m^*m^{-3} = C^*m^{-2}$ ). The contribution of  $P_s$  in the strong-field ionization of LiNbO<sub>3</sub> is the subject of article VI.

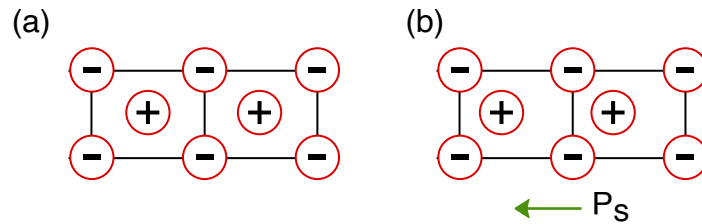


**Figure 5.3** – Sketch of centrosymmetric (a) and non-centrosymmetric crystal structures (b). The later is characterized by a spontaneous polarization  $P_s$  due to the asymmetric distribution of positive ions.

## 5.3 Laser-induced ablation

Laser-induced ablation takes place in an extreme case of strong-field ionization. Its mechanism in dielectrics depends strongly on the field intensity and pulse duration. In all cases, the conduction band of the initially transparent material is populated by free electrons, leading to plasma formation. Once the electron density in the conduction band is sufficiently high for the laser energy to be absorbed by the plasma and melt the material, alteration of the surface (damage) or crater formation

<sup>2</sup>A detailed description of the structure of LiNbO<sub>3</sub> is presented in article V.

(ablation) can occur and is visible by microscopy [209]. For nanosecond to picosecond pulses, avalanche ionization is the main contributor to the plasma generation [210]. The pulse energy is then transferred to the lattice via thermal diffusion, ablating the material within the pulse duration [211]. In the femtosecond regime, this slow thermal transfer is decoupled from the fast ‘shocklike’ deposition of energy by the laser pulse that is heating up the electrons. In this case, SFI by itself can be sufficient to reach the electron density required for inducing material ablation [212], taking place within a few hundred of femtoseconds up to several picoseconds after the laser pulse [213]. Since less energy is deposited into the material with femtosecond pulses, the ablated region is better-defined and strongly reproducible from pulse to pulse [214]. For this reason, femtosecond laser-induced ablation has become a common method for high-resolution material processing, and is also a powerful tool to probe strong-field ionization in materials.

## 5.4 Density functional theory

In Wanie *et al.* 2016 [177], we studied the molecular hydrogen ion. For this one electron, three dimensional problem, we could provide an exact solution to the time-dependent Schrödinger equation (TDSE) to support the experimental results. For larger systems, the dimensionality of the problem  $D$  increases rapidly with the number of electrons  $N$  ( $D = 3N$ ), requiring significant computational efforts. More importantly, the presence of electronic correlations in multielectron systems prevents the obtention of an exact solution to the Schrödinger equation. In the case of materials such as  $\text{LiNbO}_3$  (Articles V and VI) or large molecular systems such as adenine (Article VII), approximations must hence be employed and an approach to solve the corresponding many body Schrödinger equation is the density functional theory.

DFT is employed within the Born-Oppenheimer approximation, where nuclear and electronic degrees of freedom are treated separately. This is justified by the significant mass difference between nuclei and electrons, resulting in motions that respectively occur on different timescales. For a static configuration of atoms in a material – the unit cell – it is possible to calculate the system properties if one knows its electron density  $n(r)$ . DFT aims at converging towards the electron density for which the energy of the system is minimized, by solving the many body Schrödinger equation in an iterative manner.

To simplify the many body problem, the wavefunction describing the interacting electrons in a system can be replaced by a product of wavefunctions describing non-interacting electrons. In this way, Kohn and Sham have demonstrated a scheme in which the electron density of a many body system, including an approximation of the exchange-correlation effects, can be retrieved [215].

To do so, an initial electron density must be guessed to solve a set of one electron Schrödinger equations:

$$\left[ -\frac{\hbar}{2m} \nabla^2 + V(r) + V_H(r) + V_{xc}(r) \right] \psi_i(r) = \epsilon_i(r) \psi_i \quad (5.3)$$

where the Hamiltonian inside the brackets contains four terms. The first term is the kinetic energy operator. The second and third terms describe the classical electron-ion and electron-electron Coulomb interactions. Finally, the quantum effects related to the spin interactions between electrons are described by an exchange-correlation functional  $V_{xc}(r)$  that must be approximated.

In the self-consistent cycle proposed by Kohn-Sham, the wavefunctions obtained by solving Eqs. 5.3 are used to calculate their corresponding electron density. This resulting  $n(r)$  is employed for a new trial to solve Eqs. 5.3. This iterative process is performed until the retrieved  $n(r)$  is the same as the one employed to solve the set of equations, which is the self-consistent criterion.

## 5.5 Summaries for articles V and VI

In articles V and VI, we perform laser ablation measurements to study the strong-field ionization response of lithium niobate crystals. The experimental setup, not shown in the articles, is briefly discussed here (Fig. 5.4).

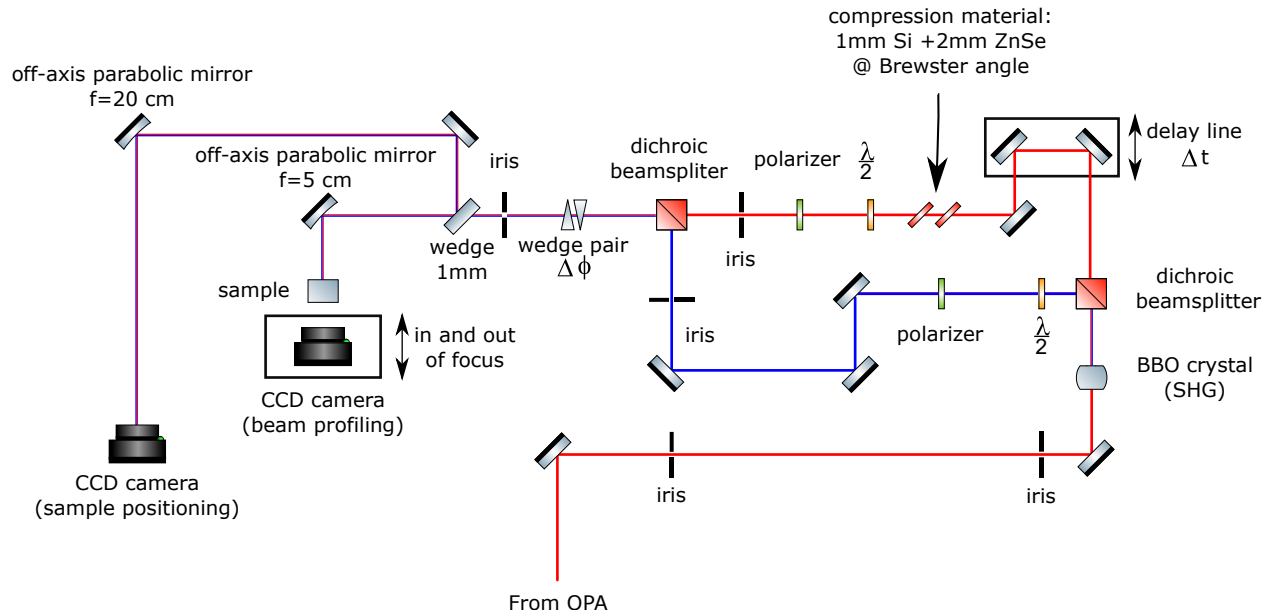


Figure 5.4 – Experimental setup for the laser ablation measurements

A 1800-nm beam is obtained from an optical parametric amplifier. A BBO crystal is used for second harmonic generation to obtain a 900-nm beam. A dichroic beamsplitter separates the two frequency components. The pulse energy for each beam is tuned with a pair of waveplate and polarizer. A delay line in the path of the 1800-nm beam allows to temporally overlap the pulses that are recombined using a second dichroic beamsplitter. A wedge pair allows to adjust the relative phase between the 1800 and 900-nm fields. The beams are then focused by an off-axis parabolic mirror ( $f = 5$  cm) in order to ablate the surface of the material. A motor stage rapidly translates the sample and provides single-shot measurements. When removing the sample, a CCD camera can be placed at the focus position to characterize and adjust the size of each beams.

For a reproducible positioning of the sample surface at the focus position and to ensure that the surface is parallel to the motor stage translation axis for the measurements, an imaging system was also built. The Fresnel reflection from the sample was collected by a 1-mm glass wedge and focused into a second CCD camera using a  $f = 20$  cm parabolic mirror. By monitoring the beam with this configuration, it is possible to adjust the parallelism of the crystal surface.

In a first experiment (article V), ablation is realized with the 1800-nm field only. The ablated area is evaluated as a function of the relative angle between the laser polarization orientation and the  $c$  axis of the crystal. The measurements are performed to compare  $x$ -cut and  $y$ -cut samples (Fig. 5.6). By comparing the experimental results (Fig. 5.7) with an ionization model based on the semiconductor Bloch equations (Fig. 5.11), we demonstrate that the ablation method, through tunnel ionization, can distinguish between each crystal cut having their own symmetry features. Density functional theory calculations (Figs. 5.8-5.10) allow to identify the Nb-O bonds of the material to be the main contributor to the band structure and to the ionization of the material. Further comparison with the experimental results shows that the ablation method provides a high-contrast observable to identify these Nb-O bonds.

In a second experiment (article VI), laser pulses combining both the 1800 and 900-nm fields are used to evaluate ablation as a function of the relative two-color phase. The measurements are performed at a single laser polarization orientation, chosen to be either parallel or anti-parallel to the  $c$  axis of  $\text{LiNbO}_3$  and therefore to the spontaneous polarization of the material. The main result of the experiment (Fig. 5.7) is a large modulation with a periodicity that identifies a contribution from the spontaneous polarization in the strong-field ionization of  $\text{LiNbO}_3$ . The role of the spontaneous polarization was clarified by simulating the ionization process with the semiconductor Bloch equations (Fig. 5.15). The calculations show that a dynamical Stark effect during the ionization process, induced by the spontaneous polarization of the material, allows to interpret qualitatively the experimental observations.

The work presented in articles V and VI demonstrate that laser-induced ablation provides a large contrast observable to study the strong-field ionization of materials. Particularly, the results obtained in article VI consist in a first proof-of-principle demonstrating permanent polarization

effects in the ionization of solid systems, in analogy to what has been observed in asymmetric gas molecules. This opens new perspectives in strong-field physics, as it may offer an additional degree of freedom for the control of HHG in ferroelectric materials. Moreover, while the experimental data presented in article VI (Fig. 5.13) have been chosen with the intention to show a clear phase offset between the curves, Fig. 5.5 also shows that better-defined modulations can be obtained. The phase sensitivity of the ablation technique presented here could thus potentially be used to identify the carrier-envelope phase of few-cycle pulses covering mid- or far-infrared spectral ranges where all-optical techniques may be difficult to implement.

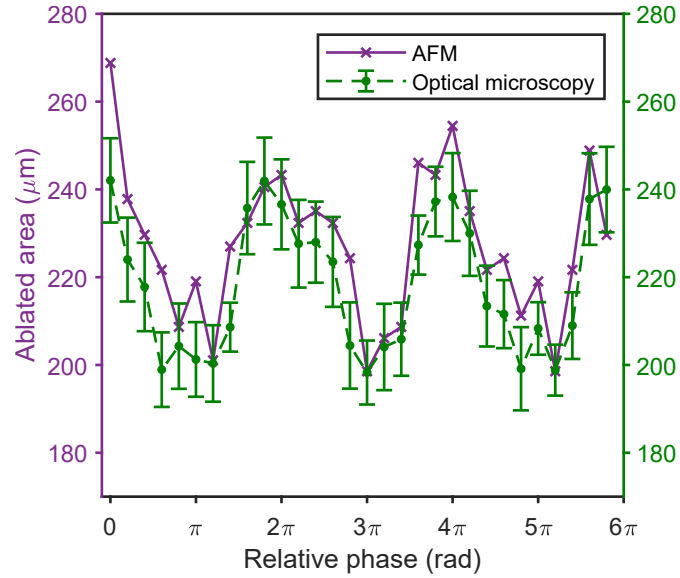


**Figure 5.5** – Ablated area as a function of the relative two-color phase evaluated by atomic force microscopy measurements (purple crosses). Due to the significant time consumption of the technique, each data point corresponds to a single analyzed crater and no averaging was performed. The results are compared to optical microscopy measurements (green dots), with a standard deviation shown over 10 ablated craters.

## 5.6 Article V – Laser polarization dependence of strong-field ionization in lithium niobate

Vincent Wanie,<sup>1,2,3</sup> Tian-Jiao Shao,<sup>4,5</sup> Philippe Lassonde,<sup>1</sup> Francesca Calegari,<sup>2,3,6</sup> François Vidal,<sup>1</sup> Heide Ibrahim,<sup>1</sup> Xue-Bin Bian,<sup>4</sup> and François Légaré<sup>1</sup>

<sup>1</sup>Centre Énergie Matériaux Télécommunications, Institut National de la Recherche Scientifique, Varennes, Québec J3X 1S2, Canada

<sup>2</sup>Center for Free-Electron Laser Science, DESY, Hamburg 22607, Germany

<sup>3</sup>Institute for Photonics and Nanotechnologies CNR-IFN, Milano 20133, Italy

<sup>4</sup>State Key Laboratory of Magnetic Resonance and Atomic and Molecular Physics, Wuhan Institute of Physics and Mathematics, Innovation Academy for Precision Measurement Science and Technology, Chinese Academy of Sciences, Wuhan 430071, China

<sup>5</sup>School of Physics, University of Chinese Academy of Sciences, Beijing 100049, China

<sup>6</sup>Physics Department, Universität Hamburg,, Hamburg 22761, Germany

Physical Review B

Received 6 April 2020

Accepted 9 June 2020

Published 26 June 2020

doi:10.1103/PhysRevB.101.214311

V.W. and P.L. built the ablation setup and performed the measurements. V.W., P.L. and H.I. analyzed the data. T.J.S. and X.B.B. provided the theoretical support. F.C. F.V. and F.L. supervised the experiments. V.W. wrote the manuscript with the help of all co-authors.

## Abstract

Laser micromachining techniques using femtosecond laser pulses are employed for the fabrication of a wide range of devices, from optical waveguides and fiber Bragg gratings to microfluidic systems. In this perspective, it is important to characterize how transparent materials respond to the high-intensity laser field in order to fully understand and control the strong-field ionization process at the core of such techniques. Here, we characterize the laser polarization dependence of  $y$ -cut and  $x$ -cut ferroelectric lithium niobate ( $\text{LiNbO}_3$ ) upon ionization. Using linearly polarized 1800-nm femtosecond pulses, we perform single-shot laser-induced ablation measurements to obtain a macroscopic observable with a large contrast compared to all-optical techniques. In the tunnel ionization regime, the crystal orientation can be correlated with the structural symmetry/asymmetry of the material. This is revealed through a variation of the ablated area when the laser polarization is rotated with respect to the  $c$  axis of the crystal. It is further found that ablation is more pronounced when the laser polarization is oriented towards angular regions containing Nb-O bonds of the unit cell, identifying the main chemical bonds contributing to the ionization of the material. The experimental results are supported by numerical simulations based on a two-band model for  $\text{LiNbO}_3$ .

## Introduction

Laser micromachining techniques such as femtosecond nonlinear lithography and laser-induced ablation (LIA) have proven to be of great use for high-resolution material processing [201] and are employed for a variety of applications including the fabrication of microfluidic devices and photonic components [216, 202]. Particularly in photonics, lithium niobate ( $\text{LiNbO}_3$ ) is an attractive material due to its strong piezoelectric, electro-optic, acousto-optic, and nonlinear properties. Indeed, the combination of such properties within the same substrate makes it very convenient, as it can fulfill several functions in the realization of integrated optical devices. For instance, recent efforts have been developed to produce high-efficiency waveguide amplifiers/lasers through doped  $\text{LiNbO}_3$  [217, 218]. In addition, the fabrication of Y-branch optical waveguides in  $\text{LiNbO}_3$ , based solely on laser-micromachining, has also been demonstrated for applications in the midinfrared spectral range ( $4\ \mu\text{m}$ ) [219]. In this case, the laser-ablated regions were created by carefully choosing the femtosecond pulse parameters. In fact, the level of precision achieved for a specific material is limited by our understanding of the interaction between the strong laser field and the sample that undergoes ionization [214]. On the one hand, this interaction critically depends on the material's properties. The role of the spontaneous polarization in the strong-field ionization of ferroelectric  $\text{LiNbO}_3$  was recently highlighted through LIA measurements [220]. On the other hand, laser pulse characteristics such as the intensity, duration, wavelength, spatial energy distribution, and polarization state are of significant importance [221, 222, 223, 224, 225]. Careful characterization of these parameters is thus necessary to enhance the precision of laser micromachining techniques.

For linearly polarized femtosecond pulses, in particular, the orientation of the polarization plane with respect to the crystal axes has shown peculiar effects. From LIA measurements, Li *et al.* reported how the incident polarization angle affects the ionization of cubic crystals with increasing bandgap energy [225]. At proper fluences, chosen to minimize the contribution of impact ionization [210], the fourfold rotational symmetry of the samples was reflected in the modulation of the ablated area and interpreted as a result of an orientation-dependent effective electron mass  $m_e$ . Based on a similar interpretation, transmission measurements by Gertsvolf *et al.* [224] and Golin *et al.* [226] have also demonstrated the critical role of  $m_e$  for the generation of free carriers in the conduction band of materials. In the aforementioned works, the crystal was always oriented to reveal the axis of highest symmetry ( $n$ -fold rotation), i.e., the  $c$  axis ( $z$ -cut) for LiNbO<sub>3</sub> crystals. Other crystal orientations can exhibit more subtle symmetry features that can be difficult to observe. The LIA technique chosen here, together with our theoretical support, is, however, capable of addressing these subtle changes due to crystal symmetries.

In this article, we study the strong-field ionization response of  $y$ -cut and  $x$ -cut lithium niobate (LiNbO<sub>3</sub>) to femtosecond laser pulses when rotating the incident linear polarization. We use LIA in the tunneling regime to identify characteristic features for each crystal cut, notably the absence or presence of a mirror symmetry within the crystal plane probed by the laser field. Moreover, ablation is found to be most efficient for orientations where the laser polarization is within those angular regions containing the Nb-O bonds of the unit cell. First principles calculations and numerical simulations based on a two-band model show how the Nb-O bonds contribute almost exclusively to the band structure of the material and to its conduction-band population during the interaction with the laser field.

## Experiments

For the experiments at the ALLS infrastructure (Canada), a white-light-seeded optical parametric amplifier (TOPAS; Light conversion) was pumped with a 2.5-kHz titanium-doped sapphire (KM-Labs) laser and delivered 70-fs pulses centered at 1800 nm (0.69 eV). To ensure that tunneling is the main ionization channel during the LIA process, this photon energy was chosen as it is well below the experimentally obtained 3.78-eV bandgap energy for LiNbO<sub>3</sub> [227]. Higher-bandgap materials such as quartz ( $\sim 9$  eV) can be studied with conventional 800-nm (1.55-eV) laser sources. The pulse duration is another critical parameter that determines the ablation regime. While the use of picosecond pulses can alter the reproducibility of ablation due to significant heating effects of the crystal lattice, those are minimized with laser pulses of a few tens of femtoseconds and hence lead to a higher level of precision [228, 214]. The beam was spatially filtered and focused with an  $f=50$  mm off-axis parabolic mirror. Its diameter at focus ( $1/e^2$  of intensity) was evaluated to 39  $\mu\text{m}$  from the fits of images acquired with a CCD camera. Single-shot exposition onto the sample surface was achieved using a fast ceramic motor translation stage (Nanomotion Ltd.) moving in the direction

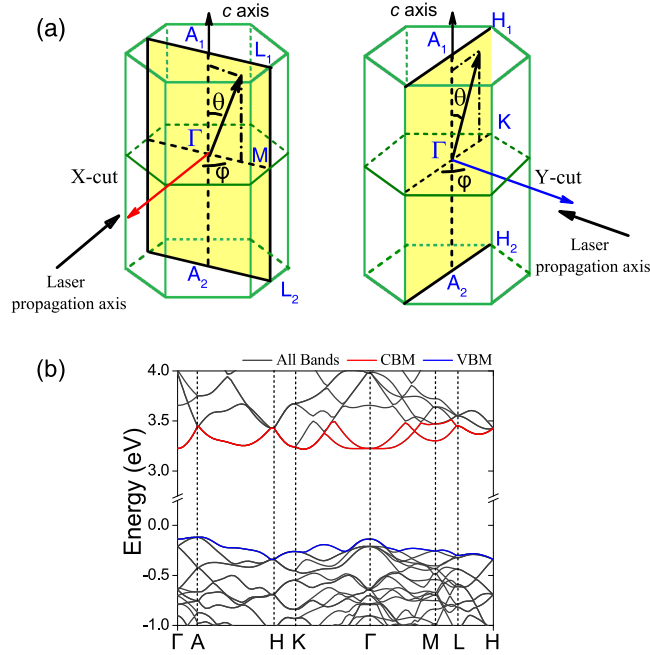


**Figure 5.6** – (a) The laser polarization is rotated by the angle  $\theta$  with respect to the  $c$  axis of LiNbO<sub>3</sub> for ablating both  $x$ -cut (left) and  $y$ -cut (right) samples with an intensity of  $2.3 \times 10^{13}$  W/cm<sup>2</sup>. Shown are the  $\Gamma$ -A-L-M and  $\Gamma$ -A-H-K planes of the Brillouin zone, corresponding, respectively, to  $x$ -cut and  $y$ -cut. (b) DFT- calculated band structure with valence-band maximum (VBM; blue curve) and conduction-band minimum (CBM; red curve).

parallel to the crystal surface. An imaging system exploiting the Fresnel back reflection from the sample surface was built and employed to precisely adjust the crystal surface position at the laser focus and the surface parallelism with respect to the translation axis. After the ablation series was completed, images of the ablated craters were acquired using an optical microscope (Nikon Eclipse) with a 100x objective. Their area was evaluated by a fitting routine and the standard deviation was defined over 10 single-shot ablated craters per orientation. A sketch of the relevant crystal planes is shown in Fig. 5.6(a). The linear polarization of the laser pulse is rotated at several incident angles  $\theta$  relative to the  $c$  axis of LiNbO<sub>3</sub> and the beam is focused onto the surface to ablate the material. The fluence is set just above the threshold for ablation and the corresponding intensity, taking into account reflective losses, ensures that ionization is described by tunneling with the Keldysh parameter  $\gamma = 0.47$ . An angular scan is performed for  $y$ -cut and  $x$ -cut crystals, corresponding, respectively, to the  $\Gamma$ -A-H-K and  $\Gamma$ -A-L-M planes of the Brillouin zone. The band structure of LiNbO<sub>3</sub> is shown in Fig. 5.6(b).

## Results and discussion

### Angle-resolved LIA measurements

The experimental ablation results are presented in Fig. 5.7, showing the ablated area of the material as a function of the laser polarization angle  $\theta$ . We first consider the most symmetric case in Fig. 5.7(a), corresponding to the  $y$ -cut crystal ablated at an intensity of  $2.3 \times 10^{13}$  W/cm<sup>2</sup>. From 0 to 360° the ablation pattern shows a symmetric behavior with respect to 180°, identified by the vertical dashed blue line and delimiting the center of the angular scan. Furthermore, each half of the scan shows a characteristic minimum at about 90° (270°) indicated by the vertical dashed yellow lines. Also shown are two symmetrically distributed maxima, at 40° (220°) and 140° (320°), i.e., 50° away from the minimum.

In Fig. 5.7(b), the orange squares show the polarization dependence of the  $x$ -cut crystal for the same laser intensity. In this case, an asymmetric structure is observed with respect to a sharp and reproducible minimum at about 90°. In its vicinity, the ablated area drops abruptly on the left-hand side (shaded area) and rises more smoothly on the right-hand side. This asymmetric structure is also reproduced when the laser intensity is reduced to  $1.9 \times 10^{13}$  W/cm<sup>2</sup> (black triangles). For visualization, the initial angular range from -15° to 195° has been shifted by 180° and is displayed from 165° to 375°. Noteworthily, the polarization dependence at this reduced intensity allows us to conveniently switch between operation above and operation below the ablation threshold. Indeed, it was possible to completely prevent ablation for the angle  $\theta = 274^\circ$ .

For all measurements presented in Fig. 5.7, it is worth noting the significant variation of the ablated area provided by LIA, and, thus, the very high measurement contrast. Depending on the experimental intensity, the observed contrast ranges from 41% ( $y$ -cut, high intensity) to 100% ( $x$ -cut, low intensity) with respect to the maximal value. Such variations have not been demonstrated with all-optical techniques, where the typical contrast is in the range of a few percent [224, 226].

### Crystal structure and symmetry

The first element to explain the difference in angular response between the  $x$ -cut and the  $y$ -cut is found by looking at the symmetry of the crystal. LiNbO<sub>3</sub> belongs to the hexagonal crystal family and is described by a trigonal system with a  $C3v$  point group (space group  $R3c$ ). A two-dimensional representation (top view) of the hexagonal structure is shown in Fig. 5.8(a). The trigonal system is characterized by a three-fold rotation axis and the symmetry elements of the  $C3v$  point group include three mirror planes that are located 60° from each other, identified by dashed black and blue lines. In our work, the definition of axes follows the same standard convention as in [208] and [229], thus the  $y$ -axis (blue arrow) in Fig. 5.8(b) lies in a plane of mirror symmetry, which is not the case for the  $x$ -axis (red arrow). For this reason, the left- and right-hand sides of the angular scan

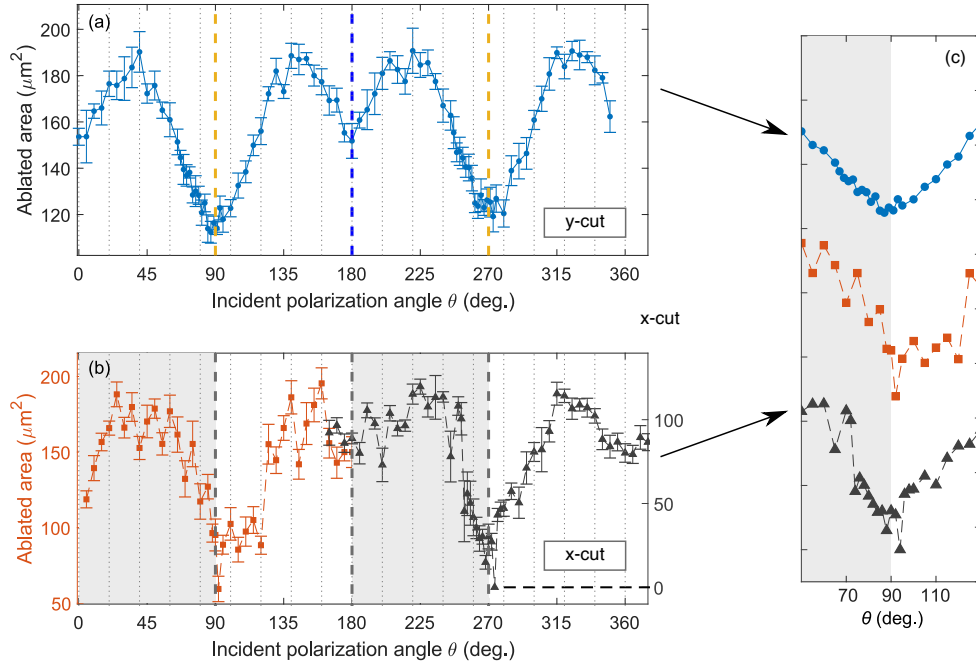


**Figure 5.7** – Single-shot ablated area of  $\text{LiNbO}_3$  as a function of the incident laser polarization angle  $\theta$ . Each data point is averaged over 10 measurements and the standard deviation is shown. (a) The blue curve displayed from  $0$  to  $355^\circ$  corresponds to the *y*-cut ablated at an intensity of  $2.3 \times 10^{13} \text{ W/cm}^2$ . Each half of the angular scan on either side of the central dashed blue line at  $180^\circ$  exhibits the same polarization dependence. Also, a symmetric distribution is observed on both sides of the minima, which are identified by the dashed yellow lines at  $90^\circ$  and  $270^\circ$ . The ablated area is maximal at  $50^\circ$  apart from each minimum. (b) Orange squares show the results for an *x*-cut crystal ablated at the same laser intensity. An asymmetric structure is observed in the region where the ablated area is the smallest, characterized by a sharp decrease on the left-hand side (shaded area) and a smooth rise on the right-hand side. The black triangles from  $165^\circ$  to  $375^\circ$  show that this asymmetric feature is reproduced at a lower intensity ( $1.9 \times 10^{13} \text{ W/cm}^2$ ). In this case, ablation is completely suppressed at  $\theta = 274^\circ$  and no ablated area was observed. (c) Inset comparing each curve in the region where ablation is minimal.

for the *y*-cut [Fig. 5.7(a)] show symmetric behavior with respect to  $180^\circ$  since the sample surface intersects perpendicularly a mirror plane. Furthermore, Figs. 5.8(c) and 3(d) display a front view of the hexagonal structure of  $\text{LiNbO}_3$  for each crystal cut. For the *y*-cut [Fig. 5.8(d)], in addition to the left-right symmetry (dashed blue line) discussed above, the horizontal dashed yellow line allows us to visualize an up-down reflection symmetry for the niobium atoms that is absent for the *x*-cut. As described in the paragraph below, these Nb atoms being one of the main contributors to the crystal band structure, their spatial distribution within the unit cell also dictates the polarization dependence on the ionization of the material. For this reason symmetric behavior with respect to  $90^\circ$  ( $270^\circ$ ) is shown in Fig. 5.7(a), which is absent for the *x*-cut in Fig. 5.7(b).

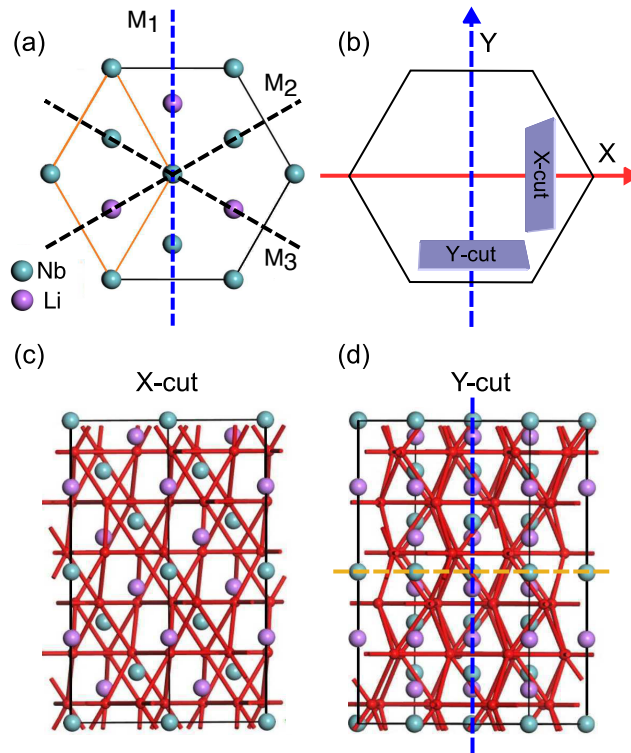


**Figure 5.8** – (a) Top view of the hexagonal structure of  $\text{LiNbO}_3$ . The edges of the conventional hexagonal unit cell are shown in orange and the dashed lines ( $M_1$ - $M_3$ ) correspond to the characteristic mirror planes of the  $C3v$  point group. (b) Illustration of the  $x$ - and  $y$ -cuts relative to the hexagonal structure. The polished surface of the  $y$ -cut sample intersects perpendicularly a mirror plane that is absent for the  $x$ -cut. (c,d) Front view of the three-dimensional structure for each cut. For the  $y$ -cut, the atomic distribution displays a left-right symmetry (dashed blue line), as well as an up-down symmetry for the niobium atoms. This up-down symmetry, which is not present in the  $x$ -cut, is displayed as a horizontal dashed yellow line as a guide for the eye to compare both cuts. The dashed blue lines in (a), (b), and (d) correspond to the mirror plane shown in Fig. 5.7(a).

### Density of states

Additional insight about the role of the structure of  $\text{LiNbO}_3$  in the angular dependence of strong-field ionization can be gained from the calculated partial and total density of states (DOS) of the material shown in Fig. 5.9. Below the Fermi energy (vertical dashed pink line), the oxygen  $2p$  orbitals [Fig. 5.9(a)] define the valence band of the crystal while the  $4d$  orbitals of the niobium atoms [Fig. 5.9(b)] define the conduction band above this level. The lithium atoms [Fig. 5.9(c)] do not contribute to any of the bands. The total DOS [Fig. 5.9(d)] that determines the band structure of the material is therefore defined by the Nb-O bonds, in agreement with previous works [230, 231]. The orbitals of these bonds form the smallest bandgap, where maximal ionization is expected because of the exponential dependence of tunneling on the bandgap energy. Figures

5.10(a) and 5.10(b) respectively display the hexagonal unit cell of  $\text{LiNbO}_3$  and the corresponding charge density for the Nb-O bonds along the  $y$ -cut surface. The relative angle for each bond with respect to the  $c$  axis of the crystal is identified. From the DOS analysis, these orientations are subject to additional damages upon laser-induced ablation. Notably, in Fig. 5.10(b) two bonds, at  $135^\circ$  (bond 1) and  $222^\circ$  (bond 3), are quasi parallel to those laser polarization orientations where ablation is most efficient in Fig. 5.7(a), at  $140^\circ$  and  $220^\circ$ , respectively. Because the experiment is not sensitive to the direction of the bond vectors but only to their orientation, these angles are also equivalent to  $40^\circ$  and  $320^\circ$ , where an enhanced ablation is observed as well. The experimental results hence reveal with high contrast the main chemical bonds contributing to the ionization of the material.

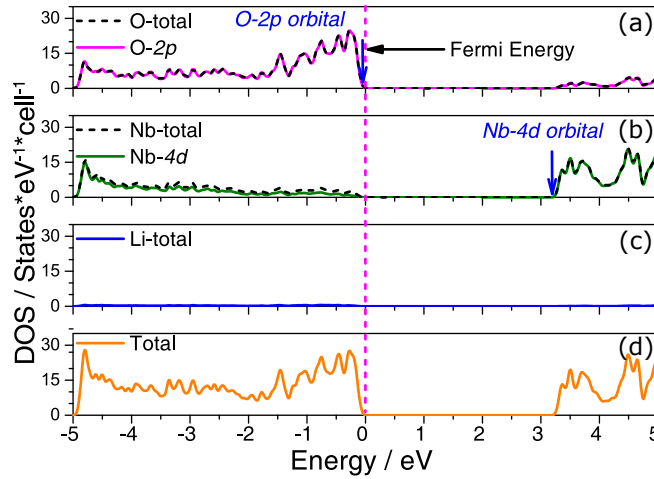


**Figure 5.9** – Partial and total density of states (DOS) of  $\text{LiNbO}_3$  with the Fermi energy (0 eV) identified by the dashed vertical line. (a) The valence band below the Fermi energy is almost exclusively composed of the oxygen 2p orbitals of the crystal structure. (b) The conduction band above the Fermi energy is mainly defined by the niobium 4d orbitals. (c) The contribution of lithium atoms is negligible. (d) Each curve is compared to this total DOS.

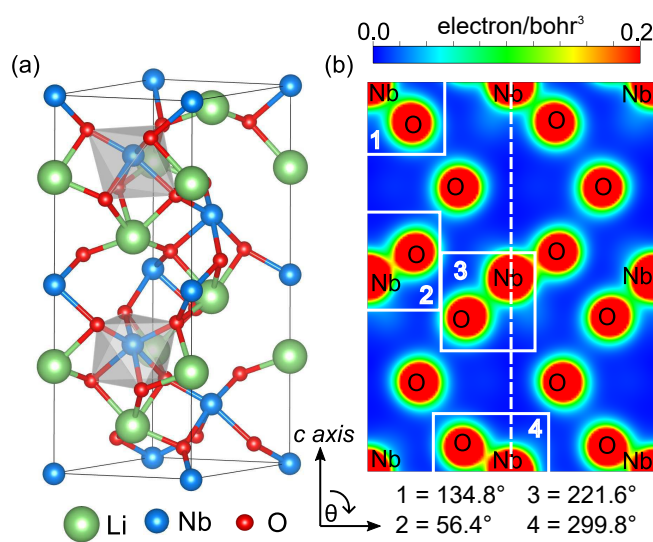


Figure 5.10 – Nb-O bond orientations in LiNbO<sub>3</sub>. (a) Hexagonal unit cell. (b) Cut of the calculated charge density along the  $y$ -cut surface. The relative angles between each Nb-O bond and the  $c$  axis of the crystal are shown.

## Semiconductor Bloch equations

To obtain a microscopic description of our angle-resolved measurements, we modeled the strong-field ionization of the material. We solved the semi-conductor Bloch equations applied to a two-band model for  $\text{LiNbO}_3$  and evaluated the conduction band population resulting from the interaction with the strong laser field for different orientations of the incident polarization. The energy bands shown in Fig. 5.6(b), the charge density in Fig. 5.10, and the dipole matrix elements were obtained from first-principles density functional theory (DFT) calculations with the Vienna Ab initio Simulation Package [232]. The local density approximation was employed to describe the exchange-correlation functional [215]. The full potential projector-augmented-wave method was used with a plane-wave cutoff of 500 eV [233]. In order to perform calculations for the converged wavefunction and band structure, the Brillouin zone of the unit cell was sampled with a  $24 \times 24 \times 8$  Monkhorst-Pack  $k$  grid for electronic self-consistent calculations. The resulting energy bands and dipole matrix elements were introduced into the semiconductor Bloch equations [234, 235].

Figure 5.11(a) shows how the conduction band population varies as a function of the laser polarization angle for both the  $x$ - (black triangles) and the  $y$ -cut (blue circles). The  $y$ -cut shows symmetry with respect to a minimum centered at  $90^\circ$  while for the  $x$ -cut, an asymmetry in the range of  $75$ - $110^\circ$  is observed (see inset). This agrees with the experimental measurements in Fig. 5.7 and the crystallography analysis in Fig. 5.8, confirming that the orientation dependence of the ablated area originates from the angle-dependent tunnel ionization. To further test the robustness of these observations, we performed additional calculations by varying the band gap energy and dephasing time for the interband polarization. In all cases, the characteristic asymmetry for the  $x$ -cut is preserved. In fact, for each crystal cut the variation of the conduction band population follows the evolution of the band structure for the different crystal orientations. This is shown in the Supplemental Material [234].

Furthermore, Fig. 5.11(b) displays the orientation-dependent reciprocal of the bandgap energy  $1/E_g$ . Note that this value is averaged over all the  $k$  points of the Brillouin zone rather than evaluated at the single gamma ( $\Gamma$ ) point since, in the latter case, the band gap energy is independent of the crystal orientation. The symmetry/asymmetry shown in the inset highlights the importance of considering the entire bands in the tunnel ionization of the material.

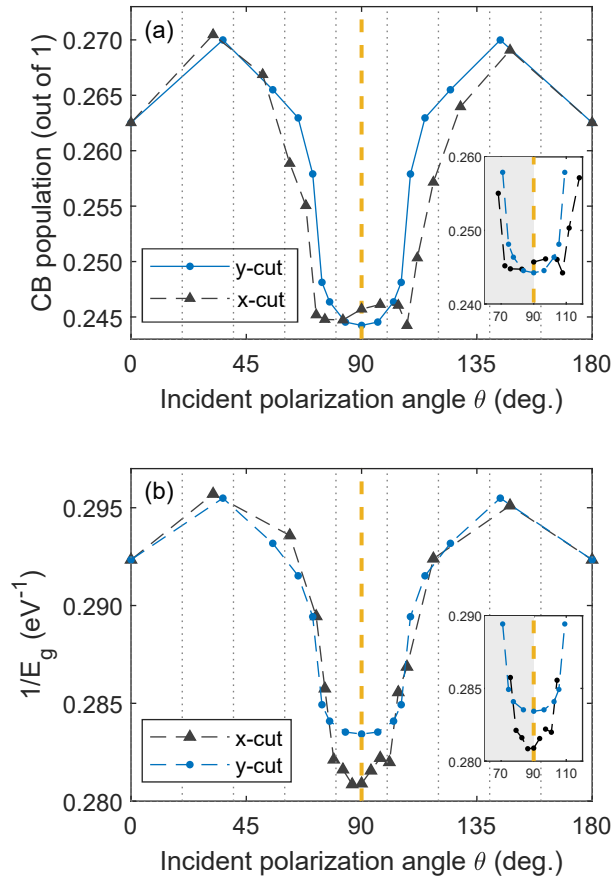


**Figure 5.11** – (a) Calculated conduction band (CB) population for  $x$ - and  $y$ -cut crystals as a function of the laser polarization angle  $\theta$ . (b) The corresponding reciprocal of the  $k$ -point-averaged band gap energy. Insets: The region in the vicinity of the minimum where the symmetry/asymmetry is observed.

## Conclusions

In this work, we have characterized the laser polarization dependence of LIA for  $x$ -cut and  $y$ -cut lithium niobate, providing a macroscopic observable with a very high contrast compared to conventional all-optical techniques. By rotating linearly polarized 1800 nm femtosecond laser pulses, we demonstrated that it is possible to image the mirror symmetries of the crystal along the plane ablated by the laser field. Moreover, the laser polarization angles where LIA is most efficient and thus leads to the largest ablated area were attributed to those angular regions containing the Nb-O bonds of the structure. Through their charge density, the spatial distribution of these bonds dictates the symmetry features in the angle-resolved measurements. These characteristic features of the laser polarization dependence on LIA were reproduced for each crystal cut by solving the semiconductor Bloch equations for  $\text{LiNbO}_3$ . In the typical two-band model employed the bands are frozen. However, it has recently been demonstrated that the high intensity of the laser field can

also affect the temporal evolution of the band structure during ionization [236]. In a more advanced model, it would be interesting to consider this effect.

Finally, laser micromachining based on LIA is a privileged technique for high precision material processing. As  $\text{LiNbO}_3$  is extensively used in optical devices that require the sample to be prepared using this technique [219], our results will contribute to reaching a better understanding and control over the writing procedure of this material.

## **Acknowledgments**

The authors acknowledge the financial support from the Canada Foundation for Innovation (CFI), the Natural Sciences and Engineering Research Council of Canada (NSERC), the Fonds de recherche du Québec – Nature et technologies (FRQNT), PROMPT and the National Natural Science Foundation of China (NSFC) (Nos. 91850121, 11674363, 11561121002). V.W. was supported by the Vanier Canada Graduate Scholarship (Vanier CGS) program.

## 5.7 Article VI – Control of strong-field ionization in ferroelectric lithium niobate: role of the spontaneous polarization

Vincent Wanie,<sup>1,2,3</sup> Tian-Jiao Shao,<sup>4,5</sup> Philippe Lassonde,<sup>1</sup> Heide Ibrahim,<sup>1</sup> Jude Deschamps,<sup>1</sup> Jia-Qi Liu,<sup>4,5</sup> Fabian A. Vargas,<sup>1</sup> Andreas Ruediger,<sup>1</sup> François Vidal,<sup>1</sup> Francesca Calegari,<sup>2,3,6</sup> Xue-Bin Bian,<sup>5</sup> and François Légaré<sup>1</sup>

<sup>1</sup>Centre Énergie Matériaux Télécommunications, Institut national de la recherche scientifique, 1650 Boul. Lionel-Boulet, Varennes, Qc, J3X 1S2, Canada

<sup>2</sup>Center for Free-Electron Laser Science, DESY, Hamburg 22607, Germany

<sup>3</sup>Institute for Photonics and Nanotechnologies CNR-IFN, Milano 20133, Italy

<sup>4</sup>University of Chinese Academy of Sciences, Beijing 100049, China

<sup>5</sup>State Key Laboratory of Magnetic Resonance and Atomic and Molecular Physics, Wuhan Institute of Physics and Mathematics, Innovation Academy for Precision Measurement Science and Technology, Chinese Academy of Sciences, Wuhan 430071, China

<sup>6</sup>Physics Department, University of Hamburg, Hamburg 22761, Germany

Received 16 August 2019

Accepted 20 March 2020

Published 07 May 2020

doi:10.1103/PhysRevB.101.184103

V.W., P.L., H.I. and F.L. designed the experiment. V.W. and P.L. performed the experiments. V.W., P.L., H.I., J.D., F.A.V. and A.R. carried out the data analysis. T.J.S., J.Q.L., F.V. and X.B.B. provided the theoretical support. V.W., T.J.S., P.L., H.I., F.V., F.C., X.B.B. and F.L. contributed to the interpretation of the results. V.W., T.J.S., H.I., and F.L. wrote the manuscript with support of all the authors.

## Abstract

We report the control of tunnel ionization in lithium niobate ( $\text{LiNbO}_3$ ) using phase-controlled two-color laser fields. Through a macroscopic observable of high contrast, we disclose the crucial contribution of the microscopic spontaneous polarization of the ferroelectric material to the ionization rate: as the relative two-color phase is varied, the ablated area of  $\text{LiNbO}_3$  is modulated by 35% when the laser and crystal polarization directions are parallel. Rotating the sample by  $180^\circ$  around the laser propagation axis leads to an out-of-phase modulation. We use a two-band model to highlight the key contribution of the material's spontaneous polarization for the symmetry breaking of the ionization rate. Our results open new perspectives for the direct control of ionization dynamics in solids by tailoring the electric field of femtosecond laser pulses.

## Introduction

Strong-field ionization (SFI) of atoms and molecules with intense laser pulses has been widely investigated in the last decades [203, 237, 71] and led to an in-depth understanding of several photoinduced ultrafast processes [6]. One of the most striking outcomes is the emergence of attosecond ( $1 \text{ as} = 10^{-18} \text{ s}$ ) science, which now allows tracking electrons on their natural timescale [116]. In semiconductor and dielectric materials, SFI is the primary step for phenomena such as refractive index changes [238], high harmonic generation [199, 200], and in the extreme case, optical breakdown [239] triggering laser-induced ablation (LIA) [221, 209]. For both, atoms and solids, Keldysh developed a common theory 55 years ago in which an adiabatic parameter  $\gamma$  is delimiting the perturbative regime ( $\gamma > 1$ ) from the tunneling one ( $\gamma < 1$ ) [71]. While the gas phase is well elucidated, experiments in solids focused mainly on interactions within the perturbative limit. Only a very few studies have explored the tunneling regime [224, 26, 240, 226, 241], even though this number is expected to increase rapidly due to the recent availability of low-frequency laser pulses in the infrared (IR) spectral range [198]. Efforts in that direction are of significant importance since various materials with large band gap compared to IR photon energies are promising candidates for numerous technological applications. For instance, lithium niobate ( $\text{LiNbO}_3$ ) and chalcogenide glasses are notable compounds used in optical switches and IR detectors [242, 243].

Many questions remain to be answered to link the well-understood gas phase to the solid state. Of particular interest is the case of non-centrosymmetric systems due to their permanent polarization. It is known that the ionization rate of noncentrosymmetric diatomics in the tunneling regime critically depends on the orientation of the molecular axis relative to the polarization of the laser field [204]. Moreover, strong-field ionization of asymmetric gas molecules typically displays preferential emission directions in molecular frame photoelectron angular distributions (MF-PADs), depending on whether the permanent dipole moment is parallel or antiparallel to the laser field [205]. For crystals, the atomic composition and configuration of the unit cell define their band

structure and physical properties. The question naturally arises whether there are similar responses to SFI for noncentrosymmetric gas molecules and materials. Furthermore, can waveform shaping of the laser electric field lead to control over SFI as in the molecular case [244, 245, 246, 247]? In this article, we extend the understanding of SFI to the solid state by investigating the interaction between intense femtosecond laser pulses and  $\text{LiNbO}_3$ , a synthetic material employed in several devices due to its ferroelectricity and distinctive optical properties [208]. We use the sensitivity of LIA to probe and control SFI in the tunneling regime by measuring the ablated area at the surface of the material as a function of the relative phase between a fundamental field (1800 nm) and its second harmonic (900 nm). The experimental results are supported by numerical simulations based on a two-band model, which establish the role of the spontaneous polarization of  $\text{LiNbO}_3$  during the photoionization process.

## Experiments

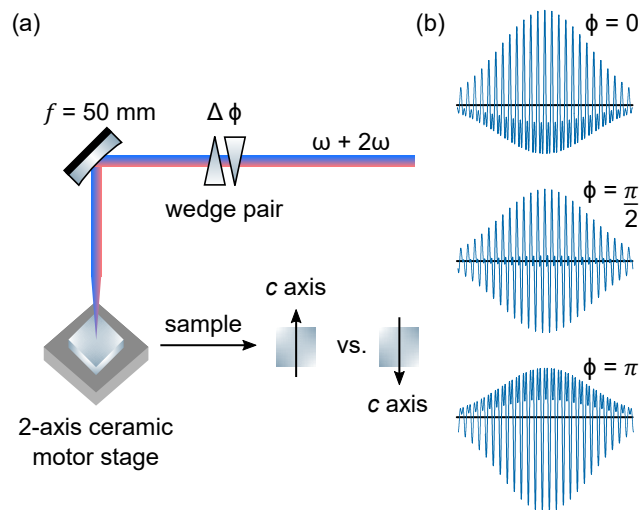


**Figure 5.12** – (a) Sketch of the experimental setup. A laser field composed of the superposition of a fundamental frequency  $\omega$  ( $\lambda = 1800 \text{ nm}$ ) and its second harmonic  $2\omega$  ( $\lambda = 900 \text{ nm}$ ) is employed to ablate the surface of  $\text{LiNbO}_3$  samples just above the threshold fluence. The relative two-color phase  $\phi$  is adjusted by translating a motorized wedge in a direction perpendicular to the laser propagation axis and the beam is focused onto the crystal with an off-axis parabolic mirror. A fast ceramic motor stage ensures single-shot ablation by translating the sample in a direction parallel to its surface. The laser polarization and the  $c$  axis of the crystal are oriented vertically. After a first ablation series, the sample is rotated by  $180^\circ$  and the procedure is repeated. (b) Waveform representation of the electric field for  $\phi = 0, \frac{\pi}{2}, \pi$  [Eq. 13]. The direction of the peak field with respect to the  $c$  axis of  $\text{LiNbO}_3$  changes every  $\Delta\phi = \pi$ .

For the experiments presented in Fig. 5.12a, the 2.5 kHz (30 fs) Ti:Sapphire laser system of the Advanced Laser Light Source (Canada) served as the input for pumping a whitelight seeded

optical parametric amplifier (TOPAS, Light Conversion) which delivered the 1800- nm pulses. After spatial filtering, 350 mW (140  $\mu$ J) were used for second-harmonic generation (SHG) in a type-1  $\beta$ -BaB<sub>2</sub>O<sub>4</sub> (BBO) ( $\Theta = 20^\circ$ ,  $\Phi = 0^\circ$ ) and both beams were sent to a Mach-Zehnder-like interferometer. Spectral separation of the 1800- and 900- nm beams was achieved by a low-dispersion dichroic beam splitter (LaserOptik). The laser polarization angle and energy were controlled in each interferometer arm using a combination of polarizer and half-waveplate. The fundamental and SH fields were recombined through a second dichroic beam splitter and sent through a pair of wedges to adjust and scan their relative phase  $\phi$ , which was actively stabilized in a similar scheme as in Refs. [248, 234]. To avoid chromatic aberrations, the resulting two-color pulses were focused at the surface of  $10 \times 10$  mm Y-cut LiNbO<sub>3</sub> samples (MTI Corporation, Curie temperature  $T_c \simeq 1160^\circ$  C) by a 50-mm focal length off-axis parabolic gold mirror. The surface thickness was 0.5 mm and its roughness below 8 Å. The experiments were performed in air and single-shot ablation craters were created due to a fast translation of the sample in the direction perpendicular to the laser propagation axis (for details on LIA see the Supplemental Material [234], and Refs [228, 211, 212, 213, 210] therein). The beam radius at focus ( $1/e^2$  of intensity) for both 1800 and 900 nm fields was  $\sim 17$   $\mu$ m and their pulse duration was characterized to 65 fs from SHG-frequency-resolved optical gating measurements. The intensities for the 1800- and 900- nm fields were respectively  $1.6 \times 10^{13}$  Wcm<sup>-2</sup> and  $7.7 \times 10^{12}$  Wcm<sup>-2</sup>. Shot-to-shot energy fluctuations were measured to be 2% at 1800 nm and 3% at 900 nm. The craters were imaged with a Nikon Eclipse microscope (100x objective) and their area was determined with a fitting routine whose accuracy was cross-checked by atomic force microscopy measurements [234].

## Results and discussion

### Two-color LIA measurements

We first address the following question: Can tunnel ionization in a solid be efficiently controlled as has been demonstrated in atomic and molecular gases [244, 245, 246, 247, 249, 250]? To do so, we experimentally used a two-color field expressed by

$$\mathcal{F}(t) = \mathcal{F}_1(t) \cos(\omega t) + \mathcal{F}_2(t) \cos(2\omega t + \phi) \quad (5.4)$$

where  $\mathcal{F}_1$  and  $\mathcal{F}_2$  are the envelope functions of the fundamental field and its second harmonic, of frequencies  $\omega$  and  $2\omega$ , respectively. By varying the relative phase  $\phi$ , one can shape the waveform of the total electric field under the envelope and control its polarity [Fig. 5.12b]. We therefore performed two-color LIA with the  $c$  axis of the crystal parallel to the laser polarization ( $\theta = 0^\circ$ ). Figure 5.13 shows the resulting ablated area in LiNbO<sub>3</sub> as a function of  $\phi$  for  $\theta = 0^\circ$  (blue solid curve). A clear phase dependence is observed with a periodicity that is half the fundamental period. The modulation amplitude corresponds to 35% of the mean value. From Eq. (13) the peak electric

field is maximal when  $\phi = 0$  or  $\pi$ , differing solely by its polarity. The successive extrema with a  $\Delta\phi = \pi$  in Fig. 5.13 thus demonstrate that the ablation process is sensitive to the field polarity for a laser polarization parallel to the crystal  $c$  axis. For a process depending on the direction of the peak electric field, one would expect that rotating the sample by  $180^\circ$  with respect to the laser polarization would revert the observed trend regardless of the mechanism. This is confirmed by the orange (dashed) curve, showing an out-of-phase dependence when repeating the measurements for  $\theta = 180^\circ$  and preserving the same initial two-color phase [234]. Experimentally, such a control is achieved most efficiently in the vicinity of the fundamental field ablation threshold. For higher intensities, the contribution of avalanche ionization to LIA reduces the sensitivity to SFI, an effect that was also observed in single-color angular LIA measurements [225]. Optimal control is obtained for a 2:1 (1800 nm:900 nm) intensity ratio, while further increasing the SH intensity leads to a loss of modulation. Moreover, the modulation amplitude vanishes completely at  $\theta = 90^\circ$ .

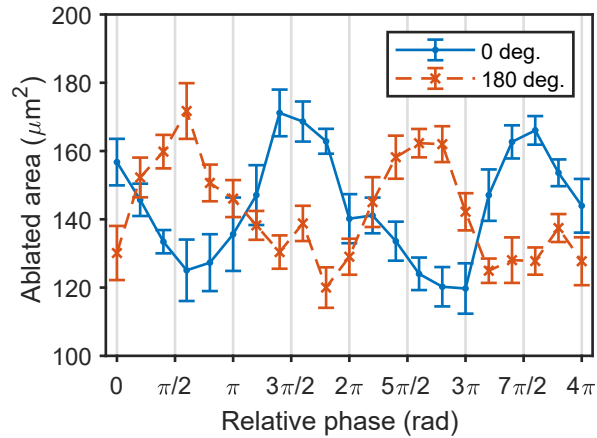


**Figure 5.13** – Single-shot ablated area as a function of the relative two-color phase for  $\theta = 0^\circ$  (solid blue) and  $\theta = 180^\circ$  (dashed orange). Each data point is averaged over ten measurements and the standard deviation is shown.

### Determination of the spontaneous polarization

In our experiment, the photon energy of 0.69 eV (1800 nm) is well below the 3.78 eV experimental band gap of  $\text{LiNbO}_3$  [251, 252]. Together with the laser intensity employed in the experiments, this ensures that ionization is due to tunneling ( $\gamma = 0.57$ ).  $180^\circ$  apart from each other, the two studied crystal orientations possess an identical band structure [234]. Therefore, the observed  $\pi$  phase shift between the curves in Fig. 5.13 suggests a non-negligible contribution from the spontaneous polarization of  $\text{LiNbO}_3$ , which is known to be particularly high along its  $c$  axis. The effect of this spontaneous polarization is comparable to an internal electric field within the material that can either add up to or subtract from the laser electric field. Consequently, the modulation amplitude in the ablated area observed in Fig. 5.13 is attributable to an effect from a parallel vs antiparallel spontaneous polarization relative to the laser peak electric field. Based on this assumption, we

estimate the spontaneous polarization of LiNbO<sub>3</sub> from the regression method that was used to determine the ablation threshold of the material. Figure 5.14 shows the ablated area of LiNbO<sub>3</sub> with increasing fluence for the 1800- nm field only. Experimentally, the ablation threshold fluence  $F_{th}$  can be evaluated according to  $A(F) = \pi/2 r_0^2 \ln(F/F_{th})$  where  $A$  is the ablated area,  $r_0$  the effective beam radius ( $1/e^2$ ), and  $F$  the laser fluence [253, 254]. From this fitting, we report  $F_{th} = 0.51$  J/cm<sup>2</sup> in lithium niobate at an 1800- nm wavelength<sup>3</sup>.

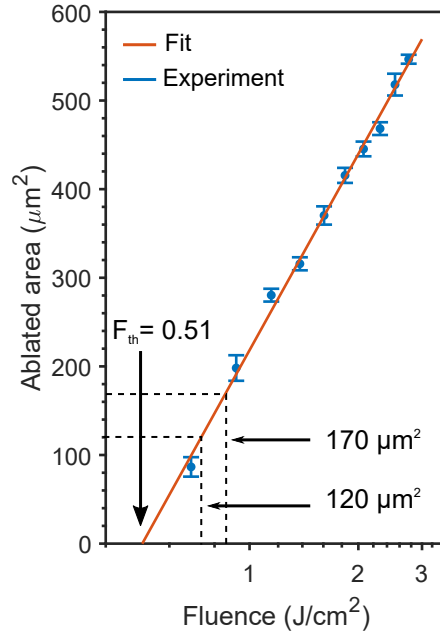


**Figure 5.14 – Determination of the spontaneous polarization.** The ablated area as a function of 1800 nm field fluence (logarithmic scale) is shown. An ablation threshold of 0.51 J/cm<sup>2</sup> is retrieved from the fit. Dashed lines show the interpolated fluences for the maximal and minimal crater area in Fig. 5.13 from which a spontaneous polarization of 0.06 C/m<sup>2</sup> is retrieved.

To retrieve the value of the effective spontaneous polarization of the material, we evaluate the peak electric field difference  $\Delta\mathcal{F}$  corresponding to the fluences that would be required to reach maxima (170 μm<sup>2</sup>) and minima (120 μm<sup>2</sup>) in the two-color measurements, as illustrated in Fig. 5.14. After considering Fresnel losses of the field  $\mathcal{F}$  [235], the resulting field in the material corresponds to  $\mathcal{F}_{LiNbO_3} = 2\mathcal{F}/(n_e + 1)$ , with the refractive index  $n_e = 2.13$  at 1800 nm. A value of  $\Delta\mathcal{F}_{LiNbO_3} = 0.46$  GV/m is obtained for which the half-value corresponds to a spontaneous polarization  $|P_s| = 0.06$  C/m<sup>2</sup> ( $\epsilon = 2.54 \times 10^{-10}$  F/m) [208]. Although there is no precise technique to characterize this property,  $|P_s|$  in LiNbO<sub>3</sub> has been reported to range between 0.6 and 0.8 C/m<sup>2</sup> from density-functional theory calculations and polarization switching measurements [255, 256, 257]. In most cases, a pure stoichiometric crystal is considered and the reported values thus correspond to an upper limit. The reduced value retrieved in our experiments may be attributed to the initial presence of free charges within the material due to defects, intrinsically present for non-stoichiometric LiNbO<sub>3</sub>

<sup>3</sup>For  $F_{th} = 0.51$  J/cm<sup>2</sup>, the 95% confidence interval obtained from the fit is 0.47-0.54 J/cm<sup>2</sup>.

samples. Screening by free carriers, together with surface charge density effects [258], are expected to reduce significantly the effective spontaneous polarization.

### Two-band model

To get deeper insight into the underlying control mechanism, we used the experimentally retrieved  $P_s$  to simulate the two-color phase dependence of the ionization process with a two-band model for LiNbO<sub>3</sub>. The calculations are performed by solving the semiconductor Bloch equations (for theoretical details, see the Supplemental Material [234] and references [227, 232, 233, 236, 215] therein). In presence of the laser field, the band gap  $E_g$  undergoes an AC Stark shift that is described to the first order by

$$E_g(\mathcal{F}) = E_g(0) - \mu \mathcal{F}(t)_{LiNbO_3} \quad (5.5)$$

where  $E_g(0)$  is the field-free band gap energy and  $\mathcal{F}(t)_{LiNbO_3}$  is the two-color laser electric field in the material. This is in direct analogy to Stark shifts experienced by asymmetric molecules in intense laser fields [259]. The permanent dipole of LiNbO<sub>3</sub> along its  $c$  axis,  $\mu$ , is obtained by multiplying  $P_s$  by the volume of the unit cell [234]. The retrieved  $P_s = \pm 0.06$  C/m<sup>2</sup> thus enters Eq. (15) via the permanent dipole  $\mu$  and the dynamical band gap energy is included in our two-band model. Figure 5.15 shows the resulting conduction band population of the material as a function of  $\phi$ . The two spontaneous polarizations  $P_s = \pm 0.05$  C/m<sup>2</sup> and  $P_s = \pm 0.1$  C/m<sup>2</sup> are compared. A sign reversal is equivalent to rotating the sample spatially from  $\theta = 0^\circ$  to  $180^\circ$ .

First, one can observe by comparing  $P_s = +0.05$  and  $-0.05$  C/m<sup>2</sup> (green squares and purple line) that reversing  $P_s$  leads to a  $\pi$ -shifted modulation. Increasing to  $P_s = +0.1$  and  $-0.1$  C/m<sup>2</sup> (blue circles and orange crosses), this feature is preserved and the modulation amplitude is enhanced. As described by Eq. (15), a larger spontaneous polarization ( $|P_s| = 0.05$  vs  $0.1$  C/m<sup>2</sup>) amplifies the AC Stark effect on the band gap energy [234]. Since the ionization rate depends exponentially on  $E_g$ , this leads to a significant increase of the modulation amplitude of the conduction band population. In agreement with the experimental results of Fig. 5.13, extrema arise every  $\Delta\phi = \pi$ , confirming the dependence of the ionization process on the electric field polarity. For comparison, the black curve describes ionization when the spontaneous polarization of LiNbO<sub>3</sub> is not taken into account ( $P_s = 0$ ). In this case, the modulation frequency is doubled and the process depends on  $|\mathcal{F}|^2$ , confirming the key role of the spontaneous polarization as the precursor for the symmetry breaking. The transition from  $P_s = 0$  to  $0.1$  C/m<sup>2</sup> in the two-color phase dependence illustrates the change of periodicity induced by the material [234]. It can be noted that in the simulations (Fig. 5.15) an extrema is observed precisely at  $\phi = 0$ , in agreement with Eq. (13). This is not observed in the experimental results (Fig. 5.13) because for this latter case the initial two-color phase  $\phi$  is unknown but arbitrarily chosen as a relative zero. While our simulations provide a qualitative interpretation, additional effects should be taken into account for a quantitative modeling. For instance, indirect

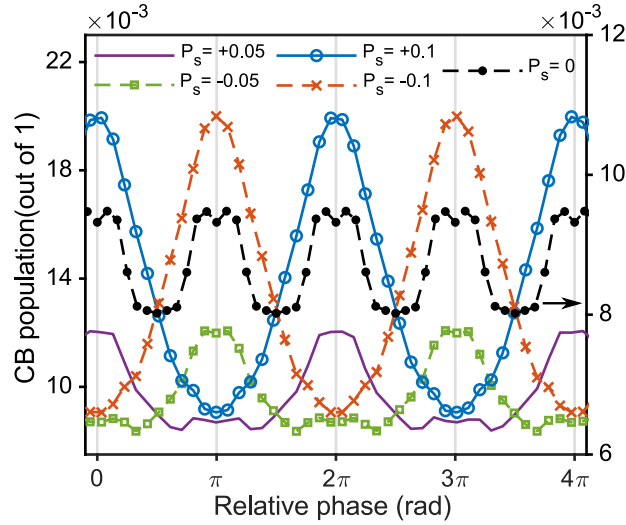


**Figure 5.15 – Two-band model calculations.** The conduction band (CB) population as a function of the relative two-color phase  $\phi$  is shown for  $\theta = 0^\circ$  and  $\theta = 180^\circ$ . The two orientations correspond to a sign reversal of the spontaneous polarization that is either parallel or anti-parallel to the laser peak electric field. Different values are compared:  $P_s = \pm 0.05$  C/m<sup>2</sup> (green squares and purple line),  $P_s = \pm 0.1$  C/m<sup>2</sup> (blue circles and orange crosses), and  $P_s = 0$  C/m<sup>2</sup> (black dots). While a sign reversal leads to a  $\pi$  phase shift of the modulation, the frequency is doubled when  $P_s = 0$  C/m<sup>2</sup> (black dots, right scale).

band gap transitions in the tunneling regime may contribute to the conduction band population. Thermodynamic properties such as electron and ion temperatures and pressures should also be considered [209].

## Conclusion

In summary, we demonstrated an efficient control of the tunnel ionization rate in lithium niobate from LIA measurements. By using a phase-controlled two-color laser field to ablate the ferroelectric material, we observed modulations as high as 35% in the ablated area when varying the relative phase between an 1800-nm field and its second harmonic. The results are explained by a two-band model, which clarifies the control mechanism as a consequence of the spontaneous polarization in LiNbO<sub>3</sub>. This is in close analogy to the molecular case, where, however, noncentrosymmetric molecules must be oriented in the laboratory frame in order to determine the influence of permanent dipole moment and polarizability [205]. From a regression method, we evaluated  $|P_s|$  to be 0.06 C/m<sup>2</sup>. Simulations show that parallel and antiparallel spontaneous polarization relative to the laser peak electric field direction influences the AC Stark shift of the band gap energy. This, in turn, impacts on the ionization rate of the material and leads to ablated craters of different sizes. Our experimental approach hence allows interpreting the role of the spontaneous polarization in the ionization of ferroelectric materials. Smaller band-gap materials with high  $P_s$  should lead

to enhanced control. This will, however, require midinfrared wavelength pulses with microjoules of energy to remain in the tunneling regime. The observed phase sensitivity of femtosecond laser-induced ablation can find applications in laser micromachining but most importantly it opens a route for the direct control of ionization dynamics within crystals through femtosecond pulse shaping. For example, our results offer new degrees of freedom for high-order harmonic generation from solids, a promising candidate for the design of compact extreme ultraviolet sources. Finally, the findings also suggest a potential phase meter scheme, exploiting solid samples, to identify the carrier-envelope phase of few-cycle laser pulses covering the mid- and far-IR spectral ranges gaining in accessibility in many laboratories.

## **Acknowledgments**

V.W. thanks Guilmot Ernotte for fruitful discussions about the interpretation of ionization dynamics in solids. The authors acknowledge financial support from Canada Foundation for Innovation (CFI), the Natural Sciences and Engineering Research Council of Canada (NSERC), the Fonds de recherche du Québec–Nature et technologies (FRQNT), PROMPT, and the National Natural Science Foundation of China (NSFC) (Grants No. 91850121, No. 11674363 and No. 11561121002). V.W. was supported by the Vanier Canada Graduate Scholarship (Vanier CGS) program and FRQNT. J.D. was supported by NSERC. V.W. and T.J.S. contributed equally to this work.



## Chapter 6

# Probing electron dynamics in bio-relevant molecules

In chapter 4, we demonstrated how femtosecond laser pulses can be employed to control electron dynamics in the dissociative ionization of hydrogen, the simplest molecule. Here, we extend our objective of reaching a better understanding over the control of photochemical processes to more complex systems. As will be described in the following section, a lot of interest has been gained in ultrafast spectroscopy towards molecules constituting our biological system, such as amino-acids and nucleobases. Understanding the ultrafast dynamics that happen within the few femtoseconds following photoionization in bio-relevant molecules can potentially allow to control the outcome of more complex events occurring at later times. In this chapter, we demonstrate how the characterization of the few-fs electron dynamics in the nucleobase adenine upon photoionization by an isolated attosecond XUV pulse revealed a laser-assisted stabilization mechanism that can be exploited to prevent the molecule to dissociate.

### 6.1 Few-femtosecond dynamics following photoionization of bio-relevant molecules

The photoionization of a molecule leaves a hole in its electron density. In large molecular systems where delocalization is possible, this positive charge can propagate over several Ångströms along the molecular structure. This phenomenon identified as *charge transfer* (CT) is mainly dictated by nuclear motion and is particularly important in biologically relevant molecules such as peptides and nucleotides. In solution, charge transfers are affected by the solvent surrounding the molecular system. For this reason, efforts have been made to study this process in the gas phase in order to understand the intrinsic nature of CT without solvent effects. In 1992, Chatteraj *et al.* proposed a

scheme to follow the charge transfer dynamics of a donor-acceptor molecular system in the gas phase [260]. The donor unit constituted of an aromatic molecule while the acceptor unit was interchanged over a few molecular species. The experimental scheme for this time-resolved experiment is presented in Figure 6.1. First, a pump pulse leads to a two-photon resonance-enhanced ionization that creates a hole localized on the donor (aromatic) unit. Over time, the positive charge can transfer to the acceptor side. By employing a delayed probe pulse, the CT can be identified by following the evolution of the resulting ions mass spectrum. For this experiment, although a signature of the CT process could be identified, the time resolution (2 ns) prevented to follow its temporal evolution. However, the pump-probe scheme employed served as a prototype for several years afterwards.

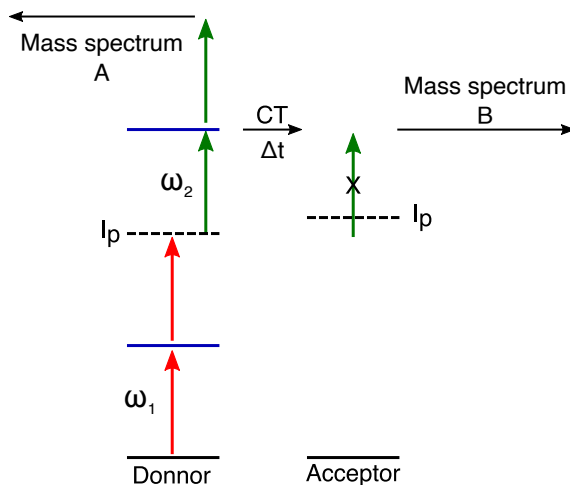


**Figure 6.1 – Probing scheme from Chattoraj *et al.* to study the charge transfer (CT) process. Resonant states are identified in blue.  $I_p$ : ionization potential.**

Employing the 2-photon resonant pump scheme from Chattoraj *et al.*, seminal work by Weinkauff *et al.* approached bio-relevant molecules by investigating charge transfer effects in small peptides with nanosecond pulses [261, 262]. In 2005, they performed a femtosecond-resolved experiment in 2-phenylethyl-N,N-dimethylamine (PENNA), having a similar structure to the amino-acid phenylalanine [263]. Again from the prototypical 2-photon resonant transition, they tracked the evolution of the CT from the phenyl group to the amine group of the molecule with a characteristic time of about 80 fs. Following this work, a theoretical model identifying the presence of a *charge migration* process in PENNA was presented by Lünemann *et al.* [264]. In comparison to the charge transfer process, charge migration is characterized to be driven by electron correlations. The calculations demonstrated that charge migration in PENNA can occur in a very short temporal window, as fast as 4 fs.

The aforementioned results justified the need for attosecond pulses to track electron dynamics in bio-relevant molecules with sufficient temporal resolution. In 2010, a first pump-probe experiment employing a 1.5 fs XUV pulse train to ionize the phenylalanine amino-acid was reported. By probing with a 6 fs NIR pulse, a charge migration process for one of the molecular fragment was identified

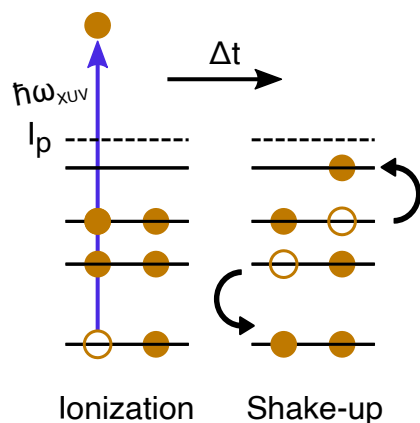


**Figure 6.2** – Illustration of a shake-up process.

to occur in about 30 fs but no oscillatory behavior could be clearly observed. This challenge was finally achieved in 2014 by Calegari *et al.* [16, 265]. By employing isolated attosecond pulses (300 as), the temporal resolution of the experiment allowed to identify electronic beatings during the charge migration with a period of about 4 fs. The experiment consisted in a first application of attosecond spectroscopy to bio-relevant molecules.

By ionizing core electrons, the high energies carried by XUV photons can also trigger other processes driven by electronic correlations such as autoionization, shake-up and Auger decays [266, 267, 268]. An example is shown in Fig. 6.2. Following the formation of a core-hole by an XUV pulse, an electronic relaxation can take place in a characteristic time  $\Delta t$ . The energy released by an electron populating a lower state can excite a second electron to a higher bound state (shake-up) or alternatively ionize this electron (Auger process). While attosecond spectroscopy has been able to characterize such processes in atoms, they have not been captured in a polyatomic molecule so far. The following article treats onto the characterization of a few-fs shake-up dynamics in the adenine nucleobase.

## 6.2 Article VII - Summary

In the context of investigating the early mechanisms at play in the radiation damage of DNA subunits, we study in Article VII the few-fs dynamics of the adenine nucleobase following photoionization by an isolated attosecond XUV pulse.

The pump-probe setup that was used for the experiment is shown in Figure 6.3. A beam splitter divides a NIR beam in two components (left side). The transmitted beam is used to generate XUV isolated attosecond pulses with the polarization gating (PG) technique that was described in section 3.2. The residual NIR is filtered out by an aluminum filter. The NIR pulse that was reflected by the beam splitter is recombined with the XUV pulse using a drilled mirror and the time-delay

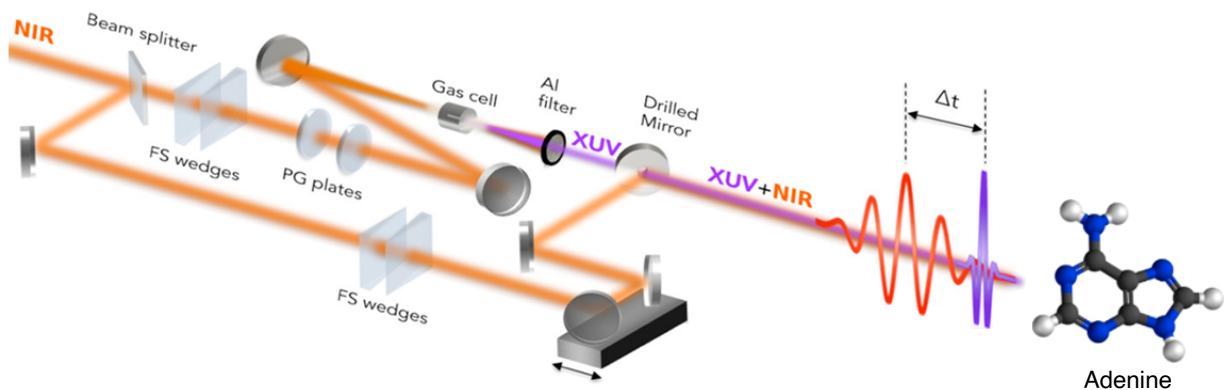


**Figure 6.3** – Scheme of the attosecond beamline at the Politecnico di Milano that was employed for the pump-probe experiment in adenine

between the two pulses is fixed but variable. Within this pump-probe approach, an adenine cation is first created by the ionizing XUV pump pulse with photon energies from 15 to 35 eV, then the delayed NIR probe pulse serves to track the photo-fragmentation dynamics of the molecule through the detection of ions using a VMI spectrometer in the time-of-flight mode (Figure 6.4a). The fragmentation spectra are recorded as a function of the time delay between the XUV and NIR pulses (Figure 6.4b).

The method described above enables to follow the formation and disappearance of molecular fragments upon ionization. The main finding in our measurements is the appearance of a stable dication of adenine ( $\text{ade}^{2+}$ ), which is found to be delayed by 2.32 fs compared to other fragments (Figure 6.5). By repeating the measurements in different experimental conditions, we also observe that when the XUV pulse contains photon energies strictly below 17 eV,  $\text{ade}^{2+}$  is not observed. This result indicated that the ionization of core electrons by high energy photons was likely to play a role in the formation of a stable adenine dication.

To support these experimental observations, simulations were necessary. Indeed, the complexity of large molecular systems such as adenine inevitably requires theoretical models, either to take into account non-adiabatic effects, or many-body interactions such as electron correlations. Therefore, DFT calculations (described in section 5.4) together with two complementary theoretical models were employed. The combination of experiment and theory allowed to make a number of conclusions on the fragmentation dynamics of adenine:

First, the combination of TD-DFT and molecular dynamics calculations shows that when the XUV pulse ionizes an electron from the highest occupied molecular orbital (HOMO), significant bond elongation in the molecule takes place as an indication of low photo-stability (Figure 6.4c). This result suggest that other relaxation processes than dissociation, involving electron correlations, must be taken into account to explain that the adenine molecule remains intact following XUV ionization.

Second, rate equations based on Fermi’s golden rule were employed to demonstrate that the population of a specific molecular orbital occurs through shake-up within a time-window that is compatible with the experimental delay for the formation of  $\text{ade}^{2+}$ . The identification of this shake-up state (LUMO+6) was also confirmed by employing a more advanced model solving the non-equilibrium Green’s function, which takes explicitly into account many-body (electron-electron) Coulomb interactions. This model also allowing to evaluate the temporal evolution of the electron density, it could further demonstrate that during the population of the relevant shake-up state, a charge migration away from the molecular plane takes place (Figure 6.7c). Within the same model, simulation of the NIR probe step shows that a second ionization following the shake-up process removes potential energy in the molecule that would be responsible for bond breaking in the absence of the NIR pulse.

By relating to Figure 6.2 illustrating the general scheme of a shake-up process, the complete mechanism to obtain an undissociated adenine dication is described as follows: (1) The photoionization by an XUV pulse creates a core hole within the adenine molecule. (2) The decay of the hole leads to the population of a shake-up state within the experimental 2.32 fs delay observed experimentally, corresponding to  $\Delta t$ . (3) A NIR pulse that is synchronized at this time ionizes a second electron, depleting the populated shake-up state. This last ionization step prevents further relaxation of the molecule through dissociative pathways.

In this work, the duration of a shake-up process taking place in a polyatomic molecule – adenine – has been characterized for the first time. The results demonstrate the importance of combining state-of-the-art theoretical calculations and experimental observations in order to reach a correct interpretation when investigating large molecular systems. This work further shows that by understanding the few-fs electron dynamics following the photoionization of a bio-relevant molecule, it is possible to control the molecular dissociation through a laser-assisted stabilization mechanism, overcoming an important goal in photochemistry.

### 6.2.1 Fitting of the fragmentation dynamics

For the fitting of the fragmentation dynamics shown in Fig. 6.5, we consider a model where an electronic state is populated in a time  $\tau_1$  with a rate  $1/\tau_1$ . Since this state also decays in a time  $\tau_2$ , its population  $N(t)$  evolves according to :

$$N(t) = \begin{cases} \frac{1}{1-\tau_1/\tau_2} \left( e^{-t/\tau_2} - e^{-t/\tau_1} \right) & , t > 0 \\ 0 & , t < 0 \end{cases} \quad (6.1)$$

In the case where  $0 \leq \tau_1 < \tau_2$ , the state population increases until it reaches a maximum and then starts to decay. Experimentally, to describe the evolution of the measured ion signal relative

to the pump-probe delay  $t$ , this function must be convoluted with the instrument response function  $\sigma_{\text{IRF}}$ . Here,  $\sigma_{\text{IRF}}$  corresponds to the Gaussian that results from the convolution of the pump and probe pulses, with a width  $W = 2\sqrt{2\ln 2}\sigma_{\text{IRF}}$ . The resulting fitting function becomes:

$$f(t) = b + \frac{h}{1 - \tau_1/\tau_2} (g_{\tau_2}(t - t_0) - g_{\tau_1}(t - t_0)). \quad (6.2)$$

with a parameter  $t_0$  that is forced to be the same for all fragments. This parameter also defines the NIR probe delay axis.  $b$  is a background offset constant and  $h$  is the height of the step of the ion signal. The convolutions  $g_{\tau_2}$  and  $g_{\tau_1}$  for each of the two exponential decays can be evaluated using [269]:

$$g_{\tau}(t) = \frac{1}{2} \operatorname{erfc} \left( \frac{\sigma_{\text{IRF}}}{\tau\sqrt{2}} - \frac{t}{\sigma_{\text{IRF}}\sqrt{2}} \right) \times \exp \left( -t/\tau + \sigma_{\text{IRF}}^2/(2\tau^2) \right) \quad (6.3)$$

As described in the manuscript, the formation of the adenine dication requires two NIR probe photons. In this specific case, since this ion signal scales with the square of the probe intensity,  $W$  for the fitting has been reduced by  $W/\sqrt{2}$ . As shown in Fig. 6.5, this model indicates that compared to all singly ionized fragments, the dication of adenine involves a state with a longer population time  $\tau_1 = 2.32$  fs.

### 6.3 Laser-assisted stabilisation of ionised adenine: preventing molecular dissociation by acting at extreme time scales

Erik P. Månsson<sup>1,2</sup>, Simone Latini<sup>3</sup>, Fabio Covito<sup>3</sup>, Vincent Wanie<sup>1,2,4</sup>, Mara Galli<sup>1,5</sup>, Enrico Perfetto<sup>6,7</sup>, Gianluca Stefanucci<sup>7,8</sup>, Hannes Hübener<sup>3</sup>, Umberto De Giovannini<sup>3,9</sup>, Mattea C. Castrovilli<sup>2,10</sup>, Andrea Trabattoni<sup>1</sup>, Fabio Frassetto<sup>11</sup>, Luca Poletto<sup>11</sup>, Jason B. Greenwood<sup>12</sup>, François Légaré<sup>4</sup>, Mauro Nisoli<sup>2,5</sup>, Angel Rubio<sup>3,13</sup> and Francesca Calegari<sup>1,2,14</sup>

<sup>1</sup> Center for Free-Electron Laser Science, DESY, Notkestr. 85, 22607 Hamburg, Germany

<sup>2</sup> Inst. for Photonics and Nanotechnologies CNR-IFN, P.za L. da Vinci 32, 20133 Milano, Italy

<sup>3</sup> Max Planck Institute for the Structure and Dynamics of Matter and Center for Free Electron Laser Science, 22761 Hamburg, Germany

<sup>4</sup> INRS-EMT, 1650 Blvd. Lionel Boulet J3X 1S2, Varennes, Canada

<sup>5</sup> Department of Physics, Politecnico di Milano, Piazza L. da Vinci 32, 20133 Milano, Italy

<sup>6</sup> CNR-ISM, Division of Ultrafast Processes in Materials (FLASHit), Area della ricerca di Roma 1, Via Salaria Km 29.3, I-00016 Monterotondo Scalo, Italy

<sup>7</sup> Dipartimento di Fisica, Università di Roma Tor Vergata, Via della Ricerca Scientifica, 00133 Rome, Italy

<sup>8</sup> INFN, Sezione di Roma Tor Vergata, Via della Ricerca Scientifica 1, 00133 Roma, Italy

<sup>9</sup> Dipartimento di Fisica e Chimica, Università degli Studi di Palermo, Via Archirafi 36, I-90123, Palermo, Italy

<sup>10</sup> Inst. for the Structure of Matter CNR-ISM, Area Ricerca di Roma1, Monterotondo, Italy

<sup>11</sup> Inst. for Photonics and Nanotechnologies CNR-IFN, Via Trasea 7, 35131 Padova, Italy

<sup>12</sup> Centre for Plasma Physics, School of Maths and Physics, Queen's University Belfast, BT7 1NN, UK

<sup>13</sup> Center for Computational Quantum Physics (CCQ), The Flatiron Institute, 162 Fifth avenue, New York NY 10010, USA

<sup>14</sup> Institut für Experimentalphysik, Universität Hamburg, Luruper Chaussee 149, D-22761 Hamburg, Germany

Submitted to Nature Physics

Received 28 November 2019

S.L., E.P., G.S., L.P., F.L., M.N., A.R. and F.Ca. supervised the project. E.M., V.W., M.G. and M.C. performed the measurements, with F.F. and J.G. contributing resources. S.L., F.Co., E.P.

and G.S. performed the simulations. E.M., S.L., F.Co., H.H., U.D., A.T. and F.Ca. wrote the manuscript.

My contribution to this work has been to operate the laser system and the attosecond beamline for the experiments. I also performed the measurements, together with Dr Erik Månsson and Mara Galli, and participated to the revision of the manuscript.

**Abstract**

Ionisation of a relatively large molecule often leads to bond breakage of the molecular subunits. Control over the molecular dissociation has so far hardly been achieved, and a better understanding of the ionisation process in subunits such as nucleic-acid bases would have implications beyond the scope of physical chemistry. Here we report on a time-resolved study of adenine photo-fragmentation following ionisation by a 15–35 eV attosecond pulse [116]. We find that, although adenine has a low photo-stability in this energy range [270], ultrafast electronic rearrangement opens up a new efficient stabilisation pathway where intact doubly charged adenine can be produced, via a second ionisation event by a laser pulse which has to be delayed by a few femtoseconds. This stabilisation-by-ionisation mechanism is supported by first-principles time-dependent simulations including electronic correlation effects. Our findings pave the way for a new control scheme for the protection of the DNA subunits – and biomolecular subunits more generally – against molecular dissociation and radiation damage.

**Main text**

The interaction of ionising radiation with large molecules, including DNA, has a high-degree of complexity [271, 272]. In ionised molecules, the excited-states dynamics considerably interfere with a variety of processes occurring between the different subunits and between the subunits and the solvent. One of the motivations to study isolated subunits, such as nucleic-acid bases, is the possibility to identify the primary relaxation mechanisms leading to fragmentation in the complete absence of external effects [273]. In this context, a complete physical picture including the role of the ionization-induced electron dynamics in the photochemistry of these molecules is still missing. While the interaction of the biomolecular subunits with their natural environment (often water) may alter their stability, also the converse may be true, i.e. the trigger of ultrafast responses in the subunits may be relevant for controlling the functionality of the biological ensemble at longer time scales. Sudden removal of one or more electrons from these molecules leads to an internal electronic rearrangement, often governed by correlated processes such as charge migration [274, 16], shake-up or Auger [267, 275] and Interatomic Coulombic Decay (ICD) [276]. These processes may initiate a chain of events leading to damage, and they occur on an extremely fast time scale now accessible by attosecond laser technology [277, 278, 116]. Recently, using trains of attosecond pulses, it has been possible to reveal that multi-electronic (shake-up) and non-adiabatic effects are fully entangled and their interplay can be identified in the relaxation dynamics following XUV-induced ionisation of organic molecules [279]. Nevertheless, this entangled effect has been demonstrated to occur on a time scale of several tens of femtoseconds and the very early stages of the light-molecule interaction, when pure electronic effects are expected to dominate, have not been investigated so far with sufficiently high temporal resolution. In this work, we report the first few-femtosecond time-resolved study of the dissociative dynamics of the nucleic-acid base adenine following sudden

ionisation by an attosecond XUV pulse, with the motivation to track many body effects *before* non-adiabatic effects take place and potentially take advantage of them to find new molecular stabilisation protocols against radiation damage.

In our experiment, ionisation of adenine is initiated by an isolated sub-300-as XUV pulse containing photon energies from 15 to 35 eV, produced by high-harmonic generation [280] in krypton gas through the polarisation gating technique [97]. A waveform-controlled 4-fs near-infrared (NIR, central photon energy 1.77 eV) probing pulse is combined with the XUV pump pulse using an interferometric approach. Adenine is sublimated and carried to the laser interaction region by using helium as a buffer gas. The produced ions are then collected as function of the XUV-pump NIR-probe delay (see Figure 6.4a), using a time-of-flight spectrometer. The ion mass spectrum resulting from ionisation by the XUV pulse alone is shown in Figure 6.4b. The observed high level of fragmentation (81% of the total yield) indicates a relatively low photo-stability of adenine in this energy range. This is also confirmed by first-principles calculations [281, 282, 283] based on time-dependent density functional theory (TDDFT) [284, 285] and Ehrenfest dynamics [286] where suddenly ionised adenine undergoes bond-elongation and eventual dissociation. As an example, in Figure 6.4c we report the time evolution of the bond lengths after removal of an electron from the third highest occupied molecular orbital (a similar analysis where the electron is removed from different occupied orbitals is reported in the Supplementary Information (SI, appendix III) and leads to the same conclusions). Several bond lengths are seen to evolve in the first few tens of femtoseconds drifting away from their equilibrium value and without reaching a new equilibrium. This is consistent with a large dissociation probability at longer time scales. A more detailed description of the molecular fragmentation induced by XUV ionization is reported in the SI. We also point out that the study of the stability of a DNA base in this energy range takes on additional relevance when one considers that strand-breakage – due to impact/attachment with secondary electrons originated in the human tissue [287] – exhibits a resonance at 10 eV and a plateau from 30 eV [288].

Further deposition of energy by the NIR pulse, simultaneously or after the XUV, leads to an overall increase of fragmentation [270]. Figure 6.5 shows the partial ion yield for several ionic fragments as a function of the pump-probe delay. The time dependent yields of the cationic fragments with mass 27, 38 and 53 u display step-like increases, followed by slower decay. The enhancement of small fragment ions occurs at the expense of the large fragments, mainly 108 u, which clearly indicates that the combination of XUV and NIR pulses leads to further excitation and therefore more efficient bond breaking. One could thus assume that the only effect of sending a control NIR laser pulse would be to decrease the photo-stability of the XUV-ionised molecule.

The most intriguing observation in the time-dependent mass spectrum is the appearance of a new ion for small positive delays at mass/charge = 67.5 u/e, corresponding to the doubly charged parent molecule (adenine<sup>2+</sup>) [289, 290, 291]. It is worth noting that a stable dication of the parent is difficult to discern in the XUV-only signal or at negative NIR delays, and none is present if we select the portion of the XUV spectrum below 17 eV (see the SI). Figure 6.5 shows that the formation of

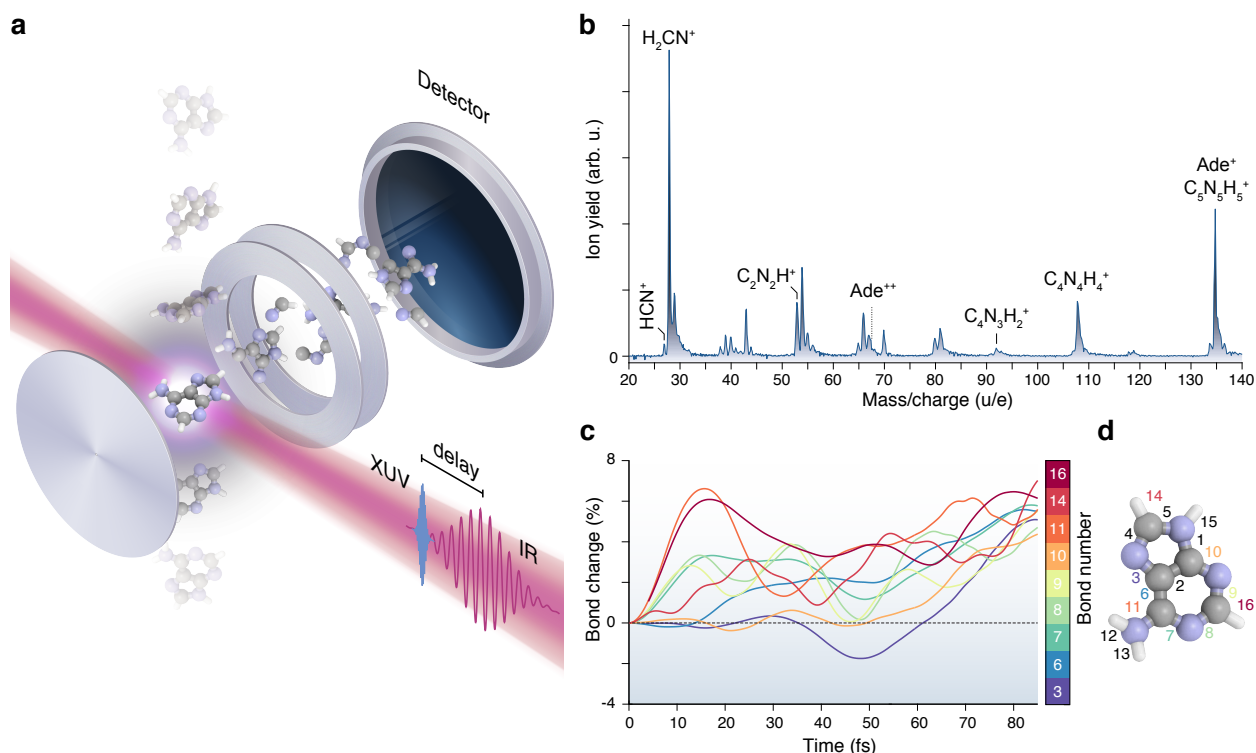


**Figure 6.4 – Dissociation of adenine.** (a) Schematic of the experiment: a molecular beam is injected into a VMI operated in the ion time-of-flight mode. Adenine ions are accelerated towards the detector and the ion yield is measured as a function of the XUV-pump IR-probe delay. (b) Measured mass spectrum resulting from ionisation of adenine by the XUV pulse only. Fragment masses constitute 81% of the spectrum. (c) Example of calculated time evolution of bond lengths following XUV ionisation, with an electron removed from the fourth highest occupied molecular orbital. Several bond lengths are seen to evolve without reaching a new equilibrium after XUV ionisation, which is consistent with a large dissociation probability. The theoretical simulations for bond elongation are performed with TDDFT. (d) The bond numbering used in the theoretical work.

the parent dication is delayed compared to the cationic fragments. Fitting the experimental data using a curve model described in the SI, we obtain for the dication pump–probe signal a delay of  $2.32 \pm 0.45$  fs ( $\tau_1$ , exponential risetime) and a decay time of  $24 \pm 3$  fs ( $\tau_2$ , exponential decay). To further verify that the steps of the cationic fragments accurately represent the absolute zero time delay (XUV-NIR overlap), we also did measurements with simultaneous injection of an atomic gas (krypton). The XUV+NIR double ionisation of krypton gives a  $\text{Kr}^{2+}$  signal at a time consistent with the adenine cations (see SI), allowing us to conclude that it is the adenine dication signal which is positively delayed. The extracted delay does not appear to depend on the NIR pulse intensity, within the explored range from  $7 \times 10^{12}$  to  $1.4 \times 10^{13}$  W/cm<sup>2</sup>. At the same time we observed that the dication yield scales quadratically with the NIR intensity (see SI), thus indicating that two NIR photons are required to doubly ionise the molecule. The detection of a doubly charged intact

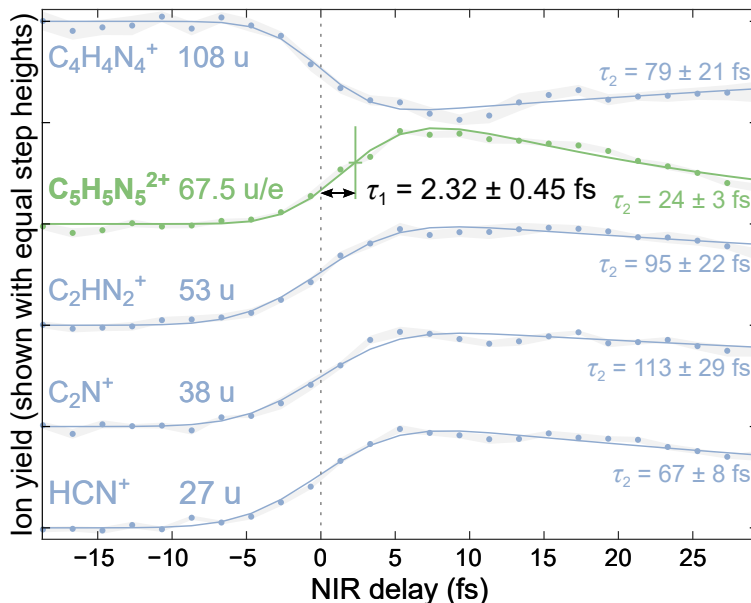


**Figure 6.5 – Experimental results: pump–probe scan.** Normalised yield of several ions (shown with a vertical offset) as a function of the XUV-pump NIR-probe delay. The yield of the ionic fragments exhibits a distinct positive or negative step-like behaviour, while the adenine parent dication (67.5 u/e) is fitted to have an exponential risetime of  $\tau_1 = 2.32 \pm 0.45$  fs (68% confidence interval). The decay lifetime ( $\tau_2$ ) is significantly shorter for the dication (green curve) than for the cations. The grey shading indicates the standard error of the mean of 7 successive scans.

molecule indicates the presence of a stabilisation mechanism that can occur only if the control NIR laser pulse arrives with a short delay after the ionising XUV pulse.

Both singly and doubly ionised adenine have stable ground states that can be found by relaxing the molecular geometry in first-principles DFT calculations. On the other hand, as stated above, TDDFT dynamics after sudden ionisation showed bond elongation and dissociation (see SI). The observed transition to a stable doubly ionised state thus requires energy to be removed by other means, with the NIR pulse having a stabilising role. We propose the following mechanism: *I*) the XUV pulse singly ionises the molecule leaving a hole in a valence state, *II*) the hole decays in a characteristic short time and, due to electronic correlations, this can lead to excitation of a second electron to a bound excited state, hereafter called "shake-up" state, *III*) the NIR pulse extracts the excited electron, hence doubly ionising and stabilising the molecule. This stabilisation mechanism is accessible only if the NIR pulse is optimally timed with respect to the XUV pulse, arriving after the shake-up process has occurred but before the excited molecular cationic state relaxes. On the other hand, if the NIR comes before the shake-up has occurred, further fragmentation is induced and the dication cannot be formed. A simplified representation of the two scenarios is pictorially illustrated in Fig. 6.6. It is worth mentioning that, even though the NIR probe pulse acts in the very early stages after XUV ionisation where pure electron dynamics dominates, the role of non-adiabatic effects such as conical intersections cannot be completely ruled out. Nevertheless, in such

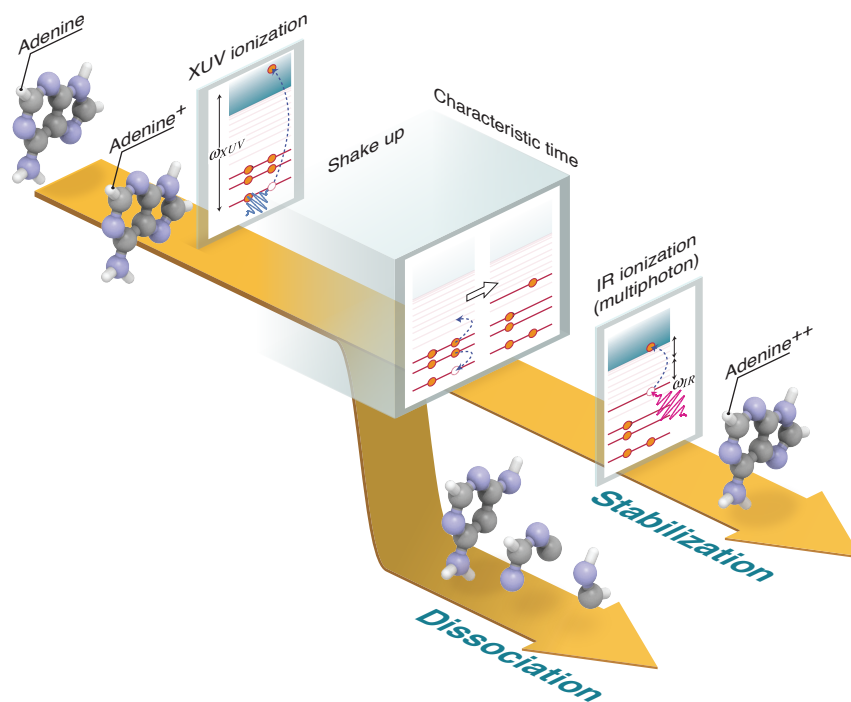


**Figure 6.6 – Overview of the molecular dynamics. Following XUV photoionisation, an NIR pulse can either lead to additional fragmentation or, if optimally time-delayed from the XUV, can give access to a stable dication. The start of the time-delay window within which the NIR has a stabilisation role is set by the characteristic time of a well defined shake-up process.**

a short time window, we do not expect these effects to remove enough energy from the system to open a pathway for stabilisation.

We find that, as described below, for a particular excited electronic state the characteristic shake-up time is compatible with the experimentally observed time delay. The shake-up process (illustrated in the level diagrams in Fig. 6.6) is purely driven by electronic correlation (two-body Coulomb interaction), not accounted for in standard TDDFT simulations [292]. Nevertheless, a simple estimation of the shake-up transition time can be obtained with a rate equation approach: the initial superposition of states created by the XUV pulse is calculated using ab-initio photoionisation probabilities, and Fermi's golden rule is used to obtain the shake-up rate due to the Coulomb interaction (see SI). Figure 6.7(a) shows the characteristic shake-up transition times for different bound excited orbitals (Kohn-Sham (KS) orbitals obtained with DFT ground-state calculations). Most of the values are of the order of few hundreds attoseconds except for three states, one of which (the LUMO+6 indicated in green) is 2.5 fs, very close to the experimentally observed delay of the dication formation. Interestingly, the energy of this orbital is in the window of two-photon

ionisation from the NIR pulse, which is in agreement with the experimental observation that two NIR photons are required for the stabilisation.

While the rate-equation approach is easy to understand and it provides a clear physical explanation of the experimental findings, it is an overly simplified description since it treats electronic correlations in first order perturbation theory and in a non-dynamical fashion and it lacks a first principles description of the XUV ionisation process. More refined and independent ab-initio calculations are required to further validate our interpretation and provide a predictive framework to address similar phenomena in other molecular complexes. To this end, we performed many-body time-dependent simulations from first-principles to take into account both the electron dynamics triggered by the XUV photo-ionisation and the absorption of a delayed NIR pulse. By solving the equations of motion for the non-equilibrium Green's function and using an efficient propagation scheme based on the generalized Kadanoff-Baym ansatz, we can obtain an accurate and controlled treatment of shake-up processes [265, 293] and describe the light-molecule interaction from first-principles using laser pulses with the same shape as in the experiment (see SI). It is important to point out that our simulations are well suited to the description of the electron dynamics but do not take into account the nuclear dynamics and therefore non-adiabatic effects (e.g conical intersections). From the calculations, we extract the orbital-resolved occupations and the spatial variation of the electronic density, all reported in Fig. 6.7. When only the XUV photoionisation is considered (Fig. 6.7b), we can confirm the results obtained with the rate equations: while most of the states exhibit sub-femtosecond rise-times, the LUMO+6 occupation (shown in green) rises over several femtoseconds due to a slow shake-up process. Fig. 6.7c shows snapshots of the change in electron density, induced by the XUV pulse. We notice a significant electronic charge inflation more than 3 Å away from the molecular plane that builds up over time. The spatial distribution of this density variation resembles the one of the LUMO+6 orbital (see SI) highlighting its dominant role in the overall electron dynamics. Furthermore, we could speculate that this rapid delocalisation far from the plane of the bonds allows for minimising the probability of bond breaking after photo-excitation. Our simulations indicate that LUMO+6 can only be accessed when ionisation is triggered by an XUV pulse polarised perpendicularly to the molecular plane. Therefore, the relative orientation between the molecule and the attosecond pulse can potentially be exploited to achieve more refined control of the stabilisation process.

Finally, we have included the NIR absorption in the simulation and calculated the time-resolved NIR-induced depletion, i.e. population reduction, of the LUMO+6 (Fig. 6.7d), for different pump-probe delays. The depletion shows an onset in the window of 2–4 fs and increases with larger delays. To clarify the delay dependence of the depletion, we calculate an average depletion over 1 fs window after the end of the NIR pulse and we plot it as a function of pump-probe delay in Fig. 6.7(e). The trend reproduces, remarkably, the one measured for the adenine dication yield (green solid line in Fig. 6.5). We point out that only the LUMO+6 state is characterised by this slow onset (other states in SI) and we can therefore conclude that the slow shake-up dynamics identified for

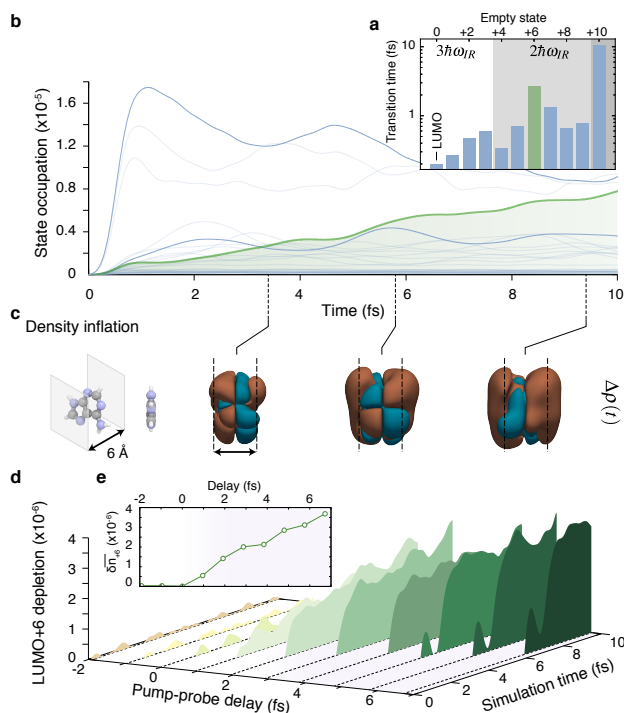


**Figure 6.7** – Identification of states involved in the stabilisation process. (a) Transition times to a given shake-up state calculated with a Fermi’s Golden rule approach. The LUMO+6 state is highlighted in green and shows a characteristic time of 2.5 fs. The states are ordered by energy and grouped (shades of gray) by the number of NIR photons (1, 2 or 3) required to ionise a second electron. The LUMO+6 state falls in the two NIR-photon group. (b) Time-dependent occupations of the adenine bound excited states after photoionisation by the XUV, calculated with the ab-initio non-equilibrium Green’s function method. The special state (LUMO+6), highlighted in green, is populated via a shake-up process and its population rises over several femtoseconds to one of the largest values. (c) Snapshots of the variation of the electronic density with respect to the density immediately after the XUV pulse. We observe that the electronic density inflates considerably away from the molecular plane. The noticeable inflation of the electronic density can be attributed to the increasing population of the LUMO+6 state, which also shows a similar inflated shape (see SI). (d) Temporal evolution of the LUMO+6 state depletion due to the combined action of XUV and NIR pulses as a function of the delay. The depletion shows a significant onset in the window of 2–4 fs and it keeps increasing with larger delays as shown in (e) where we report the state depletion averaged in a 1 fs window after the NIR pulse. The results in panels (c)–(e) are based on the non-equilibrium Green’s function method.

the LUMO+6 state explains why the NIR pulse has to be optimally delayed in order to produce the stable dication. To summarise, our theoretical calculations singled out a special excited state, described by one KS orbital, which mediates the observed laser assisted stabilisation process in photoionised adenine. The peculiarity of this LUMO+6 state can be attributed to the following characteristics: I) it has a few-femtoseconds shake-up time, compatible with the experimentally observed delay in the dication formation, II) it is a delocalised excited state that extends away from

the molecular plane and III) it couples very efficiently to the NIR pulse. Experimental findings indicate that the NIR pulse must be sent in a relative narrow time window ( $\tau_2 \approx 24$  fs) after ionisation to stabilise the molecule. Our simulations cannot describe at this stage what defines the length of this time-window, since we are not treating the combined electron and nuclear dynamics. We could however speculate that the observed decay rate is due to relaxation of this special excited state via vibronic couplings.

Control over molecular dissociation is fundamental to achieve new molecular functionalities. We have identified a robust and simple stabilisation mechanism based on a many body effect in a DNA base, where adding energy to the system actually opens a non-dissociative relaxation path. We have characterised the intrinsic time required for a specific shake-up process to occur, which to our knowledge has not been measured in real time for any polyatomic molecule before. A key aspect of the stabilisation mechanism is the efficient depletion of this particular shake-up state induced by a control NIR probe pulse. Our findings demonstrate that extreme time resolution is required for the real-time tracking of many-body effects and for acting on the system before it relaxes via non-adiabatic couplings. By complementing the experiments with covariant detection of electrons and ions and with the support of time-dependent many-body methods, which also account for the nuclear motion, we could identify ad hoc stabilisation pathways for different class of molecules. We envisage the possibility to extend this control scheme to larger molecules (including nucleobase pairs and nucleosides), thus paving the way to a new protection protocol against ionisation-induced damage.

## Acknowledgments

F.Ca. acknowledges support from the European Research Council under the ERC-2014-StG STAR-LIGHT (Grant Agreement No. 637756). F.L. and V.W. acknowledge the Fonds de recherche du Québec – Nature et technologies (FRQNT) and the National Science and Engineering Research Council (NSERC). V.W. acknowledges support from the Vanier Canada Graduate Scholarship (Vanier CGS) program. S. L. acknowledges support from the Alexander von Humboldt foundation. A. R. acknowledge financial support from the European Research Council(ERC-2015-AdG-694097). The Flatiron Institute is a division of the Simons Foundation. G.S. and E.P. acknowledge EC funding through the RISE Co-ExAN (Grant No. GA644076), the European Union project MaX Materials design at the eXascale H2020- EINFRA-2015-1, Grant Agreement No. 676598, Nanoscience Foundries and Fine Analysis-Europe H2020-INFRAIA-2014-2015, Grant Agreement No. 654360 and Tor Vergata University for financial support through the Mission Sustainability Project 2DUTOPI. J. B. G. acknowledge support from the EPSRC (UK) grant number EP/M001644/1.

## Chapter 7

# Femtosecond-resolved Rydberg states dynamics in chiral molecules

### 7.1 Introduction

Objects that are non-superimposable to their mirror image after any rotation, such as our hands, are said to be chiral. At the atomic level, the concept of chirality is important because despite having identical physical properties, each mirror image from a pair of chiral molecules of a given species – called enantiomer– can react differently with another chiral systems depending on its handedness. This chiral recognition plays an important role in many biological processes [294]. In pharmacology for example, a specific enantiomer can have medicinal properties while the opposite enantiomer be perceived as a toxin by a biological chiral receptor, requiring important precautions for the synthesis, separation and characterization of chiral compounds.

The study and characterization of enantiomers can be achieved with circularly polarized light (CPL), that is also chiral and for which the helicity defines its handedness. Circular dichroism (CD) is a common technique where the absorption difference ( $\Delta A = A_L - A_R$ ) between left- and right-CPL from a chiral sample is typically measured in the UV-visible spectral range. The method is particularly interesting to characterize the structure of proteins for instance [295]. Since a given enantiomer interacts preferentially with CPL of a given helicity, two different samples constituted of pure enantiomers will have CD values of same amplitude but opposite sign. Typical CD signal are however particularly low, on the order of  $10^{-3} - 10^{-5}$  relative to the total absorption ( $A_{tot} = A_L + A_R$ ). This is due to the fact that the CD signal is a product between electric and magnetic dipole interactions, for which the latter is particularly weak. To obtain a reasonable signal to noise ratio, CD therefore requires samples to be highly concentrated in solution and is thus unsuitable for the gas phase environment.

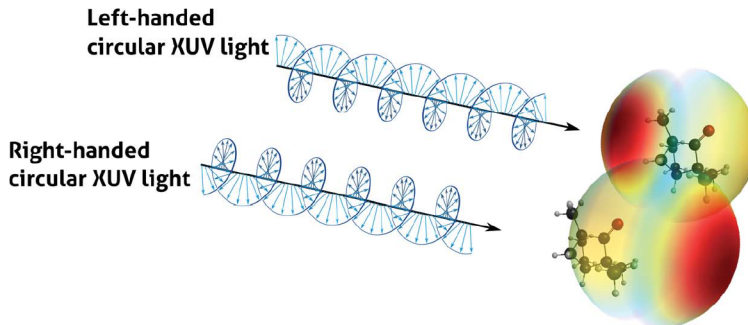


**Figure 7.1 – Principle of PECD.** The ionization of a chiral molecule by circularly polarized light creates an asymmetry in the forward/backward photoelectron angular distribution along the light propagation axis. Reversing the light helicity reverts the asymmetric distribution. Figure adapted from Beaulieu *et al.* 2016 [296].

To study chiral molecules in the gas phase, photoelectron circular dichroism (PECD) was first introduced theoretically by Ritchie *et al.* in 1976 [297] and experimentally demonstrated by Böwering *et al.* in 2001 [298]. Because this phenomenon is purely driven by electric dipole interactions, its magnitude can reach a few to several percents. In PECD, electrons that are photoionized from chiral molecules by circularly polarized light are ejected in a preferential emission direction along the beam propagation axis. The forward vs backward asymmetry in the emission direction depends both on the handedness of the enantiomer and on the helicity of the circular field (Fig. 7.1). The resulting photoelectron angular distribution (PAD) can be described in three dimensions by a series of Legendre polynomials:

$$D^p(E, \theta) = \sum_{i=0}^{2N} \beta_i^p(E) P_i(\cos(\theta)) \quad (7.1)$$

where  $N$  is the number of photons involved in the ionization scheme and  $p = \pm 1$  describes the left- or right-handed light helicity.  $P_i$  are the Legendre polynomials with their associated amplitude coefficient  $\beta_i$ . A photoelectron spectrum (PES) is defined by:

$$PES(E, \theta) = \frac{D^{-1} + D^{+1}}{2} \quad (7.2)$$

and the PECD characterizing the forward backward asymmetry is :

$$PECD(E, \theta) = \frac{D^{-1} - D^{+1}}{PES} \quad (7.3)$$

The energy ( $E$ )-dependent coefficient  $\beta_0(E)$  corresponds to the angle ( $\theta$ )-integrated PES. Even coefficients ( $\beta_{even}$ ) describe the symmetric part of the angular distribution (PES) along the light propagation axis while odd coefficients ( $\beta_{odd}$ ) describe the asymmetric part (PECD). A quantitative description of the asymmetry in terms of the  $\beta$  coefficients is given by [299]:

$$\beta - PECD(E) = \frac{1}{\beta_0} \left( 2\beta_1 - \frac{1}{2}\beta_3 + \frac{1}{4}\beta_5 - \frac{5}{32}\beta_7 + \dots \right) \quad (7.4)$$

Experimentally, the PAD is recorded with a velocity map imaging (VMI) spectrometer [300], that is schematized in Fig. 7.2. The laser focal volume where ions and electrons are generated is placed between two electrodes, a repeller consisting in a cylindrical metallic thin plate and an extractor that is drilled in the middle. These are followed by a third drilled electrode that is grounded. Few-kV voltages are applied to the repeller and extractor and the polarity is chosen depending whether ions or electrons are detected. Acting as an electrostatic lens, the VMI geometry focuses particles with identical initial momentum vector onto a specific point of a position sensitive two dimensional ( $x, y$ ) detector. From the center of the VMI image, the velocity of the charged particles increases linearly with the radius while kinetic energy scales with the square of the radius. The detector consists in a microchannel plate (MCP) coupled to a phosphor screen. A charged-coupled device (CCD) camera is used to record images from the phosphor screen. To reconstruct the three dimensional PAD and extract the  $\beta$  coefficients from the two dimensional projections acquired by the VMI spectrometer, the inverse Abel transform [301] can be used if the PAD possesses a cylindrical symmetry with respect to the detection plane. Different methods have been developed to perform the inverse Abel transform, such as the three-point method [302], the Basis Set Expansion (BASEX) method [303] and its equivalent in polar coordinates  $p$ BASEX [304].

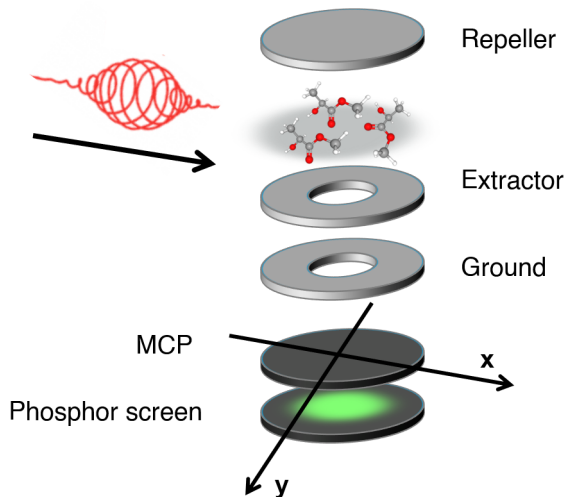


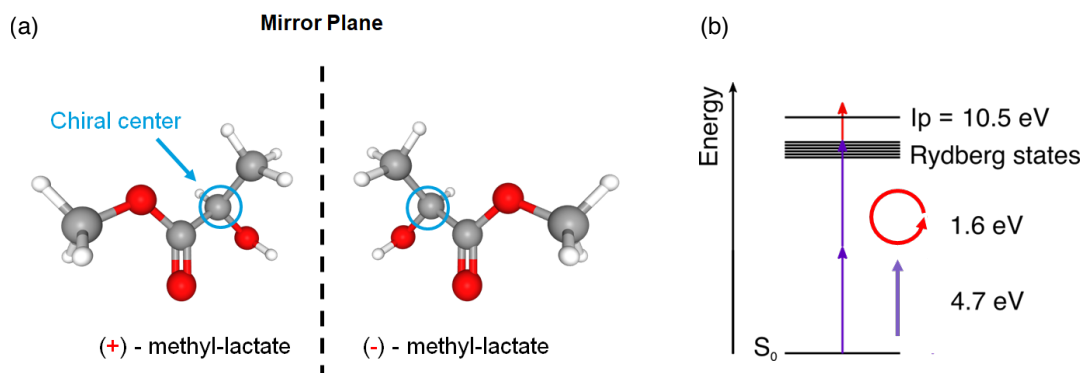
**Figure 7.2** – Scheme of the typical velocity map imaging detection system for PECD measurements.

Together with the first experimental measurements at BESSY (Berlin) [298], most of the early works regarding PECD were carried out at synchrotron facilities to demonstrate the capabilities of the technique to study chiral molecular structures. For instance, it was shown that PECD is sensitive to the ionized molecular orbital as well as to the final continuum state that is reached [305]. PECD is also efficient to identify chemical substitution [306] and molecular conformation [307, 308]. It can also distinguish isomers, i.e. molecules with identical molecular formula but with a different structure [309]. In 2015, I have participated to an experimental campaign at the SOLEIL synchrotron (France) during which we characterized the chiral response of fenchone and camphor isomers to circular vacuum ultraviolet (VUV) radiation. The work is not presented in this thesis but the results also confirmed the sensitivity of PECD to isomerism [310].

The examples described above demonstrate the potential of PECD for tracking dynamical changes in molecules. Such studies however require to use circularly polarized femtosecond pulses in order to provide sufficient temporal resolution to follow ultrafast molecular dynamics through pump-probe PECD measurements. In 2016, Comby *et al.* made a first demonstration of time-resolved PECD (TR-PECD) in chiral molecules. They tracked the relaxation dynamics of fenchone molecules photoexcited by UV-pump pulses (201 nm), probed with circularly polarized visible pulses (403 nm). Two distinct relaxation mechanisms could be observed, respectively with time constants of  $\sim 400$  fs (vibrational relaxation) and 3.28 ps (electronic relaxation). Because the temporal resolution of the experiment was limited to 170 fs, the observation of faster molecular dynamics was not possible.

## 7.2 Context of the work

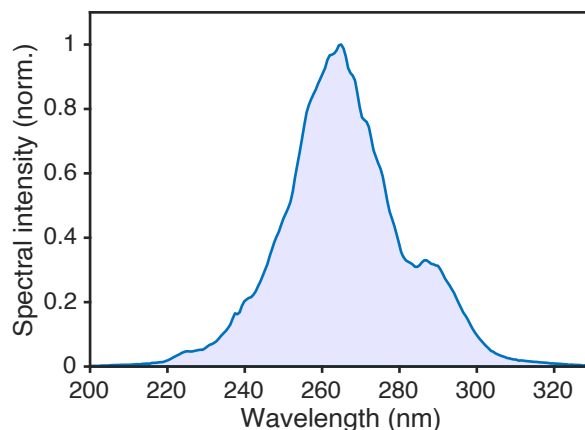
In June and September 2019, we performed a collaborative experiment with the Harmodyn group from the Centre Laser Intense and Applications (Bordeaux, France), namely Etienne Bloch (Ph.D. student), Bernard Pons, Yann Mairesse and Valérie Blanchet. The objective of the experiment was to study the ultrafast chiral dynamics of methyl-lactate, a derivative of lactic acid for which the enantiomers are shown in Fig. 7.3a. With the unique beamline that was developed during my thesis, the idea was to perform TR-PECD measurements by photoexciting the molecule with linearly polarized few-femtosecond UV pulses, and use circularly polarized IR pulses as a chiral probe during photoionization (Fig. 7.3b). Indeed, the beamline offers a temporal resolution that is currently not available at the institution of the Harmodyn team and provides the opportunity to study molecular dynamics occurring within few femtoseconds. For this work, I have been responsible for the construction and preparation of the experimental setup and also led the two experimental campaigns. I have carried out the data analysis together with Etienne Bloch – also main investigator during the experimental campaigns. A theoretical model is currently under development for reaching a final interpretation of the results that are presented in this chapter.



**Figure 7.3** – (a) The enantiomers of methyl-lactate. Oxygen atoms are shown in red, carbon atoms in grey and hydrogen atoms in white. (b) Experimental photoionization scheme. The ground state of methyl-lactate ( $S_0$ ) is excited by two linearly polarized UV (4.7 eV) photons near the ionization potential ( $I_p$ ) and the molecule is ionized by an additional circularly polarized IR (1.6 eV) photon.

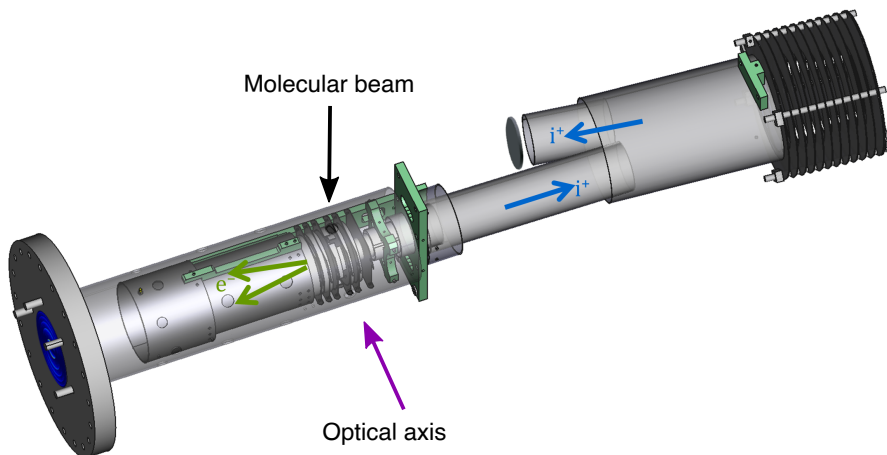
### 7.3 Experiment

The experiment was realized with a 1 kHz Titanium:Sapphire laser (FemtoPower, Spectra Physics), delivering 25-fs, 12-mJ pulses at 800 nm. 5.6 mJ were used for spectral broadening in a 1-m long hollow-core fiber filled with a gradient of helium gas. The pressure at the input side of the fiber setup was kept to  $\sim 1.8 \times 10^{-1}$  mbar, providing 1-mJ, 6-fs IR pulses at the entrance of the beamline that was described in article III. Using a beamsplitter, 30% of the beam was used for third-harmonic generation in argon gas which delivered the UV-pump pulses ( $\sim 120$  nJ) spectrally peaked at 265 nm (Fig. 7.4). The remaining part of the IR beam was focused in the experimental region by a toroidal mirror ( $f = 95$  cm) followed by a motorized quarter-waveplate in order to control the helicity of the circularly polarized probe pulses (6  $\mu$ J).



**Figure 7.4** – Spectral content of the UV pump pulses.

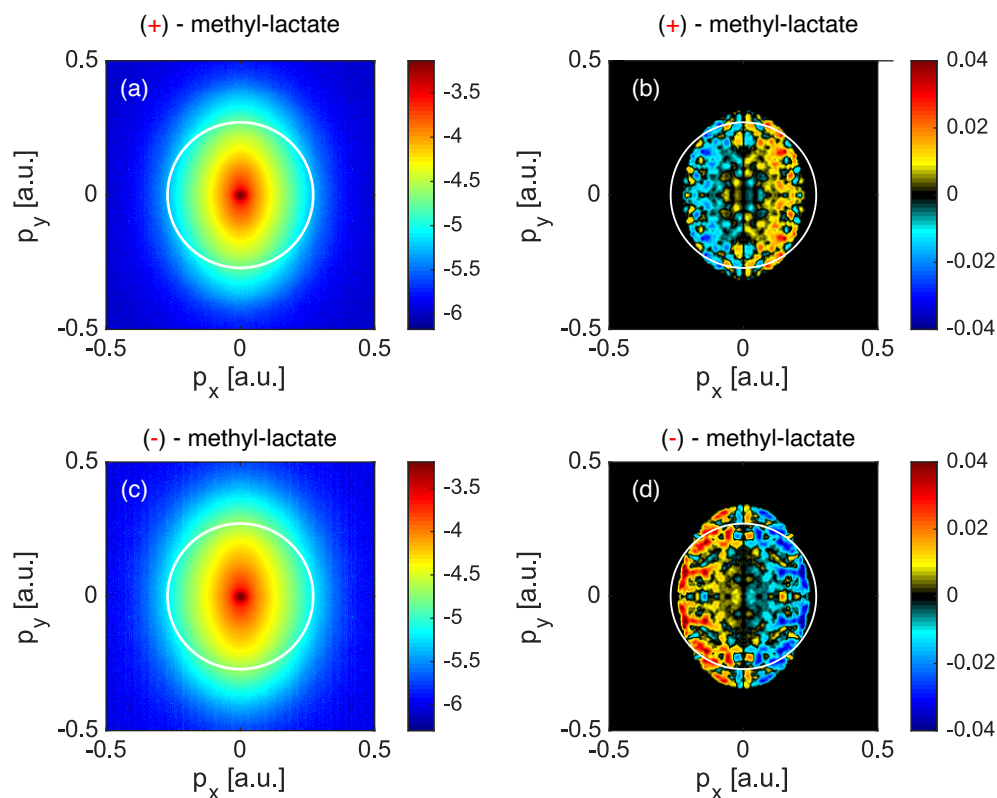
Liquid methyl-lactate was heated and evaporated to reach the experimental chamber through a 500  $\mu\text{m}$  needle. Fig. 7.5 shows a sketch of the detection system that was used for the measurements. It consists in a two-sided spectrometer which combines a VMI apparatus for recording the electron PADs, together with a reflectron side for the simultaneous detection of ion's time-of flight. This configuration allowed gaining additional information on the fragmentation dynamics of methyl-lactate under the experimental conditions. The voltages on the repeller and extractor were respectively -1.6 kV and -1.2 kV and the voltages on the reflectron's electrodes were adjusted in order to ensure a flat electric field in the hole of the electrode that acts as repeller for the electrons (through which the ions are extracted).



**Figure 7.5 – Double-sided spectrometer employed for the experiments. VMI images (left) and ion time-of-flight spectra (right) are acquired simultaneously**

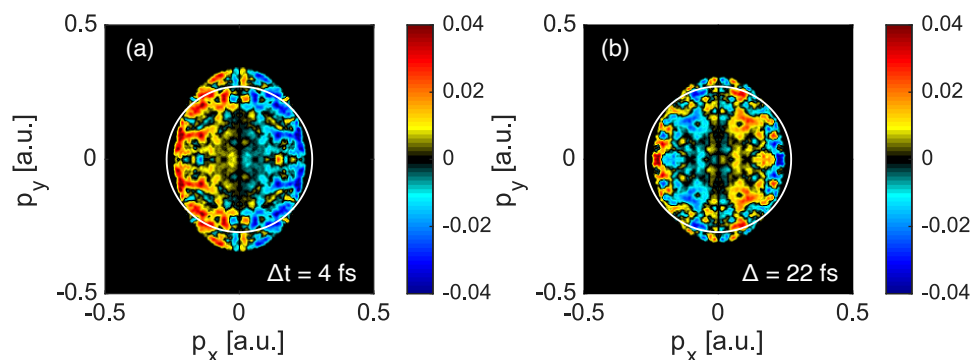
## 7.4 Results

Fig. 7.6 shows the PES and PECD for both enantiomers of methyl-lactate at the temporal overlap between the UV and the IR pulses, calculated from the raw two-dimensional projections obtained with the VMI spectrometer. While the typical PES is elongated along the laser polarization axis, no fine structure is observed and the signal monotonically decreases as a function of the photoelectron kinetic energy/momentum. The PECD was evaluated only for those pixels of the PES where the signal is at least 1.5% of the highest pixel's signal and the images were filtered by a two-dimensional Gaussian filter ( $\sigma = 1$  pixel). The white delimiting circles define a photoelectron kinetic energy region of 1 eV. Within this region the forward/backward asymmetry reverses sign when changing enantiomer. This first check was necessary to identify that the observed PECD corresponds to the chiral response of the molecule. Indeed, it was previously observed that an incorrect alignment of the spectrometer with respect to the laser focus can induce false asymmetries. A very careful positioning of the VMI electrodes relative to the laser focus position along the propagation axis was



**Figure 7.6** – PES (log scale) and PECD for both enantiomers of methyl-lactate. Note that the radial distribution describes the kinetic energy of the charged particles that is proportional to the square of the radius on the 2D detector. The white circles delimit a 1 eV region.

thus required. Finally, the difference in structure between the two PECD images can be attributed to acquisitions performed on two different days where the IR intensity was slightly different.



**Figure 7.7** – Time-resolved PECD of (-) - methyl-lactate at  $\Delta t = 4$  fs and  $\Delta t = 22$  fs. The white circles delimit a 1 eV region.

Following this verification, time-resolved measurements were acquired in (-) - methyl-lactate with an IR probe intensity estimated to  $\sim 2 \times 10^{12}$  W/cm<sup>2</sup>. Fig. 7.7 shows the PECD for time delays of the IR pulse corresponding to  $\Delta t = 4$  and  $\Delta t = 22$  fs. An evolution of the PECD within

the 1 eV region can be observed where the forward/backward preferential emission direction reverses within 18 fs. Such a dynamical inversion of PECD has never been observed before. However, it is well-known that PECD is sensitive to electronic and nuclear degrees of freedom [311]. For instance, it was observed that the PECD from successive vibrational levels can have opposite asymmetries [312]. As a first hypothesis, we therefore speculate that upon UV excitation, two different electronic states with opposite chiral responses might be competing, a first one which dominates at temporal overlap (Fig. 7.7a), the other one with a longer lifetime and that dominates at larger time delays (Fig. 7.7b).

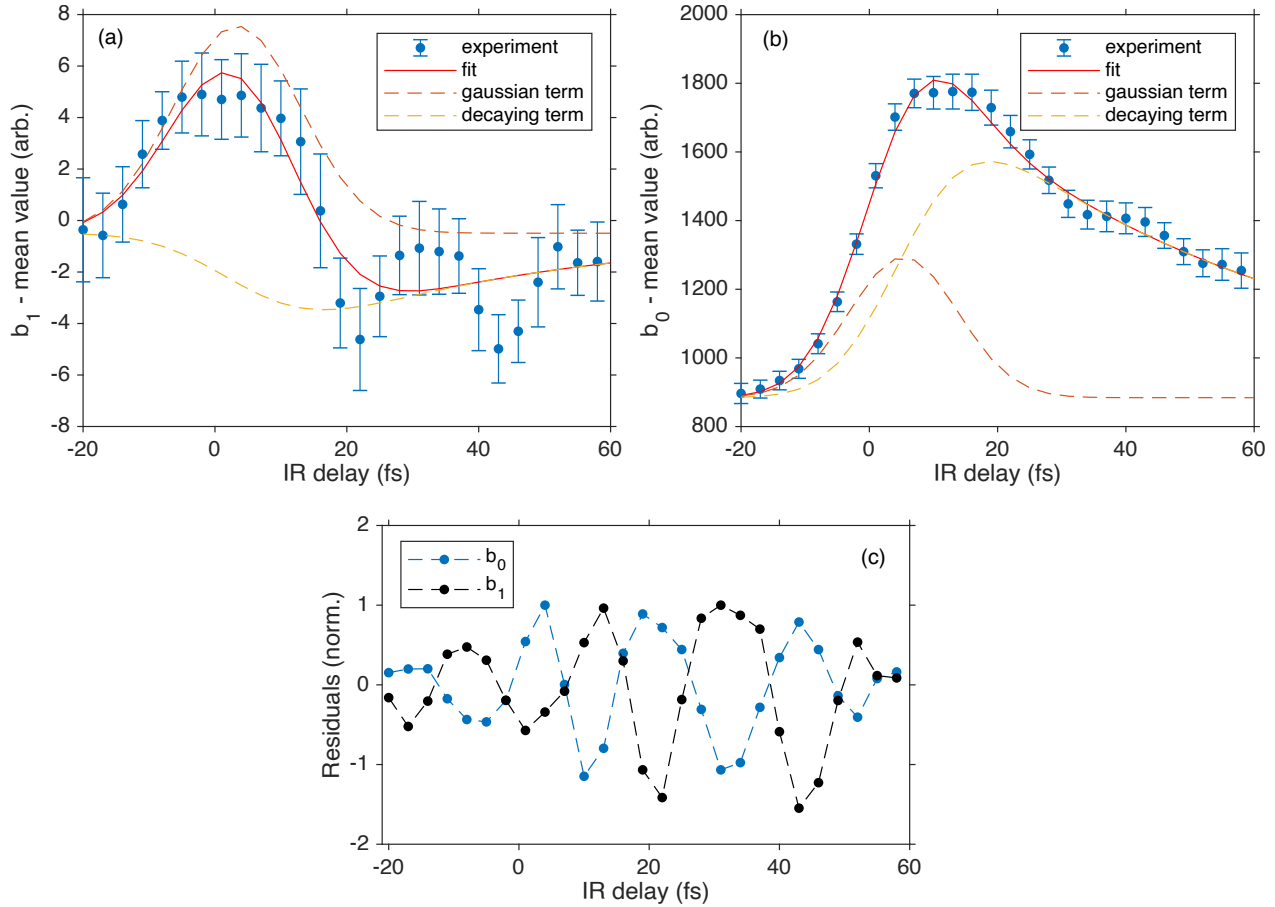


**Figure 7.8** – (a) Fit of the time-dependence for the energy-integrated  $\beta_1$  coefficient. (b) Fit for the time-dependence of the energy-integrated  $\beta_0$  coefficient. (c) Residuals obtained by subtracting the experimental data from the fits presented in (a) and (b).

To get further insight on the observed dynamics, an Abel inversion of the raw two-dimensional projections was performed in order to extract the time-dependence of the  $\beta$  parameters described by Eq. 7.1. A *p*BASEX algorithm implemented by Baptiste Fabre from the Harmodyn group was used. Fig. 7.8a (blue circles) shows the temporal evolution of the energy-integrated  $\beta_1$  averaged over 22 scans of the pump-probe delay. Each scan was smoothed by a Gaussian filter ( $\sigma = 3$  fs) and the standard error is shown. The curve was fitted with the following equation, comprising

a Gaussian term and an exponentially decaying term to describe the time-dependence of the two possible electronic states mentioned above:

$$f(t) = Ae^{-\frac{(t-t_0)^2}{2\sigma^2}} + B \left[ 1 + \operatorname{erf} \left( \frac{t-t_0}{\sqrt{2}\sigma} - \frac{\sigma}{\sqrt{2}\tau} \right) \right] \exp \left( -\frac{t-t_0}{\tau} + \frac{\sigma^2}{2\tau^2} \right) + C \quad (7.5)$$

where  $t_0$  corresponds to the pump-probe temporal overlap,  $\sigma$  is the standard deviation of the Gaussian instrument response function (IRF) defined by the convolution of the pump and probe pulses,  $\tau$  is the lifetime associated to the exponential term and  $C$  describes the background signal.  $A$  and  $B$  are coefficients that describe the amplitude of each contribution in the sum. From the fit (red curve), the values  $\sigma = 9.7$  fs and  $t_0 = 3.3$  fs are retrieved. Fig. 7.8a also shows the decomposition of the fit where one can see that the Gaussian (orange curve) and decaying (yellow curve) terms possess amplitude coefficients of opposite sign ( $A = 8.0$ ,  $B = -2.4$ ), leading to a negative  $\beta_1$  after about 20 fs. This model could therefore provide a possible interpretation to our results but has to be validated with numerical simulations. Fig. 7.8b shows the time-dependence of the energy-integrated  $\beta_0$ , corresponding to the total photoelectron yield. The experimental data (blue circles) can be fitted with Eq. 7.5 as well. From an independent fit, the retrieved values are in agreement with the results for the  $\beta_1$  coefficient ( $\sigma = 8.5$  fs and  $t_0 = 5.3$  fs). A combined fit in which shared parameters (such as  $\sigma$  and  $t_0$ ) between  $\beta_1$  and  $\beta_0$  could also be evaluated. It is also noted that, as for  $\beta_1$ , a modulation can be observed within the experimental data. Fig. 7.8c shows the residuals from the fits for both  $\beta_0$  and  $\beta_1$  when the experimental curve is subtracted from the fit. In each case, a period of  $\sim 20$  fs can be observed. Interestingly the modulations are also out-of-phase.

Fig. 7.9 shows the  $\beta$ -PECD calculated from Eq. 7.4 with (a) and without (b) the contribution from the  $\beta_3$  coefficient. The curves shows no significant difference, with an absolute variation of  $\sim 1.5\%$  between  $\Delta t = -5$  fs and  $\Delta t = 22$  fs. This comparison shows that the  $\beta$ -PECD is mainly described by the  $\beta_1$  coefficient. According to Eq. 7.1, the experimental ionization scheme involving 2-UV + 1-IR photons ( $N = 3$ ) allows contribution for coefficients up to  $\beta_5$ . However, as for the  $\beta_3$  described above, the  $\beta_5$  contribution was found negligible. Finally, additional analysis will be performed to evaluate the temporal evolution of the  $\beta$  parameters for specific kinetic energy regions for comparison with the energy-integrated results presented here.

## 7.5 Interpretation

To identify the molecular dynamics responsible for our experimental observations, a theoretical support is required. While the theoretical model is still under development during the writing of this thesis, the approach is presented here.

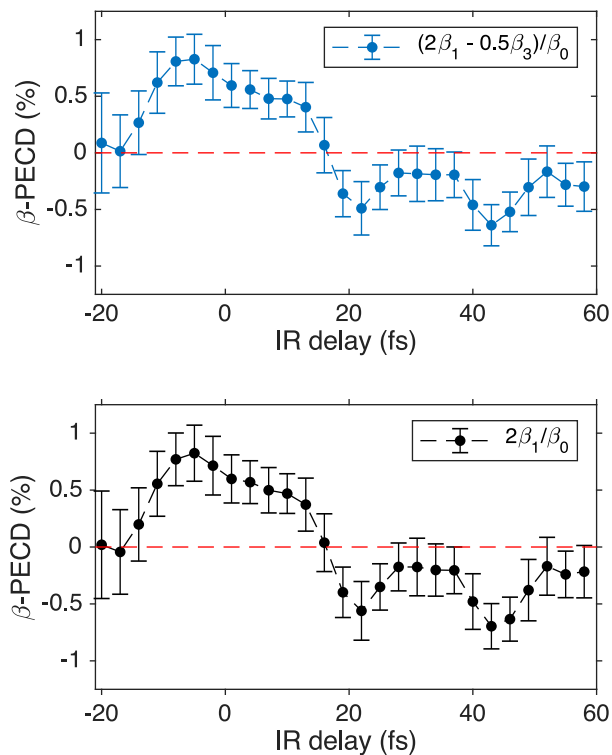


**Figure 7.9** – (a)  $\beta$ -PECD including  $\beta_3$ . (b)  $\beta$ -PECD without  $\beta_3$ .

In a first step, the two-photon excitation of methyl-lactate by the UV-pump pulse must be calculated. Thus, a detailed knowledge of the electronic states of the molecule in the energy region around 9.4 eV where the excitation occurs is necessary. The blue curve in Fig. 7.10 (black curve) shows the 1-photon absorption spectrum of methyl-lactate between 6 and 10.5 eV. It was measured by Nelson de Oliveira at the SOLEIL synchrotron on the DESIRS beamline in the context of this collaboration. Methyl-lactate having an ionization potential of 10.5 eV, the region around 9.4 eV contains several Rydberg states. To properly describe these delocalized states and reproduce the experimental absorption spectrum, a number of basis sets have been tested by Marie-Catherine Heitz and Nadia Ben Amor from the Laboratoire de Chimie et Physique Quantiques (Toulouse, France). The best result obtained by DFT calculations is shown by the blue curve of Fig. 7.10, corresponding to a 1-photon absorption spectrum described using a VTZ (valence triple zeta) basis set. The oscillator strength of the states was shifted by 50 meV and convoluted with a Gaussian with a standard deviation of 200 meV. While the experimental and theoretical curves are in good agreement, the computational cost to evaluate the two-photon absorption transition moments using this basis set is high. For this reason a modified VDZ (valence double zeta) basis set has been used<sup>1</sup>

<sup>1</sup>The exact basis set corresponds to a VDZDP (valence double zeta + diffuse + polarization) basis combined with a double Rydberg  $2s2p2d$  basis localized at the cation charge center. A  $f$  function with exponent 0.012 at the same charge center was included.

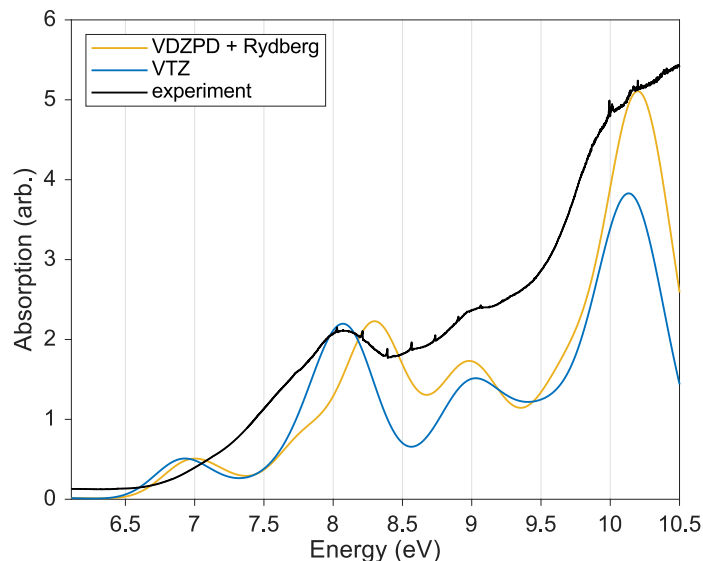


**Figure 7.10 – Experimental single-photon absorption spectrum (black line) and DFT calculated absorption spectrum with the VTZ (blue line) and VDZPD + Rydberg (yellow line) basis sets.**

(yellow curve). The agreement for energies above 9 eV validates that the description of the states in the 9.4 eV region is sufficiently robust to be used for the calculation of the two-photon excitation in our TR-PECD experiment.

Fig. 7.11a shows the spectral density corresponding to the experimental UV spectrum (blue line) used to simulate the excitation step in the PECD experiment, together with the calculated two-photon absorption transition moments of the considered electronic states (dashed dotted line). The corresponding spectrally weighted transition moments are shown in Fig. 7.11b, where the states with a dominant HOMO character are shown in red, and those with a dominant HOMO-1 character are shown in purple. The two orbitals are shown in Fig. 7.11c. The HOMO orbital with an  $I_p$  of 10.51 eV is localized on the alcohol group of the molecule while the HOMO-1 with an  $I_p$  of 10.67 eV is located on a lone pair of the carbonyl group.

The next step for the calculations will be to evaluate the PECD signal from each of these two orbitals in order to evaluate if the sum of their contribution can reproduce the experimental observations. The formalism of the theoretical approach can be found in Refs. [313, 314]. The aforementioned approach could provide a mechanism that is purely driven by electron correlations. Alternatively, because the dynamics occurs over a few tens of femtoseconds it cannot be discarded that nuclear dynamics may also play a role. Notably, the vibrational period of carbonyl (C=O) is about 20 fs, also matching the experimental oscillation period (see Fig. 7.8c). Charge resonance enhanced ionization (CREI) is a well-known process where the ionization rate increases at a specific internuclear distance in molecules [189, 187, 188]. Similarly, it is thus also possible that the observed modulation of the ionization rate (associated to  $\beta_0$ ) depends on the time-dependent C=O bond

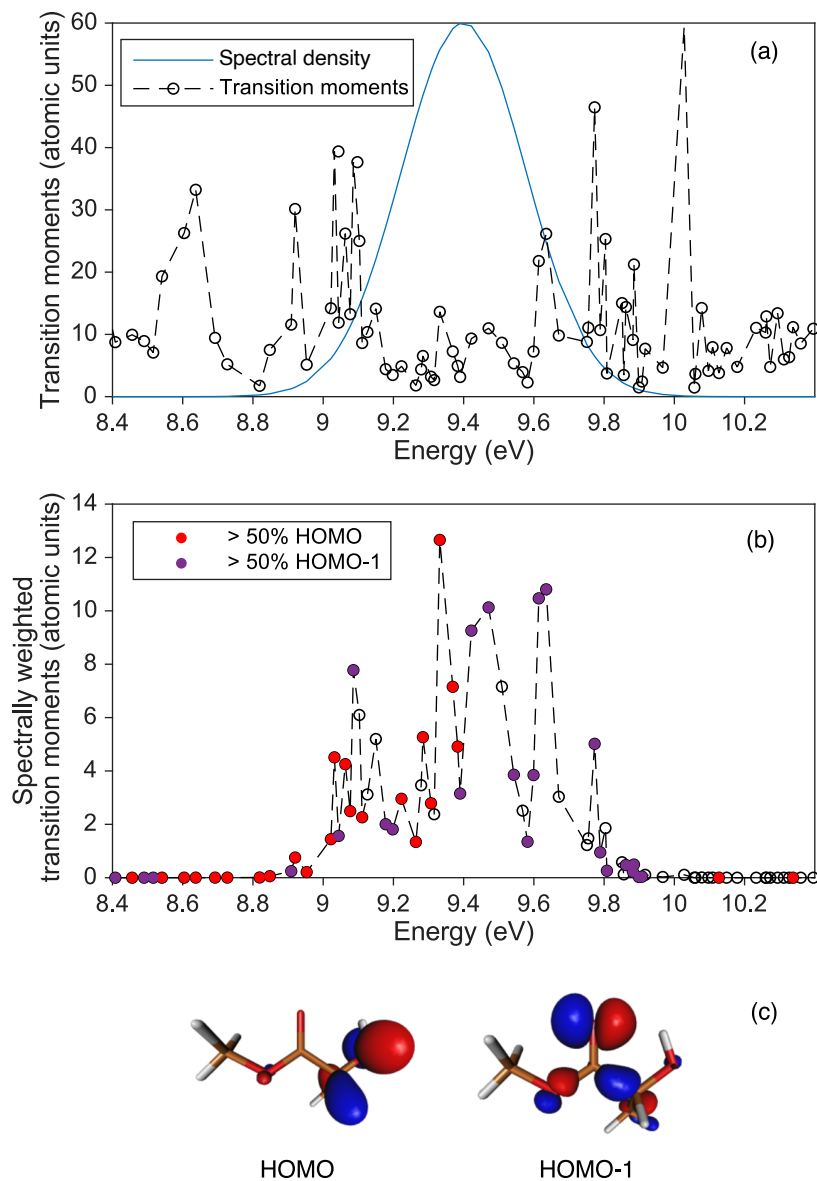


**Figure 7.11** – (a) Transition moments for the two-photon absorption (dotted) of methyl-lactate between 8.4 and 10.4 eV. The spectrum considered for the excitation step is shown by a blue line. (b) Relative transition moment amplitude for the electronic states within the region of the excitation spectrum. (c) HOMO and HOMO-1 orbitals of methyl-lactate.

elongation. More advanced calculations including nuclear dynamics would in this case be necessary to properly describe the experimental observations.

## 7.6 Conclusion

In this chapter we demonstrated the capability of our new beamline to perform time-resolved experiments using few-femtosecond UV pulses. We used PECD to study the chiral dynamics of methyl-lactate upon UV excitation. An inversion of the forward/backward electron emission occurs after about 20 fs, a time scale for which our pump-probe setup offers sufficient temporal resolution. This inversion of PECD may be explained by a competition in the chiral response between two different orbitals, each dominating at distinct time delays. Theoretical calculations are currently performed in order to confirm or discard this interpretation. Additionally, an oscillating behavior with a period of about 20 fs was observed for both the  $\beta_0$  and the  $\beta_1$  coefficients. The results demonstrate that the chiral response of methyl-lactate upon UV excitation is relatively complex and depends on a relaxation scheme that possibly involves both nuclear and electronic degrees of freedom. The high sensitivity of PECD can be used to disentangle this complex dynamics.

Although it was not exploited during our experiments, the double-sided spectrometer that was employed allows for covariance measurements [163]. Applying this method in combination with PECD would provide further information concerning the cationic states that are involved in the dynamics. Covariance however requires synchronized single shot measurements of both VMI images and mass spectra, which was not implemented at the time of the experiments.



## Chapter 8

# General conclusions and perspectives

The work presented in this thesis demonstrates the versatility of the femtosecond laser technology for manipulating light properties in order to address ultrafast dynamics of matter over a broad range of topics, from the gas phase to the solid state. Starting from Ti:Sapphire lasers emitting at about 800 nm, the generation of ultrashort laser pulses was demonstrated over different spectral ranges, including the mid- and near-infrared, the ultraviolet and extreme ultraviolet as well as the soft x-ray spectral domains: (i) Through the development of a high-energy optical parametric amplifier followed by a post-compression scheme using a stretched hollow-core fiber, the production of 5 mJ, 12 fs pulses at 1800 nm (two optical cycles) was demonstrated. The high-energy OPA was also employed for the generation of soft x-ray in the water window between 284 and 543 eV with sufficient photon flux for single-shot measurements at the carbon *K*-edge. (ii) Starting from 5 fs pulses at 770 nm obtained via hollow-core fiber post-compression, the generation of ultrabroadband sub-2-fs UV pulses centered at 255 nm with 150 nJ energy was demonstrated using quasi dispersion-free third-harmonic generation in argon gas. The light source was integrated into a beamline also providing isolated attosecond XUV pulses with photon energies between 15 and 50 eV that were produced by polarization gated high-harmonic generation.

Each of the spectral domains described above possesses unique properties to address specific problems in ultrafast spectroscopy, of interest in fields ranging from physics, photo-chemistry and photo-biology to materials science. Hence, by tailoring the light properties through frequency conversion, as well as via the manipulation of the polarization state and waveform of the electric field of femtosecond laser pulses, a number of dynamics have been investigated:

The utilization of ultrashort laser pulses at 1800 nm allowed revisiting the control of photo-chemical reactions via tailoring of the waveform of the electric field, in the particular case where a longer optical period (6 fs) compared to 800 nm pulses (2.7 fs) approaches the vibrational periods in molecules. Through waveform shaping using a two-color scheme, an enhanced level of control was

obtained for the prototypical electron localization during the dissociative ionization of molecular hydrogen.

With a photon energy (0.69 eV) that is well below the bandgap energy of a number of semiconductor and dielectric materials, the application of the two-color method at 1800 nm also enabled to investigate the control of strong-field ionization in condensed matter. By borrowing concepts from molecular science, we exploited a fundamental property of asymmetric systems – the permanent polarization – to control the ionization rate in lithium niobate ( $\text{LiNbO}_3$ ), observed via femtosecond laser-induced ablation measurements. The results can potentially open new perspectives for the control of the HHG process in ferroelectric materials. It was also shown that the symmetry properties of the crystal can be probed by studying the ablation process in the tunneling regime as a function of the orientation of the linearly polarized 1800 nm field relative to the crystal axes.

The control of photo-chemical processes was further extended to large biomolecules by studying the molecular response of the adenine nucleobase following attosecond XUV photoionization. Here, by using a pump-probe scheme, it was possible to identify a path where an intact adenine dication can be produced by synchronizing with high precision (2.3 fs) a NIR probe after the occurrence of a shake-up dynamics that was observed in the polyatomic molecule. Finally, by replacing the typical isolated attosecond XUV pump pulses (15–35 eV) by few-femtosecond UV pulses (4.7 eV) for pump-probe measurements, we demonstrated the access to neutral state dynamics of bio-relevant molecular system with high temporal resolution. Using photoelectron circular dichroism, we observed an inversion of the forward/backward photoelectron angular distribution in methyl-lactate, taking place about 20 fs following UV excitation. The underlying molecular relaxation mechanism responsible for this inversion of chiral response still needs to be elucidated.

The above results show that understanding the mechanisms underlying ultrafast processes often leads to a mean of controlling these very same processes. Starting from the control of simple systems such as molecular hydrogen, the level of complexity was increased towards ferroelectric materials ( $\text{LiNbO}_3$ ) and bio-relevant molecules (adenine and methyl-lactate). As a perspective, the study of even larger molecular systems can be envisaged. However, due to the increasing size and complexity of molecular structures, advanced detection schemes become mandatory. Upon photoionization, the energy and angular distribution of the generated photoions and photoelectrons contain rich information about a molecular dynamics. Coincidence detection schemes, where the momentum vector ( $p_x, p_y, p_z$ ) for each charged particle is obtained, can identify particles issued from the same molecule and offer the opportunity for interpreting more complex dynamics. In this case, apparatus for coincidence detection imaging based on the concept of reaction microscope [315, 316] must be employed but require operation at high repetition rate ( $>100$  kHz) to perform experiments in a reasonable amount of time with high statistics [317]. Therefore, the next challenges in ultrafast spectroscopy not only require efforts in generating pulses with reduced duration, but also in producing such pulses at high repetition rate with sufficient photon flux.

The development of high repetition rate, high average power laser systems based on ytterbium-doped gain media is rapidly emerging and overtaking the Ti:Sapphire technology, paving the way to achieve these challenges. The generation of ultrashort UV pulses at high repetition rate, combined with coincidence detection imaging, will open new perspectives to investigate the interplay between nuclear and electronic degrees of freedom in neutral biomolecules with extreme temporal resolution, and will provide an unprecedented amount of information for their interpretation. In addition, manipulating the polarization state of ultrabroadband UV pulses will provide access to the chiral character of a number of biomolecules via photoelectron circular dichroism measurements for instance. Finally, the generation of high flux, high repetition rate, high-order harmonics will surely benefit expanding the capabilities of attosecond science. There is still a lot to do.



## Part II

# Résumé de la thèse en français



# Imagerie et contrôle de dynamiques femtosecondes par impulsions laser ultra-brèves: des gaz aux solides

Suivant les normes linguistiques de l'INRS, cette section contient un résumé en français pour chaque article présenté dans ce document de thèse.

## 9.1 Article I - Impulsions de 0.42 TW et 2 cycles optiques à 1.8 $\mu\text{m}$ par compression dans une fibre creuse

Tel que décrit à la section 2.1, la durée d'impulsion des lasers Ti:Sapphire multi-mJ est généralement limitée à environ 25 fs [20]. Pour réduire davantage cette durée, les impulsions doivent subir un élargissement spectral supplémentaire, pouvant être obtenu par automodulation de phase (SPM) dans une fibre creuse (HCF) [22]. L'utilisation de HCFs rigides pour l'obtention d'impulsions multi-mJ à 800 nm de quelques cycles optiques est une méthode maintenant bien établie.

Comme alternative aux HCFs rigides, il est possible d'utiliser des HCFs flexibles de plusieurs mètres de long avec un coeur de grande taille, plus facile à fabriquer. Nagy *et al.* ont démontré un schéma où une telle fibre flexible peut être mécaniquement étirée, assurant une bonne transmission et montrant des résultats prometteurs dans l'infrarouge proche [38, 40]. Dans l'article I, nous démontrons les capacités de la technologie HCF flexible pour la génération d'impulsions à 1800 nm de quelques cycles optiques, dans le but d'augmenter la puissance crête disponible dans cette région spectrale. Dans ce contexte, nous examinons la dépendance en longueur d'onde des paramètres pertinents lors de la post-compression par fibre creuse, tels que l'indice de réfraction non linéaire  $n_2$ , la contribution du plasma à l'indice de réfraction, l'atténuation du guide d'ondes et la puissance critique pour l'autofocalisation. Notamment,  $n_2$  à 1800 nm n'est que 60 % de la valeur à 800 nm (tableau 2.1). Une augmentation de l'intensité laser ou de la densité du gaz pourrait compenser cet effet, mais augmenterait en même temps les pertes dues à une augmentation de l'indice de

réfraction du plasma, qui est plus important pour les grandes longueurs d'onde. Pour cette raison, il est préférable d'allonger la longueur de propagation pour le processus d'automodulation de phase. Expérimentalement, le système OPA décrit dans la Sec. 2.2 a donc été couplé à une fibre creuse de 3 m de long et de 1 mm de diamètre, remplie d'un gaz d'argon (Fig. 2.6). Un gradient de gaz le long de la fibre a été utilisé, avec une densité de gaz décroissante vers l'entrée afin de minimiser l'ionisation. En évaluant l'énergie en sortie de fibre en fonction de l'énergie à l'entrée (Fig. 2.7), des impulsions de 5 mJ ont été obtenues pour l'énergie d'entrée maximale disponible de 11 mJ, ce qui correspond à un rendement de 45 %. La figure 2.8 montre l'élargissement spectral résultant et la caractérisation temporelle des impulsions. La compression avec des fenêtres de silice fondue dans le régime de dispersion anormale a permis de compresser les impulsions à 12 fs (deux cycles optiques) avec 5 mJ d'énergie/impulsion.

Le travail décrit à l'article I a été en partie réalisé afin d'optimiser une source de rayons X mous ayant été développée au Laboratoire de sources femtosecondes « Advanced Laser Light Source » (ALLS). Bien que, dans le cadre de la thèse, cette optimisation n'ait pas été effectuée avec les impulsions de 12 fs provenant du système de fibre creuse flexible, les impulsions de 30 fs provenant directement de l'OPA à haute énergie ont préalablement été utilisées pour développer cette source de rayons X mous. L'article complet n'est pas présenté dans cette thèse [82], mais les résultats principaux sont décrits à la section suivante.

## 9.2 Article supplémentaire - Auto-guidage de la génération d'harmonique dans la fenêtre de l'eau

Nous avons développé à ALLS une source de rayons X mous à haut flux à partir d'impulsions lasers centrées à 1.8  $\mu\text{m}$ . Pour obtenir un milieu générateur de haute densité, une cellule de gaz de 8 mm de longueur a été interfacée à une vanne Parker pulsée fonctionnant à 100 Hz et pour laquelle le temps d'ouverture a été optimisé. Un gaz d'hélium à haute pression a été utilisé. La vanne a été synchronisée avec le système OPA décrit à la section 2.2, délivrant des impulsions de 8 mJ d'une durée de 30 fs. Une géométrie de focalisation longue a été utilisée avec une lentille de 60 cm. La figure 2.14 montre les spectres harmoniques qui ont été obtenus, s'étendant de 100 à environ 550 eV et couvrant ainsi toute la fenêtre de l'eau. L'énergie de coupure obtenue est en accord avec les prédictions théoriques considérant la durée de nos impulsions et la longueur d'onde fondamentale [78, 79]. Pour calibrer les spectres, une série de filtres a été utilisée: un filtre de Mylar (polyéthylène téréphtalate) de 200 nm d'épaisseur pour identifier le seuil  $K$  du carbone à 284 eV et un filtre de titane (Ti) de 200 nm d'épaisseur pour identifier le seuil  $L_2$  du Ti à 460 eV. L'encadré montre la région du seuil  $K$  de l'oxygène à 543 eV lors de l'utilisation d'un filtre d'aluminium. Pour démontrer les capacités de la source pour des mesures résolues en temps dans la fenêtre de l'eau, la figure 2.15 montre également des mesures mono coups acquises avec le filtre Mylar. Une coupe nette au seuil  $K$

du carbone est visible dans les spectres. En utilisant une caméra CCD XUV (PI-MTE, Princeton Instruments), un flux de photons de  $8 \times 10^4$  photon/coup a été mesuré pour la région de la fenêtre de l'eau.

### 9.3 Article II - Génération d'impulsions ultraviolettes sub-2-fs

Dans l'article II, nous décrivons notre approche pour la génération d'impulsions UV de quelques femtosecondes par génération de troisième harmonique (THG) à partir d'impulsions de 5 fs (770 nm) obtenues par post-compression dans une fibre creuse. En tenant compte des restrictions décrites dans la section 3.1 pour limiter la dispersion, nous discutons de l'utilisation d'une cellule en verre pouvant supporter une pression de gaz importante afin d'améliorer l'efficacité de conversion du processus THG (Figure 3.5b,c). Nous avons étudié la mise à l'échelle de l'énergie et de la largeur spectrale des impulsions UV (Figure 3.6) en fonction de la pression pour le gaz d'argon. Pour une pression absolue supérieure à 1.1 bar, nous constatons une saturation de l'énergie d'impulsion lorsque l'ionisation et les effets du plasma deviennent dominants. Avec 1.1 bar d'argon, une énergie d'impulsion de 150 nJ avec un rendement de conversion de  $10^{-4}$  sont obtenus. À cette pression, nous obtenons un important élargissement spectral, correspondant à une limite de Fourier (TL) de 1.45 fs. En raison de cette très large bande spectrale, la caractérisation temporelle des impulsions UV ne peut pas être facilement réalisée avec les techniques optiques conventionnelles dans lesquelles le milieu de transmission introduirait une dispersion importante. Pour cette raison, nous présentons une caractérisation temporelle de la durée des impulsions en utilisant une méthode de corrélation croisée dans un gaz de xénon. Avec un spectromètre de masse à temps de vol, le signal des atomes photoionisés en fonction du délai entre une impulsion pompe UV et une impulsion sonde NIR est mesuré. Une durée d'impulsion de 1.9 fs est obtenue.

Pour mettre ce résultat en perspective, une comparaison avec la littérature récente est présentée dans Table 3.2. Chaque technique présentée exploite un milieu gazeux pour la génération d'impulsions UV. Tout comme la technique d'émission d'ondes de dispersion dans les fibres à cristal photonique (PCF), l'exploitation du processus THG dans les gaz peut fournir des impulsions inférieures à 3 fs avec des énergies de l'ordre du nanojoule. Une autre technique intéressante pour obtenir des impulsions courtes a été reportée par Reislöhner *et al.* 2019 [101], mais l'énergie des impulsions au niveau pJ n'est pas suffisante pour nos applications spectroscopiques. Travers *et al.* 2019 ont également démontré des performances impressionnantes en utilisant l'émission d'ondes dispersives à l'aide de PCFs [155], mais nous notons que dans ce cas, la durée d'impulsion de 1.2 fs a été corrigée en considérant des matériaux dispersifs présents dans l'appareil de mesure. Par rapport aux travaux susmentionnés, la particularité de notre source d'impulsions UV ultracourtes est qu'elle a été intégrée à notre nouvelle ligne de lumière attoseconde pour réaliser des expériences résolues en temps, celle-ci étant décrite dans l'article III.

## 9.4 Article III – Ligne de lumière versatile combinant des impulsions attosecondes XUV avec des impulsions UV et infrarouges proches de quelques femtosecondes pour expériences résolues en temps

Dans cet article, nous fournissons une description détaillée de la ligne de lumière attoseconde qui a été construite pendant la majeure partie de la thèse. La nouveauté de cette ligne de lumière réside dans la combinaison des impulsions UV de quelques fs décrites dans l'article II, avec des impulsions attosecondes isolées XUV et des impulsions NIR de quelques cycles optiques. Nous présentons les aspects techniques du fonctionnement de la ligne de lumière ainsi que les performances de chaque composant.

La plupart des lignes de lumière attosecondes combinent des impulsions XUV avec des impulsions NIR de quelques cycles optiques pour étudier des dynamiques en phase gazeuse ou solide [136, 140]. Une autre classe de lignes de lumière combine des impulsions NIR avec des impulsions attosecondes dans le domaine spectral des rayons X mous, généralement pour des expériences d'absorption transitoire attoseconde dans la fenêtre de l'eau (décrite au chapitre 1). Ici, notre objectif est d'étudier avec une résolution temporelle sans précédent les dynamiques de molécules d'intérêt biologique qui sont déclenchées par une excitation à l'aide de rayonnement UV. Avec notre ligne de lumière, l'étape de sondage peut être effectuée soit en utilisant des impulsions NIR de quelques cycles optiques, soit des impulsions attosecondes isolées XUV.

L'un des principaux défis consistait à travailler dans un environnement sous ultra-haut vide, constitué de six chambres à vide différentes (Fig. 3.8). D'abord pour éviter la dispersion des impulsions UV mais également afin d'empêcher l'absorption du rayonnement XUV. Afin de préserver un bon niveau de vide malgré la forte pression de gaz requise pour le processus THG, la cellule de gaz hautement pressurisée (Fig. 3.9) est placée dans un système de pompage différentiel à trois niveaux (Fig. 3.10). Cette configuration nous permet d'atteindre  $10^{-3}$  mbar dans la chambre à vide où le processus THG se produit tout en ayant en même temps plusieurs Bar à l'entrée de la cellule de gaz. De cette façon, une pression finale de  $10^{-7}$  mbar est obtenue dans la chambre de sortie de la ligne de lumière qui est interfacée avec un appareil expérimental permettant la détection de particules chargées. Celle-ci requiert un tel niveau de vide afin de réaliser nos expériences.

Une autre difficulté rencontrée lors du développement de la ligne de lumière est la très grande consommation de gaz requise pour le processus THG. Afin d'éviter des opérations coûteuses, nous avons développé un système de recyclage de gaz pour collecter et recomprimer le gaz THG résiduel. Nous présentons les performances de ce système avec une efficacité de 96 % (Fig. 3.11). Ce montage pourra notamment être transposé vers d'autres applications nécessitant de fortes consommations de gaz, tel la génération d'impulsions attosecondes dans la région des rayons X mous [25, 83].

Nous décrivons ensuite la génération d'impulsions XUV grâce à la génération d'harmonique d'ordres élevés (HHG) ainsi que la configuration optique permettant d'isoler les impulsions attosecondes, en utilisant la technique de porte de polarisation (PG) décrite dans la section 3.2. La dépendance des spectres XUV en fonction de la phase de la porteuse (CEP) de l'impulsion à 800 nm est démontrée afin d'identifier les impulsions d'attosecondes isolées (Fig. 3.15).

Nous présentons également le spectromètre XUV de la ligne de lumière qui a été conçu en collaboration avec Luca Poletto et Fabio Frassetto du CNR-IFN, Italy (Fig. 3.14). En combinant un réseau de diffraction conventionnel avec un miroir cylindrique divergent, nous montrons qu'il est possible d'obtenir un spectromètre très compact (80 cm) tout en conservant un long bras d'entrée nécessaire à l'insertion de chambres de détection expérimentales de grande taille.

Enfin, nous décrivons notre approche pour obtenir une stabilité du délai pompe-sonde de l'ordre de l'attoseconde au sein du montage interférométrique dont le parcours optique est de 5.75 m. En compensant les dérives thermiques et les instabilités mécaniques pouvant affecter la ligne de lumière, nous obtenons une stabilité de délai inférieure à 20 attosecondes sur 11 heures d'acquisition (Fig. 3.16).

## 9.5 Article IV – Contrôle cohérent de l'ionisation dissociative dans $D_2/H_2$ à l'aide d'un champ laser à deux couleurs dans l'infrarouge moyen

À l'article IV, nous appliquons les concepts décrits dans la section 4.1 pour contrôler la densité électronique pendant la dissociation de  $H_2^+$  et de  $D_2^+$ . Nous combinons un champ laser à 1800 nm et son second harmonique (SH) à 900 nm pour coupler l'état fondamental de l'ion ( $1s \sigma_g$ ) et son premier état excité ( $2p \sigma_u$ ) (voir article Fig. 4.3). Pendant la dissociation, l'électron unique de la molécule peut être sélectivement localisé par le champ laser sur l'un des deux atomes d'hydrogène avec une efficacité donnée, de la même manière que sur la figure 4.1. Deux aspects ont motivé notre intérêt pour l'étude de cette réaction prototype:

Ray *et al.* 2009 ont réalisé une expérience similaire à deux couleurs en utilisant des impulsions laser combinant un champ à 800 nm et son SH à 400 nm [172]. Notre premier objectif était de vérifier l'influence de l'utilisation de plus grandes longueurs d'onde pour localiser sélectivement l'électron. Aussi, comme alternative à l'utilisation d'un champ laser à deux couleurs pour contrôler la localisation de l'électron dans l'ionisation dissociative de l'hydrogène moléculaire, plusieurs expériences ont utilisé des impulsions stabilisées en phase de l'onde porteuse (CEP). Ces expériences ont été réalisées indépendamment à une longueur d'onde de 800 nm [173, 174, 175] et à 2.1  $\mu\text{m}$  [176]. La complétion de la série d'expériences mentionnées précédemment a permis de tirer des conclusions supplémentaires et de mieux comprendre la réaction cette réaction prototype.

Les résultats présentés dans Wanie *et al.* 2016 confirment que l'utilisation de champs laser à deux couleurs (1800 & 900 nm), comparativement à des impulsions stabilisées en CEP, permettent un meilleur contrôle de la localisation de l'électron dans la molécule [177], ce qui corrobore l'observation faite par Ray *et al.* 2009 [172]. En effet, toutes les expériences ci-dessus utilisant des impulsions stables en CEP font l'objet d'un niveau de contrôle plus faible. De plus, il a été observé qu'un champ laser deux couleurs à des longueurs d'onde supérieures à 800 nm permet de contrôler un canal de dissociation supplémentaire dans la molécule.

Les résultats expérimentaux ont également été comparés avec des calculs solvant l'équation de Schrödinger dépendante du temps (TDSE) pour l'ion moléculaire, en utilisant l'intensité évaluée expérimentalement de nos impulsions laser. Bien qu'un accord qualitatif ait été obtenu pour reproduire les résultats expérimentaux, les calculs démontrent que la composition initiale du paquet d'ondes nucléaires (NWP) préparé sur l'état  $\sigma_g$  joue un rôle crucial dans la localisation de l'électron pendant la dissociation. Le principe de Frank-Condon (FC) est un concept qui permet de décrire la distribution des fonctions d'ondes vibrationnelles peuplées suite à une transition électronique dans une molécule. La distribution est obtenue en supposant une transition électronique verticale qui est instantanée par rapport au mouvement nucléaire et pour laquelle il n'y a pas d'échange d'énergie avec les noyaux. La phase relative initiale entre chacune des composantes vibrationnelles est donc nulle. Notre travail suggère que les conditions expérimentales ne suivent pas le principe de Franck-Condon, car le meilleur accord avec les résultats expérimentaux n'est pas obtenu avec une distribution FC. En effet, en utilisant une approche pompe-sonde, des travaux ont démontrés que le NWP initial sur  $H_2^+$  peut se former sur une échelle de temps d'environ 1 fs, les composantes vibrationnelles ayant ainsi différentes phases [178].

## **9.6 Article V – Dépendance en polarisation laser de l'ionisation en champ fort du niobate de lithium**

**&**

## **Article VI – Contrôle de l'ionisation en champ fort dans le niobate de lithium : rôle de la polarisation spontanée**

Dans les articles V et VI, nous effectuons des mesures d'ablation laser pour étudier la réponse d'ionisation en champ fort de cristaux de niobate de lithium. Le dispositif expérimental, qui n'est pas présenté dans les articles, est brièvement abordé à la Fig. 5.4.

Un faisceau à 1800 nm est obtenu à partir d'un amplificateur paramétrique optique (OPA). Un cristal de BBO est utilisé pour la génération de second harmonique afin d'obtenir un deuxième faisceau à 900 nm. Un miroir dichroïque sépare les deux composantes de fréquence. L'énergie d'impulsion de chaque faisceau est accordée avec une paire lame demi-onde/polariseur. Une ligne à

retard dans le parcours du faisceau à 1800 nm permet de synchroniser temporellement les impulsions qui sont recombinaées à l'aide d'un deuxième miroir dichroïque. Une paire de coins de verre permet d'ajuster la phase relative entre les champs à 1800 et 900 nm. Les faisceaux sont ensuite focalisés par un miroir parabolique hors axe ( $f = 5$  cm) afin d'ablater la surface du matériau. Une platine de translation motorisée déplace rapidement l'échantillon afin d'obtenir des mesures monocoups. Avant la prise de mesures, une caméra CCD est placée au foyer optique pour caractériser et ajuster la taille de chaque faisceau. Pour un positionnement reproductible de la surface de l'échantillon au point de focalisation et afin de s'assurer que la surface est parallèle à l'axe de translation de la platine motorisée, un système d'imagerie a également été construit. La réflexion de Fresnel sur l'échantillon est collectée par un coin de verre de 1 mm et focalisée dans une deuxième caméra CCD à l'aide d'un miroir parabolique de focale  $f = 20$ cm. En contrôlant le faisceau à l'aide de ce montage, il est possible d'ajuster le parallélisme de la surface du cristal.

Dans la première expérience (article V), l'ablation du niobate de lithium est effectuée avec le champ à 1800 nm seulement. L'aire ablatée est évaluée en fonction de l'angle relatif entre l'orientation de la polarisation du laser et l'axe  $c$  du cristal. Les mesures sont effectuées pour comparer les échantillons de coupes  $x$  et  $y$  (Fig. 5.6). En comparant les résultats expérimentaux (Fig. 5.7) avec un modèle d'ionisation basé sur les équations de Bloch pour les semi-conducteurs (5.15), nous démontrons que la méthode d'ablation, en régime d'ionisation tunnel, peut distinguer chaque coupe de cristal ayant des propriétés de symétrie distinctes. Des calculs employant la théorie de la fonctionnelle de la densité (Figs. 5.8-5.10) permettent d'identifier les liaisons Nb-O du matériau comme étant contributeurs principaux à la structure de bande et à l'ionisation du matériau. Cette comparaison avec les résultats expérimentaux montre que la méthode d'ablation fournit un observable de contraste élevé pour identifier ces liaisons Nb-O.

Dans une deuxième expérience (article VI), des impulsions laser combinant les champs à 1800 et 900 nm sont utilisées pour évaluer l'aire ablatée du matériau en fonction de la phase relative du champ laser à deux couleurs. Les mesures sont effectuées selon une seule orientation de polarisation laser, choisie pour être soit parallèle soit antiparallèle à l'axe  $c$  du  $\text{LiNbO}_3$  et donc à la polarisation spontanée du matériau. Le résultat principal de l'expérience (Fig. 5.13) est une modulation ayant une amplitude de 35 % et dont la périodicité permet d'identifier une contribution de la polarisation spontanée dans l'ionisation en champ fort du  $\text{LiNbO}_3$ . Le rôle de cette polarisation spontanée a été clarifié en simulant le processus d'ionisation à l'aide des équations de Bloch pour les semi-conducteurs (5.15). Les calculs montrent qu'un effet Stark dynamique pendant le processus d'ionisation, induit par la polarisation spontanée du matériau, permet d'interpréter qualitativement les observations expérimentales.

Les travaux présentés dans les articles V et VI démontrent que l'ablation induite par laser fournit un observable de grand contraste pour étudier l'ionisation en champ fort des matériaux. En particulier, les résultats obtenus dans l'article VI consistent en une première preuve de principe démontrant des effets de polarisation permanente lors de l'ionisation des systèmes solides, en analogie

avec ce qui a été observé dans les gaz moléculaires asymétriques. Il serait donc intéressant de poursuivre la caractérisation d'autres matériaux. Cela ouvre de nouvelles perspectives en physique des champs forts, offrant un degré de liberté supplémentaire pour le contrôle du processus HHG dans les matériaux ferroélectriques. Enfin, bien que les données expérimentales présentées à la figure 5.13 ont été choisies dans l'intention de montrer une nette relation hors-phase entre les courbes, la figure 5.5 montre également qu'il est possible d'obtenir des modulations beaucoup mieux définies. Cette sensibilité du processus d'ablation à la phase du champ laser pourrait donc être utilisée pour identifier la phase de l'onde porteuse d'impulsions de quelques cycles optiques couvrant certaines régions spectrales de l'infrarouge moyen ou lointain, pour lesquelles des techniques tout-optiques peuvent être difficiles à employer.

## 9.7 Article VI – Stabilisation assistée par laser de l'adénine ionisée: prévenir la dissociation moléculaire en agissant à des échelles temporelles extrêmes

Dans le cadre de l'étude des mécanismes primaires en jeu lors des dommages causés aux sous-unités de l'ADN par les radiations, nous étudions dans l'article VII la dynamique de la base nucléique adénine pendant les quelques fs après photoionisation par une impulsion XUV attoseconde isolée.

La configuration pompe-sonde utilisée pour l'expérience est indiquée dans Figure 6.3. Un séparateur de faisceau divise un faisceau NIR en deux composantes (côté gauche). Le faisceau transmis est utilisé pour générer des impulsions attoseconde isolées XUV en employant la technique de porte de polarisation (PG) qui a été décrite à la section 3.2. Le NIR résiduel est filtré par un filtre en aluminium. L'impulsion NIR qui a été réfléchiée par le séparateur de faisceau est recombinaée avec l'impulsion XUV à l'aide d'un miroir troué et le délai entre les deux impulsions est fixe mais variable. Dans cette approche pompe-sonde, un cation de l'adénine est d'abord créé par l'impulsion pompe ionisante XUV dont les énergies de photon couvrent un domaine entre 15 et 35 eV, puis l'impulsion sonde NIR permet de suivre la dynamique de photo-fragmentation de la molécule grâce à la détection d'ions, ceci à l'aide d'un spectromètre VMI en mode temps de vol (Figure 6.4a). Les spectres de fragmentation sont enregistrés en fonction du délai entre les impulsions XUV et NIR (Figure 6.4b).

La méthode décrite ci-dessus permet de suivre la formation et la disparition de fragments moléculaires lors de l'ionisation. La principale observation lors de nos mesures est l'apparition d'un dication stable de l'adénine ( $\text{ade}^{2+}$ ), retardée de 2.32 fs par rapport aux autres fragments (Figure 6.5). En répétant les mesures dans différentes conditions expérimentales, on observe également que lorsque l'impulsion XUV contient des énergies de photon strictement inférieures à 17 eV, l' $\text{ade}^{2+}$  n'est pas

observé. Ce résultat indique que l'ionisation d'électrons de cœur par des photons de haute énergie est susceptible de jouer un rôle dans la formation d'un dication stable de l'adénine.

Pour interpréter ces observations expérimentales, des simulations ont été nécessaires. En effet, la complexité de systèmes moléculaires polyatomiques comme l'adénine nécessite inévitablement des modèles théoriques de pointe, soit pour prendre en compte des effets non-adiabatiques, soit pour évaluer des interactions entre plusieurs corps telles que des corrélations électroniques. C'est pourquoi des calculs utilisant la théorie de la fonctionnelle de la densité (DFT) (décrits dans la section 5.4) ainsi que deux modèles théoriques complémentaires ont été utilisés. La combinaison de l'expérience et de la théorie a permis de tirer un certain nombre de conclusions sur la dynamique de fragmentation de l'adénine:

Premièrement, la combinaison de calculs de TD-DFT et de dynamique moléculaire montre que lorsque l'impulsion XUV ionise un électron à partir de l'orbitale moléculaire occupée de plus haute énergie (HOMO), un allongement significatif des liaisons dans la molécule a lieu, ce qui indique une faible photo-stabilité (Figure 6.4c). Ce résultat suggère que des processus de relaxation autre que la dissociation, impliquant des corrélations électroniques, doivent être pris en compte pour expliquer le fait que la molécule d'adénine reste intacte après l'ionisation XUV.

Deuxièmement, des équations de taux de transition basées sur la règle d'or de Fermi ont été utilisées pour démontrer que la population d'une orbitale moléculaire spécifique se produit par phénomène 'shake-up' à l'intérieur d'une fenêtre temporelle compatible avec le délai expérimental de formation de l'ade<sup>2+</sup>. L'identification de cet état 'shake-up' (LUMO+6) a également été confirmée par l'utilisation d'un modèle plus avancé résolvant la fonction de Green hors-équilibre, qui prend en compte les interactions de Coulomb à corps multiples (électrons-électrons). Ce modèle permettant également d'évaluer l'évolution temporelle de la densité électronique, il démontre également que pendant la population de l'état 'shake-up' concerné, une migration de charge s'éloignant du plan moléculaire a lieu (??c). À l'aide du même modèle, la simulation de l'étape sonde NIR montre qu'une seconde ionisation suivant le processus de 'shake-up' permet de dissiper de l'énergie potentielle dans la molécule, qui autrement mènerait à la rupture de la liaison en l'absence de l'impulsion NIR.

En se référant à la figure Figure 6.2 illustrant le schéma général d'un processus 'shake-up', le mécanisme complet pour obtenir le dication d'adénine non dissociée est décrit comme suit : (1) La photoionisation par une impulsion XUV crée un trou dans la molécule d'adénine. (2) La décroissance du trou conduit à la population d'un état 'shake-up' à l'intérieur d'un délai de 2.32 fs observé expérimentalement, correspondant à  $\Delta t$ . (3) Une impulsion NIR synchronisée à ce moment ionise un second électron, réduisant la population de cet état 'shake-up'. Cette dernière étape d'ionisation empêche la molécule de relaxer par des voies dissociatives.

Dans ce travail, la durée d'un processus de type 'shake-up' se déroulant dans une molécule polyatomique – l'adénine – a été caractérisée pour la première fois. Les résultats démontrent

l'importance de combiner des calculs théoriques de pointe avec les observations expérimentales afin de parvenir à une interprétation correcte lors de l'étude de larges systèmes moléculaires. Ces travaux montrent en outre qu'en comprenant la dynamique des électrons à l'échelle de quelques fs suite à la photoionisation d'une molécule d'intérêt biologique, il est possible de contrôler la dissociation moléculaire grâce à un mécanisme de stabilisation assisté par laser, relevant ainsi un objectif important en photochimie.

## 9.8 Dynamiques moléculaires induites par excitation UV ultra-brève et sondée par dichroïsme circulaire de photoélectrons

Le travail présenté ci-dessous est en cours lors de la rédaction de cette thèse.

Dans le chapitre 7, nous étudions la dynamique chirale du lactate de méthyle par dichroïsme circulaire de photoélectrons (PECD). Lors de mesures PECD, du rayonnement polarisé circulairement ionise un ensemble de molécules chirales, ce qui crée une asymétrie avant/arrière dans la distribution angulaire de photoélectrons le long de l'axe de propagation de la lumière (Fig. 7.1). Cette asymétrie s'inverse en changeant d'énantiomère ou en inversant l'hélicité du rayonnement.

Dans le cadre d'une collaboration avec le groupe Harmodyn du Centre Laser Intense et Applications (Bordeaux, France), à savoir Etienne Bloch (doctorant), Bernard Pons, Yann Mairesse et Valérie Blanchet, nous avons exploité la ligne de lumière développée lors de ma thèse (articles II et III) pour des mesures PECD résolues en temps dans le lactate de méthyl, un dérivé de l'acide lactique (Fig. 7.3a). Une dynamique chirale est induite dans l'état neutre de la molécule par une impulsion UV de quelques femtosecondes dont le spectre est présenté à la figure 7.4, puis sondée par une impulsion circulaire de quelques cycles optiques à 800 nm (Fig. 7.3).

Un premier résultat de cette expérience est présenté à la figure 7.7, montrant le PECD pour les délais entre les impulsions UV-pompe et IR-sonde correspondant à  $\Delta t = 4$  fs (a) et  $\Delta t = 22$  fs (b). Une évolution du PECD est observée, pendant laquelle la direction d'émission préférentielle avant/arrière des photoélectrons possédant une énergie cinétique inférieure à 1 eV (cercle blanc) s'inverse après 18 fs. Une telle inversion dynamique du PECD n'a jamais été observée auparavant. Cependant, il est bien connu que le PECD est sensible aux degrés de liberté électroniques et nucléaires [305]. Par exemple, il a été observé que le PECD pour des niveaux vibrationnels successifs peut présenter des asymétries opposées [312]. Comme première hypothèse, nous supposons donc que lors de l'excitation UV, deux états électroniques différents ayant des réponses chirales opposées sont en compétition, un premier qui domine au chevauchement temporel entre les impulsions pompe et sonde (Fig. 7.7a), l'autre avec une durée de vie plus longue et qui domine à des délais pompe-sonde plus élevés (Fig. 7.7b).

Afin d'interpréter les résultats expérimentaux, un support théorique est en développement. Fig 7.11a montre le moment de transition à deux photons pour les états électroniques dans la région d'énergie d'absorption à deux photons UV. La densité spectrale correspondant au spectre UV expérimental est montrée par la courbe bleue. Le produit de ces deux contributions est illustré à la Figure 7.11b. Dans ce cas les états ayant un caractère d'orbitale moléculaire occupée de plus haute énergie (HOMO) supérieur à 50% sont identifiés en rouge. Ceux ayant un caractère HOMO-1 supérieur à 50% sont illustrés en mauve. Le PECD sera calculé pour chacun de ces paquets d'ondes électroniques pour comparaison avec les résultats expérimentaux.

Ce travail démontre la capacité de notre nouvelle ligne de lumière pour étudier des dynamiques ultrarapides de molécules à l'état neutre à partir d'impulsions UV de quelques femtosecondes, offrant une résolution temporelle élevée. Nous avons utilisé le PECD pour étudier la dynamique moléculaire du lactate de méthyle suivant une excitation UV. Une inversion de l'asymétrie avant/arrière dans la distribution angulaire de photoélectrons se produit après environ 20 fs, une échelle de temps ultrarapide accessible grâce à notre montage expérimental unique. Il est possible que cette inversion de PECD provienne d'une compétition entre les réponses chirales de deux paquets d'ondes électroniques, chacun dominant à des délais pompe-sonde distincts. Des calculs théoriques sont actuellement effectués pour confirmer ou rejeter cette interprétation.



## Part III

# Appendices and References



# Appendices



# Appendix A

## Supplemental Material for article V – Laser polarization dependence of strong-field ionization in lithium niobate

### Theoretical model

The semiconductor Bloch equations (SBEs) in the momentum  $k$ -space can be written as [235],

$$\dot{\pi}(K, t) = -\frac{1}{T_2}\pi(K, t) - i\Omega(K, t)w(K, t)e^{-iS(K, t)}, \quad (1)$$

$$\dot{n}_b(K, t) = is_b\Omega^*(K, t)\pi(K, t)e^{iS(K, t)} + c.c., \quad (2)$$

where  $\pi(K, t)$  relates to the polarization  $p(K, t)$  between the conduction band (C) and the valence band (V) via:

$$p(K, t) = d(K + A(t))\pi(K, t)e^{iS(K, t)} + c.c. \quad (3)$$

$K = k - A(t)$  is the crystal momentum which depends on the laser vector potential  $A(t)$  and  $t$  is the time.  $\Omega(K, t) = d(K, t)E(t)$  is the Rabi frequency with  $d(K, t)$  being the transition dipole moment and  $E(t)$  the laser electric field.  $w(K, t) = n_{b=C}(K, t) - n_{b=V}(K, t)$  is the population difference between C and V.  $s_b$  is constant and equals to  $-1$  and  $1$  for the valence band and the conduction band, respectively. In our calculations, the classical action  $S(K, t) = \int_{-\infty}^t \varepsilon_g(K + A(t'))dt'$  is used to describe the phase accumulated by the electrons and holes moving along the bands with  $\varepsilon_g$  being the band gap.  $T_2$  is the dephasing time describing the coherence between the conduction band and the valence band and it is equal to 5 fs in our work.

The conduction band population  $n_C$  is obtained by solving the SBEs and the input band structure and transition dipole moments are obtained by density functional theory (DFT) calculations using the simulation package VASP [232].

The band structure calculated by DFT is fitted by Fourier series,

$$\varepsilon_{CB}(K_X) = \epsilon_g + \sum_{j=0}^n \alpha_{CB}^j \cos(jK_X a_X), \quad (4)$$

$$\varepsilon_{VB}(K_X) = \sum_{j=0}^n \alpha_{VB}^j \cos(jK_X a_X), \quad (5)$$

where  $a_X$  is the lattice parameter of the LiNbO<sub>3</sub> unit cell along the high symmetry point direction (see Table 1), and  $K_X$  is the crystal momentum. The polarization direction of the laser  $\hat{E}$  is along the high symmetry point direction. The SBEs are solved by the Euler method with the finite difference method. In each orientation, 300  $k$ -space points (full BZ) are used.

## Band gap effect on the conduction band population of LiNbO<sub>3</sub>

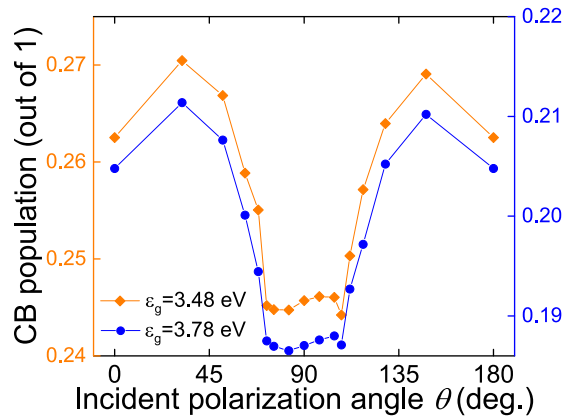


**Figure 1 – The band gap effect on the conduction band population of  $x$ -cut LiNbO<sub>3</sub>.  $\varepsilon_g = 3.48$  eV (orange diamonds) and  $\varepsilon_g = 3.78$  eV (blue dots) are compared with  $T_2 = 5$  fs.**

Figure 1 shows the effect of the band gap value  $\varepsilon_g$  on the conduction band population of  $x$ -cut LiNbO<sub>3</sub>. The experimental  $\varepsilon_g = 3.78$  eV [227] (blue dots) is slightly larger than our DFT predicted  $\varepsilon_g = 3.48$  eV (orange diamonds). Therefore, the conduction band population decreases for  $\varepsilon_g = 3.78$  eV due to exponential dependence of the tunnel ionization rate on the band gap energy, but the dependence of the conduction band population on the laser polarization angle is conserved.

## Dephasing time effect on the conduction band population of LiNbO<sub>3</sub>

Figure 2 shows further analysis of the dephasing time ( $T_2$ ) effect on the conduction band population of  $x$ -cut LiNbO<sub>3</sub>. For  $T_2=2.5$  fs, 5.0 fs, and 10 fs, one can find that the asymmetry of the curve is preserved.

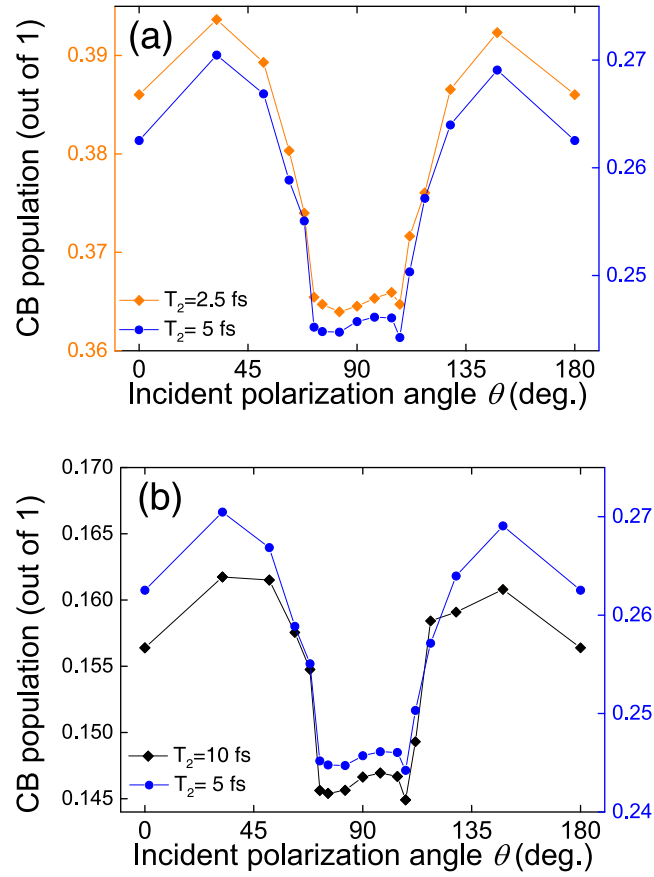


**Figure 2** – The dephasing time effect on the conduction band population of  $x$ -cut LiNbO<sub>3</sub>. (a)  $T_2=2.5$  fs (orange diamonds) and  $T_2=5$  fs (blue dots); (b)  $T_2=10$  fs (black diamonds) and  $T_2=5$  fs (blue dots).

## Laser polarization angle-dependent band structure

For the hexagonal lattice with corresponding parameters  $a$  and  $c$ , the interplanar distance  $d_{hkl}$  between a family of planes  $(hkl)$  is [318],

$$\frac{1}{d_{hkl}^2} = \frac{4}{3} \left( \frac{h^2 + hk + k^2}{a^2} \right) + \frac{l^2}{c^2} \quad (6)$$

The cosine value of the angle  $\theta$  between the two planes with indices  $(h_1k_1l_1)$  and  $(h_2k_2l_2)$  can be expressed by,

$$\cos \theta = \frac{4}{3a^2} \left[ h_1h_2 + k_1k_2 + \frac{1}{2} (h_1k_2 + h_2k_1) + \frac{3a^2}{4c^2} l_1l_2 \right] \times d_{h_1k_1l_1} d_{h_2k_2l_2} \quad (7)$$

According to Eq. 7, the angle  $\theta$  between the direction of the high symmetry points shown in Fig. 1(a) of the main text and  $\Gamma A$  is obtained. This correspondence between the  $k$ -space high symmetry point direction and the laser polarization angle is shown in Table 1.

In this work, the angle-dependent band structure is evaluated for both the  $x$ -cut and  $y$ -cut crystals, as shown in Fig. 3. The Fermi-energy is at the level of zero energy. The blue-solid and the magenta-solid lines show the conduction band minimum (CBM) and valence band maximum (VBM) employed in the two-band SBEs model.

As shown in Fig. 3 (a-1), the electronic band structure (VBM and CBM) shows symmetry with respect to  $90^\circ$ . The color coding identifies angles that are equidistant from  $90^\circ$  but with opposite rotation direction of the laser polarization. Therefore, the band structures for  $\Gamma_{x_1}$  ( $32.0^\circ$ ),  $\Gamma_{x_3}$  ( $72.3^\circ$ ),  $\Gamma_{H_1}$  ( $79.1^\circ$ ),  $\Gamma_{y_1}$  ( $82.7^\circ$ ) and  $\Gamma_{y_2}$  ( $86.3^\circ$ ) are identical to  $\Gamma_{s_4}$  ( $148.0^\circ$ ),  $\Gamma_{s_2}$  ( $107.7^\circ$ ),  $\Gamma_{H_2}$  ( $100.9^\circ$ ),  $\Gamma_{z_2}$  ( $97.3^\circ$ ) and  $\Gamma_{z_1}$  ( $93.7^\circ$ ), respectively. This causes the symmetry of the observed ablation area in the experiments (main text, Fig. 2a) and the calculated conduction band population (main text, Fig. 6) for the  $y$ -cut.

According to Fig. 3 (m-x), the band structure for each angle in the  $x$ -cut does not show symmetry with respect to  $90^\circ$ . This supports the observation of an asymmetry in the variation of the ablated area for the  $x$ -cut (main text, Fig. 2b) and is also in accordance with the crystallography discussed in this work.

**Table 1 – High symmetry point directions in the  $k$ -space and their corresponding orientation angle  $\theta$  in lithium niobate.**

$k$ -point	coordinates in $k$ -space	$\theta_{x-cut}$ (deg.)	$k$ -point	coordinates in $k$ -space	$\theta_{y-cut}$ (deg.)
$A$	0.0 0.0 0.5	0.00	$A$	0.0 0.0 0.5	0.00
$x_1$	0.0 0.1 0.5	32.05	$x_1$	-0.0667 0.1333 0.5	35.86
$x_2$	0.0 0.2 0.5	51.39	$x_2$	-0.1333 0.2667 0.5	55.33
$x_3$	0.0 0.3 0.5	61.97	$x_3$	-0.2000 0.4000 0.5	65.25
$x_4$	0.0 0.4 0.5	68.23	$x_4$	-0.2667 0.5333 0.5	70.92
$L_1$	0.0 0.5 0.5	72.28	$H_1$	-0.3333 0.6667 0.5	74.54
$y_1$	0.0 0.5 0.4	75.66	$y_1$	-0.3333 0.6667 0.4	77.52
$y_2$	0.0 0.5 0.2	82.72	$y_2$	-0.3333 0.6667 0.2	83.69
$M$	0.0 0.5 0.0	90.00	$K$	-0.3333 0.6667 0.0	90.00
$z_1$	0.0 0.5 -0.2	97.28	$z_1$	-0.3333 0.6667 -0.2	96.31
$z_2$	0.0 0.5 -0.4	104.34	$z_2$	-0.3333 0.6667 -0.4	102.48
$L_2$	0.0 0.5 -0.5	107.72	$H_2$	-0.3333 0.6667 -0.5	105.46
$s_1$	0.0 0.4 -0.5	111.77	$s_1$	-0.2667 0.5333 -0.5	109.08
$s_2$	0.0 0.3 -0.5	118.03	$s_2$	-0.2000 0.4000 -0.5	114.75
$s_3$	0.0 0.2 -0.5	128.61	$s_3$	-0.1333 0.2667 -0.5	124.67
$s_4$	0.0 0.1 -0.5	147.95	$s_4$	-0.0667 0.1333 -0.5	144.14
$A_2$	0.0 0.0 -0.5	180.0	$A_2$	0.0000 0.0000 -0.5	180.00

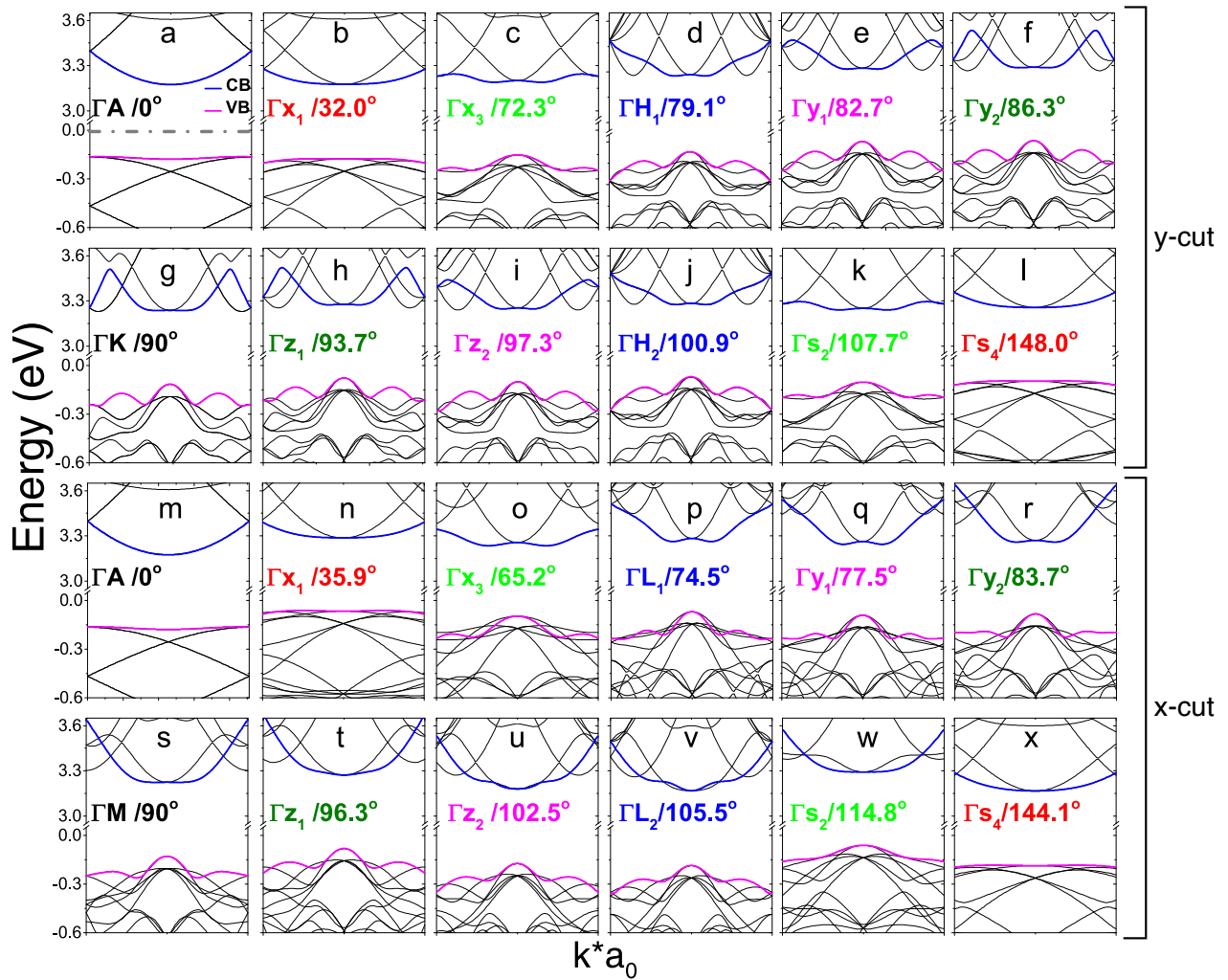


Figure 3 – Band structure vs laser polarization angle (Table 1) for the *y*-cut (a-l) and the *x*-cut (m-x). The color coding identifies angles that are equidistant from  $90^\circ$  but with opposite rotation direction of the laser polarization. The valence band maximum (pink line) and conduction band minimum (blue line) show symmetry with respect to  $90^\circ$  for the *y*-cut only.

# Appendix B

## Supplementary Material for article VI: Control of strong-field ionization in ferroelectric lithium niobate: Role of the spontaneous polarization

### Theoretical details

#### Two-band model

The electron dynamics within a solid crystal is described by the semiconductor Bloch equations in the reciprocal momentum space, which is written in a two-band model [235, 319] as:

$$\dot{\pi}(K, t) = -\frac{1}{T_2}\pi(K, t) - i\Omega(K, t)N(K, t)e^{-iS(K, t)}, \quad (8)$$

$$\dot{n}_b(K, t) = is_b\Omega^*(K, t)\pi(K, t)e^{-iS(K, t)} + c.c., \quad (9)$$

where  $T_2$  and  $N(K, t)$  are respectively the polarization dephasing time and the population difference between the conduction ( $n_{b=c}$ ) and the valence ( $n_{b=v}$ ) bands. In our calculations, the dephasing time describing the coherence between these two band states is used as a free parameter and was fixed at  $T_2 = 1.0$  fs.  $s_{b=c} = 1$  and  $s_{b=v} = -1$  are constants used to describe (from unity) the band populations variation from the initial state of the system where all electrons are in the valence band.

$\Omega(K, t) = \mathcal{F}(t)d(K + A(t))$  is the Rabi frequency for a given laser field  $\mathcal{F}(t)$  (with corresponding vector potential  $A(t) = -\int_{-\infty}^t \mathcal{F}(t')dt'$  and transition dipole  $d(K)$ ). Since both the laser field  $\mathcal{F}(t)$  and the transition dipole  $d(K + A(t))$  are vectors,  $\Omega(K, t) = \mathcal{F}_x(t)d_x(K + A(t)) + \mathcal{F}_y(t)d_y(K + A(t)) + \mathcal{F}_z(t)d_z(K + A(t))$ . In our case, the laser polarization is along the  $z$ -axis, therefore,  $\Omega(K, t) = \mathcal{F}_z(t)d_z(K + A(t))$ .

$S(K, t) = \int_{t_0}^t E_g(K + A(t')) dt'$  is the classical action from the start of the laser pulse at time  $t_0$  for an electron with crystal momenta  $K$  transformed into a moving frame  $K = K + A(t)$ , and  $E_g$  being the bandgap energy. The variable  $\pi(K, t)$  is related to the polarization  $p(K, t)$  by :

$$p(K, t) = d(K, A(t))\pi(K, t)e^{-iS(K, t)} + c.c. \quad (10)$$

The transition dipole can be expressed by  $d(k) = i \int d^3u_{v,k}^*(x) \nabla u_{c,k}^*(x)$  with  $u_{m,k}$  being the periodic part of the solution of the Bloch equation.

## First-principle calculations

We perform our first-principles calculations using the Vienna *ab initio* simulation package (VASP) [232], which self-consistently solve the Kohn-Sham equations for eigenvalues and eigenfunctions of the periodic system. The transition dipole moments are obtained by using the Post-Processing Program VASPKIT. The local density approximation (LDA) is chosen for describing the exchange-correlation functional [215]. The projector augmented wave (PAW) formalism is used to describe the ion-electron interactions [233], and a plane-wave energy cutoff of 500 eV is used for all calculations.

The LiNbO<sub>3</sub> hexagonal conventional cell has 30 atoms and belongs to the R3C space group. The unit cell is built from the experimentally measured lattice parameters ( $a = 5.148 \text{ \AA}$ ,  $c = 13.863 \text{ \AA}$  [208]) and the volume and internal ion coordinates are fully relaxed to the equilibrium position with respect to the pseudo-potential using a  $6 \times 6 \times 4$  k-grid. The optimized lattice parameters  $a = 5.093 \text{ \AA}$  and  $c = 13.8069 \text{ \AA}$  are obtained.

In the self-consistent cycle, the Brillouin zone is sampled by a  $20 \times 20 \times 10$  k-grid for obtaining the converged charge density and wavefunction. An indirect bandgap of 3.48 eV is obtained, in agreement with the reported 3.48 eV using the Generalized Gradient Approximation (GGA) [320]. In our work, a rigid shift to 3.78 eV is applied prior to the calculations using the two-band model. Electron-hole attraction effects that are not taken into account within the LDA and GGA are known to underestimate the bandgap of LiNbO<sub>3</sub> [251, 252]. The chosen bandgap corresponds to the commonly reported experimental value of 3.78 eV obtained from optical measurements [227].

The band dispersion curves in the reciprocal space are originally computed from VASP and fitted by Fourier series,

$$E_{CB}(k_X) = E_g + \sum_{j=0}^n \alpha_{CB}^j \cos(jk_X a_X) \quad (11)$$

$$E_{VB}(k_X) = \sum_{j=0}^n \alpha_{VB}^j \cos(jk_X a_X) \quad (12)$$

where  $a_x$  is the length of the lattice and  $k_x$  is the Bloch vector. We use  $j$  up to  $n = 20$  along the  $\Gamma A$  direction to expand the band dispersion curves. The coefficients can be found in Table I. The laser polarization is chosen to be along the  $\Gamma A$  direction with  $a_x = 26.091$  Bohr for the optimized unstrained  $\text{LiNbO}_3$  cell. As shown in the Supplemental Material, the semiconductor Bloch equations are solved for a two-band model by the finite difference method with 1000  $k$ -space points (full Brillouin zone) along  $\Gamma A$ . The band structure and Brillouin zone of  $\text{LiNbO}_3$  are displayed in Fig. 4.

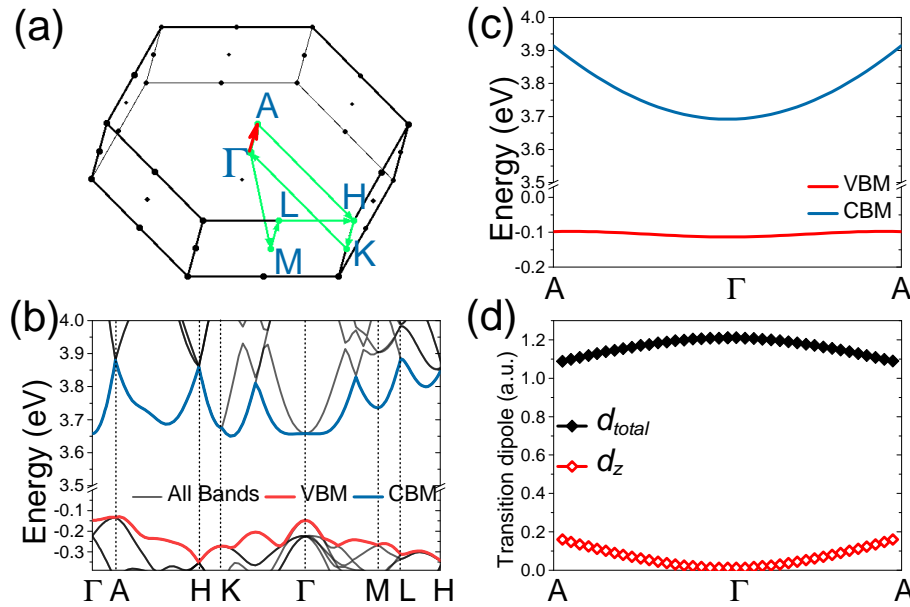


**Figure 4 – Reciprocal space of  $\text{LiNbO}_3$ .** (a) The Brillouin zone of  $\text{LiNbO}_3$  and its high symmetry points  $\Gamma$ , A, H, K, M and L. (b) The band structure of  $\text{LiNbO}_3$ . (c) The conduction band minimum (CBM) and valence band maximum (VBM) along  $\Gamma A$  direction of the BZ. (d) The total modulus of transition dipole moment (black diamonds) and its component along the  $k_z$  direction (red diamonds).

**Table 2 – Bands expansion coefficients of LiNbO<sub>3</sub> along  $\Gamma A$** 

	Valence (eV)	Conduction (eV)	dipole (atomic units)
$\alpha_0$	-0.1049	3.7682	0.0712
$\alpha_1$	$-8.125 \times 10^{-3}$	$-9.15 \times 10^{-2}$	$-6.78 \times 10^{-2}$
$\alpha_2$	$-6.766 \times 10^{-4}$	$2.18 \times 10^{-2}$	$1.208 \times 10^{-2}$
$\alpha_3$	$2.871 \times 10^{-4}$	$-9.693 \times 10^{-3}$	$-5.55 \times 10^{-3}$
$\alpha_4$	$-1.763 \times 10^{-4}$	$5.526 \times 10^{-3}$	$2.976 \times 10^{-3}$
$\alpha_5$	$1.266 \times 10^{-4}$	$-3.6098 \times 10^{-3}$	$-1.999 \times 10^{-3}$
$\alpha_6$	$-7.665 \times 10^{-5}$	$2.542 \times 10^{-3}$	$1.184 \times 10^{-3}$
$\alpha_7$	$6.697 \times 10^{-5}$	$-1.915 \times 10^{-3}$	$-8.857 \times 10^{-4}$
$\alpha_8$	$-4.813 \times 10^{-5}$	$1.539 \times 10^{-3}$	$5.514 \times 10^{-4}$
$\alpha_9$	$4.318 \times 10^{-5}$	$-1.233 \times 10^{-3}$	$-1.028 \times 10^{-4}$
$\alpha_{10}$	$-3.002 \times 10^{-5}$	$1.05 \times 10^{-3}$	$6.832 \times 10^{-4}$
$\alpha_{11}$	$3.07 \times 10^{-5}$	$-9.226 \times 10^{-4}$	-
$\alpha_{12}$	$-8.649 \times 10^{-6}$	$8.191 \times 10^{-4}$	-
$\alpha_{13}$	$2.141 \times 10^{-5}$	$-7.28 \times 10^{-4}$	-
$\alpha_{14}$	$-6.495 \times 10^{-6}$	$6.742 \times 10^{-4}$	-
$\alpha_{15}$	$1.344 \times 10^{-5}$	$-6.11 \times 10^{-4}$	-
$\alpha_{16}$	$-3.689 \times 10^{-5}$	$5.662 \times 10^{-4}$	-
$\alpha_{17}$	$8.348 \times 10^{-6}$	$-5.526 \times 10^{-4}$	-
$\alpha_{18}$	$-1.023 \times 10^{-5}$	$5.331 \times 10^{-4}$	-
$\alpha_{19}$	$2.689 \times 10^{-5}$	$-5.34 \times 10^{-4}$	-
$\alpha_{20}$	$-1.499 \times 10^{-5}$	$2.551 \times 10^{-4}$	-

### Asymmetric two-color laser field

The waveform of a two-color laser field is described by:

$$\mathcal{F}(t) = \mathcal{F}_1(t) \cos(\omega t) + \mathcal{F}_2(t) \cos(2\omega t + \phi) \quad (13)$$

where  $\mathcal{F}_1$  and  $\mathcal{F}_2$  are the envelope functions of the fundamental field and its second harmonic, of frequencies  $\omega$  and  $2\omega$ , respectively. To highlight the positive-negative asymmetry of the electric field polarity, Fig. 5 shows the laser pulse waveform for three distinct relative phases  $\phi$ , using the experimental 2:1 (1800 : 900 nm) intensity ratio.

### Field strength inside the crystal

After considering the Fresnel losses [235], the field strength inside the crystal is expressed by  $\mathcal{F}_{LiNbO_3} = 2\mathcal{F}/(n_e + 1)$  where  $n_e$  is the crystal refractive index. The intensity and corresponding field strength used in the calculations are listed in Table 3.

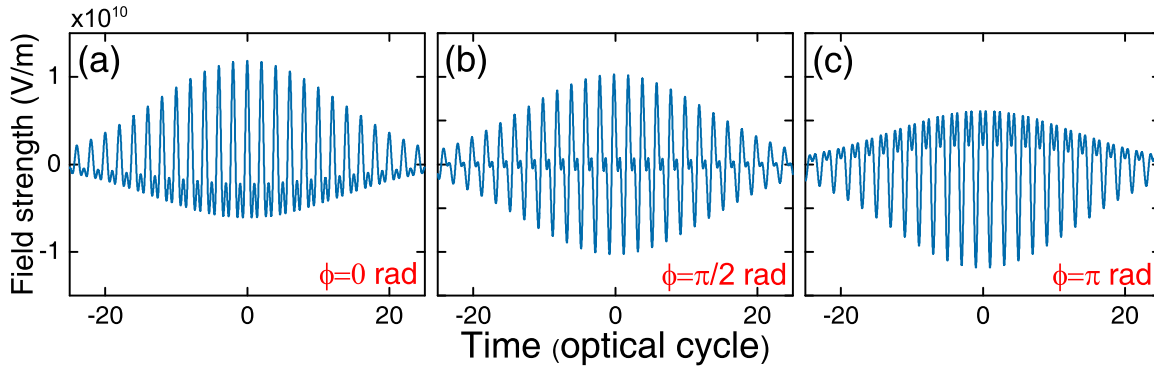


**Figure 5 – Two-color laser field simulations.** Waveform for (a)  $\phi = 0$ , (b)  $\phi = \pi/2$  and (c)  $\phi = \pi$ . The relative phase of the two-color field modulates the field amplitude along the positive and negative polarization direction.

**Table 3 – Field strength used for calculations and corresponding Keldysh parameter  $\gamma$**

$\lambda$	1800 nm	900 nm
Laser Intensity ( $10^{13} \text{ Wcm}^{-2}$ )	1.6	0.77
Refractive index $\eta_e$	2.1312	2.1665
$\mathcal{F}_{air}$ (atomic units)	0.02135	0.01481
$\mathcal{F}_{LiNbO_3}$ (atomic units)	0.013637	0.009354
$\gamma$	0.5679	1.6559

### Spontaneous polarization in LiNbO<sub>3</sub>

The spontaneous polarization of LiNbO<sub>3</sub> is given by,

$$P_s = \frac{\mu}{v_0} \quad (14)$$

where  $\mu$  is the electric dipole and  $v_0 = 310.16 \text{ \AA}^3$  is the volume of the hexagonal LiNbO<sub>3</sub> unit cell. For the calculations, we convert  $P_s$  to electric dipole. The resulting electric dipole values for 0.1 and  $0.05 \text{ C/m}^2$  are respectively  $3.1016 \times 10^{-29} \text{ C/m}$  (3.6582 atomic units) and  $1.5508 \times 10^{-29} \text{ C/m}$  (1.8291 atomic units).

The effective band gap can be expressed by,

$$E_g(\mathcal{F}) = E_g(0) - \mu\mathcal{F}(t)_{LiNbO_3} \quad (15)$$

where  $E_g(0)$  corresponds to the field-free bandgap energy. Fig. 6 shows the temporal evolution of the spontaneous polarization induced Stark shift for the relative two-color phase  $\phi = 0$ . For lower bandgap energy values as in the  $\theta = 180^\circ$  case, an increased conduction band population arises due to the exponential dependence of the ionization rate on  $E_g$ . In our two-band model,  $E_g(\mathcal{F})$  is inserted into the semiconductor Bloch equations through the classical action  $S(K, t)$ .

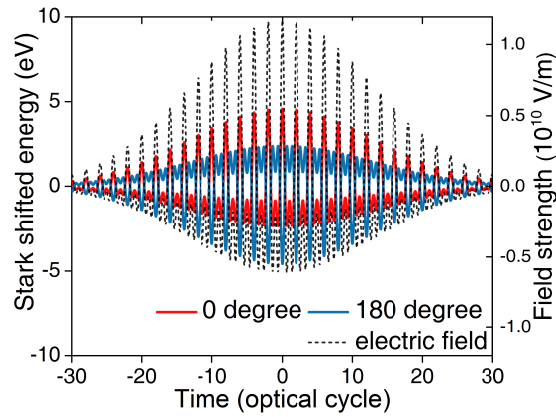


**Figure 6 – Stark effect on the bandgap energy.** Predicted Stark shifted bandgap energy from Eq. (15) as a function of the relative two-color phase for  $\theta = 0^\circ$  (red) and  $\theta = 180^\circ$  (blue) when  $|P_s| = 0.2 \text{ C/m}^2$ . The black dashed line is the two-color electric field at zero phase shift ( $\phi = 0$ ).

Additional calculations of strong-field ionization from the two-band model of  $\text{LiNbO}_3$

Fig. 7 shows the two-color phase dependence of the ionization process on the spontaneous polarization amplitude in  $\text{LiNbO}_3$ , ranging from  $P_s = 0$  to  $0.15 \text{ C/m}^2$ . The gradual change of periodicity highlights the interplay between the laser electric field strength and the amplitude of the spontaneous polarization, which dynamically modulates the bandgap energy of the material during ionization.

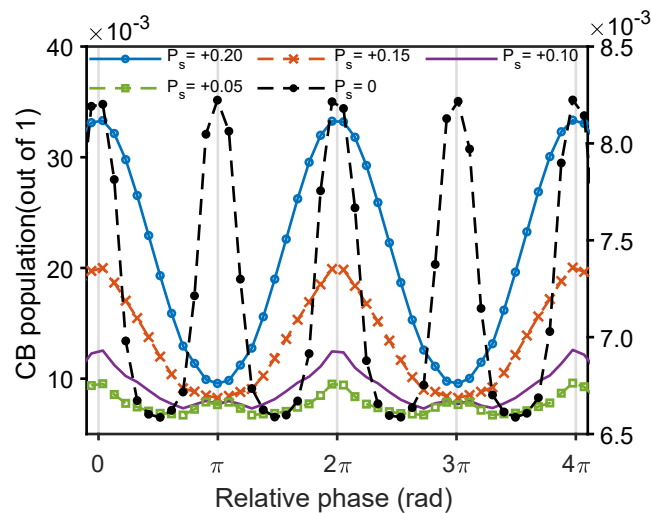


**Figure 7 – Spontaneous polarization scaling of the two-color phase dependence.** Conduction band population as a function of the relative two-color phase  $\phi$  for increasing  $P_s$  from 0 to  $0.15 \text{ C/m}^2$ .

## Comparison to the Keldysh model

In the Keldysh model, the electron effective mass  $m_e^*$  required to calculate the ionization rate is evaluated from the electronic dispersion relation  $E(k)$  in momentum space :

$$\frac{1}{m_e^*} = \frac{1}{\hbar} \frac{\partial^2 E(k_a)}{\partial k_a^2} \quad (16)$$

and expressed as :

$$\frac{1}{m_e^*} = \frac{1}{|m_c^*|} + \frac{1}{|m_v^*|} \quad (17)$$

where  $m_c^*$  and  $m_v^*$  are the electron effective masses at the  $\Gamma$  point in the conduction (C) and valence (V) bands.  $m_c^* = 0.6736 m_e$  is obtained for the  $\Gamma A$  direction. The ionization rate  $w_{tunnel}(\gamma)$  in the tunneling approximation is calculated from :

$$w_{tunnel}(\gamma) = \frac{2}{9\pi^2} \frac{E_g(\mathcal{F})}{\hbar} \left( \frac{m_c^* E_g(\mathcal{F})}{\hbar^2} \right)^{3/2} \left( \frac{\hbar\omega}{E_g(\mathcal{F})\gamma} \right)^{5/2} \exp\left( -\frac{\pi E_g(\mathcal{F})}{2\hbar\omega} \gamma \left( 1 - \frac{1}{8} \gamma^2 \right) \right) \quad (18)$$

where the Keldysh parameter for solids is defined as :

$$\gamma = \omega \frac{\sqrt{E_g(\mathcal{F}) m_c^*}}{e\mathcal{F}} \quad (19)$$

$\omega$ ,  $e$  corresponding respectively to the angular frequency and elementary charge.  $\mathcal{F}$  is the time-dependent laser field strength from Eq. 13, carrying the effect of the temporal waveform of the two-color field on the ionization process. The conduction band population is obtained by integrating the transient ionization rate predicted by the Keldysh model. The time-dependent bandgap  $E_g(\mathcal{F})$  evaluated in Eq. (15) is used to simulate the effect of the spontaneous polarization. On the basis of the Keldysh model [71], our numerical codes reproduce the results of ionization in GaAs crystal [226], which testifies the reliability of our numerical results.

Fig. 8(a) shows the ionization rate for LiNbO<sub>3</sub> along  $\Gamma A$ , using a band gap of 3.78 eV and a reduced mass of 0.6736  $m_e$ . While the two-band model provides a better description of the ionization

dynamics in solids, the Keldysh model also provides an intuitive picture to explain our experimental observations.

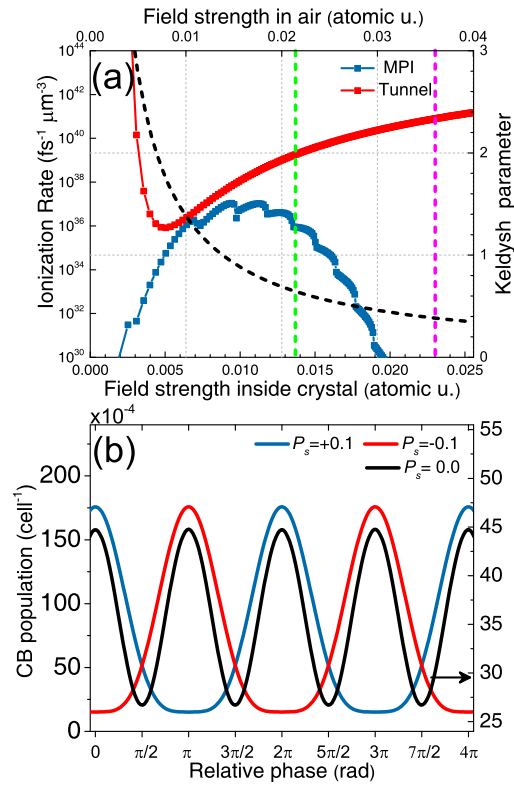


**Figure 8** – Calculations based on the Keldysh model. (a) Predicted ionization rates in the multiphoton ionization (MPI) approximation (blue dots) and tunneling approximation (red squares) along  $\Gamma A$ . The black dashed line is the Keldysh parameter (right scale). The green and magenta dashed lines corresponds respectively to the experimental intensities for the 1800 nm field only and two-color field reported in Table II. (b) Conduction band (CB) population as a function of the relative two-color phase for  $P_s = +0.1 \text{ C/m}^2$  (red) and  $P_s = -0.1 \text{ C/m}^2$  (blue).  $P_s = 0 \text{ C/m}^2$  (black) is compared.

## Interferometer stabilization

In the experiments, the time required to perform a single scan of the relative two-color phase was about 20 min. To prevent slow drifts during this time window, the interferometer was actively stabilized. This also provides a relative zero reference to compare the two-color phase dependence for different crystal orientations. The active stabilization is based on the feedback regulation of a pair of fused silica wedge from  $2\omega - 2\omega$  spectral interferometry (Fig. 9a) [248]. Fig. 9b shows the phase steps induced by the pair of fused silica wedge for crystal orientations  $\theta = 0^\circ$  and  $\theta = 180^\circ$ .

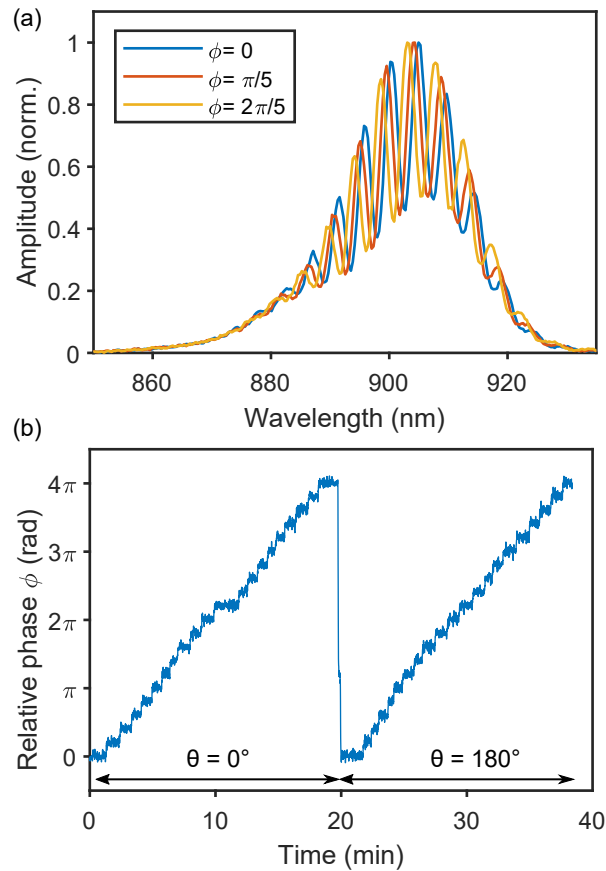


**Figure 9** – Monitoring of the relative two-color phase. (a)  $2\omega - 2\omega$  spectral interference used to define and control the relative two-color phase. Three consecutive steps of  $\pi/5$  induced by the wedge pair are shown. (b) Steps corresponding to the scan of the relative two-color phase for  $\theta = 0^\circ$  and  $\theta = 180^\circ$  (see main text, Fig. 2).

## Details on laser-induced ablation and data analysis

### Laser-induced ablation

The mechanism underlying LIA in dielectrics depends strongly on the field intensity and pulse duration. In all cases, the conduction band of the initially transparent material is populated by free electrons, leading to plasma formation. Once the electron density in the conduction band reaches a value for which sufficient laser energy can be absorbed by the plasma to melt the material, alteration of the surface (damage) or crater formation (ablation) can occur and is visible by microscopy [209]. For nanosecond to picosecond pulses, avalanche ionization is the main contributor to the plasma generation [210]. The pulse energy can be transferred to the lattice via thermal diffusion, ablating the material within the pulse duration [211]. In the femtosecond regime, this slow thermal transfer is decoupled from the fast 'shocklike' deposition of energy by the laser pulse that is heating up the electrons. In this case, SFI by itself can be sufficient to reach the electron density required for inducing material ablation [212], occurring on a timescale longer than the pulse duration [213]. Since less energy is deposited into the material with femtosecond pulses, the ablated region is better-defined and strongly reproducible from pulse to pulse [228]. It has been shown that LIA is sensitive to the symmetry of crystals when rotating a single color linearly polarized field and ablating at several incident angles [225]. As demonstrated by our experimental results, femtosecond electron-driven ablation also provides a sensitive observable for the control of SFI in solids with two-color laser fields.

### Optical microscopy

Fig. 10 shows an example of optical microscopy image for two consecutive laser shots under the same experimental conditions. A Nikon Eclipse microscope combined to a 100x objective was used.

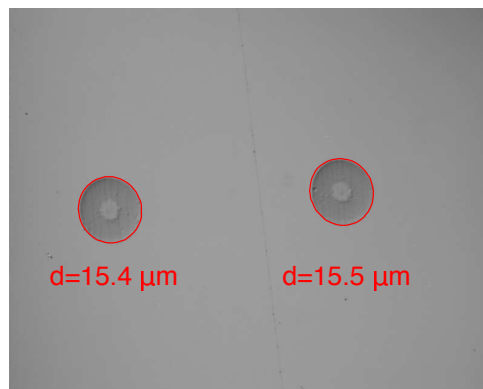


**Figure 10 – Optical microscopy image. Example for the fit of the ablated craters diameter from which the area is calculated.**

## Atomic force microscopy (AFM) measurements

To validate the results obtained from optical microscopy analysis, the surface morphology of the generated craters was also investigated by atomic force microscopy (AFM, Smart SPM1000-AIST-NT Inc.) in intermittent mode (Fig. 11). Silicon cantilever tips (Model PPP-NCHR-50 from NANOSENSORS) with typical tip radius  $< 10$  nm, length  $125 \mu\text{m}$  and tip height  $10\text{-}15 \mu\text{m}$  have been used.

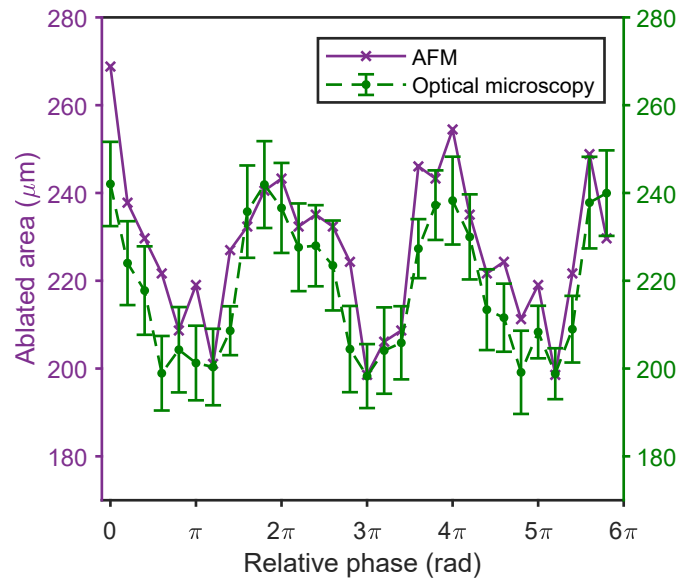


**Figure 11 – AFM measurements.** Ablated area as a function of the relative two-color phase (purple crosses). Due to the significant time consumption of the technique, each data point corresponds to a single analyzed crater and no averaging was performed. The results are compared to the optical microscopy measurements (green dots). The same periodicity is observed for both techniques.

## Ablation thresholds evaluation

To minimize the contribution of avalanche ionization, which is likely to mask the electric field effect on laser-induced ablation, intensities in the vicinity of the ablation threshold of the material are necessary. Fig. 12 describes the procedure employed to evaluate the ablation thresholds for each individual 1800 nm and 900 nm laser fields.

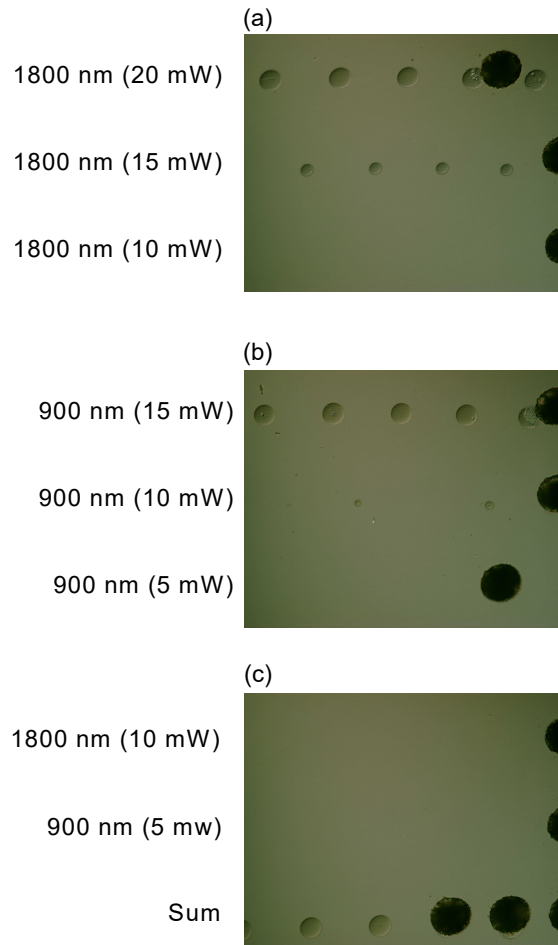


**Figure 12 – Determination of the experimental conditions in proximity of the ablation threshold. (a), (b), Optical microscopy images of laser-induced craters both at 1800 nm (a) and 900 nm (b). Each line corresponds to single laser shots for a same laser power value, allowing statistics to be made. The ablation threshold is defined as the power value where there is no visible damage. Black craters correspond to ablated areas by several laser shots. (c) Ablation thresholds for both the 1800 nm (10 mW) and 900 nm (5 mW) fields. The third line shows that ablated craters are visible only when both field are applied together.**

# Appendix C

Supplementary Information for article VII – Laser-assisted stabilisation of ionised adenine: preventing molecular dissociation by acting at extreme time scales

Cet article a dû être retiré de la version électronique en raison de restrictions liées au droit d'auteur.

# References

- [1] T. Maiman, “Stimulated Optical Radiation in Ruby,” *Nature*, vol. 187, pp. 493–494, 1960.
- [2] A. H. Zewail, “Femtochemistry: Atomic-Scale Dynamics of the Chemical Bond,” *The Journal of Physical Chemistry A*, vol. 104, no. 24, pp. 5660–5694, 2000.
- [3] A. McPherson, G. Gibson, H. Jara, U. Johann, T. S. Luk, I. A. McIntyre, K. Boyer, and C. K. Rhodes, “Studies of multiphoton production of vacuum-ultraviolet radiation in the rare gases,” *Journal of the Optical Society of America B*, vol. 4, no. 4, p. 595, 1987.
- [4] M. Ferray, A. L’Huillier, X. F. Li, L. A. Lompre, G. Mainfray, and C. Manus, “Multiple-harmonic conversion of 1064 nm radiation in rare gases,” *Journal of Physics B: Atomic, Molecular and Optical Physics*, vol. 21, no. 3, 1988.
- [5] K. C. Kulander, K. J. Schafer, and J. L. Krause, “Dynamics of Short-Pulse Excitation, Ionization and Harmonic Conversion,” *Super-Intense Laser-Atom Physics*, vol. 316, pp. 95–100, 1993.
- [6] P. B. Corkum, “Plasma Perspective on Strong-Field Multiphoton Ionization,” *Physical Review Letters*, vol. 71, no. 13, pp. 1994–1997, 1993.
- [7] P. M. Paul, E. S. Toma, P. Breger, G. Mullot, F. Augé, P. Balcou, H. G. Muller, and P. Agostini, “Observation of a train of attosecond pulses from high harmonic generation,” *Science*, vol. 292, no. 5522, pp. 1689–1692, 2001.
- [8] M. Hentschel, R. Kienberger, C. Spielmann, G. a. Reider, N. Milosevic, T. Brabec, P. Corkum, U. Heinzmann, M. Drescher, and F. Krausz, “Attosecond metrology,” *Nature*, vol. 414, no. 6863, pp. 509–513, 2001.
- [9] V. Véniard, R. Taïeb, and A. Maquet, “Phase dependence of  $(N + 1)$ -color  $(N > 1)$  ir-uv photoionization of atoms with higher harmonics,” *Physical Review A*, vol. 54, no. 1, pp. 721–728, 1996.
- [10] J. Itatani, F. Quéré, G. L. Yudin, M. Y. Ivanov, F. Krausz, and P. B. Corkum, “Attosecond streak camera,” *Physical review letters*, vol. 88, p. 173903, 2002.

- [11] M. Schultze, M. Fieß, N. Karpowicz, J. Gagnon, M. Korbman, M. Hofstetter, S. Neppl, A. L. Cavalieri, Y. Komninos, T. Mercouris, C. A. Nicolaides, R. Pazourek, S. Nagele, J. Feist, J. Burgdörfer, A. M. Azzeer, R. Ernstorfer, R. Kienberger, U. Kleineberg, E. Goulielmakis, F. Krausz, and V. S. Yakovlev, “Delay in photoemission,” *Science*, vol. 328, no. 5986, pp. 1658–1662, 2010.
- [12] M. Isinger, R. J. Squibb, D. Busto, S. Zhong, A. Harth, D. Kroon, S. Nandi, C. L. Arnold, M. Miranda, J. M. Dahlström, E. Lindroth, R. Feifel, M. Gisselbrecht, and A. L’Huillier, “Photoionization in the time and frequency domain,” *Science*, vol. 358, no. 6365, pp. 893–896, 2017.
- [13] S. Haessler, B. Fabre, J. Higuët, J. Caillat, T. Ruchon, P. Breger, B. Carré, E. Constant, A. Maquet, E. Mével, P. Salières, R. Taïeb, and Y. Mairesse, “Phase-resolved attosecond near-threshold photoionization of molecular nitrogen,” *Physical Review A*, vol. 80, no. 1, p. 011404, 2009.
- [14] A. L. Cavalieri, N. Müller, T. Uphues, V. S. Yakovlev, A. Baltuska, B. Horvath, B. Schmidt, L. Blümel, R. Holzwarth, S. Hendel, M. Drescher, U. Kleineberg, P. M. Echenique, R. Kienberger, F. Krausz, and U. Heinzmann, “Attosecond spectroscopy in condensed matter.,” *Nature*, vol. 449, no. 7165, pp. 1029–1032, 2007.
- [15] G. Sansone, F. Kelkensberg, J. F. Pérez-Torres, F. Morales, M. F. Kling, W. Siu, O. Ghafur, P. Johnsson, M. Swoboda, E. Benedetti, F. Ferrari, F. Lépine, J. L. Sanz-Vicario, S. Zherebtsov, I. Znakovskaya, A. L’huillier, M. Y. Ivanov, M. Nisoli, F. Martin, and M. J. J. Vrakking, “Electron localization following attosecond molecular photoionization.,” *Nature*, vol. 465, no. 7299, pp. 763–766, 2010.
- [16] F. Calegari, D. Ayuso, A. Trabattoni, L. Belshaw, S. De Camillis, S. Anumula, F. Frassetto, L. Poletto, A. Palacios, P. Decleva, J. B. Greenwood, F. Martín, and M. Nisoli, “Ultrafast electron dynamics in phenylalanine initiated by attosecond pulses,” *Science*, vol. 346, pp. 336–339, 2014.
- [17] F. Lépine, M. Y. Ivanov, and M. J. Vrakking, “Attosecond molecular dynamics: Fact or fiction?,” *Nature Photonics*, vol. 8, no. 3, pp. 195–204, 2014.
- [18] N. Thiré, S. Beaulieu, V. Cardin, A. Laramée, V. Wanie, B. E. Schmidt, and F. Légaré, “10 mJ 5-cycle pulses at 1.8  $\mu\text{m}$  through optical parametric amplification,” *Applied Physics Letters*, vol. 106, no. 9, p. 091110, 2015.
- [19] D. Strickland and G. Mourou, “Compression of amplified chirped optical pulses,” *Optics Communications*, vol. 56, no. 3, pp. 219–221, 1985.
- [20] A. Anderson, F. Lücking, T. Prikozovits, M. Hofer, Z. Cheng, C. C. Neacsu, M. Scharrer, S. Rammler, P. S. J. Russell, G. Tempea, and A. Assion, “Multi-mJ carrier envelope phase

- stabilized few-cycle pulses generated by a tabletop laser system,” *Applied Physics B: Lasers and Optics*, vol. 103, no. 3, pp. 531–536, 2011.
- [21] L. Canova, X. Chen, A. Trisorio, A. Jullien, A. Assion, G. Tempea, N. Forget, T. Oksenhendler, and R. Lopez-Martens, “Carrier-envelope phase control using a transmission grating compressor and an AOPDF,” *Optics Letters*, vol. 34, no. 9, pp. 1333–1335, 2009.
- [22] M. Nisoli, S. De Silvestri, and O. Svelto, “Generation of high energy 10 fs pulses by a new pulse compression technique,” *Applied Physics Letters*, vol. 68, no. 20, pp. 2793–2795, 1996.
- [23] C. P. Hauri, W. Kornelis, F. W. Helbing, A. Heinrich, A. Couairon, A. Mysyrowicz, J. Biegert, and U. Keller, “Generation of intense, carrier-envelope phase-locked few-cycle laser pulses through filamentation,” *Applied Physics B: Lasers and Optics*, vol. 79, no. 6, pp. 673–677, 2004.
- [24] T. Popmintchev, M.-C. Chen, D. Popmintchev, P. Arpin, S. Brown, S. Alisauskas, G. Andriukaitis, T. Balciunas, O. D. Mucke, A. Pugzlys, A. Baltuska, B. Shim, S. E. Schrauth, A. Gaeta, C. Hernandez-Garcia, L. Plaja, A. Becker, A. Jaron-Becker, M. M. Murnane, and H. C. Kapteyn, “Bright Coherent Ultrahigh Harmonics in the keV X-ray Regime from Mid-Infrared Femtosecond Lasers,” *Science*, vol. 336, no. 6086, pp. 1287–1291, 2012.
- [25] S. L. Cousin, F. Silva, S. Teichmann, M. Hemmer, B. Buades, and J. Biegert, “High-flux table-top soft x-ray source driven by sub-2-cycle, CEP stable, 185- $\mu\text{m}$  1-kHz pulses for carbon K-edge spectroscopy,” *Optics Letters*, vol. 39, no. 18, p. 5383, 2014.
- [26] S. Ghimire, A. D. Dichiaro, E. Sistrunk, U. B. Szafruga, P. Agostini, L. F. Dimauro, and D. A. Reis, “Redshift in the optical absorption of ZnO single crystals in the presence of an intense midinfrared laser field,” *Physical Review Letters*, vol. 107, no. 16, p. 167407, 2011.
- [27] M. Meckel, D. Comtois, D. Zeidler, A. Staudte, D. Pavičić, H. C. Bandulet, H. Pépin, J. C. Kieffer, R. Dörner, D. M. Villeneuve, and P. B. Corkum, “Laser-induced electron tunneling and diffraction,” *Science*, vol. 320, no. 5882, pp. 1478–1482, 2008.
- [28] T. Zuo, A. D. Bandrauk, and P. B. Corkum, “Laser-induced electron diffraction: A new tool for probing ultrafast molecular dynamics,” *Chemical Physics Letters*, vol. 259, no. 3-4, pp. 313–320, 1996.
- [29] G. Cerullo and S. De Silvestri, “Ultrafast optical parametric amplifiers,” *Review of Scientific Instruments*, vol. 74, no. 1 I, pp. 1–18, 2003.
- [30] B. E. Schmidt, A. D. Shiner, P. Lassonde, J. C. Kieffer, P. B. Corkum, D. M. Villeneuve, and F. Légaré, “CEP stable 1.6 cycle laser pulses at 1.8  $\mu\text{m}$ ,” *Optics express*, vol. 19, no. 7, pp. 6858–6864, 2011.

- [31] C. Manzoni, C. Vozzi, E. Benedetti, G. Sansone, S. Stagira, O. Svelto, S. De Silvestri, M. Nisoli, and G. Cerullo, “Generation of high-energy self-phase-stabilized pulses by difference-frequency generation followed by optical parametric amplification,” *Optics Letters*, vol. 31, no. 7, p. 963, 2006.
- [32] J. Moses, S.-W. Huang, K.-H. Hong, O. D. Mücke, E. L. Falcão-Filho, A. Benedick, F. Ö. Ilday, A. Dergachev, J. A. Bolger, B. J. Eggleton, and F. X. Kärtner, “Highly stable ultra-broadband mid-IR optical parametric chirped-pulse amplifier optimized for superfluorescence suppression,” *Optics Letters*, vol. 34, no. 11, p. 1639, 2009.
- [33] B. E. Schmidt, N. Thiré, M. Boivin, A. Laramée, F. Poitras, G. Lebrun, T. Ozaki, H. Ibrahim, and F. Légaré, “Frequency domain optical parametric amplification,” *Nature Communications*, vol. 5, no. May, pp. 1–8, 2014.
- [34] V. Gruson, G. Ernotte, P. Lassonde, L. Di Mauro, P. Corkum, H. Ibrahim, B. Schmidt, and F. Légaré, “Two-cycle, 2.5 TW pulse generation at 1.8  $\mu\text{m}$  via frequency domain optical parametric amplification,” *Optics Express*, vol. 25, no. 22, p. 27706, 2017.
- [35] M. Nisoli, S. De Silvestri, O. Svelto, R. Szipöcs, K. Ferencz, C. Spielmann, S. Sartania, and F. Krausz, “Compression of high-energy laser pulses below 5 fs,” *Optics Letters*, vol. 22, no. 8, p. 522, 1997.
- [36] R. Abrams, “Coupling Losses in Hollow Waveguide Laser Resonators,” *IEEE Journal of Quantum Electronics*, vol. 8, no. 11, 1972.
- [37] J. Park, J.-h. Lee, and C. H. Nam, “Generation of 1.5 cycle 0.3 TW laser pulses using a hollow-fiber pulse compressor,” *Optics Letters*, vol. 34, no. 15, p. 2342, 2009.
- [38] T. Nagy, M. Forster, and P. Simon, “Flexible hollow fiber for pulse compressors,” *Applied Optics*, vol. 47, no. 18, pp. 3264–3268, 2008.
- [39] E. A. Marcatili and R. A. Schmeltzer, “Hollow Metallic and Dielectric Waveguides for Long Distance Optical Transmission and Lasers,” *Bell System Technical Journal*, vol. 43, no. 4, pp. 1783–1809, 1964.
- [40] T. Nagy, V. Pervak, and P. Simon, “Optimal pulse compression in long hollow fibers,” *Optics Letters*, vol. 36, no. 22, pp. 4422–4424, 2011.
- [41] D. Herrmann, L. Veisz, R. Tautz, A. Buck, F. Tavella, K. Schmid, V. Pervak, M. Scharrer, P. Russell, and F. Krausz, “Generation of sub-three-cycle, 16 TW light pulses by use of optical parametric chirped pulse amplification,” *Optics Letters*, vol. 34, no. 16, pp. 2459–2461, 2009.
- [42] S. Witte and K. S. Eikema, “Ultrafast optical parametric chirped-pulse amplification,” *IEEE Journal on Selected Topics in Quantum Electronics*, vol. 18, no. 1, pp. 296–307, 2012.

- [43] D. Brida, S. Bonora, G. Cirimi, C. Manzoni, S. De Silvestri, G. Cerullo, and P. Villoresi, "Sub-two-cycle light pulses at 1.6  $\mu\text{m}$  from an optical parametric amplifier," *Optics Letters*, vol. 33, no. 7, pp. 741–743, 2008.
- [44] Y. Deng, A. Schwarz, H. Fattahi, M. Ueffing, X. Gu, M. Ossiander, T. Metzger, V. Pervak, H. Ishizuki, T. Taira, T. Kobayashi, G. Marcus, F. Krausz, R. Kienberger, and N. Karpowicz, "Carrier-envelope-phase-stable, 1.2 mJ, 1.5 cycle laser pulses at 2.1  $\mu\text{m}$ ," *Optics Letters*, vol. 37, no. 23, pp. 4973–4975, 2012.
- [45] N. Ishii, K. Kaneshima, K. Kitano, T. Kanai, S. Watanabe, and J. Itatani, "Sub-two-cycle, carrier-envelope phase-stable, intense optical pulses at 1.6  $\mu\text{m}$  from a BiB3O6 optical parametric chirped-pulse amplifier N.," *Optics Letters*, vol. 37, no. 20, pp. 1180–1180, 2012.
- [46] A. Braun, X. Liu, G. Korn, D. Du, J. Squier, and G. Mourou, "Self-channeling of intense femtosecond laser pulses in air," *Optics Letters*, vol. 20, no. 1, pp. 73–75, 1995.
- [47] G. Stibenz, N. Zhavoronkov, and G. Steinmeyer, "Self-compression of millijoule pulses to 7.8 fs duration in a white-light filament," *Optics Letters*, vol. 31, no. 2, pp. 274–276, 2006.
- [48] C. P. Hauri, A. Guandalini, P. Eckle, W. Kornelis, J. Biegert, and U. Keller, "Generation of intense few-cycle laser pulses through filamentation - parameter dependence," *Optics Express*, vol. 13, no. 19, p. 7541, 2005.
- [49] A. J. Verhoef, A. V. Mitrofanov, E. E. Serebryannikov, D. V. Kartashov, A. M. Zheltikov, and A. Baltuška, "Optical detection of tunneling ionization," *Physical Review Letters*, vol. 104, no. 16, p. 163904, 2010.
- [50] Y. Matsuura, T. Oyama, and M. Miyagi, "Soft-x-ray hollow fiber optics with inner metal coating," *Applied Optics*, vol. 44, no. 29, pp. 6193–6196, 2005.
- [51] X. Jiang, D. Chen, and G. Hu, "Suspended hollow core fiber for terahertz wave guiding," *Applied Optics*, vol. 52, no. 4, pp. 770–774, 2013.
- [52] P. S. J. Russell, "Photonic-Crystal Fibers," *Journal of Lightwave Technology*, vol. 24, no. 12, pp. 4729–4749, 2006.
- [53] C. Fourcade Dutin, A. Dubrouil, S. Petit, E. Mével, E. Constant, and D. Descamps, "Pulses Using Gas Ionization," *Optics Letters*, vol. 35, no. 2, pp. 253–255, 2010.
- [54] J. Rothhardt, S. Hädrich, A. Klenke, S. Demmler, A. Hoffmann, T. Gotschall, T. Eidam, M. Krebs, J. Limpert, and A. Tünnermann, "53 W average power few-cycle fiber laser system generating soft x rays up to the water window," *Optics Letters*, vol. 39, no. 17, p. 5224, 2014.
- [55] M. Nurhuda, A. Suda, K. Midorikawa, M. Hatayama, and K. Nagasaka, "Propagation dynamics of femtosecond laser pulses in a hollow fiber filled with argon: constant gas pressure

- versus differential gas pressure,” *Journal of the Optical Society of America B*, vol. 20, no. 9, pp. 2002–2011, 2003.
- [56] S. Bohman, A. Suda, T. Kanai, S. Yamaguchi, and K. Midorikawa, “Generation of 5-fs, 5-mJ pulse using hollow-fiber pulse compression at 1 kHz,” *Optics Letters*, vol. 35, no. 11, pp. 1887–1889, 2010.
- [57] W. Ettoumi, Y. Petit, J. Kasparian, and J.-P. Wolf, “Generalized Miller Formulæ,” *Optics Express*, vol. 18, no. 7, p. 6613, 2010.
- [58] D. Wang, Y. Leng, and Z. Xu, “Measurement of nonlinear refractive index coefficient of inert gases with hollow-core fiber,” *Applied Physics B*, vol. 111, no. 3, pp. 447–452, 2013.
- [59] G. Andriukaitis, D. Kartashov, D. Lorenc, A. Pugžlys, A. Baltuška, L. Giniūnas, R. Danielius, J. Limpert, T. Clausnitzer, E.-B. Kley, A. Voronin, and A. Zheltikov, “Hollow-fiber compression of 6 mJ pulses from a continuous-wave diode-pumped single-stage Yb,Na:CaF<sub>2</sub> chirped pulse amplifier,” *Optics Letters*, vol. 36, no. 10, pp. 1914–1916, 2011.
- [60] G. Fibich and A. L. Gaeta, “Critical power for self-focusing in bulk media and in hollow waveguides,” *Optics Letters*, vol. 25, no. 5, pp. 335–337, 2000.
- [61] S. Bohman, A. Suda, M. Kaku, M. Nurhuda, T. Kanai, S. Yamaguchi, and K. Midorikawa, “Generation of 5 fs, 0.5 TW pulses focusable to relativistic intensities at 1 kHz,” *Optics Express*, vol. 16, no. 14, p. 16684, 2008.
- [62] B. E. Schmidt, P. B ejot, M. Gigu ere, A. D. Shiner, C. Trallero-Herrero,  . Bisson, J. Kasparian, J. P. Wolf, D. M. Villeneuve, J. C. Kieffer, P. B. Corkum, and F. L egar e, “Compression of 1.8  $\mu\text{m}$  laser pulses to sub two optical cycles with bulk material,” *Applied Physics Letters*, vol. 96, no. 12, 2010.
- [63] A. Suda, M. Hatayama, K. Nagasaka, and K. Midorikawa, “Generation of sub-10-fs, 5-mJ-optical pulses using a hollow fiber with a pressure gradient,” *Applied Physics Letters*, vol. 86, no. 11, 2005.
- [64] J. Crenn, “Optical theory of Gaussian beam transmission through a hollow circular dielectric waveguide,” *Applied Optics*, vol. 22, no. 10, p. 4533, 1983.
- [65] P. B ejot, B. E. Schmidt, J. Kasparian, J. P. Wolf, and F. L egar e, “Mechanism of hollow-core-fiber infrared-supercontinuum compression with bulk material,” *Physical Review A*, vol. 81, no. 6, 2010.
- [66] D. Anderson and M. Lisak, “Nonlinear asymmetric self-phase modulation and self-steepening of pulses in long optical waveguides,” *Physical Review A*, vol. 27, no. 3, pp. 1393–1398, 1983.
- [67] A. L. Gaeta, “Catastrophic collapse of ultrashort pulses,” *Physical Review Letters*, vol. 84, no. 16, pp. 3582–3585, 2000.

- [68] O. Razskazovskaya, T. T. Luu, M. Trubetskov, E. Goulielmakis, and V. Pervak, “Nonlinear absorbance in dielectric multilayers,” *Optica*, vol. 2, no. 9, pp. 803–811, 2015.
- [69] X. Chen, A. Jullien, A. Malvache, L. Canova, A. Borot, A. Trisorio, C. Durfee, and R. Lopez-Martens, “Carrier-envelope phase stable mJ level few-cycle pulse generation via compression of circularly polarized pulses in a gas-filled hollow-core fiber,” *Optics Letters*, vol. 34, no. 10, pp. 1588–1590, 2009.
- [70] K. J. Schafer, B. Yang, L. F. Dimauro, and K. C. Kulander, “Above threshold ionization beyond the high harmonic cutoff,” *Physical Review Letters*, vol. 70, no. 11, pp. 1599–1602, 1993.
- [71] L. V. Keldysh, “Ionization in the field of a strong electromagnetic wave,” *Soviet Physics JETP*, vol. 20, no. 5, pp. 1307–1314, 1965.
- [72] P. B. Corkum and F. Krausz, “Attosecond science,” *Nature Physics*, vol. 3, p. 381, 2007.
- [73] M. Lewenstein, P. Balcou, M. Y. Ivanov, A. L’Huillier, and P. B. Corkum, “Theory of high-harmonic generation by low-frequency laser fields,” *Physical Review A*, vol. 49, no. 3, pp. 2117–2132, 1994.
- [74] K. Varjú, Y. Mairesse, B. Carré, M. B. Gaarde, P. Johnsson, S. Kazamias, R. López-Martens, J. Mauritsson, K. J. Schafer, P. Balcou, A. L’Huillier, and P. Salières, “Frequency chirp of harmonic and attosecond pulses,” *Journal of Modern Optics*, vol. 52, no. 2-3, pp. 379–394, 2005.
- [75] M. B. Gaarde, F. Salin, E. Constant, P. Balcou, K. J. Schafer, K. C. Kulander, and A. L’Huillier, “Spatiotemporal separation of high harmonic radiation into two quantum path components,” *Physical Review A*, vol. 59, no. 2, pp. 1367–1373, 1999.
- [76] J. Rothhardt, M. Krebs, S. Hädrich, S. Demmler, J. Limpert, and A. Tünnermann, “Absorption-limited and phase-matched high harmonic generation in the tight focusing regime,” *New Journal of Physics*, vol. 16, 2014.
- [77] C. M. Heyl, J. Güttele, A. Lhuillier, and U. Höfer, “High-order harmonic generation with  $\mu\text{J}$  laser pulses at high repetition rates,” *Journal of Physics B: Atomic, Molecular and Optical Physics*, vol. 45, no. 7, 2012.
- [78] T. Popmintchev, M. C. Chen, A. Bahabad, M. Gerrity, P. Sidorenko, O. Cohen, S. Backus, X. Zhang, G. Taft, I. P. Christov, M. M. Murnane, and H. C. Kapteyn, “Phase matching of high harmonic generation in the soft and hard X-ray regions of the spectrum,” *Proceedings of the National Academy of Sciences of the United States of America*, vol. 106, no. 26, pp. 10515–10521, 2009.

- [79] M. C. Chen, P. Arpin, T. Popmintchev, M. Gerrity, B. Zhang, M. Seaberg, D. Popmintchev, M. M. Murnane, and H. C. Kapteyn, “Bright, coherent, ultrafast soft x-ray harmonics spanning the water window from a tabletop light source,” *Physical Review Letters*, vol. 105, no. 17, 2010.
- [80] P. Rudawski, C. M. Heyl, F. Brizuela, J. Schwenke, A. Persson, E. Mansten, R. Rakowski, L. Rading, F. Campi, B. Kim, P. Johnsson, A. L. Huillier, P. Rudawski, C. M. Heyl, F. Brizuela, J. Schwenke, A. Persson, and E. Mansten, “A high-flux high-order harmonic source A high-flux high-order harmonic source,” vol. 073103, no. 2013, 2013.
- [81] A. D. Shiner, C. Trallero-Herrero, N. Kajumba, H. C. Bandulet, D. Comtois, F. Légaré, M. Giguère, J. C. Kieffer, P. B. Corkum, and D. M. Villeneuve, “Wavelength scaling of high harmonic generation efficiency,” *Physical Review Letters*, vol. 103, no. 7, 2009.
- [82] V. Cardin, B. E. Schmidt, N. Thiré, S. Beaulieu, V. Wanie, M. Negro, C. Vozzi, V. Tosa, and F. Légaré, “Self-channelled high harmonic generation of water window soft x-rays,” *Journal of Physics B: Atomic, Molecular and Optical Physics*, vol. 51, no. 17, 2018.
- [83] S. M. Teichmann, F. Silva, S. L. Cousin, M. Hemmer, J. Biegert, and M. Random Author, “0.5-keV Soft X-ray attosecond continua,” *Nature Communications*, vol. 7, no. May, pp. 1–6, 2016.
- [84] Y. Pertot, C. Schmidt, M. Matthews, A. Chauvet, M. Huppert, V. Svoboda, A. von Conta, A. Tehlar, D. Baykusheva, J.-p. Wolf, and H. J. Wörner, “Time-resolved x-ray absorption spectroscopy with a water window high-harmonic source,” *Science*, vol. 355, no. January, pp. 264–267, 2017.
- [85] A. D. Smith, T. Balčiū Nas, Y. P. Chang, C. Schmidt, K. Zinchenko, F. B. Nunes, E. Rossi, V. Svoboda, Z. Yin, J. P. Wolf, and H. J. Wörner, “Femtosecond Soft-X-ray Absorption Spectroscopy of Liquids with a Water-Window High-Harmonic Source,” *Journal of Physical Chemistry Letters*, vol. 11, no. 6, pp. 1981–1988, 2020.
- [86] V. Cardin, T. Balciunas, K. Légaré, A. Baltuska, H. Ibrahim, E. Jal, B. Vodungbo, N. Jaouen, C. Varin, J. Lüning, and F. Légaré, “Wavelength scaling of ultrafast demagnetization in Co/Pt multilayers,” *Physical Review B*, vol. 101, no. 5, pp. 1–6, 2020.
- [87] A. Cavalleri, T. Dekorsy, H. H. Chong, J. C. Kieffer, and R. W. Schoenlein, “Evidence for a structurally-driven insulator-to-metal transition in VO<sub>2</sub>: A view from the ultrafast timescale,” *Physical Review B - Condensed Matter and Materials Physics*, vol. 70, no. 16, pp. 1–4, 2004.
- [88] C. E. Crespo-Hernandez, B. Cohen, P. M. Hare, and B. Kohler, “Ultrafast excited-state dynamics in nucleic acids,” *Chemical Reviews*, vol. 104, no. 4, pp. 1977–2019, 2004.

- [89] C. T. Middleton, K. de La Harpe, C. Su, Y. K. Law, C. E. Crespo-Hernández, and B. Kohler, “DNA Excited-State Dynamics: From Single Bases to the Double Helix,” *Annual Review of Physical Chemistry*, vol. 60, no. 1, pp. 217–239, 2009.
- [90] R. Improta, F. Santoro, and L. Blancafort, “Quantum Mechanical Studies on the Photophysics and the Photochemistry of Nucleic Acids and Nucleobases,” *Chemical Reviews*, vol. 116, no. 6, pp. 3540–3593, 2016.
- [91] R. W. Boyd, *Nonlinear Optics*. Academic Press, Inc., 2008.
- [92] J. Young, B. G.C., K. A.H., R. Miles, and S. Harris, “Third-Harmonic Generation in Phase-Matched Rb Vapor,” *Physical Review Letters*, vol. 27, no. 23, pp. 1551–1553, 1971.
- [93] R. B. Miles and S. E. Harris, “Optical Third-Harmonic Generation in Alkali Metal Vapors,” *IEEE Journal of Quantum Electronics*, vol. 9, no. 4, pp. 470–484, 1973.
- [94] A. Nazarkin, G. K. L. Wong, F. Biancalana, P. S. J. Russell, N. Y. Joly, J. Nold, W. Chang, and P. Ho, “Bright Spatially Coherent Wavelength-Tunable Deep-UV Laser Source Using an Ar-Filled Photonic Crystal Fiber,” vol. 106, p. 203901, 2011.
- [95] H. Lehmeier, W. Leupacher, and A. Penzkofer, “Nonresonant third order hyperpolarizability of rare gases and N<sub>2</sub> determined by third harmonic generation,” *Optics Communications*, vol. 56, no. 1, pp. 67–72, 1985.
- [96] U. Gubler and C. Bosshard, “Optical third-harmonic generation of fused silica in gas atmosphere: Absolute value of the third-order nonlinear optical susceptibility,” *Physical Review B*, vol. 61, no. 16, pp. 10702–10710, 2000.
- [97] I. J. Sola, E. Mével, L. Elouga, E. Constant, V. Strelkov, L. Poletto, P. Villoresi, E. Benedetti, J.-P. Caumes, S. Stagira, C. Vozzi, G. Sansone, and M. Nisoli, “Controlling attosecond electron dynamics by phase-stabilized polarization gating,” *Nature Physics*, vol. 2, no. 5, pp. 319–322, 2006.
- [98] K. S. Budil, P. Salières, M. D. Perry, and A. L’Huillier, “Influence of ellipticity on harmonic generation,” *Physical Review A*, vol. 48, no. 5, pp. 3437–3440, 1993.
- [99] V. Strelkov, A. Zaïr, O. Tcherbakoff, R. López-Martens, E. Cormier, E. Mével, and E. Constant, “Single attosecond pulse production with an ellipticity-modulated driving IR pulse,” *Journal of Physics B: Atomic, Molecular and Optical Physics*, vol. 38, no. 10, 2005.
- [100] S. G. Rykovanov, M. Geissler, J. Meyer-ter Vehn, and G. D. Tsakiris, “Intense single attosecond pulses from surface harmonics using the polarization gating technique,” *New Journal of Physics*, vol. 10, 2008.
- [101] J. Reislöhner, C. Leithold, and A. N. Pfeiffer, “Harmonic Concatenation of 1.5 fs Pulses in the Deep Ultraviolet,” *ACS Photonics*, vol. 6, no. 6, pp. 1351–1355, 2019.

- [102] M. Galli, V. Wanie, D. P. Lopes, E. P. Månsson, A. Trabattoni, L. Colaizzi, K. Saraswathula, A. Cartella, F. Frassetto, L. Poletto, F. Légaré, S. Stagira, M. Nisoli, R. Martínez Vázquez, R. Osellame, and F. Calegari, “Generation of deep ultraviolet sub-2-fs pulses,” *Optics Letters*, vol. 44, no. 6, p. 1308, 2019.
- [103] F. Reiter, U. Graf, M. Schultze, W. Schweinberger, H. Schröder, N. Karpowicz, A. M. Azzeer, R. Kienberger, F. Krausz, and E. Goulielmakis, “Generation of sub-3 fs pulses in the deep ultraviolet,” *Optics Letters*, vol. 35, no. 13, p. 2248, 2010.
- [104] C. Brahms, D. R. Austin, F. Tani, A. S. Johnson, D. Garratt, J. C. Travers, J. W. Tisch, P. S. Russell, and J. P. Marangos, “Direct characterization of tuneable few-femtosecond dispersive-wave pulses in the deep UV,” *Optics Letters*, vol. 44, no. 4, pp. 731–734, 2019.
- [105] T. Fuji and T. Suzuki, “Generation of sub-two-cycle mid-infrared pulses by four-wave mixing through filamentation in air,” *Optics Letters*, vol. 32, no. 22, p. 3330, 2007.
- [106] F. Belli, A. Abdolvand, J. C. Travers, and P. S. J. Russell, “Highly efficient deep UV generation by four-wave mixing in gas-filled hollow-core photonic crystal fiber,” *Optics Letters*, vol. 44, no. 22, pp. 5509–5512, 2019.
- [107] F. Reiter, U. Graf, E. E. Serebryannikov, W. Schweinberger, M. Fiess, M. Schultze, A. M. Azzeer, R. Kienberger, F. Krausz, A. M. Zheltikov, and E. Goulielmakis, “Route to attosecond nonlinear spectroscopy,” *Physical Review Letters*, vol. 105, no. 24, pp. 1–4, 2010.
- [108] A. Comby, S. Beaulieu, D. Descamps, S. Petit, and Y. Mairesse, “Absolute gas density profiling in high-order harmonic generation,” *Optics Express*, vol. 26, no. 5, pp. 6001–6009, 2018.
- [109] J. N. Sweetser, D. N. Fittinghoff, and R. Trebino, “Transient-grating frequency-resolved optical gating,” vol. 22, no. 8, pp. 519–521, 1997.
- [110] Y. Kida, “Transient grating in a thin gas target for characterization of extremely short optical pulses,” *Optics Letters*, vol. 45, no. 8, p. 2231, 2020.
- [111] T. Gustavsson, R. Improta, and D. Markovitsi, “DNA/RNA: Building blocks of life under UV irradiation,” *Journal of Physical Chemistry Letters*, vol. 1, no. 13, pp. 2025–2030, 2010.
- [112] C. E. Crespo-Hernández, B. Cohen, and B. Kohler, “Base stacking controls excited-state dynamics in A · T DNA,” *Nature*, vol. 436, no. 7054, pp. 1141–1144, 2005.
- [113] D. Fabris, T. Witting, W. A. Okell, D. J. Walke, P. Matia-Hernando, J. Henkel, T. R. Barillot, M. Lein, J. P. Marangos, and J. W. Tisch, “Synchronized pulses generated at 20 eV and 90 eV for attosecond pump-probe experiments,” *Nature Photonics*, vol. 9, no. 6, pp. 383–387, 2015.
- [114] G. Sansone, E. Benedetti, F. Calegari, C. Vozzi, L. Avaldi, R. Flammini, L. Poletto, P. Villoresi, C. Altucci, R. Velotta, S. Stagira, S. De Silvestri, and M. Nisoli, “Isolated Single-Cycle Attosecond Pulses,” *Science*, vol. 314, no. 5798, pp. 443–446, 2006.

- [115] F. Krausz and M. Ivanov, “Attosecond physics,” *Reviews of Modern Physics*, vol. 81, no. 1, pp. 163–234, 2009.
- [116] F. Calegari, G. Sansone, S. Stagira, C. Vozzi, and M. Nisoli, “Advances in attosecond science,” *Journal of Physics B: Atomic, Molecular and Optical Physics*, vol. 49, no. 6, p. 062001, 2016.
- [117] S. L. Cousin, N. Di Palo, B. Buades, S. M. Teichmann, M. Reduzzi, M. Devetta, A. Kheifets, G. Sansone, and J. Biegert, “Attosecond streaking in the water window: A new regime of attosecond pulse characterization,” *Physical Review X*, vol. 7, no. 4, pp. 1–14, 2017.
- [118] M. T. Hassan, T. T. Luu, A. Moulet, O. Raskazovskaya, P. Zhokhov, M. Garg, N. Karpowicz, A. M. Zheltikov, V. Pervak, F. Krausz, and E. Goulielmakis, “Optical attosecond pulses and tracking the nonlinear response of bound electrons,” *Nature*, vol. 530, no. 7588, pp. 66–70, 2016.
- [119] P. Baum, S. Lochbrunner, and E. Riedle, “Generation of tunable 7-fs ultraviolet pulses: Achromatic phase matching and chirp management,” *Applied Physics B*, vol. 79, pp. 1027–1032, 2004.
- [120] P. Tzankov, T. Fiebig, and I. Buchvarov, “Tunable femtosecond pulses in the near-ultraviolet from ultrabroadband parametric amplification,” *Applied Physics Letters*, vol. 82, no. 4, pp. 517–519, 2003.
- [121] Y. Kida, J. Liu, T. Teramoto, and T. Kobayashi, “Sub-10 fs deep-ultraviolet pulses generated by chirped-pulse four-wave mixing,” *Optics Letters*, vol. 35, no. 11, pp. 1807–1809, 2010.
- [122] C. G. Durfee, S. Backus, H. C. Kapteyn, M. M. Murnane, C. G. Durfee III, C. G. D. Iii, S. Backus, H. C. Kapteyn, M. M. Murnane, C. G. Durfee, S. Backus, H. C. Kapteyn, M. M. Murnane, C. G. D. Iii, S. Backus, H. C. Kapteyn, M. M. Murnane, C. G. Durfee III, S. Backus, H. C. Kapteyn, and M. M. Murnane, “Intense 8-fs pulse generation in the deep ultraviolet,” *Optics Letters*, vol. 24, no. 10, pp. 697–699, 1999.
- [123] F. Köttig, F. Tani, C. M. Biersach, J. C. Travers, and P. S. Russell, “Generation of microjoule pulses in the deep ultraviolet at megahertz repetition rates,” *Optica*, vol. 4, no. 10, p. 1272, 2017.
- [124] J. Ringling, G. Korn, J. Squier, O. Kittelmann, and F. Noack, “Tunable femtosecond pulses in the near vacuum ultraviolet generated by frequency conversion of amplified Ti:sapphire laser pulses,” *Optics Letters*, vol. 18, no. 23, p. 2035, 1993.
- [125] G. H. C. New and J. F. Ward, “Optical third-harmonic generation in gases,” *Physical Review Letters*, vol. 19, no. 10, pp. 556–559, 1967.
- [126] A. Marcinkevicius, S. Juodkazis, M. Watanabe, M. Miwa, S. Matsuo, H. Misawa, and J. Nishii, “Microfabrication in Silica,” *Optics Letters*, vol. 26, no. 5, pp. 277–279, 2001.

- [127] K. C. Vishnubhatla, N. Bellini, R. Ramponi, G. Cerullo, and R. Osellame, “Shape control of microchannels fabricated in fused silica by femtosecond laser irradiation and chemical etching,” *Optics Express*, vol. 17, no. 10, p. 8685, 2009.
- [128] E. Bothschafter, A. Schiffrin, F. Krausz, R. Ernstorfer, and R. Kienberger, “Collinear generation of ultrashort UV and XUV pulses for pump/probe spectroscopy,” *Optics Express*, vol. 18, no. 9, pp. 9173–9180, 2010.
- [129] L. Allen, D. G. C. Jones, and D. G. Schofield, “Radiative Lifetimes and Collisional Cross Sections for Xe I and II,” *Journal of the Optical Society of America*, vol. 59, no. 7, p. 842, 1969.
- [130] S. Kröll and W. K. Bischel, “Two-photon absorption and photoionization cross-section measurements in the  $5p^5 6p$  configuration of xenon,” *Physical Review A*, vol. 41, no. 3, pp. 1340–1349, 1990.
- [131] A. Schmitt and H. Schmoranzler, “Radiative lifetimes of the  $5p^5 6p$ -fine-structure levels of xenon measured by beam-gas-laser spectroscopy,” *Physics Letters, Section A*, vol. 263, no. 3, pp. 193–198, 1999.
- [132] A. G. Ciriolo, R. M. Vazquez, G. Crippa, D. Facciala, M. Negro, M. Devetta, D. P. Lopes, A. Pusala, C. Vozzi, R. Osellame, and S. Stagira, “High-order harmonic generation in femtosecond laser-micromachined devices,” in *Conference on Lasers and Electro-Optics, CLEO*, vol. 1, pp. 2–3, 2018.
- [133] L. Gallmann, C. Cirelli, and U. Keller, “Attosecond Science: Recent Highlights and Future Trends,” *Annual Review of Physical Chemistry*, vol. 63, no. 1, pp. 447–469, 2012.
- [134] M. Fie, M. Schultze, E. Goulielmakis, B. Dennhardt, J. Gagnon, M. Hofstetter, R. Kienberger, and F. Krausz, “Versatile apparatus for attosecond metrology and spectroscopy,” *Review of Scientific Instruments*, vol. 81, no. 9, pp. 1–8, 2010.
- [135] F. Frank, C. Arrell, T. Witting, W. A. Okell, J. McKenna, J. S. Robinson, C. A. Haworth, D. Austin, H. Teng, I. A. Walmsley, J. P. Marangos, and J. W. Tisch, “Invited review article: Technology for attosecond science,” *Review of Scientific Instruments*, vol. 83, no. 7, 2012.
- [136] S. J. Weber, B. Manschwetus, M. Billon, M. Böttcher, M. Bougeard, P. Breger, M. Géléoc, V. Gruson, A. Huetz, N. Lin, Y. J. Picard, T. Ruchon, P. Salières, and B. Carré, “Flexible attosecond beamline for high harmonic spectroscopy and XUV/near-IR pump probe experiments requiring long acquisition times,” *Review of Scientific Instruments*, vol. 86, no. 3, pp. 1–13, 2015.
- [137] M. Sabbar, S. Heuser, R. Boge, M. Lucchini, L. Gallmann, C. Cirelli, and U. Keller, “Combining attosecond XUV pulses with coincidence spectroscopy,” *Review of Scientific Instruments*, vol. 85, no. 10, 2014.

- [138] E. Magerl, S. Neppel, A. L. Cavalieri, E. M. Bothschafter, M. Stanislowski, T. Uphues, M. Hofstetter, U. Kleineberg, J. V. Barth, D. Menzel, F. Krausz, R. Ernstorfer, R. Kienberger, and P. Feulner, “A flexible apparatus for attosecond photoelectron spectroscopy of solids and surfaces,” *Review of Scientific Instruments*, vol. 82, no. 6, 2011.
- [139] M. F. Jager, C. Ott, C. J. Kaplan, P. M. Kraus, D. M. Neumark, and S. R. Leone, “Attosecond transient absorption instrumentation for thin film materials: Phase transitions, heat dissipation, signal stabilization, timing correction, and rapid sample rotation,” *Review of Scientific Instruments*, vol. 89, no. 1, 2018.
- [140] R. Locher, M. Lucchini, J. Herrmann, M. Sabbar, M. Weger, A. Ludwig, L. Castiglioni, M. Greif, M. Hengsberger, L. Gallmann, and U. Keller, “Versatile attosecond beamline in a two-foci configuration for simultaneous time-resolved measurements,” *Review of Scientific Instruments*, vol. 85, no. 1, 2014.
- [141] B. Frietsch, R. Carley, K. Döbrich, C. Gahl, M. Teichmann, O. Schwarzkopf, P. Wernet, and M. Weinelt, “A high-order harmonic generation apparatus for time- and angle-resolved photoelectron spectroscopy,” *Review of Scientific Instruments*, vol. 84, no. 7, 2013.
- [142] Y. Liu, J. E. Beetar, M. Hosen, G. Dhakal, C. Sims, F. Kabir, M. B. Etienne, K. Dimitri, S. Regmi, M. Neupane, and M. Chini, “Extreme ultraviolet time- and angle- resolved photoemission setup with 21 . 5 meV resolution using high-order harmonic generation from a turn-key Yb : KGW amplifier,” *Review of Scientific Instruments*, vol. 91, no. 013102, 2020.
- [143] V. Stooß, M. Hartmann, P. Birk, G. D. Borisova, T. Ding, C. Ott, and T. Pfeifer, “XUV-beamline for attosecond transient absorption measurements featuring a broadband common beam-path time-delay unit and in situ reference spectrometer for high stability and sensitivity,” *Review of Scientific Instruments*, vol. 90, no. 053108, 2019.
- [144] G. D. Lucarelli, B. Moio, G. Inzani, N. Fabris, L. Moscardi, F. Frassetto, L. Poletto, M. Nisoli, and M. Lucchini, “Novel beamline for attosecond transient reflection spectroscopy in a sequential two-foci geometry,” 2020.
- [145] I. Makos, I. Orfanos, A. Nayak, J. Peschel, B. Major, I. Liontos, E. Skantzakis, N. Papadakis, C. Kalpouzios, M. Dumergue, S. Kühn, K. Varju, P. Johnsson, A. L’Huillier, P. Tzallas, and D. Charalambidis, “A 10-gigawatt attosecond source for non-linear XUV optics and XUV-pump-XUV-probe studies,” *Scientific Reports*, vol. 10, no. 3759, pp. 1–18, 2020.
- [146] E. P. Mansson, S. De Camillis, M. C. Castrovilli, M. Galli, M. Nisoli, F. Calegari, and J. B. Greenwood, “Ultrafast Dynamics in the DNA Building Blocks Thymidine and Thymine Initiated By Ionizing Radiation,” *Phys. Chem. Chem. Phys.*, pp. 19815–19821, 2017.
- [147] E. Perfetto, A. Trabattoni, F. Calegari, M. Nisoli, A. Marini, and G. Stefanucci, “Ultrafast Quantum Interference in the Charge Migration of Tryptophan,” *Journal of Physical Chemistry Letters*, vol. 11, no. 3, pp. 891–899, 2020.

- [148] J. Itatani, F. Quéré, G. L. Yudin, M. Y. Ivanov, F. Krausz, and P. B. Corkum, “Attosecond streak camera.,” *Physical review letters*, vol. 88, no. 17, p. 173903, 2002.
- [149] R. Kienberger, E. Goulielmakis, M. Uiberacker, A. Baltuska, V. Yakovlev, F. Bammer, A. Scrinzi, T. Westerwalbesloh, U. Kleineberg, U. Heinzmann, M. Drescher, and F. Krausz, “Atomic transient recorder,” *Nature*, vol. 427, pp. 817–821, 2004.
- [150] P. A. Franken, A. E. Hill, C. W. Peters, and G. Weinreich, “Generation of optical harmonics,” *Physical Review Letters*, vol. 7, no. 4, pp. 118–119, 1961.
- [151] S. N. Zhu, Y. Y. Zhu, and N. B. Ming, “Quasi-phase-matched third-harmonic generation in a quasi-periodic optical superlattice,” *Science*, vol. 278, no. 5339, pp. 843–846, 1997.
- [152] T. Nagy and P. Simon, “Generation of 200-microJ, sub-25-fs deep-UV pulses using a noble-gas-filled hollow fiber.,” *Optics Letters*, vol. 34, no. 15, pp. 2300–2, 2009.
- [153] T. Fuji, T. Suzuki, E. E. Serebryannikov, and A. Zheltikov, “Experimental and theoretical investigation of a multicolor filament,” *Physical Review A*, vol. 80, no. 6, pp. 2–6, 2009.
- [154] U. Graf, M. Fiess, M. Schultze, R. Kienberger, F. Krausz, and E. Goulielmakis, “Intense few-cycle light pulses in the deep ultraviolet.,” *Optics express*, vol. 16, no. 23, pp. 18956–18963, 2008.
- [155] J. C. Travers, T. F. Grigorova, C. Brahms, and F. Belli, “High-energy pulse self-compression and ultraviolet generation soliton dynamics in hollow capillary fibres,” *Nature Photonics*, vol. 13, no. August, pp. 547–554, 2019.
- [156] C. Brahms, T. F. Grigorova, F. Belli, and J. C. Travers, “High-energy ultraviolet dispersive-wave emission in compact hollow capillary systems,” *Optics Letters*, vol. 44, no. 12, pp. 2990–2993, 2019.
- [157] T. Latka, V. Shirvanyan, M. Ossiander, O. Razskazovskaya, A. Guggenmos, M. Jobst, M. Fieß, S. Holzner, A. Sommer, M. Schultze, C. Jakubeit, J. Riemensberger, B. Bernhardt, W. Helml, F. Gatti, B. Lasorne, D. Lauvergnat, P. Decleva, G. J. Halász, A. Vibók, and R. Kienberger, “Femtosecond wave-packet revivals in ozone,” *Physical Review A*, vol. 99, no. 6, pp. 1–9, 2019.
- [158] T. Harada, K. Takahashi, H. Sakuma, and A. Osyczka, “Optimum design of a grazing-incidence flat-field spectrograph with a spherical varied-line-space grating,” *Applied Optics*, vol. 38, no. 13, p. 2743, 1999.
- [159] L. Poletto, G. Naletto, and G. Tondello, “Grazing-incidence flat-field spectrometer for high-order harmonic diagnostics,” *Optical Engineering*, vol. 40, no. 2, pp. 178–185, 2001.

- [160] F. Ferrari, F. Calegari, M. Lucchini, C. Vozzi, S. Stagira, G. Sansone, and M. Nisoli, “High-energy isolated attosecond pulses generated by above-saturation few-cycle fields,” *Nature Photonics*, vol. 4, no. 12, pp. 875–879, 2010.
- [161] J. Bechhoefer, “Feedback for physicists: A tutorial essay on control,” *Reviews of Modern Physics*, vol. 77, no. 3, pp. 783–836, 2005.
- [162] E. P. Månsson, S. L. Sorensen, C. L. Arnold, D. Kroon, D. Guénot, T. Fordell, F. Lépine, P. Johnsson, A. L’Huillier, and M. Gisselbrecht, “Multi-purpose two- and three-dimensional momentum imaging of charged particles for attosecond experiments at 1 kHz repetition rate,” *Review of Scientific Instruments*, vol. 85, no. 12, 2014.
- [163] L. Rading, J. Lahl, S. Maclot, F. Campi, H. Coudert-Alteirac, B. Oostenrijk, J. Peschel, H. Wikmark, P. Rudawski, M. Gisselbrecht, and P. Johnsson, “A versatile velocity map ion-electron covariance imaging spectrometer for high-intensity XUV experiments,” *Applied Sciences*, vol. 8, no. 6, 2018.
- [164] N. V. Golubev and A. I. Kuleff, “Control of charge migration in molecules by ultrashort laser pulses,” *Physical Review A*, vol. 91, no. 5, pp. 1–5, 2015.
- [165] H. Ibrahim, C. Lefebvre, A. D. Bandrauk, A. Staudte, and F. Légaré, “H<sub>2</sub>: The benchmark molecule for ultrafast science and technologies,” *Journal of Physics B: Atomic, Molecular and Optical Physics*, vol. 51, no. 4, p. 42002, 2018.
- [166] I. I. Rabi, “Space quantization in a gyrating magnetic field,” *Physical Review*, vol. 51, no. 8, pp. 652–654, 1937.
- [167] W. S. Warren, “Effects of pulse shaping in laser spectroscopy and nuclear magnetic resonance,” *Science*, vol. 242, no. 4880, pp. 878–884, 1988.
- [168] P. Brumer and M. Shapiro, “Control of unimolecular reactions using coherent light,” *Chemical Physics Letters*, vol. 126, no. 6, pp. 541–546, 1986.
- [169] M. Shapiro, J. W. Hepburn, and P. Brumer, “Simplified laser control of unimolecular reactions: Simultaneous ( $\omega_1, \omega_3$ ) excitation,” *Chemical Physics Letters*, vol. 149, no. 5-6, pp. 451–454, 1988.
- [170] C. Chen, Y. Y. Yin, and D. S. Elliott, “Interference between optical transitions,” *Physical Review Letters*, vol. 64, no. 5, pp. 507–510, 1990.
- [171] V. D. Kleiman, L. Zhu, X. Li, and R. J. Gordon, “Coherent phase control of the photoionization of H<sub>2</sub>S,” *The Journal of chemical physics*, vol. 102, pp. 5863–5866, 1995.

- [172] D. Ray, F. He, S. De, W. Cao, H. Mashiko, P. Ranitovic, K. P. Singh, I. Znakovskaya, U. Thumm, G. G. Paulus, M. F. Kling, I. V. Litvinyuk, and C. L. Cocke, “Ion-energy dependence of asymmetric dissociation of D<sub>2</sub> by a two-color laser field,” *Physical Review Letters*, vol. 103, no. 22, pp. 1–4, 2009.
- [173] M. F. Kling, C. Siedschlag, A. J. Verhoef, J. I. Khan, M. Schultze, T. Uphues, Y. Ni, M. Uiberacker, M. Drescher, F. Krausz, and M. J. Vrakking, “Control of electron localization in molecular dissociation,” *Science*, vol. 312, no. 5771, pp. 246–248, 2006.
- [174] M. Kremer, B. Fischer, B. Feuerstein, V. L. B. De Jesus, V. Sharma, C. Hofrichter, A. Rudenko, U. Thumm, C. D. Schröter, R. Moshhammer, and J. Ullrich, “Electron localization in molecular fragmentation of H<sub>2</sub> by carrier-envelope phase stabilized laser pulses,” *Physical Review Letters*, vol. 103, no. 21, pp. 1–4, 2009.
- [175] H. Xu, J. P. MacLean, D. E. Laban, W. C. Wallace, D. Kielpinski, R. T. Sang, and I. V. Litvinyuk, “Carrier-envelope-phase-dependent dissociation of hydrogen,” *New Journal of Physics*, vol. 15, p. 023034, 2013.
- [176] I. Znakovskaya, P. Von Den Hoff, G. Marcus, S. Zherebtsov, B. Bergues, X. Gu, Y. Deng, M. J. Vrakking, R. Kienberger, F. Krausz, R. De Vivie-Riedle, and M. F. Kling, “Subcycle controlled charge-directed reactivity with few-cycle midinfrared pulses,” *Physical Review Letters*, vol. 108, no. 6, pp. 1–5, 2012.
- [177] V. Wanie, H. Ibrahim, S. Beaulieu, N. Thiré, B. E. Schmidt, Y. Deng, A. S. Alnaser, I. V. Litvinyuk, X.-M. Tong, and F. Légaré, “Coherent control of D<sub>2</sub>/H<sub>2</sub> dissociative ionization by a mid-infrared two-color laser field,” *Journal of Physics B: Atomic, Molecular and Optical Physics*, vol. 49, no. 2, p. 025601, 2016.
- [178] Y. Nabekawa, Y. Furukawa, T. Okino, A. Amani Eilanlou, E. J. Takahashi, K. Yamanouchi, and K. Midorikawa, “Settling time of a vibrational wavepacket in ionization,” *Nature Communications*, vol. 6, no. 8197, 2015.
- [179] M. F. Kling, P. Von Den Hoff, I. Znakovskaya, and R. De Vivie-Riedle, “(Sub-)femtosecond control of molecular reactions via tailoring the electric field of light,” *Physical Chemistry Chemical Physics*, vol. 15, no. 24, pp. 9448–9467, 2013.
- [180] S. Zherebtsov, T. Fennel, J. Plenge, E. Antonsson, I. Znakovskaya, A. Wirth, O. Herrwerth, F. Sümann, C. Peltz, I. Ahmad, S. A. Trushin, V. Pervak, S. Karsch, M. J. Vrakking, B. Langer, C. Graf, M. I. Stockman, F. Krausz, E. Rühl, and M. F. Kling, “Controlled near-field enhanced electron acceleration from dielectric nanospheres with intense few-cycle laser fields,” *Nature Physics*, vol. 7, no. 8, pp. 656–662, 2011.
- [181] I. Znakovskaya, P. Von Den Hoff, S. Zherebtsov, A. Wirth, O. Herrwerth, M. J. J. Vrakking, R. De Vivie-Riedle, and M. F. Kling, “Attosecond control of electron dynamics in carbon monoxide,” *Physical Review Letters*, vol. 103, no. 10, pp. 2–5, 2009.

- [182] F. Kelkensberg, W. Siu, J. F. Pérez-Torres, F. Morales, G. Gademann, A. Rouzée, P. Johnsson, M. Lucchini, F. Calegari, J. L. Sanz-Vicario, F. Martín, and M. J. J. Vrakking, “Attosecond control in photoionization of hydrogen molecules,” *Physical Review Letters*, vol. 107, no. 4, pp. 1–4, 2011.
- [183] K. P. Singh, F. He, P. Ranitovic, W. Cao, S. De, D. Ray, S. Chen, U. Thumm, A. Becker, M. M. Murnane, H. C. Kapteyn, I. V. Litvinyuk, and C. L. Cocke, “Control of electron localization in deuterium molecular ions using an attosecond pulse train and a many-cycle infrared pulse,” *Physical Review Letters*, vol. 104, no. 2, pp. 1–4, 2010.
- [184] V. Roudnev and B. D. Esry, “General theory of carrier-envelope phase effects,” *Physical Review Letters*, vol. 99, no. 22, pp. 1–4, 2007.
- [185] P. H. Bucksbaum, A. Zavriyev, H. G. Muller, and D. W. Schumacher, “Softening of the H<sub>2</sub><sup>+</sup> molecular bond in intense laser fields,” *Physical Review Letters*, vol. 64, no. 16, pp. 1883–1886, 1990.
- [186] A. Giusti-Suzor, X. He, O. Atabek, and F. Mies, “Above-Threshold Dissociation of H<sub>2</sub><sup>+</sup> in Intense Laser Fields,” *Physical review letters*, vol. 64, no. 5, pp. 515–518, 1990.
- [187] T. Zuo and A. D. Bandrauk, “Charge-resonance-enhanced ionization of diatomic molecular ions by intense lasers,” *Physical Review A*, vol. 52, no. 4, pp. 2511–2514, 1995.
- [188] D. Villeneuve, M. Ivanov, and P. Corkum, “Enhanced ionization of diatomic molecules in strong laser fields: A classical model,” *Physical Review A*, vol. 54, no. 1, pp. 736–741, 1996.
- [189] T. Seideman, M. Ivanov, and P. B. Corkum, “Role of Electron Localization in Intense-Field Molecular Ionization,” *Physical Review Letters*, vol. 75, no. 15, pp. 2819–2822, 1995.
- [190] A. S. Alnaser, X. M. Tong, T. Osipov, S. Voss, C. M. Maharjan, B. Shan, Z. Chang, and C. L. Cocke, “Laser-peak-intensity calibration using recoil-ion momentum imaging,” *Physical Review A*, vol. 70, no. 2, pp. 1–6, 2004.
- [191] X. M. Tong, Z. X. Zhao, and C. D. Lin, “Theory of molecular tunneling ionization,” *Physical Review A*, vol. 66, no. 3, pp. 1–11, 2002.
- [192] X. M. Tong and C. D. Lin, “Empirical formula for static field ionization rates of atoms and molecules by lasers in the barrier-suppression regime,” *Journal of Physics B: Atomic, Molecular and Optical Physics*, vol. 38, no. 15, pp. 2593–2600, 2005.
- [193] X. M. Tong, Z. X. Zhao, and C. D. Lin, “Correlation dynamics between electrons and ions in the fragmentation of D<sub>2</sub> molecules by short laser pulses,” *Physical Review A*, vol. 68, p. 043412, 2003.

- [194] X. M. Tong, Z. X. Zhao, and C. D. Lin, “Probing Molecular Dynamics at Attosecond Resolution with Femtosecond Laser Pulses,” *Physical Review Letters*, vol. 91, no. 23, p. 233203, 2003.
- [195] I. V. Litvinyuk, A. S. Alnaser, D. Comtois, D. Ray, A. T. Hasan, J. C. Kieffer, and D. M. Villeneuve, “Wavelength-dependent study of strong-field Coulomb explosion of hydrogen,” *New Journal of Physics*, vol. 10, p. 083011, 2008.
- [196] T.-Y. Xu and F. He, “Influence of laser intensities on the dissociation of hydrogen molecular ions,” *Physical Review A*, vol. 90, no. 5, pp. 1–7, 2014.
- [197] H. Wang, Y. Xu, S. Ulonska, J. S. Robinson, P. Ranitovic, and R. A. Kaindl, “Bright high-repetition-rate source of narrowband extreme-ultraviolet harmonics beyond 22 eV,” *Nature Communications*, vol. 6, 2015.
- [198] H. Liang, P. Krogen, Z. Wang, H. Park, T. Kroh, K. Zawilski, P. Schunemann, J. Moses, L. F. Dimauro, F. X. Kärtner, and K.-h. Hong, “High-energy mid-infrared sub-cycle pulse synthesis from a parametric amplifier,” *Nature Communications*, vol. 8, p. 141, 2017.
- [199] S. Ghimire, A. D. Dichiara, E. Sistrunk, P. Agostini, L. F. Dimauro, and D. A. Reis, “Observation of high-order harmonic generation in a bulk crystal,” *Nature Physics*, vol. 7, no. 2, pp. 138–141, 2011.
- [200] G. Vampa, T. J. Hammond, N. Thiré, B. E. Schmidt, F. Légaré, C. R. McDonald, T. Brabec, D. D. Klug, and P. B. Corkum, “All-Optical Reconstruction of Crystal Band Structure,” *Physical Review Letters*, vol. 115, no. 19, 2015.
- [201] K. Sugioka and Y. Cheng, “Ultrafast lasers-reliable tools for advanced materials processing,” *Light: Science and Applications*, vol. 3, no. 390, pp. 1–12, 2014.
- [202] R. R. Gattass and E. Mazur, “Femtosecond laser micromachining in transparent materials,” *Nature Photonics*, vol. 2, no. 4, pp. 219–225, 2008.
- [203] P. Agostini, F. Fabre, G. Mainfray, G. Petite, and N. K. Rahman, “Free-free transitions following six-photon ionization of xenon atoms,” *Physical Review Letters*, vol. 42, no. 17, pp. 1127–1130, 1979.
- [204] H. Akagi, T. Otobe, A. Staudte, A. Shiner, F. Turner, R. Dorner, D. M. Villeneuve, and P. B. Corkum, “Laser Tunnel Ionization from Multiple Orbitals in HCl,” *Science*, vol. 325, no. 5946, pp. 1364–1367, 2009.
- [205] L. Holmegaard, J. L. Hansen, L. Kalhøj, S. Louise Kragh, H. Stapelfeldt, F. Filsinger, J. Küpper, G. Meijer, D. Dimitrovski, M. Abu-Samha, C. P. Martiny, and L. Bojer Madsen, “Photoelectron angular distributions from strong-field ionization of oriented molecules,” *Nature Physics*, vol. 6, no. 6, pp. 428–432, 2010.

- [206] B. T. Matthias and J. P. Remeika, "Ferroelectricity in the ilmenite structure," *Physical Review*, vol. 76, no. 12, pp. 1886–1887, 1949.
- [207] G. Boyd, R. Miller, K. Nassau, W. Bond, and A. Savage, "LiNbO<sub>3</sub> : an efficient phase matchable nonlinear optical material," *Applied Physics Letters*, vol. 5, no. 11, pp. 234–236, 1964.
- [208] R. S. Weis and T. K. Gaylord, "Lithium Niobate: Summary of Physical Properties and Crystal Structure," *Applied Physics A*, vol. 37, pp. 191–203, 1985.
- [209] B. Chimier, O. Uteza, N. Sanner, M. Sentis, T. Itina, P. Lassonde, F. Legare, F. Vidal, and J. C. Kieffer, "Damage and ablation thresholds of fused-silica in femtosecond regime," *Physical Review B*, vol. 84, no. 9, p. 094104, 2011.
- [210] F. Seitz, "On the Theory of Electron Multiplication," *Phys. Rev.*, vol. 76, no. 9, pp. 1376–1393, 1949.
- [211] B. C. Stuart, M. D. Feit, S. Herman, A. M. Rubenchik, B. W. Shore, and M. D. Perry, "Optical ablation by high-power short-pulse lasers," *Journal of the Optical Society of America B*, vol. 13, no. 2, p. 459, 1996.
- [212] B. C. Stuart, M. D. Feit, S. Herman, A. M. Rubenchik, B. W. Shore, and M. D. Perry, "Nanosecond-to-femtosecond laser-induced breakdown in dielectrics," *Physical Review B*, vol. 53, no. 4, pp. 1749–1761, 1996.
- [213] F. Vidal, T. W. Johnston, S. Laville, O. Barthélemy, M. Chaker, B. Le Drogoff, J. Margot, and M. Sabsabi, "Critical-point phase separation in laser ablation of conductors," *Physical Review Letters*, vol. 86, no. 12, pp. 2573–2576, 2001.
- [214] M. Lenzner, J. Krüger, W. Kautek, and F. Krausz, "Precision laser ablation of dielectrics in the 10-fs regime," *Applied Physics A: Materials Science and Processing*, vol. 68, no. 3, pp. 369–371, 1999.
- [215] W. Kohn and L. Sham, "Self-Consistent Equations Including Exchange and Correlation Effects," *Physical Review*, vol. 140, no. 4A, pp. 1133–1138, 1965.
- [216] K. Sugioka, J. Xu, D. Wu, Y. Hanada, Z. Wang, Y. Cheng, and K. Midorikawa, "Femtosecond laser 3D micromachining: A powerful tool for the fabrication of microfluidic, optofluidic, and electrofluidic devices based on glass," *Lab on a Chip*, vol. 14, no. 18, pp. 3447–3458, 2014.
- [217] D. Brüske, S. Sunstov, C. E. Rüter, and D. Kip, "Efficient ridge waveguide amplifiers and lasers in Er-doped lithium niobate by optical grade dicing and three-side Er and Ti in-diffusion," *Optics Express*, vol. 25, no. 23, p. 29374, 2017.
- [218] D. Brüske, S. Sunstov, C. E. Rüter, and D. Kip, "Efficient Nd:Ti:LiNbO<sub>3</sub> ridge waveguide lasers emitting around 1085 nm," *Optics Express*, vol. 27, no. 6, p. 8884, 2019.

- [219] L. Li, W. Nie, Z. Li, Q. Lu, C. Romero, J. R. Vázquez De Aldana, and F. Chen, “All-laser-micromachining of ridge waveguides in LiNbO<sub>3</sub> crystal for mid-infrared band applications,” *Scientific Reports*, vol. 7, no. 1, pp. 1–7, 2017.
- [220] V. Wanie, T. Shao, P. Lassonde, H. Ibrahim, J. Deschamps, J.-Q. Liu, F. A. Vargas, F. Vidal, A. Ruediger, F. Calegari, X.-B. Bian, and F. Légaré, “Control of strong-field ionization in ferroelectric lithium niobate: role of the spontaneous polarization,” *Physical Review B*, vol. 101, no. 18, p. 184103, 2020.
- [221] C. B. Schaffer, A. Brodeur, and E. Mazur, “Laser-induced breakdown and damage in bulk transparent materials induced by tightly focused femtosecond laser pulses,” *Measurement Science and Technology*, vol. 12, no. 11, pp. 1784–1794, 2001.
- [222] A. C. Tien, S. Backus, H. Kapteyn, M. Murnane, and G. Mourou, “Short-pulse laser damage in transparent materials as a function of pulse duration,” *Physical Review Letters*, vol. 82, no. 19, pp. 3883–3886, 1999.
- [223] J. B. Ashcom, R. R. Gattass, C. B. Schaffer, and E. Mazur, “Numerical aperture dependence of damage and supercontinuum generation from femtosecond laser pulses in bulk fused silica,” *Journal of the Optical Society of America B*, vol. 23, no. 11, p. 2317, 2006.
- [224] M. Gertsvolf, H. Jean-Ruel, P. P. Rajeev, D. D. Klug, D. M. Rayner, and P. B. Corkum, “Orientation-dependent multiphoton ionization in wide band gap crystals,” *Physical Review Letters*, vol. 101, no. 24, p. 243001, 2008.
- [225] X. Li, W. Rong, L. Jiang, K. Zhang, C. Li, Q. Cao, G. Zhang, and Y. Lu, “Generation and elimination of polarization-dependent ablation of cubic crystals by femtosecond laser radiation,” *Optics Express*, vol. 22, no. 24, p. 30170, 2014.
- [226] S. M. Golin, S. E. Kirkwood, D. D. Klug, D. M. Villeneuve, D. M. Rayner, C. A. Herrero, and P. B. Corkum, “Strong field processes inside gallium arsenide,” *Journal of Physics B*, vol. 47, no. 20, p. 204025, 2014.
- [227] A. Dhar and A. Mansingh, “Optical properties of reduced lithium niobate single crystals,” *Journal of Applied Physics*, vol. 68, no. 11, pp. 5804–5809, 1990.
- [228] X. Liu, D. Du, and G. Mourou, “Laser ablation and micromachining with ultrashort laser pulses,” *IEEE Journal of Quantum Electronics*, vol. 33, no. 10, pp. 1706–1716, 1997.
- [229] S. Sanna and W. G. Schmidt, “Lithium niobate X-cut, Y-cut, and Z-cut surfaces from ab initio theory,” *Physical Review B*, vol. 81, no. 21, p. 214116, 2010.
- [230] A. Riefer, S. Sanna, A. Schindlmayr, and W. G. Schmidt, “Optical response of stoichiometric and congruent lithium niobate from first-principles calculations,” *Physical Review B - Condensed Matter and Materials Physics*, vol. 87, no. 19, p. 195208, 2013.

- [231] R. Husin, F. W. Badrudin, M. F. Taib, and M. Z. Yahya, “Effects of strain on electronic and optical properties of LiNbO<sub>3</sub>: A first principles study,” *Materials Research Express*, vol. 6, no. 11, 2019.
- [232] G. Kresse and J. Hafner, “Ab initio molecular dynamics for liquid metals,” *Physical Review B*, vol. 47, no. 1, pp. 558–561, 1993.
- [233] P. E. Blöchl, “Projector augmented-wave method,” *Physical Review B*, vol. 50, no. 24, pp. 17953–17979, 1994.
- [234] “See Supplemental Material for details on the theoretical model and complementary calculations..”
- [235] G. Vampa, C. R. McDonald, G. Orlando, P. B. Corkum, and T. Brabec, “Semiclassical analysis of high harmonic generation in bulk crystals,” *Physical Review B*, vol. 91, no. 6, p. 064302, 2015.
- [236] C. R. McDonald, G. Vampa, P. B. Corkum, and T. Brabec, “Intense-Laser Solid State Physics: Unraveling the Difference between Semiconductors and Dielectrics,” *Physical Review Letters*, vol. 118, no. 17, p. 173601, 2017.
- [237] S. M. Hankin, D. M. Villeneuve, P. B. Corkum, and D. M. Rayner, “Intense-field laser ionization rates in atoms and molecules,” *Physical Review A*, vol. 64, no. 1, p. 013405, 2001.
- [238] D. Homoelle, S. Wielandy, A. L. Gaeta, N. F. Borrelli, and C. Smith, “Infrared photosensitivity in silica glasses exposed to femtosecond laser pulses,” *Optics Letters*, vol. 24, no. 18, p. 1311, 1999.
- [239] N. Bloembergen, “Laser Induced Electric Breakdown in Solids,” *IEEE Journal of Quantum Electronics*, vol. 10, no. 3, pp. 375–386, 1974.
- [240] A. V. Mitrofanov, A. J. Verhoef, E. E. Serebryannikov, J. Lumeau, L. Glebov, A. M. Zheltikov, and A. Baltuka, “Optical detection of attosecond ionization induced by a few-cycle laser field in a transparent dielectric material,” *Physical Review Letters*, vol. 106, no. 14, p. 147401, 2011.
- [241] A. Schiffrin, T. Paasch-Colberg, N. Karpowicz, V. Apalkov, D. Gerster, S. Mühlbrandt, M. Korbman, J. Reichert, M. Schultze, S. Holzner, J. V. Barth, R. Kienberger, R. Ernstorfer, V. S. Yakovlev, M. I. Stockman, and F. Krausz, “Optical-field-induced current in dielectrics,” *Nature*, vol. 493, no. 7430, pp. 70–74, 2013.
- [242] A. Guarino, G. Poberaj, D. Rezzonico, R. Degl’Innocenti, and P. Günter, “Electro-optically tunable microring resonators in lithium niobate,” *Nature Photonics*, vol. 1, no. 7, pp. 407–410, 2007.

- [243] B. J. Eggleton, B. Luther-Davies, and K. Richardson, “Chalcogenide photonics,” *Nature Photonics*, vol. 5, no. 3, pp. 141–148, 2011.
- [244] H. Li, D. Ray, S. De, I. Znakovskaya, W. Cao, G. Laurent, Z. Wang, M. F. Kling, A. T. Le, and C. L. Cocke, “Orientation dependence of the ionization of CO and NO in an intense femtosecond two-color laser field,” *Physical Review A*, vol. 84, no. 4, p. 043429, 2011.
- [245] H. Ohmura, N. Saito, and T. Morishita, “Molecular tunneling ionization of the carbonyl sulfide molecule by double-frequency phase-controlled laser fields,” *Physical Review A*, vol. 89, no. 1, p. 013405, 2014.
- [246] Q. Liao, P. Lu, P. Lan, W. Cao, and Y. Li, “Phase dependence of high-order above-threshold ionization in asymmetric molecules,” *Physical Review A*, vol. 77, no. 1, p. 013408, 2008.
- [247] G. L. Kamta and A. D. Bandrauk, “Phase dependence of enhanced ionization in asymmetric molecules,” *Physical Review Letters*, vol. 94, no. 20, p. 203003, 2005.
- [248] T. Endo, H. Fujise, Y. Kawachi, A. Ishihara, A. Matsuda, M. Fushitani, H. Kono, and A. Hishikawa, “Selective bond breaking of CO<sub>2</sub> in phase-locked two-color intense laser fields: Laser field intensity dependence,” *Physical Chemistry Chemical Physics*, vol. 19, no. 5, pp. 3550–3556, 2017.
- [249] S. Watanabe, K. Kondo, Y. Nabekawa, A. Sagisaka, and Y. Kobayashi, “Two-color phase control in tunneling ionization and harmonic generation by a strong laser field and its third harmonic,” *Physical Review Letters*, vol. 73, no. 20, pp. 2692–2695, 1994.
- [250] D. W. Schumacher, F. Weihe, H. G. Muller, and P. H. Bucksbaum, “Phase dependence of intense field ionization: A study using two colors,” *Physical Review Letters*, vol. 73, no. 10, pp. 1344–1347, 1994.
- [251] C. Thierfelder, S. Sanna, A. Schindlmayr, and W. G. Schmidt, “Do we know the band gap of lithium niobate?,” *Physica Status Solidi C*, vol. 7, no. 2, pp. 362–365, 2010.
- [252] A. Riefer, M. Friedrich, S. Sanna, U. Gerstmann, A. Schindlmayr, and W. G. Schmidt, “LiNbO<sub>3</sub> electronic structure: Many-body interactions, spin-orbit coupling, and thermal effects,” *Physical Review B*, vol. 93, no. 7, p. 075205, 2016.
- [253] J. M. Liu, “Simple technique for measurements of pulsed Gaussian-beam spot sizes,” *Optics Letters*, vol. 7, no. 5, p. 196, 1982.
- [254] O. Uteza, B. Bussi ere, F. Canova, J. P. Chambaret, P. Delaporte, T. Itina, and M. Sentis, “Laser-induced damage threshold of sapphire in nanosecond, picosecond and femtosecond regimes,” *Applied Surface Science*, vol. 254, no. 4, pp. 799–803, 2007.

- [255] S. R. Phillpot and V. Gopalan, “Coupled displacive and order–disorder dynamics in LiNbO<sub>3</sub> by molecular-dynamics simulation,” *Applied Physics Letters*, vol. 84, no. 11, pp. 1916–1918, 2004.
- [256] V. Gopalan, T. E. Mitchell, Y. Furukawa, and K. Kitamura, “The role of nonstoichiometry in 180 degrees domain switching of LiNbO<sub>3</sub> crystals,” *Applied Physics Letters*, vol. 72, no. 16, pp. 1981–1983, 1998.
- [257] D. Lee, H. Xu, V. Dierolf, V. Gopalan, and S. R. Phillpot, “Structure and energetics of ferroelectric domain walls in LiNbO<sub>3</sub> from atomic-level simulations,” *Physical Review B*, vol. 82, p. 014104, 2010.
- [258] F. Johann and E. Soergel, “Quantitative measurement of the surface charge density,” *Applied Physics Letters*, vol. 95, no. 23, p. 232906, 2009.
- [259] A. Etches and L. B. Madsen, “Extending the strong-field approximation of high-order harmonic generation to polar molecules: Gating mechanisms and extension of the harmonic cut-off,” *Journal of Physics B: Atomic, Molecular and Optical Physics*, vol. 43, no. 15, p. 155602, 2010.
- [260] M. Chattoraj, S. L. Laursen, B. Paulson, D. D. Chung, G. L. Closs, and D. H. Levy, “Intramolecular electron transfer in a molecular beam,” *Journal of Physical Chemistry*, vol. 96, no. 22, pp. 8778–8784, 1992.
- [261] R. Weinkauff, P. Schanen, D. Yang, S. Soukara, and E. W. Schlag, “Elementary processes in peptides: Electron mobility and dissociation in peptide cations in the gas phase,” *Journal of Physical Chemistry*, vol. 99, no. 28, pp. 11255–11265, 1995.
- [262] R. Weinkauff, P. Schanen, A. Metsala, E. W. Schlag, M. Bürgle, and H. Kessler, “Highly efficient charge transfer in peptide cations in the gas phase: Threshold effects and mechanism,” *Journal of Physical Chemistry*, vol. 100, no. 47, pp. 18567–18585, 1996.
- [263] L. Lehr, T. Horneff, R. Weinkauff, and E. W. Schlag, “Femtosecond dynamics after ionization: 2-phenylethyl-N,N-dimethylamine as a model system for nonresonant downhill charge transfer in peptides,” *Journal of Physical Chemistry A*, vol. 109, no. 36, pp. 8074–8080, 2005.
- [264] S. Lünemann, A. I. Kuleff, and L. S. Cederbaum, “Ultrafast charge migration in 2-phenylethyl-N,N-dimethylamine,” *Chemical Physics Letters*, vol. 450, no. 4-6, pp. 232–235, 2008.
- [265] E. Perfetto and G. Stefanucci, “CHEERS: A tool for correlated hole-electron evolution from real-time simulations,” *Journal of Physics Condensed Matter*, vol. 30, no. 46, p. 465901, 2018.
- [266] M. Uiberacker, T. Uphues, M. Schultze, A. J. Verhoef, V. Yakovlev, M. F. Kling, J. Rauschenberger, N. M. Kabachnik, H. Schröder, M. Lezius, K. L. Kompa, H. G. Muller, M. J. Vrakking,

- S. Hendel, U. Kleineberg, U. Heinzmann, M. Drescher, and F. Krausz, "Attosecond real-time observation of electron tunnelling in atoms," *Nature*, vol. 446, no. 7136, pp. 627–632, 2007.
- [267] M. Drescher, M. Hentschel, R. Kienberger, M. Uiberacker, V. Yakovlev, A. Scrinzi, T. Westerwalbesloh, and U. Kleineberg, "Time-resolved atomic inner-shell spectroscopy," *Nature*, vol. 419, no. October, pp. 803–807, 2002.
- [268] S. Gilbertson, M. Chini, X. Feng, S. Khan, Y. Wu, and Z. Chang, "Monitoring and controlling the electron dynamics in helium with isolated attosecond pulses," *Physical Review Letters*, vol. 105, no. 26, pp. 1–4, 2010.
- [269] J. Lacoursière, M. Meyer, L. Nahon, P. Morin, and M. Larzillière, "Time-resolved pump-probe photoelectron spectroscopy of helium using a mode-locked laser synchronized with synchrotron radiation pulses," *Nuclear Inst. and Methods in Physics Research, A*, vol. 351, no. 2-3, pp. 545–553, 1994.
- [270] S. Pilling, A. Lago, L. Coutinho, R. de Castilho, G. de Souza, and A. Naves de Brito, "Dissociative photoionization of adenine following valence excitation," *Rapid Communications in Mass Spectrometry*, vol. 21, pp. 3646–3652, 2007.
- [271] K. K. Khanna and S. P. Jackson, "DNA double-strand breaks: Signaling, repair and the cancer connection," *Nature Genetics*, vol. 27, no. 3, pp. 247–254, 2001.
- [272] M. K. Shukla and J. Leszczynski, *Radiation induced molecular phenomena in nucleic acids: a comprehensive theoretical and experimental analysis*. Springer, 2008.
- [273] S. Pan, X. Sun, and J. K. Lee, "DNA Stability in the Gas Versus Solution Phases: A Systematic Study of Thirty-One Duplexes with Varying Length, Sequence, and Charge Level," *Journal of the American Society for Mass Spectrometry*, vol. 17, no. 10, pp. 1383–1395, 2006.
- [274] L. S. Cederbaum and J. Zobeley, "Ultrafast charge migration by electron correlation," *Chemical Physics Letters*, vol. 307, no. 3-4, pp. 205–210, 1999.
- [275] A. M. Hanna, O. Vendrell, A. Ourmazd, and R. Santra, "Laser control over the ultrafast Coulomb explosion of  $N_2^{2+}$  after Auger decay: A quantum-dynamics investigation," *Physical Review A*, vol. 95, no. 4, pp. 1–10, 2017.
- [276] V. Averbukh, P. V. Demekhin, P. Kolorenč, S. Scheit, S. D. Stoychev, A. I. Kuleff, Y. C. Chiang, K. Gokhberg, S. Kopelke, N. Sisourat, and L. S. Cederbaum, "Interatomic electronic decay processes in singly and multiply ionized clusters," *Journal of Electron Spectroscopy and Related Phenomena*, vol. 183, no. 1-3, pp. 36–47, 2011.
- [277] M. Nisoli, P. Decleva, F. Calegari, A. Palacios, and F. Martín, "Attosecond Electron Dynamics in Molecules," *Chemical Reviews*, vol. 117, no. 16, pp. 10760–10825, 2017.

- [278] G. Sansone, T. Pfeifer, K. Simeonidis, and A. I. Kuleff, “Electron correlation in real time,” *ChemPhysChem*, vol. 13, no. 3, pp. 661–680, 2012.
- [279] A. Marciniak, V. Despré, V. Loriot, G. Karras, M. Hervé, L. Quintard, F. Catoire, C. Joblin, E. Constant, A. I. Kuleff, and F. Lépine, “Electron correlation driven non-adiabatic relaxation in molecules excited by an ultrashort extreme ultraviolet pulse,” *Nature Communications*, vol. 10, no. 1, pp. 1–8, 2019.
- [280] P. B. Corkum, N. H. Burnett, and M. Y. Ivanov, “Subfemtosecond pulses,” *Optics Letters*, vol. 19, no. 22, pp. 1870–1872, 1994.
- [281] M. A. Marques, A. Castro, G. F. Bertsch, and A. Rubio, “Octopus: A first-principles tool for excited electron-ion dynamics,” *Computer Physics Communications*, vol. 151, no. 1, pp. 60–78, 2003.
- [282] A. Castro, H. Appel, M. Oliveira, C. A. Rozzi, X. Andrade, F. Lorenzen, M. A. Marques, E. K. Gross, and A. Rubio, “Octopus: A tool for the application of time-dependent density functional theory,” *Physica Status Solidi (B) Basic Research*, vol. 243, no. 11, pp. 2465–2488, 2006.
- [283] X. Andrade, D. Strubbe, U. De Giovannini, A. H. Larsen, M. J. Oliveira, J. Alberdi-Rodriguez, A. Varas, I. Theophilou, N. Helbig, M. J. Verstraete, L. Stella, F. Nogueira, A. Aspuru-Guzik, A. Castro, M. A. Marques, and A. Rubio, “Real-space grids and the Octopus code as tools for the development of new simulation approaches for electronic systems,” *Physical Chemistry Chemical Physics*, vol. 17, no. 47, pp. 31371–31396, 2015.
- [284] E. Runge and E. Gross, “Time-dependent density-functional theory for multicomponent systems,” *Physical Review A*, vol. 52, no. 12, pp. 997–1000, 1984.
- [285] G. F. Bertsch, J. I. Iwata, A. Rubio, and K. Yabana, “Real-space, real-time method for the dielectric function,” *Physical Review B*, vol. 62, no. 12, pp. 7998–8002, 2000.
- [286] J. L. Alonso, X. Andrade, P. Echenique, F. Falceto, D. Prada-Gracia, and A. Rubio, “Efficient formalism for large-scale ab initio molecular dynamics based on time-dependent density functional theory,” *Physical Review Letters*, vol. 101, no. 9, p. 096403, 2008.
- [287] A. Muñoz, J. C. Oller, F. Blanco, J. D. Gorfinkiel, P. Limão-Vieira, and G. García, “Electron-scattering cross sections and stopping powers in H<sub>2</sub>O,” *Physical Review A - Atomic, Molecular, and Optical Physics*, vol. 76, no. 5, pp. 1–7, 2007.
- [288] M. A. Huels, B. Boudaïffa, P. Cloutier, D. Hunting, and L. Sanche, “Single, double, and multiple double strand breaks induced in DNA by 3-100 eV electrons,” *Journal of the American Chemical Society*, vol. 125, no. 15, pp. 4467–4477, 2003.

- [289] F. Alvarado, S. Bari, R. Hoekstra, and T. Schlathölter, “Interactions of neutral and singly charged keV atomic particles with gas-phase adenine molecules,” *Journal of Chemical Physics*, vol. 127, no. 3, p. 034301, 2007.
- [290] R. Brédy, J. Bernard, L. Chen, G. Montagne, B. Li, and S. Martin, “Fragmentation of adenine under energy control,” *Journal of Chemical Physics*, vol. 130, no. 11, p. 114305, 2009.
- [291] P. J. M. Van Der Burgt, F. Mahon, G. Barrett, and M. L. Gradziel, “Electron impact fragmentation of thymine: Partial ionization cross sections for positive fragments,” *European Physical Journal D*, vol. 69, p. 173, 2015.
- [292] C. S. Cucinotta, D. Hughes, and P. Ballone, “Real-time real-space TD-DFT for atoms: Benchmark computations on a nonspherical logarithmic grid,” *Physical Review B*, vol. 86, no. 4, p. 045114, 2012.
- [293] F. Covito, E. Perfetto, A. Rubio, and G. Stefanucci, “Real-time dynamics of Auger wave packets and decays in ultrafast charge migration processes,” *Physical Review A*, vol. 97, no. 6, p. 061401, 2018.
- [294] A. Zehnacker and M. A. Suhm, “Chirality recognition between neutral molecules in the gas phase,” *Angewandte Chemie - International Edition*, vol. 47, no. 37, pp. 6970–6992, 2008.
- [295] N. J. Greenfield, “Using circular dichroism spectra to estimate protein secondary structure,” *Nature Protocols*, vol. 1, no. 6, pp. 2876–2890, 2007.
- [296] S. Beaulieu, A. Comby, B. Fabre, D. Descamps, A. Ferré, G. Garcia, R. Géneaux, F. Légaré, L. Nahon, S. Petit, T. Ruchon, B. Pons, V. Blanchet, and Y. Mairesse, “Probing ultrafast dynamics of chiral molecules using time-resolved photoelectron circular dichroism,” *Faraday Discussions*, vol. 194, pp. 325–348, 2016.
- [297] B. Ritchie, “Theory of the angular distribution for ejection of photoelectrons from optically active molecules and molecular negative ions. II,” *Physical Review A*, vol. 14, no. 1, pp. 359–362, 1976.
- [298] N. Böwering, T. Lischke, B. Schmidtke, N. Müller, T. Khalil, and U. Heinzmann, “Asymmetry in photoelectron emission from chiral molecules induced by circularly polarized light,” *Physical Review Letters*, vol. 86, no. 7, pp. 1187–1190, 2001.
- [299] C. S. Lehmann, N. B. Ram, I. Powis, and M. H. Janssen, “Imaging photoelectron circular dichroism of chiral molecules by femtosecond multiphoton coincidence detection,” *Journal of Chemical Physics*, vol. 139, no. 23, 2013.
- [300] A. T. J. B. Eppink and D. H. Parker, “Velocity map imaging of ions and electrons using electrostatic lenses: Application in photoelectron and photofragment ion imaging of molecular oxygen,” *Review of Scientific Instruments*, vol. 68, no. 9, pp. 3477–3484, 1997.

- [301] A. J. Heck and D. W. Chandler, "Imaging technique for the study of chemical reaction dynamics," *Annual Review of Physical Chemistry*, vol. 46, pp. 335–372, 1995.
- [302] C. J. Dasch, "One-dimensional tomography: a comparison of Abel, onion-peeling, and filtered backprojection methods," *Applied Optics*, vol. 31, no. 8, p. 1146, 1992.
- [303] V. Dribinski, A. Ossadtchi, V. A. Mandelshtam, and H. Reisler, "Reconstruction of Abel-transformable images: The Gaussian basis-set expansion Abel transform method," *Review of Scientific Instruments*, vol. 73, no. 7, p. 2634, 2002.
- [304] G. A. Garcia, L. Nahon, and I. Powis, "Two-dimensional charged particle image inversion using a polar basis function expansion," *Review of Scientific Instruments*, vol. 75, no. 11, pp. 4989–4996, 2004.
- [305] L. Nahon, G. A. Garcia, C. J. Harding, E. Mikajlo, and I. Powis, "Determination of chiral asymmetries in the valence photoionization of camphor enantiomers by photoelectron imaging using tunable circularly polarized light," *Journal of Chemical Physics*, vol. 125, no. 11, p. 114309, 2006.
- [306] G. A. Garcia, H. Dossmann, L. Nahon, S. Daly, and I. Powis, "Photoelectron circular dichroism and spectroscopy of trifluoromethyl- and methyl-oxirane: A comparative study," *Physical Chemistry Chemical Physics*, vol. 16, no. 30, pp. 16214–16224, 2014.
- [307] G. A. Garcia, L. Nahon, C. J. Harding, and I. Powis, "Chiral signatures in angle-resolved valence photoelectron spectroscopy of pure glycidol enantiomers," *Physical Chemistry Chemical Physics*, vol. 10, no. 12, pp. 1628–1639, 2008.
- [308] S. Turchini, D. Catone, G. Contini, N. Zema, S. Irrera, M. Stener, D. Di Tommaso, P. Decleva, and T. Prospero, "Conformational effects in photoelectron circular dichroism of alaninol," *ChemPhysChem*, vol. 10, no. 11, pp. 1839–1846, 2009.
- [309] I. Powis, C. J. Harding, G. A. Garcia, and L. Nahon, "A valence photoelectron imaging investigation of chiral asymmetry in the photoionization of fenchone and camphor," *ChemPhysChem*, vol. 9, no. 3, pp. 475–483, 2008.
- [310] L. Nahon, L. Nag, G. A. Garcia, I. Myrgorodska, U. Meierhenrich, S. Beaulieu, V. Wanie, V. Blanchet, R. Géneaux, and I. Powis, "Determination of accurate electron chiral asymmetries in fenchone and camphor in the VUV range: Sensitivity to isomerism and enantiomeric purity," *Physical Chemistry Chemical Physics*, vol. 18, no. 18, pp. 12696–12706, 2016.
- [311] L. Nahon, G. A. Garcia, and I. Powis, "Valence shell one-photon photoelectron circular dichroism in chiral systems," *Journal of Electron Spectroscopy and Related Phenomena*, vol. 204, pp. 322–334, 2015.

- [312] G. A. Garcia, L. Nahon, S. Daly, and I. Powis, “Vibrationally induced inversion of photoelectron forward-backward asymmetry in chiral molecule photoionization by circularly polarized light,” *Nature Communications*, vol. 4, pp. 1–6, 2013.
- [313] S. Beaulieu, A. Comby, D. Descamps, B. Fabre, G. A. Garcia, R. Généaux, A. G. Harvey, F. Légaré, Z. Mašín, L. Nahon, A. F. Ordonez, S. Petit, B. Pons, Y. Mairesse, O. Smirnova, and V. Blanchet, “Photoexcitation circular dichroism in chiral molecules,” *Nature Physics*, vol. 14, no. 5, pp. 484–489, 2018.
- [314] R. E. Goetz, T. A. Isaev, B. Nikoobakht, R. Berger, and C. P. Koch, “Theoretical description of circular dichroism in photoelectron angular distributions of randomly oriented chiral molecules after multi-photon photoionization,” *Journal of Chemical Physics*, vol. 146, no. 2, 2017.
- [315] R. Dörner, V. Mergel, H. Bräuning, M. Achler, T. Weber, K. Khayyat, O. Jagutzki, L. Spielberger, J. Ullrich, R. Moshhammer, Y. Azuma, M. H. Prior, C. L. Cocke, and H. Schmidt-Böcking, “Recoil ion momentum spectroscopy a ‘momentum microscope’ to view atomic collision dynamics,” vol. 330, pp. 334–346, 2009.
- [316] J. Ullrich, R. Moshhammer, A. Dorn, R. Dörner, L. P. H. Schmidt, and H. Schmidt-Böcking, “Recoil-ion and electron momentum spectroscopy: Reaction-microscopes,” *Reports on Progress in Physics*, vol. 66, no. 9, pp. 1463–1545, 2003.
- [317] S. Mikaelsson, J. Vogelsang, C. Guo, I. Sytceвич, A.-L. Viotti, F. Langer, Y.-C. Cheng, S. Nandi, W. Jin, A. Olofsson, R. Weissenbilder, J. Mauritsson, A. L’Huillier, M. Gisselbrecht, and C. L. Arnold, “A high-repetition rate attosecond light source for time-resolved coincidence spectroscopy,” *Nanophotonics*, vol. 0, no. 0, 2020.
- [318] G.-C. Wang and T.-M. Lu, *RHEED Transmission Mode and Pole Figures*. Springer New York, 2014.
- [319] C. R. McDonald, G. Vampa, P. B. Corkum, and T. Brabec, “Intense-Laser Solid State Physics: Unraveling the Difference between Semiconductors and Dielectrics,” *Physical Review Letters*, vol. 118, no. 17, p. 173601, 2017.
- [320] S. Mamoun, A. E. Merad, and L. Guilbert, “Energy band gap and optical properties of lithium niobate from ab initio calculations,” *Computational Materials Science*, vol. 79, pp. 125–131, 2013.